University of Bath

PHD

Effect of TiO2 on the electrical conductivity of Al2O3

Uppal, Rajeev

Award date:
2000

Awarding institution:
University of Bath

Link to publication

Effect of TiO_2 on the Electrical Conductivity of Al_2O_3

Submitted by **Rajeev Uppal**
For the degree of PhD of the University of Bath
2000

RAJEEV UPPAL

ProQuest LLC
789 East Eisenhower Parkway
P.O. Box 1346
Ann Arbor, MI 48106-1346

Summary

The present study was under-taken to improve the performance of the alumina insulators used in Super-Klystron application. The intention was to develop a composition that would have physical characteristics similar to the existing alumina insulator but have lower electrical resistivity and could be incorporated into the insulator by preparing as a functional gradient material. The low resistivity compositions were successfully prepared by adding TiO_2, Cr_2O_3 and V_2O_5 dopants to the original alumina insulator composition.

The experimental programme involved, a study of the reference commercial alumina insulator for its microstructure and chemical characteristics, evaluation of the sample preparation procedures for electron microscopy, development of a base composition in order to emulate the reference material, and finally doping this material with various percentages of TiO_2, V_2O_5 and Cr_2O_3. The samples when so prepared were tested for their electrical properties using an Impedance Spectroscopy technique. An explanation for the reduced resistivity was linked to the defect chemistry, the microstructural features and phases present.

The TiO_2 present in the compositions studied became more conductive when the densified samples were subsequently annealed in H_2 atmosphere. The best results for reduced resistivity were obtained for a TiO_2 addition which, it is suggested, reached a threshold value so as to form a percolation path between conducting TiO_2 rich precipitates. Compositions containing both TiO_2 and V_2O_5 were more successful in reducing the resistivity in the as-fired state. However V_2O_5 had an opposite effect on annealing in H_2, as it caused a marginal increase in the resistivity of the ceramic.

A preliminary investigation was carried out to study the feasibility for the processing of a functional gradient material. The sintering kinetics of the base composition was compared with each of the doped compositions by studying the sintering shrinkage by the means of dilatometry. Though the chosen compositions had large difference in shrinkage rates, the study has shown that a functional gradient material is practical and can be made by preparing a multi-layer compact.

CONTENTS

8.1 Introduction
8.2 Conclusions to this project

LIST OF FIGURES

LIST OF SYMBOLS AND ABBREVIATIONS

RF	Radio Frequency
PCA	Polycrystalline alumina
$\tan\delta$	Loss tangent of a dielectric
SEE	Secondary electron emission
σ	conductivity
σ_i	ionic conductivity
σ_{el}	electronic conductivity
t_i	ionic transference number
t_{el}	electronic transference number
p_{O2}	partial pressure of oxygen
V_{Al}'''	Vacancy at an Al site with 3 free electrons
$Al_i^{\bullet\bullet\bullet}$	Aluminium ion in an interstitial site with 3 excess holes.
$V_O^{\bullet\bullet}$	Oxygen vacancy minus of 2 electrons
O_i''	O^{2-} ion in interstitial site
Co_{Al}'	Cobalt at an aluminium site with one free electron
$h^{\bullet}$	electron hole
e'	electron
R	resistance
C	capacitance
ω	angular frequency
f	frequency
Z	AC impedance
Z'	real part of impedance
Z''	imaginary part of impedance
ε	permittivity
SEM	Scanning electron microscope
TEM	Transmission electron microscope
EDX	Energy Dispersive X-ray

EPMA	Electron Probe Micro-Analysis
XRD	X-ray Diffraction
BS	British standard
ASTM	American Society for Testing of Materials

ACKNOWLEDGEMENTS

I take this opportunity to thank my Supervisor, Professor Ronald Stevens, whose constant guidance and suggestions were a great source of motivation for the project.

I would also like to thank Dr. Paul John of Marconi Applied Technologies who helped with the H_2 firing. My thanks to Professor Daryl Almond for numerous suggestions especially on the electrical testing. I thank all the staff and fellow students of the department who helped me during my studies.

I would be failing in my duty if I fail to thank the ORS committee and the University of Bath for the financial support, and BHEL for giving the leave to take up this study.

I would like to give my gratitude to my parents and my wife Geeta for their moral support and patience throughout my education.

Finally I wish to dedicate this thesis to my son Hiten, whose birth last year was a big turn in my life and who became a great source to unwind on returning home after hard days work.

CHAPTER I

INTRODUCTION

The chapter gives the introduction to the project and includes the motivation for the work.

1. INTRODUCTION

Alumina as an engineering ceramic material became popular in the first half of the 20th century. Today it accounts for more than three quarters of the world engineering ceramics production. Its high popularity is a result of the remarkable range of properties it shows and the areas of applications it covers, which include mechanical, chemical, thermal, electrical and electronic devices. Its high resistivity, low tanδ and low permitivity has made it a popular electrical insulator. Furthermore its high refractoriness, low out-gassing, chemical inertness and ease of metallizing, in comparison with the competing insulators such as porcelain, glass and polymers, has resulted in it being the choice for the most demanding application for electron insulation devices. The range of applications has grown from traditional support and stand off insulators at high temperature, to insulators in vacuum windows in RF environment and microwave heating systems in fusion applications. One such area is the use of alumina insulator in Super-klystron devices.

The Super-klystron device is used in physics laboratories as a source of radio frequency (RF) power and as a test bed for determining the electric stand off properties of various materials and geometric shapes. A typical super-klystron manufactured by Marconi Applied Technologies is shown in figure 1.1. In klystrons a high purity alumina window is used to separate the components under vacuum from those at atmospheric pressure. A 94% alumina insulator is utilised to maintain a voltage stand-off between anode and cathode. Both these alumina parts are metallized with a molybdenum-manganese coating, which helps in forming a hermetic seal with the metal parts, cathodes, etc, and prevent vacuum leakage through the sealed joints. The high voltages, high frequencies and vacuum atmosphere put the components under a high electrical stress.

This work was undertaken on account of the problems associated with the alumina ceramic failure in the Super-klystron device and other electron insulation devices. There are two major problems faced by the insulators.

1) thermal breakdown under microwave conditions and
2) excessive charge build up on the alumina surface, which when unable to leak to ground, leads to voltage spikes (figure 1.2). These spikes interfere with the electronics

of the device and the resulting over-voltage breakdown cascade can cause costly failure of the downline electronics system.

A possible solution to this problem is to use a lower resistivity (10^{11} to $5x10^9\Omega$cm) surface layer on the insulator that permits the leakage current to disperse the built up charge. Earlier attempts to use a low conductivity glaze layer on an alumina insulator were unsuccessful due to the interference of the glaze layer with the metallizing {1} and its unstable nature in reduced oxygen atmospheres. Similarly, the use of TiN coating on a surface has also been unsuccessful (discussed in section 2.1). TiO_2 is known to be useful as an agent for dissipating the charge in alumina thread guides. This indicates its potential for use as a dopant for charge dissipation from an alumina surface in a klystron application.

The present work outlines studies on the additions of TiO_2 and other dopants as a means of generating an alternate conducting mechanism for overcoming the electrical failure. The incorporation of dopants to the alumina insulator is achieved by preparing a functional gradient material, such that the doping results in the inner surface layer having reduced resistivity, in the range of $5x10^9$-10^{11} Ωcm, while the outer surface is the same as the original composition presently in use (> $10^{14}\Omega$-cm). The reference material used is a *liquid phase sintered** 94%Alumina insulator manufactured by Seagoe for English Electric Valves (now Marconi Applied Technologies). The work is such that the composition of the base insulator matches that of the Seagoe alumina and the shrinkage of the new composition matches the shrinkage of the base insulator. This is necessary to prevent the outgrowth of firing stresses in a functional gradient insulator while sintering takes place.

---

*- *There are three different forms of alumina ceramic, single crystal, polycrystalline and liquid phase sintered. Single crystal alumina typically are the naturally occurring or synthetically grown corundum, sapphire and ruby crystals. Polycrystalline alumina (PCA) or solid state sintered alumina involves the coagulation of active alumina particles by controlled grain growth through surface diffusion to produce very high purity alumina ceramic (>99%). Liquid phase sintered alumina (LPS Alumina) involves the use of glass in form of a second phase at the grain boundary that helps in the bonding of alumina particles to form a dense ceramic, typically <98% pure. This is commercially the most popular alumina type.*

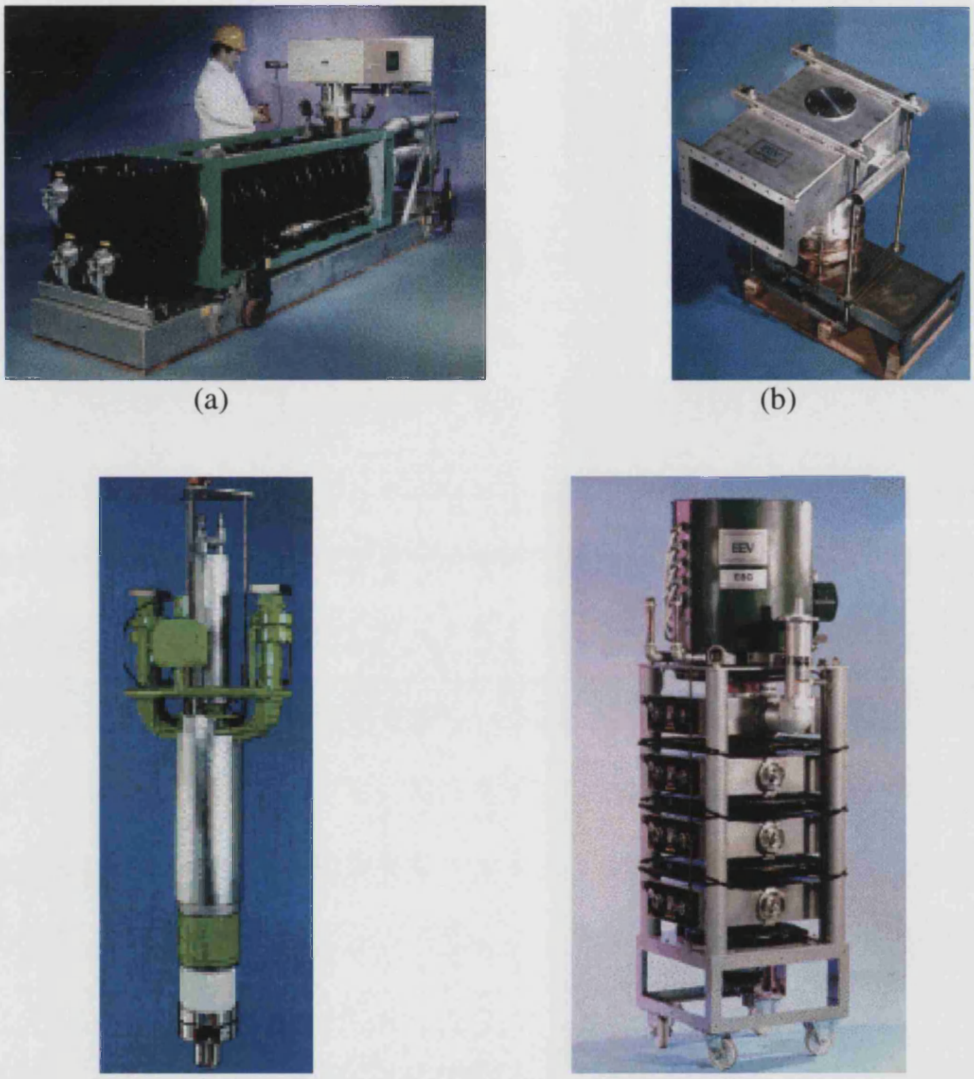

(a) (b)

(c) (d)

Figure 1.1: Klystrons (a) Super-klystron (b) RF window, containing alumina window (c) Pulsed klystron (d) another low power klystron

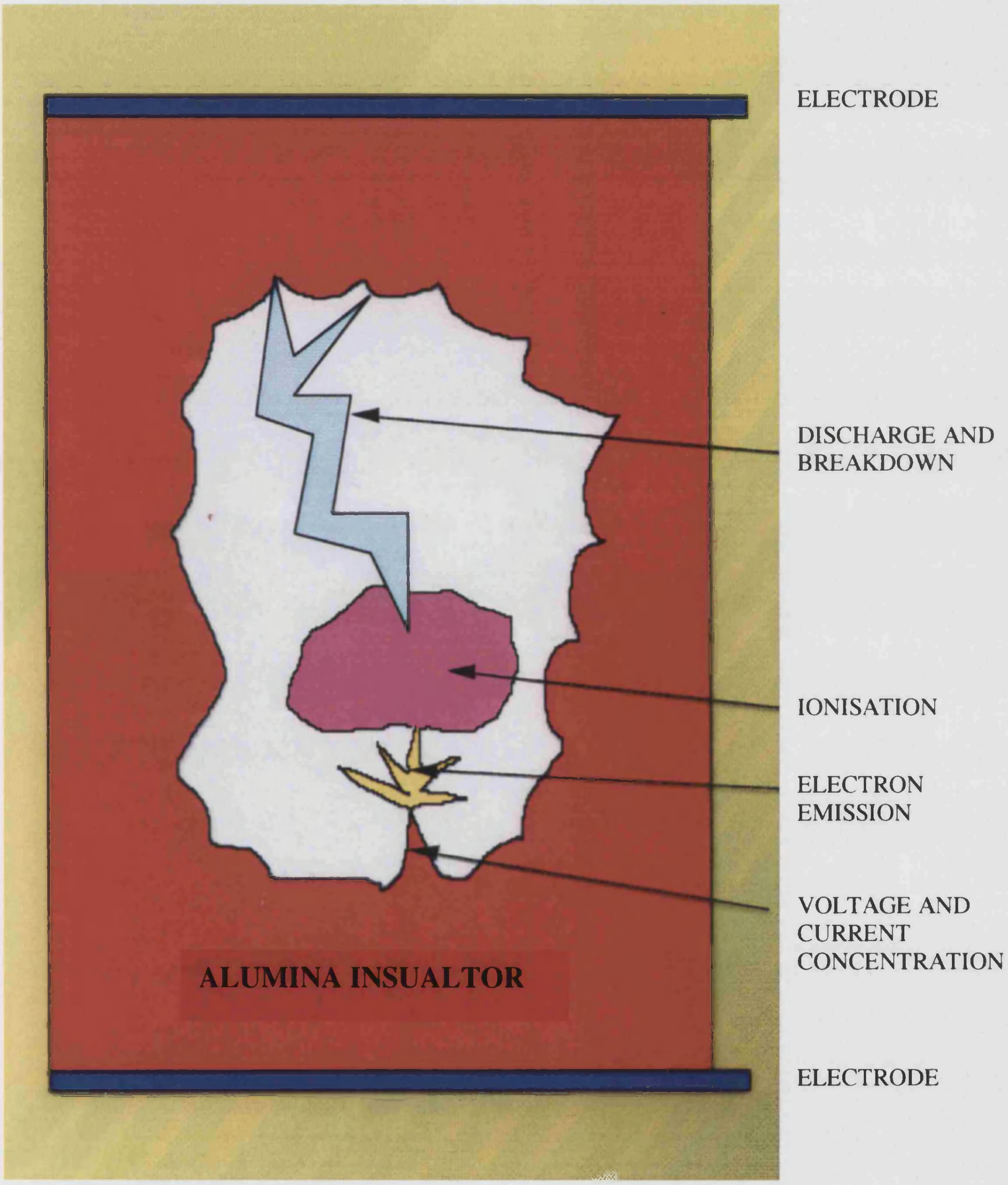

Figure 1.2: Breakdown events in alumina insulator

The research work undertaken involves the following steps:

1. Literature Review
2. A study of the Seagoe insulator sample for microstructure and composition
3. Preparation of 94% Alumina composition to match that of Seagoe material
4. Study effect of varying percentages of TiO_2 and on the electrical and physical properties and microstructure of Alumina.
5. Study other dopants which could have an effect on the resistivity of alumina
6. Study the effect of dopants on the firing shrinkage of alumina.
7. Elucidate the conduction mechanism(s).
8. Investigate the process for manufacture of functional gradient material.

Microstructural studies using optical and electron optical techniques, together with studies, electrical and physical characterisation are carried out at the various stages of research.

CHAPTER II

LITERATURE REVIEW

The review covers the discussion on the klystron failure, past work to solve the problem of the failure of Al_2O_3 *insulator, fundamentals of electrical conductivity, dielectric behaviour, microstructure in* Al_2O_3*, and impedance spectroscopy*

2. LITERATURE REVIEW

The Literature survey covers the following areas:

a) Alumina dielectric breakdown in klystrons: To understand the design and to study the problems faced by klystrons concerning alumina ceramic.

b) Electrical conductivity and the defect structure in alumina

  i) This includes the effect of TiO_2 on electrical conductivity & transport properties of alumina

  ii) Effect of other dopants on electrical and transport properties of alumina: Since the alumina under study is of 94% purity, glass forming additives other than TiO_2 will have an effect on the electrical properties of alumina. This study also includes the additions of other dopants, which may alter the defect structure and conductivity of alumina

c) Microstructure in alumina: liquid phase sintering in alumina: Since the alumina being studied is liquid phase sintered, for the better understanding of this process it has been discussed in greater detail.

d) Impedance spectroscopy has been used to study the electrical resistivity of alumina. The theory and applications of impedance spectroscopy pertinent to this project are included.

2.1. Alumina breakdown in Klystrons

Electron accelerator devices such as klystrons can generate peak RF power as high as 200MW and operating frequency in the GHz range{2}. As a result several components in the device are under high electric stress. The extreme requirements of these devices necessitate that the insulating dielectric materials should have {3}

- high dielectric strength
- low $\tan\delta$ and high thermal conductivity to avoid excessive heating
- low permittivity to match the impedance easily
- capability of metallizing and
- high thermal shock resistance and mechanical strength to face the thermal stresses posed by the multiple bake out process.

Good quality alumina ceramic exhibits these characteristics and thus finds application in klystrons. There are two major areas where it is utilised {2}:

a) Gun Area: 94% pure alumina ceramic cylinder is used as a voltage stand-off between cathode (typically pulsed to a voltage of -350kV with a pulse repetition rate of 180/sec for pulse widths 5.0μs) and anode.

b) An alumina ceramic window is used as a low loss ceramic window to direct RF power generated at the output cavity to the external load with minimum attenuation whilst maintaining a 10^{-7} Pa vacuum between the inside of klystron to the external environment.

In spite of its generally good properties, the alumina insulator has not been very successful when exposed to electric fields of around 360kV/cm under microwave conditions. Its breakdown and the build up of surface charge in these conditions has been attributed to its high yield of "*secondary electron emission*"[**] (SEE) {3}. In an alternating RF field, the secondary electrons are accelerated and multiplied, leading to excessive build-up of charge on the inner insulator surface. The high resistivity of alumina, which is the significant property governing its use as an insulator here becomes responsible for restricting the surface charge from leaking to the ground {2}. The problem of localised charge accumulation is further aggravated due to the alumina being under a vacuum, as gas phase conduction, which could have been an alternative source of charge leakage, is now unavailable to redistribute the charge evenly over the ceramic surface {4}. These conditions can lead to a surface flashover {5} and more seriously to a '*multipactor*'[†] breakdown (figure 2.1), characterised by high intensity optical emission {6} as a form of luminescence on the ceramic surface {7}. Primary electrons for this breakdown, might well be generated at the '*triple junction*'[‡] due to field emission, or

---

[**] ***Secondary Electron Emission**: Emission of electrons from the surface of a conducting material by the bombardment of the surface by electrons from another source(called primary electrons)*

[†] ***Multipactor**-Electron multipactor effect-resonant multiplication, in the RF field, of secondary emitted electrons at the alumina surface*

[‡] ***triple junction**: interface where cathode meets the insulator and forms an interface of vacuum, cathode and insulator.*

perhaps are created at the insulator surface due to ionisation of adsorbed molecules such as contamination and water molecules {5}.

Mechanisms for the failure of alumina ceramics in the gun and window areas have been explained by Vlieks et al{2}. In the gun area, they found a failure arc through a high voltage ceramic seal resulting in punctures at the breakdown voltage (≈165-200kV), each time, at the same axial location in the ceramic. This breakdown phenomenon was explained by the following mechanism:

'Emission of a small flow of charge from the cathode support structure to the ceramic causes the ceramic to acquire an excess charge density. This charge resides within the bulk of the ceramic. Additional charge accumulates from electrons arriving at the ceramic surface near the corona ring and enters the ceramic to a mean depth of approximately 0.026cm. This results in a large accumulation of charge build up within the ceramic. The high bulk resistivity of alumina prevents this charge from rapidly bleeding off to ground or to the closest metallic surface (the inner or outer corona ring in this case). This results in the accumulation rate exceeding the discharge rate causing a surface charge build up to a level so as to cause a ceramic failure.'

Authors {2} advocated a solution to the problem of cracking in the stand-off insulator by eliminating the arcing due to the outer corona ring by reducing its size. This could eliminate the problem of puncturing in the ceramic seal. However the authors have not mentioned the problem of voltage spikes on the ceramic surface which is the main concern in this study.

For the case of the window failure, the authors {2} have defined three possible mechanisms. These are:

(i) Dielectric failure, due to one or more of the following reasons:

- excessive electrical field across the window resulting from build up of negative charge on the upstream and positive charge on the opposite side of window
- impurities or voids in the ceramic
- multipactor phenomena.

(ii)Thermal Failure: Radial cracking occurs due to the excessive heating of the ceramic surface as the RF fields are converted to heat energy.

(iii)Boundary Failure: Due to defects in the braze interface that may extend into the ceramic.

However the problem of a high secondary electron emission (SEE) coefficient remains the main cause of alumina failure in klystrons. The major cause of high SEE coefficients in alumina has been linked to the generation of *F^+-centre defects*§ following electron irradiation (multipactor bombardment), from F-centres by the degradation reaction {9}:

$$F \Rightarrow F^+ + e^-$$

Irradiation can excite impurities and defects present in the ceramic and transfer a trapped electron from an F^+ centre into the alumina conduction band, thus turning the defect into an active trap {10}. Michizono et al {9} believe that more of these defects are produced in alumina with higher values of dielectric loss (tanδ). F-centres, created by multipactor events, can further increase the value of tanδ at the surface from the conductive charges of free ions or electrons. This is accompanied by a rise in surface temperature {3} and leads to resultant runaway breakdown phenomena {11}. Thus keeping the value of tanδ as low as possible is an important prerequisite for alumina used in this application {12}. Factors, which cause it to increase, are discussed later in section 2.3.1.

One method for making the alumina less liable to F centres is to have a dense structure and crystallised sintering additives {3}. A method of crystallising the grain boundary liquid phase has been discussed in section-2.4.4. However it needs to be mentioned here that a ceramic with a dense structure usually requires a small grain size (≈1-2μm) and this is unsuitable for the klystron applications due to the difficulties involved in metallizing small grain size alumina. As an alternate, if a ceramic with a large grain size is used (≈20-50μm), the structure will have many voids. These voids plus the impurities also result in

---

§ *F Centre defects -O_2 vacancies with two electrons and F+ Centre defect- O_2 vacancies with one electron{8}* high tanδ values for the ceramic. There thus is a need for a complex balance of additives and microstructures to optimise properties.

Another factor that contributes to the failure of ceramics in klystrons is the presence of mechanical defects and disorder. Dielectrically weak voids and grain boundary matrices can be the starting points for puncture, as well as the path for propagation of the initial failure {13}. More importantly they can be sources of high mobility electrons as well as trap sites under a high electrical field {14}. The excess mobile electrons can become re-trapped in dislocations and microcracks and result in a localised charge accumulation {15}. The degree to which this charge accumulates will depend on the defect density in the bulk ceramics and on residual stresses at the surface {5,16}. Controlling the dislocation population {17} and annealing to reduce mechanical defects{18} can reduce the density of trap sites for mobile electrons under rf power. Annealing can also reduce the density of F^+ centres due to the reverse conversion of F^+ to F vacancies resulting in a electron detrapping {18}. However annealing is reported to have increased the SEE yield in alumina and is thus incapable of reducing the number of trap sites {19}. Additionally charge de-trapping and relaxation of the energy of polarisation can also be responsible for surface breakdown phenomena {20}.

In order to lower the incidence of alumina ceramic failure it is believed that if the surface of alumina can be modified in such a way so as to have a low SEE coefficient, keeping the bulk unchanged, it should help in reducing multipactor breakdown. One method of modifying the surface is to apply a low SEE coefficient coating.

Sudarshan and Cros {21} have given a criterion for the choice of such coatings. They explained that the positive charging of a surface occurs when secondary electron yield per incident electron is greater than unity. For a material with this factor less than one, the surface could not acquire positive charge even under direct voltages resulting in a higher insulation strength than that of uncoated alumina. The secondary electron yield per incident electron for some materials vis a vis alumina is as given below.

Insulator	Secondary electron yield
Al_2O_3	6.4
Cu_2O	1.25
Cr_2O_3	0.98

However a popular coating used in this application is titanium nitride (TiN) {13,22}. Though TiN coating is a lower resistivity coating, its lower SEE coefficient compensates by reducing the effect of multipactor events on the insulator {13,22}. Nevertheless even ceramics with TiN coatings have not been free from their problems. Saito et al {14} found occasional discharges on the surface of TiN coatings at RF voltages greater than 200MV. These caused development of flashover tracks, evaporation of the TiN films and melting of alumina with a tree like pattern. Nyaiesh et al{23} found that TiN coating is effective only for lower power levels (<35MW peak power) and short pulses(2.5μs). For higher power insulators (≥50MW) and longer pulse lengths (5μs), coating required extremely close control over deposition conditions and *areal density*[*] with special handling and baking provisions. Instead they found Cr coated windows to be more effective than TiN, as the former were capable of withstanding operation at 100 MW of RF power, 6μs pulse length, without thermal or multipactor induced failure. The reason for the better performance of Cr coated windows vis a vis TiN coated windows was explained as:

"A thin layer of TiO_2 is formed on the surface of TiN during air exposure. TiO_2 is subject to decomposition on heating from electron bombardment. Since its secondary emission coefficient is very different from that of TiN, there is a wide variation in the SEE coefficient under klystron processing conditions. On the other hand the surface corrosion layer on Cr (Cr_2O_3) is considerably thicker and relatively stable under heating. The high defect concentration on the Cr_2O_3 layer is responsible for the relatively low secondary yield (compared to other insulators) of coated windows".

---

[*] : *weight of deposited layer per unit area*

Miller and co-workers {24,25} who studied Mn and Ti based quasi-metallizing for reducing SEE also found that the coatings with a higher Ti content, though better at reducing the multipactor failure and consequently improving voltage hold off performance, are more prone to suffer permanent damage during high voltage breakdown. Further quasi-metallizing also has the additional advantage of decreasing the amount of gas desorbed from the insulator surface during electron bombardment{26}.

The effectiveness of a surface coating for insulating ceramics against the surface charge build up also depends on the source of the input energy. This was observed by Sudarshan and Cros{21} when Cr_2O_3 coating was found to improve the insulation of alumina by a factor of 2.7 under dc, 1.8 at 60Hz ac and 1.4 at 2-50μs impulse voltage. The reason for this difference under different sources of energy is accounted for by the concept that the coating draws a small leakage current and hence is used for suppressing flashover. At all energies the surface becomes negatively charged by electron collisions and will stabilise with a negative charge. Equilibrium will be established between charge deposition by bombardment and loss by leakage. This negative surface charge will reduce the field at the critical cathode insulator junction and thus increase withstand voltage. The short time available to develop surface charge was the cause for the smaller improvement in insulation under the impulse voltage test. Under ac conditions, as the junction fields alternately change polarity, both junctions become active rather than only the anode junction, leading to a lower withstand level. This concept of surface charging has also been explained by DeTourreil and Srivastava {27}. A further reason for the coatings being unsuccessful is the coating-ceramic interface becoming another potential trap site and aggravating the surface-charging problem {18}.

Although various techniques have been utilised to reduce the ceramic failure problem in the klystrons, the problem is still largely unsolved. Modifying the surface is one method. However since surface coatings can be potential trap sites, it is believed that any surface treatment may be effective provided that the insulator is produced with a permittivity gradient across its thickness, with a minimum SEE at the surface. This idea has been utilised in present work and a functional gradient material is proposed to be prepared to overcome insulator breakdown. However before proceeding there is a need to understand the conductivity mechanisms prevalent within alumina ceramics and how these can be altered by the presence of various extraneous factors. This is covered in subsequent sections. Also the charge build-up is due to the polarisation of various charge carrying species within the bulk of the ceramic. The capability of an insulator to store polarisation energy will depend on the extent of electrical degradation under RF fields, and the dielectric polarisation and relaxation processes prevalent within the insulator. The compositional and microstructural factors that affect the dielectric behaviour become significant and have been discussed in the following sections.

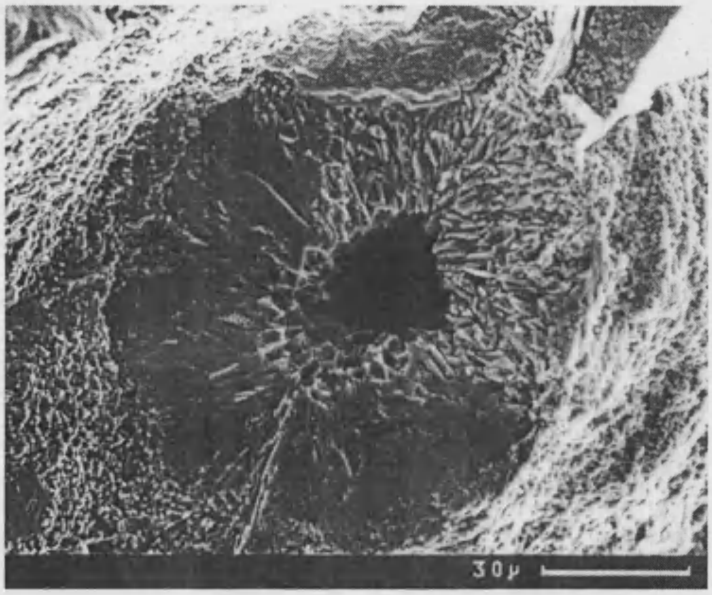

Figure 2.1: Multipactor breakdown in Alumina

Summary of section 2.1

Alumina insulators used in high-power klystrons face problems in the support insulator in the gun area and the RF window. Multipactor and surface charging due to high secondary electron emission of alumina with the development of excessive charge on its surface is considered to be the main reason for puncturing of the insulator. The reasons identified for the problem are surface and microstructural defects in alumina and the lack of a mechanism to release the surface charge build up. The same reasons are considered to be the cause of surface flashover which is more severe in vacuum than in air. Alumina with low tanδ and a lower tendency to form F-centre defects is likely to be more successful in high RF power environment. One of the methods used to reduce ceramic damage from multipactor events is the use of Ti based low SEE coefficient coating on the insulator surface. However it has had only a limited success. Cr based coatings though better, have also been of limited help.

2.2. Electrical Conductivity in Alumina

Alumina ceramic has been found to be a very good insulator due to its very high resistivity i.e it has a very large gap between the valence and conduction band (>10eV). In such large band gap materials, due to high energy of defect formation (>5eV), the intrinsic conduction becomes significant only above a certain temperature, depending on the level and type of dopant, and defect structure. For example in a pure polycrystalline alumina intrinsic conduction is insignificant below 1100°C {28}. Any conductivity at low temperatures is dominated by impurities or dopants {29}. The electrical conduction 'σ' in a solid is related to the carrier concentration 'n' (number per unit volume), charge 'q' and mobility 'μ' of major and minor inherent native defects, by means of the relationship{30}

$$\sigma = n.q.\mu.$$

For more than one operative charge carrier, the bulk conductivity is the sum of the conductivities 'σ_X' of all the individual types of charge carriers, i.e. electrons and holes (for electronic conductivity-σ_{el}), cations and anions (for ionic conductivity σ_i). Thus:

$$\sigma = \Sigma\sigma_X = \Sigma n_X\, q_X\, \mu_X = \sigma_i + \sigma_{el}$$

The relative magnitude of the factors $n_X\, q_X\, \mu_X$ determines whether the conductivity is dominant in ionic or electronic species. The individual contributions that either component will make will depend on temperature and partial pressure of oxygen in which the insulator is in operation {31}. A division of the total conductivity (σ_{tot}) into ionic and electronic components is done by measuring electromotive force (emf) in a concentration cell and evaluating the transfer number (t_i or t_{el}) {32}. The conductivity due to the ionic component then becomes

$$\sigma_i = t_i \, \sigma_{tot}$$

Furthermore the ionic conductivity is directly proportional to the diffusivity of the fastest diffusing ionic species. The diffusion in turn is affected by the partial pressure of oxygen (p_{O2}), temperature, grain size, impurity or dopant content, their segregation tendency and type of diffusion path. In the case of electronic charge carriers, the high mobility of electrons and electron holes can result in even a small concentration of carriers making an appreciable contribution to the conductivity. Common charged defects that may cause ionic conductivity in alumina {33} are:

V_{Al}''' = Vacancy at an Al site with 3 free electrons

$Al_i^{\bullet\bullet\bullet}$ = Aluminium ion in an interstitial site with 3 excess holes.

$V_O^{\bullet\bullet}$ = Oxygen vacancy minus of 2 electrons

O_i'' = O^{2-} ion in interstitial site

The carriers for electronic conductivity may be the holes and electrons contributed by either the non-stoichiometry in alumina or from impurities. Non-stoichiometry resulting from an alternate ratio of Al^{3+} to O^{2-} ions may result in an added electron or hole to maintain the electronic neutrality. Similarly, the presence of an impurity atom with a valency different from Al^{3+} may result in quasi-free electrons due to unfilled d and f bands. Electronic carriers are of greater importance for their effect on the alumina in RF applications for their use in the discharge of excess surface charge from secondary electrons. An appreciation of the factors promoting the conduction by the electronic mechanism is thus apparent. Overall, the type of conductivity that alumina shows is a function of the disorder of its structure that in turn depends on the partial pressure of oxygen (p_{O2}), temperature, grain size, impurity or dopant content, their segregation tendency and type of diffusion path {34}. Impurities provide the excess charges through the formation of lattice defects, and the atmospheric conditions affect their mobility. Temperature may also affect the mobility of carriers by increasing lattice vibrations at high temperature and by altering the association between carrier and lattice in the case of small polaron hopping.

2.2.1. Factors affecting the measurement of conductivity

Many authors have used emf measurement, as explained by Dutt et al {32}, for studying the conductivity in alumina. Volume resistivity determined by the dc method {35} and ac measurement by the Wayne-Kerr Bridge {36} have been carried out. A significant scatter has been seen in the conductivity values reported by various authors. The possible factors causing this variation are the uncertainty in the composition, impurities, measurement method used, size and design of sample and manufacture history. However the scatter due to these factors is within one order of magnitude. The major factor that has resulted in conductivity errors greater than 2 orders of magnitude is the gas phase conduction {37,38}. Especially at higher temperatures the surface conduction gets very close to the bulk value, resulting in the conductivity results being influenced by the characteristics of insulator surface rather than the bulk {39}. Many authors {38-44} have recognised this error and have used ways such as the blocking of surface conduction by the use of a volume guard to overcome the problem at high temperature measurements {42,44}. However, Will and Janora {45} believe that the use of a fully guarded three terminal technique is insufficient in eliminating surface and gas phase conduction unless the voltage between the guard and guarded electrode is typically below 100μV. Another electrode system to overcome these effects has been designed by Özkan and Moulson {40}, and the use of a three electrode system to eliminate shunting of volume conductance has been proposed by Moulson and Popper {41}. In addition the authors have also referred to the need to guard against the effect on conductivity measurements from surface contamination, especially from sodium salts which may result from handling. The authors {41} also raised a doubt concerning the possible effect of the electrode material on the measured conductance, but have left the question unanswered. A dopant such as Co can be another source of error, as in Co doped single crystal alumina, the Fermi level gets pinned close to a defect level of Co_{Al}' {32}.

One of the errors in a.c. measurements is due to the conductivity becoming frequency dependent. As for polycrystalline alumina, increase in frequency results in an increase in conductivity in the temperature range of 1425° to 1725°C, due to space charge polarisation from the presence of the grain boundary as well as the electrode {46}. Kizilyalli and Mason {47} though believe the polarisation at the electrode is absent. Comparing the dc conductivity (σ_{dc}) v/s ac(σ_{ac}), at temperatures above 1200°C, they found the ac conductivity to be higher than the value of dc conductivity with the difference becoming larger at lower temperatures and higher p_{O2}. At higher frequencies, the value of σ_{ac} increases significantly above the value of σ_{dc} due to the increased random jumping of charge carriers between neighbouring sites till the frequency matches the highest jump frequency and saturates the value of $\sigma_{ac}(f)$. Thus care should be taken to check the testing procedure used and the design and size of sample while interpreting any results from the alumina analysis.

Most of the work carried out on the conductivity in alumina has been carried out on samples in the form of either single crystal or polycrystalline. The study on liquid phase sintered alumina is very limited at present. Nevertheless the work on single crystal and polycrystalline samples can be used to understand the role played by the intra grain and grain boundary respectively, on the conductivity mechanisms and defect structure at different temperatures, atmospheres and dopants. The behaviour should be very similar for the grains in liquid phase sintered material. How these various factors will affect the mechanisms of conductivity within alumina has been set out below.

2.2.2. Factors affecting conductivity mechanisms in alumina

2.2.2.1. Effect of p_{O2} and temperature

The effect of atmosphere and temperature on conductivity in alumina was first discussed by Pappis and Kingery {46}. They reported conductivity at 1500°C increasing at both small and large partial pressures of oxygen (p_{O2}) with a minimum at intermediate pressures (10^{-6} to 10^{-4} bar). The intermediate range of conductivity became extended at lower temperatures and was same, irrespective of the type of dopant used, showing alumina to behave as a non-stoichiometric semiconductor {42}. Cohen {48} had earlier assumed alumina to be an electronic material though later authors found the conduction is mixed {46,49}, with the ratio of ionic and electronic carriers varying as a function of temperature and p_{O2}. The dominant carriers are electronic at $p_{O2} > 10^{-7}$ atm and ionic at $p_{O2} < 10^{-10}$ atm {50}. For electronic carriers, the holes dominate at $p_{O2} > 10^{-5}$ atm, while electrons predominate at lower pressures {42}, the intermediate range being the zone of changeover from p to n type. However in a study on MgO crystals, Mitoff {43} claimed that a conductivity minimum in intermediate p_{O2} is due to the intrinsic Fe impurity changing its valence state with oxygen pressure. As per Harrop and Creamer{51}, pure alumina, which has up to 100ppm of Fe{52}, might be exhibiting the same mechanism of Fe controlled conductivity. However there is no experimental evidence to prove this point. Lloyd et al{53} further believe this effect is due to the controlling impurity species changing from Fe_{Al}^{x} to Si_{Al}^{x}.

At higher temperatures, the ionic conductivity is evident even at p_{O2} as high as 10^{-4} atm{54}. Brook et al {38}, found the existence of high ionic conduction at all temperatures above 1400°C. However other authors {42,55-58} have reported ionic conduction below 1300°C and in the intermediate p_{O2} range. This concept has been opposed by Will et al {59} and Miranzo et al {60}. The former believe that the ionic conductivity is negligible below 1200°C due to the low Al^{3+} and O'' diffusion coefficients. The reason for the error by earlier authors has been linked to the fundamentally incorrect use of temperature dependence of emf for the ionic transference test. They reported complete electronic conduction in the range 400-900°C and ambient air atmosphere, and negligible ionic conduction below 1200°C due to very low Al^{3+} and O'' diffusion. Furthermore any ionic conduction above 1200°C is only from the Al^{3+} diffusion {61}, as it is significantly higher than the O'' diffusion {62,63}. El-Aiat et al have reported the activation energy of ionic conduction around 5.1eV {64}. Yee and Kröger {54} determined the activation energy of conduction of alumina in air to be ~1.3eV which increased to 1.6eV at p_{O2} ~10^{-4} atm and as a consequence of decrease in p_{O2} resulted in the change in ratio of electronic to ionic conduction. His experiments showed an ionic transference number ~0.1 to 0.3 (for temperatures in the range 1216°C to 1415°C) in the p_{O2} range of 1 to 10^{-2} atm which increased to 0.9 when the p_{O2} was lowered to 3×10^{-4} atm. However a wide variation in the value of changeover from ionic to electronic conduction has been reported by various authors. Kizilyalli and Mason {47} believe that it is a result of the difference in the range of impurity content in crystals used by various authors and stray experimental factors such as contacts blocking ionic or electronic currents differently over different temperatures and p_{O2} ranges.

The defects believed responsible for ionic conductivity at temperatures above 1600°C are V_{Al}''' at high p_{O2} {46,49,65} and $Al_i^{\bullet\bullet\bullet}$ at $p_{O2} < 10^{-5}$ atm {46,49}. Pappis and Kingery {46} and Brook et al {38} proposed $V_O^{\bullet\bullet}$ as another possible defect at low p_{O2}, but this idea was opposed by Kröger {49} based on the faster self diffusion rates of Al^{3+} {61} compared to O'' {62}. Also the higher charge on Al^{3+} results in a faster increase in its defect concentration due to any extraneous factors such as, an increase in impurity within Al_2O_3 {44}. The electronic component of conductivity that is dominant in the 400-1300°C range is believed by some authors to be due to electrons {55,66-67}, while domination by holes is proposed by others {68,69}. Nevertheless in the temperature range -173° to +600°C, most authors found the electrons are the dominant species {70,71}. This is in-spite of the fact that, as proposed by Mohapatra and Kröger {72}, the electronic defects are in a minority at temperatures below 900°C {72}. The higher electronic conductivity is due to the higher mobility of electrons and holes as compared to the ionic defects at these temperatures. Reduced electronic conduction at higher temperatures is considered to be due to the increased lattice vibrations that cause lattice scattering, which in turn reduces the mobility of free electrons {73} according to the relationship {59}:

$$\mu_e \propto T^{-3/2}$$

where μ_e is the mobility of electrons and T is absolute temperature.

2.2.2.2.Effect of grain boundaries

The amount of grain boundary and the composition of the grain boundary phase have a significant effect on the electrical properties of pure and liquid phase sintered alumina. The presence of grain boundaries can cause an increase in the electronic component of conductivity {42} in alumina with the major carriers being electron holes {74}. Hole conduction increases with an increase in the grain size, till the grains reach 10μm, and thereafter it becomes independent of size. When both high and low energy boundaries are present, large grains are formed due to the high energy boundaries disappearing during crystallisation, to give only low energy boundaries at large grain sizes. This makes hole conductivity independent of grain size. Grain boundaries hinder the ionic conductivity {64} to such an extent that it becomes negligible in very high purity alumina {74}. It was found to be independent of grain size in alumina doped with Fe. The probable reason given by Hou et al {74} is due to the segregation of dopants at grain boundaries, which might affect the increase or decrease in conductivity with grain size, itself becoming ineffective at higher grain sizes. The absence of a decrease in ionic conductivity at higher grain diameter with Fe doping indicates that there is no fast grain boundary transport for either oxygen or aluminium ions in the acceptor dominated Al_2O_3 . However fast grain boundary diffusion by neutral oxygen is still possible. In the presence of such oxygen transport, aluminium transport through the bulk could possibly be by ambipolar diffusion of charged ionic and electronic species, specifically $Al_i^{\bullet\bullet\bullet}$ and $h^{\bullet}$.

Furthermore the total conductivity will increase with an increase in grain size {75} if the grain boundary represents a favourable current path, i.e. grain boundary conduction {76}, and will decrease with increase in grain size {40} if the grain boundary acts as a barrier {76}. Space charge polarisation at the grain boundary results in the conductivity becoming frequency dependent while making a.c. measurements {46}. Significantly higher values of σ_{ac}, at high frequencies, as compared with σ_{dc} have been attributed to the increased random jump rates of charge carriers between the neighbouring sites till the frequency matches the highest jump frequency and saturates the value of $\sigma_{ac}(f)$ {47}. Thus polarisation at the grain boundary, at GHz frequency, has a major influence on the performance of alumina in klystron applications

2.2.2.3.Effect of dopants

Dopants have the most significant influence on the electrical conductivity in alumina. Impurities as low as 1ppm can contribute donors, acceptors or other point defects at a concentration of the order of 10^{16} carriers/cc, which is much higher than the intrinsic carrier concentration of about 10^{9}carriers/cc present in undoped alumina at 1000°C {77}. Especially at low temperatures, when the number of charge carriers is very low, a small change in the dopant concentration can vary the conductivity values significantly. Further defects produced by the presence of donors or acceptors can act as electron liberating or trapping sites, depending on the energy difference between the level of the occupied state and the top of the valence band or the bottom of the conduction band.

Donor impurities in Al_2O_3 are the foreign ions more deficient in electrons than Al^{3+}, e.g. Ti^{4+} and Si^{4+}, promoting negatively charged V_{Al}''', O_i'' defects and quasi-free electrons to maintain local electrical neutrality and defect equilibria. Acceptors such as Fe^{2+} and Mg^{2+} are less deficient in electrons than Al^{3+}, promoting the formation of positively charged defects such as $Al_i^{\bullet\bullet\bullet}$, $V_O^{\bullet\bullet}$ and electron holes {33}. Conduction is normally proportional to the concentration of charged point defects, which in turn is related to the concentration of the impurities {50}. However for the impurities with variable valency (Fe, Co, and Ti), the nature of the defect structure may also be affected by the valence state in which the impurity is present, especially when one valence state is iso-valent with

Al^{3+}. This is especially the case with the acceptors at high p_{O2} when the concentration of their iso-valent state increases. For such dopants, an increase in concentration of dopant may not necessarily influence the concentration of native defects {74}. As an example, in Fe doping only a fraction of the Fe is present in the form of Fe^{2+} to act as a acceptor dopant, most is in form of Fe^{3+} which is iso-valent with Al. Thus an increase in concentration of Fe doping may not necessarily influence the concentration of native defects {74}. This however is not a valid reason for Y_2O_3 as an iso-electric donor{78}, where the large size of the Y^{3+} ion forces up the electronic energy level and contributes to an increase in conductivity {79}. Overall, doping increases the hole conductivity at high p_{O2} and ionic conductivity at low p_{O2} {32,80} with acceptors having a more dominating effect on Al^{3+} bulk diffusion rather than on O^{2-} {81}.

Kröger{49} reported the dominant carriers in donor dominated crystals are electrons and in acceptor doped alumina are holes. Nevertheless due to the ionic nature of metal oxide dopants, an ionic component is present in the total conductivity of alumina {82}. The defect governing the ionic conductivity is the same as that governing the defect structure of the material. The type of defect formed can be determined by the knowledge of disorder mechanism, which in turn can be studied through a set of properties, in terms of the p_{O2} and dopant concentration. This property could be ionic conductivity, self diffusion, rates of diffusional creep and sintering and is related to p_{O2} and dopant concentration as{72}:

$$\text{Property} \propto p_{O2}{}^{r}\,[\text{dopant}]^{s}$$

Where r and s are calculated from the defect model

The dominant disorder in donor or acceptor doped Al_2O_3 is predicted as Frenkel by Hollenberg and Gordon {83}, and Schottky by Mohapatra and co-workers {72,84}. The latter's claim was based on the higher value of the energy of Schottky defect formation as compared with Frenkel disorder {85}. Al^{3+} moves through the bulk as either $Al_i^{\bullet\bullet\bullet}$ or as V_{Al}''' in acceptor and donor dominated material respectively {64,86-88}, while oxygen moves along grain boundaries, as a neutral species O_i^x {62}. The presence of electronic defects prevents the development of an electrical field due to any charged species moving alone {64}.

An undoped alumina is an acceptor governed electronic material, since as even the purest of alumina contains Mg^{2+} as an intrinsic impurity {64} and this keeps it acceptor dominant at small donor concentration {89}. Only when donors compensate for the acceptor concentration, does alumina start showing donor domination. When donors and acceptors are equal, the ionic conduction is at a minimum due to the pairing of the negative and the positive defects contributed by donors and acceptors respectively.

2.2.2.3.1 MgO as an acceptor dopant

Major carriers in Mg doped alumina are ionic at $p_{O2} < 10^{-5}$ atm and holes at $p_{O2} > 10^{-2}$ atm {90}. Mixed conduction has been reported in the intermediate range {91}. In α-alumina with 8ppm Mg, Wang et al{92} noticed electronic conductivity in the temperature range 1200-1600°C and at p_{O2} above 10^{-1} Pa. As discussed before, MgO is an acceptor in alumina, however when heated in H_2 atmosphere, Mg doped alumina can show donor domination due to the charged hydrogen species ($H_O^{\bullet}$ and H_i') which, together with ionic and electronic species (V_{Al}''', $Al_i^{\bullet\bullet\bullet}$ and e',$h^{\bullet}$) contributes to the conductivity in this alumina {93}.

In the acceptor governed material, MgO promotes Al^{3+} ion diffusion by an interstitial mechanism {86} resulting in the dominant compensating defect for Mg_{Al}' being $Al_i^{\bullet\bullet\bullet}${89}. MgO in alumina may be present as a spinel phase $MgAl_2O_4$ segregated at the grain boundary. The Al_2O_3/ $MgAl_2O_4$ interface can act as deep traps {94} and can be contributors to the surface charge build up in radio frequency environments. Nevertheless MgO presence in alumina is important for improving its sintered microstructure and density and is thus an essential component of the ceramic body. This is discussed in section 2.4.

2.2.2.3.2 *Fe and Si dopants*

Fe and Si are other dominant impurities. Fe makes alumina dominant in electronic carriers at all p_{O2}. In samples doped wit both Fe and Si, when the dopant concentration is low (0.5-0.09 wt % Fe) holes dominate at high p_{O2} due to the thermal ionisation of the ferric iron:

$$Fe_{Al}^{x} \rightleftharpoons Fe_{Al}^{'} + h^{\bullet}$$

and electrons dominate at low p_{O2} due to the thermal ionisation of Si :

$$Si_{Al}^{x} \rightleftharpoons Si_{Al}^{\bullet} + e'$$

In heavily doped samples (5 wt % Fe), when its limit of solubility in Al_2O_3 is exceeded, the opposite behaviour is found i.e. holes are dominant at low p_{O2} and electrons at high p_{O2}. In the intermediate p_{O2} range, when the controlling impurity species changes from Fe_{Al}^{x} to Si_{Al}^{x}, the total conductivity is at a minimum {53}. Presence of iron oxide in the glassy phase decreases the conductivity of the ceramic while lime and silica increase it and decrease its temperature coefficient {95}.

Dutt and Kröger {96} reported that Fe containing α-alumina is rich in holes ($h^{\bullet}$) at high p_{O2} and $Al_i^{\bullet\bullet\bullet}$ ions at low p_{O2}. However the presence of pores can increase the hole conductivity while simultaneously reducing the ionic component {97}.

SiO_2 acts as a donor in alumina. It results in ionic carriers dominating at high p_{O2} and electronic at low p_{O2} {88}. However when the Si concentration is too low to compensate for the intrinsic carriers, conduction at low p_{O2}, is ionic {98}. Schmalzried{98} found appreciable conduction from electrons at $p_{O2}<10^{-15}$ atm while holes dominating at $p_{O2}>10^{-8}$ atm.

2.2.2.3.3 Other dopants

Cr^{3+} can substitute in the lattice as a trivalent ion without the need for compensation and thus should have little effect on conductivity {38} as it would form a neutral defect like Cr_{Al}^{x} rather than a charged defect like $Cr_{Al}^{'}$. Hensler and Henry {99} have reported an increase limited to maximum 1%. However when added in conjunction with TiO_2, it increases the conductivity of alumina {100} with holes as the dominant carriers in an air atmosphere and at temperatures above 1280°C {51}. The fall in resistivity at a p_{O2} of 1 atm, with the addition of these two dopants, as reported by Watanabe et al {100} is in the table below:

	Additives %		Resistivity in Ωcm
	TiO_2	Cr_2O_3	
1	1.2	3.5	$7x10^{11}$
2	1.5	16.5	$1x10^{11}$
3	1.4	20.8	$5x10^{10}$
4	2.8	0	$5x10^{8}$
5	2.4	3.3	$2x10^{7}$

Addition of TiO_2 and Cr_2O_3 is also believed to result in an increase of dielectric constant with decreasing frequency {4}. However TiO_2 /Cr_2O_3 doping is understood to have caused electrical inhomogeneity in Al_2O_3. The cause of this is believed to be the difference in resistivity of Al_2O_3 grains from that of the Si rich grain boundary phase, the latter containing greater amount of TiO_2 and having lower resistivity than the grain. This inhomogeneity results in a complicated potential distribution in the material when high voltage is applied, which may cause surface damage on the electrode {100}.

Similarly Co additions will also increase the conductivity of alumina, but only when present as Co^{2+}, rather than Co^{3+}, forming a Co_{Al}' defect. Co doped corundum crystal {32} shows ionic conductivity, due to $Al_i^{\bullet\bullet\bullet}$, at low p_{O2} ($<10^{-3}$) and electronic, due to holes, at high p_{O2}. Nevertheless $Al_i^{\bullet\bullet\bullet}$ is dominant only in a heavily doped sample, while in a lightly doped sample $V_O^{\bullet\bullet}$ is still the carrier as is the case for undoped material.

In contrast, El-Aiat and Kröger {79} have reported yttrium as a special case of an iso-electric donor. Being iso-electric with alumina, Y will form a neutral Y_{Al}^x, but it is known to act as a donor in polycrystalline Al_2O_3 when added in quantities of around 300ppm. The reason for a lowered electronic energy level has been attributed to O^{2-} next to Y^{3+}, the level of the O^{2-} being forced up as a result of the large size of the yttrium ion. However practical difficulties are encountered since the Al_2O_3:Y system reduces the sintering rate due to the segregation of Y at the grain boundaries.

Addition of NiO and ZnO to Al_2O_3 has also been found to increase the conductivity, though only by a small amount, at around 1% addition {101}.

Activation energies for some of the acceptors as calculated by Hou et al {74} at constant composition for Al_i^{3+} are:
Al_2O_3 : Mg = 4.60eV
Al_2O_3 : Fe = 2.84eV
Al_2O_3 : Co = 3.97eV

By far the most significant impurity for this project is TiO_2. Its use as an agent for dissipating the charge in alumina thread guides gives it a potential to use as a dopant for charge dissipation in the insulator in klystron applications. In view of the significance of additions of TiO_2 it is discussed in greater detail below.

2.2.2.4. *Effect of TiO_2 dopant*

Ti^{4+}, a transition metal donor, has a significantly greater influence on conduction of alumina due to its tendency to become non-stoichiometric at high temperature (TiO_{2-x}) {102} and to change the alumina defect structure {4}. Even though the difference between the conduction band and the Ti band is similar to that of Si (1.66eV) the addition of the former to alumina has a far greater influence on the resistivity. Further Ti addition to alumina results in it shifting to donor domination only above a concentration of 80ppm. This is because an undoped alumina has about 2.5×10^{18} acceptors/cc, and on addition of 20ppm of Ti, only 10^{18}donors/cc are present, which is not enough to compensate the acceptors. At a concentration of 80ppm, the concentration increases to 4×10^{18}donors/cc changing the alumina conductivity to a donor dominated mechanism.

Ti is an aliovalent ion and may be present as Ti^{3+} or Ti^{4+}, depending on the p_{O2}. Of these Ti^{3+} being a smaller size ion, has greater solubility in Al_2O_3 as compared with the latter, which has solubility only at the grain boundaries {50} and is limited to 500ppm in α-alumina crystals {103}. Most authors believe {80, 104-106} that, it is the valence state of Ti which determines the extent to which conductivity increases. Normally Ti^{3+} being iso-valent with Al^{3+}, its higher solubility will not contribute to a greater concentration of native defects {104-105} and conductivity {80}, while Ti^{4+} will result in the formation of substitutional defects ($Ti_{Al}^{\bullet}$) {107} that will be electrically compensated by $[Ti_{Al}^{\bullet}]^3=[V_{Al}''']$ {80} and cause an increase in conductivity. On the other hand Tsuar and Kröger {50} reported that the Ti increases the alumina conductivity by the formation of aluminium titanate. Precipitation of Al_2TiO_5 to the grain boundary, at TiO_2 concentration high enough to exceed its solubility limit in Al_2O_3, is reported to cause a steep increase in the value of conductivity {50}. A steep increase in conductivity with TiO_2 addition at low oxygen pressures has been reported by Watanabe et al {106}. This has been linked to the decrease in the level of oxygen from TiO_2 causing an increased charge carrier concentration and making the Ti rich grain boundary semiconducting {108}. Ti^{3+} on reduction from Ti^{4+}, as occurs in rutile {108-110}, thus behaves as a semiconductor. However, conductivity is reduced if the Ti concentration is low enough to allow full dissolution into the alumina grain, or if the dissolution is increased by repeated heat treatment {106}.

The major carrier at small Ti concentration is V_{Al}''' when p_{O2} is above 1 atm {87}, and is electrons at p_{O2} of 10^{-8} atm {80,103}. At a Ti concentration high enough to precipitate at the grain boundary, the active ionic species changes to $Al_i^{\bullet\bullet\bullet}$ {87} and electrons are replaced by the holes as major carriers {64}. Furthermore the ionic conductivity seen at 1650°C, is a result of the V_{Al}''' defect {80,103,107,111}. Measuring the conductivity of these samples under CO/CO_2 atmosphere, resulted in the gas phase C dissolving into alumina {112-114} and forming titanium carbide or oxy-carbide precipitates, which increased the concentration of Ti^{3+} and reduced the ionic transference number from 0.74 to 0.05 at 1400°C {103}. Also the electronic component of the conductivity decreases with the increase in grain size {64}, due to the increased migration of oxygen along the boundary {62} as a neutral species {115}. Electronic conduction by *electron hopping*[§] between Ti^{4+} and Ti^{3+} reported in the zirconia-titania system {116}, could be a further mechanism which could account for the high conductivity levels found in alumina, though this is yet to be discussed in the literature.

Thus TiO_2, if present in high concentrations at the insulator surface, can act as a charge carrier by reducing the surface conductivity. This can be of help in microwave applications since the ceramic is operating at low p_{O2} that can cause TiO_2 to become semiconducting. Also the dominance of electronic carriers in alumina with some impurities, at the operating conditions of microwave devices (low p_{O2}), gives the possibility of finding a solution by using their higher mobility to bleed the charge build-up to ground. However impurities that can provide additional charges for charge transfer from the surface can also provide sites for charge trapping and de-trapping.

[§] *Conduction due to electron hopping, called small polaron hopping conduction, is an exponential increase of mobility associated with the localisation of charge carriers at ions or vacant sites. Due to thermally activated lattice vibrations the ionic carriers are considered to hop from one site to another, thus leading to an exponential temperature dependence of conduction. As a result the mobility associated with carriers tends to increase exponentially with temperature. For example in ferrites hopping is visible between* Fe^{2+} *and* Fe^{3+} *{117}.*

Summary to section 2.2

Electrical conductivity in alumina can be ionic or electronic depending on the partial pressure of oxygen, temperature, grain size and type of dopant. Alumina conductivity is lowest at a p_{O2} of 10^{-6} to 10^{-4} atm and increases at lower and higher pressures. Conductivity is high in ionic component at low p_{O2} and high in electronic at high p_{O2}. The ionic region is rich in V_{Al}''' at low p_{O2} and high in $V_O^{\bullet\bullet}$ and $Al_i^{\bullet\bullet}$ at high p_{O2}. The electronic part is n-type at lower p_{O2} and p-type at higher p_{O2}. With respect to temperature, alumina is an ionic conductor at lower temperatures and electronic at higher temperatures.

Measurement of electrical conductivity values at high temperature is affected by the presence of surface conduction and the size of test specimen, which can lead to erroneous results unless suitable precautions are taken.

The grain size, if less than 10μm, has a significant effect on ionic and hole conductivity. At higher grain sizes it affects ionic conductivity in undoped alumina, but has no effect on the hole conductivity. Alumina conductivity also increases with increase in frequency of the energy source. Dopants affect the dominant charge carrier according to whether they are acceptors or donors.

Most of the dopants discussed here are acceptors (Fe, Mg, Co, Ni, etc), except Si which is a donor and Y which is an iso-electric donor. Acceptors will alter the Al bulk diffusion rate. Mg and Fe promote Al ion bulk diffusion by an interstitial mechanism. In Mg doping electronic conductivity is hole dominant. In Fe and Si, it is p-type at high p_{O2} and n-type at low p_{O2}. Si increases the concentration of negatively charged defects. The ionic conductivity for Si doping is constant at high p_{O2} and increases with decreasing p_{O2}.

TiO_2 doping has the most significant affect on the electrical properties and the microstructure of Al_2O_3. TiO_2, a donor in Al_2O_3, causes the change in dominant ionic defect from V_{Al}''' to $Al_i^{\bullet\bullet\bullet}$, with electrons as dominant electronic defects at the lower concentrations of TiO_2 and holes at the higher(>500ppm) concentrations. Ionic conductivity dominates in the system at high p_{O2} and electronic conductivity at lower pressures. The ionic conductivity is independent of the grain size, but electronic conductivity decreases with an increase in grain size. Ti when present in Al_2O_3 as the Ti^{3+} ion (Ti_2O_3), has better solubility in the alumina grain as compared to Ti^{4+} (TiO_2). However due to its iso-valent state with alumina, Ti^{3+} is unable to affect Al_2O_3 resistivity. The fall in resistivity is attributed to the presence of Ti^{4+} alone. However a semiconducting Ti^{3+} conflicts with this mechanism. A significantly greater decrease in resistivity is reported when TiO_2 is added in conjunction with Cr_2O_3 in Al_2O_3.

2.3. Dielectric Properties in Alumina

Ceramics exposed to radiation and high voltages at radio frequencies undergo transient and permanent changes to their dielectric properties which results in a complex dependence on temperature and frequency of operation. Also the insulators operating in vacuum will have a lower surface dielectric strength when compared to properties in the ambient state {118}. Dielectric properties thus play an important role in the choice of alumina used in microwave frequency applications. Among the factors affecting these properties, the impurities present are most significant as they provide the electronic charges for polarisation events. The time required for polarisation shows up as a phase shift due to the time lag between applied voltage and induced current, causing loss currents and energy dissipation in ac circuits, and is qualified by the loss tangent tanδ. The product of tanδ and dielectric constant gives an estimate of the energy loss in a dielectric, known as the "loss factor". Loss is the primary criterion determining the usefulness of alumina as an insulator. Power dissipated in the ceramic is proportional to it, and in terms of the conductivity (σ) is represented by the relationship {73}:

$$k' \tan\delta = \frac{\sigma}{2\pi f \varepsilon_o}$$

where, k′ is the dielectric constant, ε_o is the dielectric constant of a vacuum = 8.85×10^{14} F/cm and f is the frequency of applied voltage.

Pure alumina has dielectric constant values in the range of 9.8-9.9 {119-120}. For liquid phase sintered alumina this value increases with increase in alumina content and decrease in glass phase. For example the dielectric constant of 85% pure alumina is ~ 8.2 {120} and increases to 9-9.1 for ceramics with 94% alumina {120}. At higher temperature this value increases. Both types of alumina have very low value of $\tan\delta \simeq 0.0002$ {120-121}. The value is affected largely by extrinsic factors such as impurities, defects, grain boundaries etc, rather than the intrinsic factors such as the crystal structure. The manner in which these factors affect the value of $\tan\delta$ is discussed below.

2.3.1 Factors affecting tanδ

The presence of grain boundaries in alumina tends to increase the value of loss tangent {122}. This is a result of the space charge polarisation arising due to differences between the conductivity of various phases and the phase boundary causing a build-up of charges at the interface. However various types of relaxation phenomena at different frequencies have been reported. Molla et al {123} identified the loss in alumina as being due only to intrinsic factors at Ghz frequency. However Atlas et al {124} reported interfacial polarisation as operative at low frequencies and Hippel {125} reported free electron conduction in the intermediate frequency range.

The presence of impurities normally increases the values of $\tan\delta$ of alumina (figure 2.2). Gibbs {126} reported that impurities in α-alumina crystals cause dielectric loss peaks. The impurity ions penetrate the body of the crystal along dislocation lines and result in the formation of high conductivity tubes. These high conductivity regions along dislocation lines cause an increase in the loss. Heating the sample can volatilise the impurity atoms, and eliminate the loss peaks. A linear relationship between the impurity concentration and the $\tan\delta$ has been reported by Atlas et al {124}. The maximum increase was caused by silicon ions with Mg, Ti and Ca causing progressively smaller increases and Cr and Fe ions causing only a relatively minor effect. However, Alfred and Penn {127} noticed the addition of TiO_2 reduced the value of tanδ. This was attributed to improvements in the sintering kinetics and reduced porosity. The reverse would have been expected as TiO_2 leads to an increase in grain size, and according to Penn et al {121}, losses increase with the increase in grain size above 3μm. However, in the case of TiO_2 the increase in grain size does not increase the losses since it is not accompanied by an increase in porosity {122} which had happened in the samples studied by Penn et al {121}.

Similarly Mg, which is the most commonly used sintering aid and grain growth inhibitor in alumina {128,129}, should help in lowering the values of tanδ as a result of the improved microstructure. However Molla et al {91} reported an increase in the loss factor with the addition of Mg. This was found to occur up to a concentration of 400 ppm, in this case the solubility limit of magnesia in alumina. The increase is due to the presence of substitutional Mg^{2+} introducing a negative charge by the formation of a Mg_{Al}' defect. This defect constitutes an orientational dipole causing a polarisation and resultant increase in loss factor. The dipole concentration increases with the increasing concentration of Mg up to its solubility limit. At higher concentrations, the excess Mg precipitates as a Mg-alumina spinel and causes a decrease in dissolved Mg^{2+}, which then results in a decreased dipole concentration and a lower tanδ.

In conclusion, a medium-high purity alumina could have a lower tanδ than a very high purity one {130}. Nevertheless, tanδ and permittivity can improve even in very high purity alumina if it is prepared under well-controlled processing conditions and has a dense microstructure {131}.

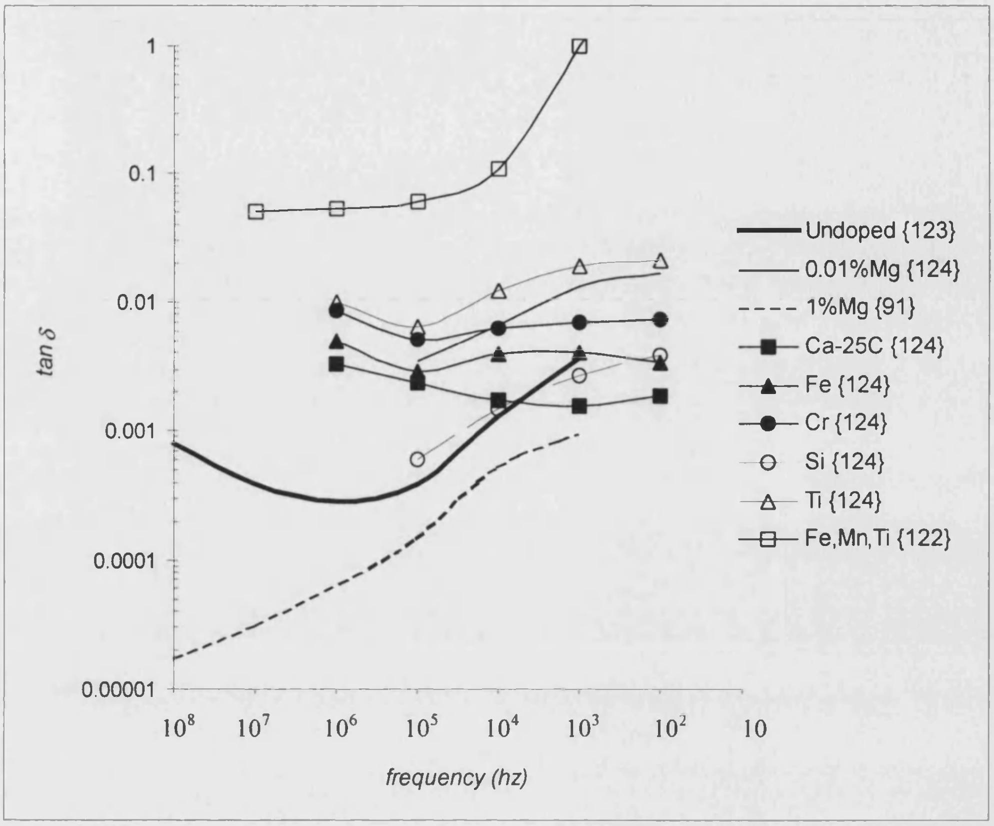

Figure 2.2: tanδ v/s frequency for alumina with different dopants as studied by different authors (referred in the legend)

2.3.2 *Factors affecting the Dielectric Constant*

The dielectric constant, (the capacity of a material to absorb the charge) and the loss factor increase with increase in temperature, but becomes independent of the type and concentration of impurity, together with imperfections, at temperatures below 25-30°C {122}. The value of the dielectric constant increases with an increase in the volume fraction of alumina and with a decrease in volume fraction of grain boundary phase. Large amounts of grain boundary impurities cause an increase in permittivity {122} at frequencies below 70Hz {47}, a result of the space charge polarisation {73,132} and of free charge carriers at the grain boundary {73}. Similarly, differences in dielectric and magnetic properties of individual additives also influence its value {122}. The insignificant effect of space charge polarisation at high frequencies {73} results in the dielectric constant becoming frequency independent above 10kHz {47}. Penn et al {121} have reported porosity as another factor, that if increased, decreases the dielectric constant.

2.3.3 Dielectric Strength

The dielectric breakdown strength is a very important property for alumina used in high voltage applications. It is affected significantly by the temperature of measurement, as at high temperature, higher conduction through the grain boundary impurities can result in a decrease in breakdown strength. Overall, the decrease in strength is gradual till 900°C and very steep at higher temperatures. Wide variation in the tested values of dielectric breakdown strength are possible due to its inverse proportionality with the sample thickness, given by the relationship {133} between the electrical strength (E_s) and sample thickness (d);

$$E_s \approx 1/d^n \text{ where } n=0.1\text{-}0.5.$$

This results from the larger samples having a higher probability of the presence of electrically weak defects. For example the strength for sapphire samples varied from a value of 7000kV/cm for 2.5μm thick sample to a value as low as 1400KV/cm for 190μm thick sample {133}. Values were further improved for the samples with recession in the centre {133}. Thus the strength data must be interpreted meaningfully only in the light of testing conditions.

The mechanism of dc breakdown has been reported as avalanche at up to 450°C {134} and thermal runaway at higher temperatures (133,134} caused by localised joule heating {135}. Avalanche breakdown is the enormous increase in the reverse current in a dielectric due to the the generation of electron-hole pairs by impact ionisation of charged species. Thermal runaway breakdown has been found to leave a 100μm diameter circular track within the insulator, and occurs at the weakest point which may be at scratches, grain boundaries, second phase or pores {135}. Breakdown in ac circuitry due to a high density of secondary electrons, as in microwave applications, is due to the increased concentration of charge carriers in the defect regions which when unable to bleed to the ground results in an increase in the local field and temperature. This results in a temperature gradient across the material {136} and the formation of microcracks near the defect region {137}. Further propagation of these cracks takes place by an avalanche mechanism {137,138} as a result of the formation of local potential gradients across the pores and voids. This leads to a breakdown channel in any grain boundary glass phase nearest to the axis of the electric conduction path for dielectric breakdown, finally leading to the collapse of voltage, together with an explosion {136}. Neither the purity of alumina, nor the constituents of the glass phase, has an affect on the breakdown strength as much as do the microstructural defects. It is also apparent that the electrical strength can be improved if the surface or bulk defects are removed from the polycrystalline alumina.

From the discussion above, it is implicit that the impurities in general have a deleterious effect on all the dielectric properties. This might lead to the conclusion that the use of a very high purity alumina as a dielectric material would be beneficial. Theoretically the value of $\tan\delta$ can be lowered by having a minimum level of impurities or sintering additives at the grain boundary {73}. However very high purity alumina ceramics are more difficult to process and have a greater tendency towards generating microstructural defects such as porosity, which is most undesirable. Also, the ceramic with higher alumina content will have a higher SEE yield {19}, especially since the common liquid forming additives, MgO and SiO_2 can be absorbers of secondary electrons {19}, and therefore this the high purity Al_2O_3 will not be useful in this application. On the other hand a controlled addition of impurities like TiO_2 can reduce the microstructural defects and improve dielectric properties. It is for this reason, in addition to cost, that insulators with 94-96% alumina purity are the most popular for use in electron insulation elements. The type of additives that are introduced and the factors affecting the microstructure are reviewed in the following section.

Summary of Section 2.3

Control of dielectric properties in alumina insulator becomes more significant under microwave conditions. The loss increases with increase in impurities. Since grain boundaries and porosity have even a greater effect on the increase in value of loss, impurities such as TiO_2 and MgO that improve alumina microstructures could on the other hand lower the loss. Impurities and porosity have a deleterious effect on the dielectric constant but not at frequencies above 10kHz. The values of breakdown strength decrease significantly with increase in temperature and microstructural defects. Impurities can be useful in reducing the breakdown by multipactor events as they can reduce the SEE yield of alumina.

2.4. Microstructure in Alumina

There are two accepted mechanisms for the consolidation of alumina. One is the solid state sintering and the other is the liquid phase assisted sintering (LPSA). The former involves the coagulation of active alumina particles by controlled grain growth through surface diffusion. The latter mechanism involves the generation of a glass in form of a second phase at the grain boundary, which helps in the bonding of alumina particles, resulting in a dense ceramic. Solid state sintering is utilised to produce very high purity alumina ceramics (>99%); it does not involve the presence of glass forming impurities and requires an alumina starting powder of sub-micron particle size. For production of alumina ceramic of lower purity (98% and below), glass forming additives are incorporated into a reasonably high purity alumina powder (>99.5%) to allow a liquid phase formed at the grain boundary to produce a dense ceramic. The ceramic under study in the present work is a liquid phase sintered 94% pure alumina and the literature study concentrates on the understanding of this sintering mechanism.

Bunag and Koenig {135} believe that liquid phase sintering is more successful in reducing the porosity, which could weaken the ceramic phase and facilitate mechanical vibration under an applied RF electrical field. They add that porosity can be lowered by increasing the liquid volume though the experimental evidence has shown that this is not true.

Some of the earliest work on solid state sintering in alumina was reported in the 1920's. However, with respect to liquid phase sintering, earlier work concentrated only on the effect of the presence of liquid forming impurities at the grain boundaries in a solid state sintered material. It was during the late 1980's when the first work on mechanisms involving liquid phase sintering in alumina was reported. This mechanism however is yet to be well understood. The sintering mechanisms proposed by some authors are as below.

2.4.1 Mechanism of liquid phase sintering in alumina

Among them, the most recent paper on this subject is by German {139}, who reported the driving force for microstructural coarsening in liquid phase sintering as being the decrease in interfacial energy of a solid-liquid interface. A measure of the microstructural coarsening has been given as the grain size. Smaller grains having a greater solubility in the liquid phase disappear with elapsed sintering time while the larger grains keep growing. The rate of grain growth for a particular grain has been found to depend on its relative difference from the size of its neighbours. The grains of size smaller than average shrink and those of a size larger than average grow, with grain size distribution, over time, converging to a steady state. This causes the mean grain size to increase resulting in a decrease of solid liquid interfacial area and a slowing down of the growth rate. The kinetics of grain growth are then given by the relation:

$$G^n = kt$$

where 't' is the isothermal time and $n = 2\text{-}4$ depending on the material and k is a constant. The author further added that if the initial grain growth is rapid, the sintered product has a wide grain size distribution.

Ives et al {140} proposed that the grain growth is due to the increased diffusion path length following an incorporation of the liquid by atom transport. Taruta et al

{141} have described 'Particle rearrangement' and 'solution re-precipitation' as possible mechanisms for liquid phase sintering of bimodal distributed alumina particles. Particle rearrangement takes place using liquid forming additives. Material transfer for solution re-precipitation involves small particles dissolving into the liquid phase and then the solute re-precipitating on the larger particles. Kwon and Messing {142} believe the rate controlling mechanism for liquid phase sintered alumina is 'diffusion' when the activation energy for diffusion of Al^{3+} or O^{2-} through glass is low, and is 'interface reaction' when the activation energy is high (say 400-500 kJ/mol). Further, with increasing liquid volume, the isothermal time required to achieve best possible density in alumina reduces. They believe the driving force for this is the interface area decrease with increase in liquid {142}.

2.4.2 *Microstructural features*

One of the major features of liquid phase sintered alumina is that it results in abnormal grain growth. The some abnormal grain growth is also visible in the undoped and doped polycrystalline alumina, the anisotropy is significantly greater in the liquid phase sintered alumina. Abnormal grains may be in form of platelike, equiaxed, elongated or platelet type{143}. Several reasons have been given for this. Park{144} reported the inhomogenous distribution of liquid phase as one of the causes for abnormal grain growth. The reason given for this was the lower mobility of boundaries wetted by the silicate liquid phase as compared with the mobility of un-wetted boundaries, causing a differential growth rate for different boundaries {145}. Seabaugh et al{146} explained the phenomenon of abnormal grain growth happening due to intrinsic and extrinsic factors. One intrinsic factor is the surface energy anisotropy which is a driving force for anisotropic grain growth both for liquid phase as well as for solid state sintering. The extrinsic factors are the grain and grain boundary interface free energy which in turn are affected by the microstructure formation during the intermediate sintering stage. The grain boundary liquid is associated with the increased rate of dissolution from the grain to the boundary causing anisotropic grain growth. The viscosity of the liquid and the solubility of the matrix grain become important rate controlling factors in this case.

Song and Coble{143} have reported reasons, other than the presence of liquid phase and alumina purity, that may result in the development of abnormal grains. These are:

a) Higher green density compacts result in a greater density of platelike grains on firing.
b) Fewer platelike grains are produced if the crystallite size of starting powder is increased.
c) Increase in isothermal sintering time above 1600°C increases the kinetics for the growth of platelike crystals.
d) Powders with a narrow particle size distribution give a more platelike morphology, and a broader particle size distribution produces more equiaxed and elongated grains.
e) Co-doping can be another cause when the dopants have two common factors, namely:
    (i) one cation has a valency lower than and one higher than Al^{3+}.
    (ii) one cation has ionic radius smaller than and other larger than Al^{3+}.
    For example, in their experiments authors found platelike crystals appearing for doping combinations of Na_2O, SrO, BaO and CaO with SiO_2 systems. Equiaxed were noted for the combination of MgO, CaO and SiO_2,and elongated for CaO and TiO_2 systems.

The most important cause for the formation of abnormal grains has been found to be the presence of calcia in the liquid phase. The presence of excessive Ca in the platelike grains of alumina led Park{144} to infer that the anorthite liquid was responsible for increasing the interfacial anisotropy and initiating abnormality. In a study on alumina with anorthite liquid phase, Kaysser et al {147} found anisotropy, due to the basal facets with continuous liquid films having slow growth in the <0001> direction relative to other crystallographic directions. CaO causing a degradation in the mechanical properties of alumina as a result of the formation of $CaO.6Al_2O_3$ at the grain boundaries has been reported in many papers {148-150}. $CaO.6Al_2O_3$ is believed to have a layered structure which makes the grain boundary phase weaker than the bulk and reduces its mechanical strength{151}. However use of CaO as a glass forming additive in liquid phase alumina is a common commercial practice.

The degree to which either Si or Ca cause abnormal grain growth in alumina is dependent on their solubility limits. Bae and Baik{152} reported the solubility of CaO in Al_2O_3 to be lower than that of SiO_2 due to the larger ionic size of Ca^{2+}(0.99Å) as compared to that of Al^{3+}(0.53Å) or Si^{4+}(0.41Å). However impurities such as Na, K , Fe, Ga etc. are believed to reduce the solubility of Si and/or Ca and facilitate calcia-alumina-silica glass formation.

Techniques to prevent abnormal grain growth for solid state sintering have been discussed by many authors. The role of MgO in preventing abnormal grain growth in solid state sintered Al_2O_3 is well accepted {128,129,153}. Some of the work carried out for solid state sintered alumina has importance in liquid phase sintering. Addition of MgO to promote stable microstructural development is considered to be a result of it segregating to the grain boundaries to control the rate of grain growth and reduce the anisotropy from Ca segregation {154}. A mechanism for prevention of CaO segregation at the grain boundary by MgO addition has been explained by Baik and Moon{155} They hypothesise that Ca^{2+} ions, being twice the size of Al^{3+}, can be accommodated only at a grain boundary. When Ca and Mg compete for the site at the grain boundary, Mg is more likely to win due to its smaller ionic radius. Once at this site Mg ions repel the Ca ions from the boundary and modifies the microstructural evolution of alumina by preventing anisotropic Ca segregation, in the process preventing any abnormal grain growth.

The role of MgO in preventing abnormal grain growth in liquid phase sintered alumina can be discussed on the same lines. However Kaysser et al {147} reported that MgO prevents the faceting in Al_2O_3 only when no liquid phase is present or when the liquid phase is below a critical percentage. MgO had no effect on faceting behaviour in the presence of a substantial amount of liquid phase. Song and Coble {143}, while supporting their claim, added that abnormal grain growth could be prevented by increasing the amount of MgO to a level where it becomes a dominant impurity in Al_2O_3. Park{144} further clarified that, even in the presence of liquid phase, MgO reduces the interfacial anisotropy though not sufficiently to completely eliminate anisotropic grain growth.

Another method used to prevent abnormal grain growth has been discussed by Stearns and Harmer{156} who reported the pinning of Al_2O_3 grain boundaries by the addition of SiC. They found that the grain growth rate for alumina, at 100hrs as a function of annealing time at 1700°C, reduces to 1nm/hr from 5μm/hr when 20vol.% SiC was added to pure Al_2O_3. Use of zirconia to inhibit grain growth in alumina was reported by Taruta et al{157}. In a study on alumina powder with bimodal size distribution they found zirconia improved the densification of compacts which had small amounts of coarse powder but showed no improvement in compacts with larger amounts of coarse fraction.

The presence of porosity in alumina used in klystrons will weaken the ceramic phase and facilitate mechanical vibration under an applied RF electrical field {135}. Liquid phase sintering is more successful in reducing the porosity than solid state sintering. The amount of porosity can be lowered by increasing the volume of liquid phase

TiO_2 is another impurity that contributes to the grain growth control. Since it is an important feature for this work, its influence on the alumina microstructure has been reviewed in greater detail below.

2.4.3 Effect of TiO_2 on Al_2O_3 Microstructure

The effect of TiO_2 on the sintering kinetics of Al_2O_3 and the resultant microstructure, both for solid state and liquid phase sintered alumina, has been discussed in many papers. Both MgO and TiO_2 are effective in controlling grain growth by a mechanism based on accelerated pore removal and increased aluminium ion diffusion, resulting in a more uniform grain size as compared with undoped Al_2O_3 {86}.

Ikegami et al{158} found that TiO_2 enhances densification of Al_2O_3 during both initial and intermediate stages(1200-1400°C), whereas MgO inhibits densification during the initial stage, but promotes it in the final stage. Furthermore the ultimate density of MgO doped alumina is higher than for the TiO_2 doped after final sintering. TiO_2 addition has been found to give a final relative density of 97-98% while an MgO addition can give >99% of theoretical density. This is because TiO_2 doping enhances the Al_2O_3 grain growth, that promotes the pore growth and suppresses the pore shrinkage resulting in a lower final density when compared with MgO doping. Grimes{107} has suggested that the co-solution of magnesia and titania is more favourable than for either oxide separately due to the lowering of the co-solution energy. Also, the presence of TiO_2 assists the dissolution of CaO though the converse is not true.

The effect of TiO_2 concentration on the sintering rate of alumina has been studied by Bagley et al{159}. They reported that the sintering rate increases till the maximum solubility of TiO_2 in Al_2O_3 is reached and thereafter it levels off. A further increase in TiO_2 may cause a slight decrease due to the formation of a second phase which may inhibit sintering. A solubility limit of 0.25 and

0.3 mole% TiO_2 in Al_2O_3, for samples fired in air at 1300°C has been reported by Winkler et al{160}. A higher solubility of 1 mole % at 1600°C and 2.5 mole % at 1700°C, has also been reported for samples fired in hydrogen rather than in air {104}. Similarly a solubility limit of 500ppm by weight of Ti has been reported by Petot-Ervas et al{103} at p_{O2} of 10^{-4} atm and firing temperature of 1530°C. The reason for improved solubility in reducing atmospheres is the reduction of Ti^{4+} to Ti^{3+}, the latter having a higher solubility in alumina due to its smaller ionic radius. Nonetheless, higher dissolution of Ti^{3+} does not contribute to an improved density. Beyond the solubility limit, TiO_2 diffuses to the grain boundary to form a second phase. The diffusion at the grain boundary as well as lattice diffusion is proportional to Ti impurity level and relates to the diffusion rate of aluminium (D_{Al}) by the relationship{89}:

$$D_{Al} \approx [Ti]^3$$

Watanabe et al{106} have added that Ti, in addition to being dissolved in Al_2O_3, is present in places as rutile or as other Ti compounds such as spinel in the Mg rich portion, and is also dissolved in the SiO_2 glassy phase. Coarse needle shaped alumina grains have been associated with the dissolution of Ti in alumina grains and the quantity of this dissolution is proportional to the presence of TiO_2. They controlled the reduction in alumina density following TiO_2 addition, by the simultaneous increase of MgO in the composition. Sintered density was also improved by firing in a reducing atmosphere and further improvement by subsequently heat treating at 1580°C. This has also been linked to the increased dissolution of Ti into alumina under reducing atmosphere. Ti doped alumina when fired in vacuum gives a pink colour on the surface as a result of TiO_2 reducing to Ti_2O_3. This causes a density gradient from the edge to the centre {161}, and this difference in microstructure between sample centre and edge driven by the impurity valence difference can help develop a graded microstructure.

The TiO_2 content necessary to give the maximum sintering rate varies with the particle size of Al_2O_3 at any given temperature. This change could be a result of the changing mechanisms for diffusion of TiO_2 in Al_2O_3 grains. It was suggested to occur by volume diffusion for a particle size less than 1μm, by grain boundary diffusion for particle size greater than 2μm and by both mechanisms when particles are 1-2μm in size. Alternately it could be due to the increased grain boundary area of the finer grained material and the migration of Ti^{4+} to this region {104}. A subsequent study did show that Ti^{4+} segregates to the alumina grain boundary and forms a liquid phase in the presence of Na_2O {162}. Furthermore McKee Jr. and Aleshin{104} found that TiO_2 affects densification and grain growth of Al_2O_3 by grain boundary action rather than by a defect mechanism involving substitutional Ti^{4+} ions in the corundum lattice.

An important facet of TiO_2 doped Al_2O_3 has been a microstructure showing anisotropic grain growth. Kebbede et al{163} described a microstructure of elongated grains in a matrix of small equiaxed grains with average grain size of 2.5 μm. Elongated grains formed about 50% of the matrix. They believe that the anisotropy is due to the non differential segregation of titanium at the grain boundaries. Results suggest that local interfacial energies promote wetting along grain boundaries that are parallel to the basal planes. Though liquid phase could also be one of the reason for anisotropic grain growth, it has been reported by Horn and Messing{164} that anisotropy in Ti doped alumina is not linked to the presence of a liquid phase. Furthermore studies {165-167} on the sintering of Si_3N_4 have found that the presence of anisotropic grains embedded in an equiaxed matrix can result in an improvement of mechanical properties. However no work is available to support this claim in alumina.

2.4.4 Recrystallisation of Alumina ceramic for Klystron applications

It has been discussed in section 2.1 that, for greater durability of alumina in RF window applications {12}, one way of lowering tanδ and consequently, lowered generation of F centres, can be achieved by crystallising the grain boundary liquid phase and producing a dense structure {3,19}. Re-crystallisation of this glass phase can be facilitated by heating the ceramic to 1100°C for 42.5 hours @ 10°C/min followed by cooling at 5°C/min. This allows the formation of multiple crystalline phases with varying coefficients of thermal expansion {168}. A dense structured ceramic, can be produced if the sintered grain size is kept small (≈1-2μm). However this grain size will be unsuitable for insulators in microwave applications due to the difficulties involved in *metallizing*✡ the small grain size ceramic, since insulators undergo a metallizing operation for producing a hermetic sealing with the metal electrode. Though active metal brazing can be utilised for forming the hermetic seal, however it has been know to result in a brittle joint. Alternatively a ceramic with a large grain size (≈20-50μm), will invariably have many voids present that would result in high values of tanδ. There thus is a need for a complex balance of additives and microstructures to optimise the desired properties.

The microstructure of alumina has been studied extensively in this work, using electron microscopy. Linking of microstructural features to the electrical properties and defect structure has been studied by electrochemical techniques such as frequency response analysis, using impedance spectroscopy. This technique has been discussed in the following section.

Summary of section 2.4

Liquid phase sintering is an important but poorly understood phenomenon. The possible controlling mechanisms have been described as being diffusion or interface reaction controlled. The kinetics and the extent of grain growth at any point during the sintering cycle is influenced by the size and distribution of grains present at that moment. Unlike

---

✡ *Operation involving application of Molybdenum-manganese based metal coating on the alumina surface which is used to braze the ceramic to metal for applications requiring vacuum leak free joints called hermetic joints.*

solid state sintering this process is more forgiving to the presence of impurities and the particle size of the starting powder. However its major drawback is that it results in abnormal grain growth, especially when the quantity of liquid phase is low and its distribution is inhomogenous. The prime reason for the development of this microstructure is the function of the dopant present, CaO at the grain boundary is especially effective.

To prevent anisotropic grain growth, MgO additions, as in solid state sintering, have been useful, though by a different mechanism and to a lesser degree. Other techniques used are grain boundary pinning by SiC or by ZrO_2 additions to the starting powder.

TiO_2 affects the microstructure as it enhances the sintering rate of Al_2O_3 at the initial stage, but results in an anisotropic grain growth. It lowers the density of liquid phase sintered alumina, which could be avoided by the addition of higher amounts of MgO. It results in the development of a microstructure consisting of elongated grains, which is due to the enhanced grain boundary diffusion as a result of Ti^{4+} segregation to the boundaries.

2.5. Impedance Spectroscopy

Electrical conductivity in polycrystalline materials is sensitive to intergranular contacts and thus microstructure. Impedance spectroscopy is a technique used to characterise bulk electrical properties and is sensitive to interfaces such as grain boundaries. It is based on the concept that the properties of the electrode-material system are time variant. The purpose of impedance spectroscopy is to determine these time variant properties of materials, their interrelations, their dependence on such controllable variables as temperature, oxygen partial pressure, applied pressure, applied static voltage and current bias.

2.5.1 Theory of Impedance Spectroscopy{169}.

Impedance spectroscopy involves the use of alternating current impedance techniques and is a common method for investigation of electrochemical reactions. Impedance is an ac analogue of a dc resistance. Unlike resistance, impedance is a vector quantity having a magnitude and a phase angle associated with it. This can be explained based on ac circuit theory. A sinusoidal ac voltage can be represented as a vector rotating at an angular frequency of ω rad /sec given by the equation:

$$V = V_0 \sin\omega t$$

where V_0 is the amplitude of the applied voltage.

When this voltage is applied across a linear resistor R, a sinusoidal output current having the same amplitude and angular frequency as the voltage is produced. This is represented by:

$$I = I_0 \sin\omega t$$

suggesting that the ac circuit follows ohms law $V_0 = I_0 R$.

Now if instead a capacitor is present in this circuit, current passing through it will be:

$$I = dQ/dt = CdV/dt.$$

The current then can be written as

$$I = \omega C V_0 \cos\omega t = \omega C V_0 \sin(\omega t+90)$$

i.e. it is now out of phase with the voltage and leads it by an angle of 90°. If a pure inductor is present then the relation will be

$$V = LdI/dt$$

and current will lag voltage by 90°. In other words depending on the components present in an ac circuit, output current is given by :

$$I = I_0 \cos(\omega t+\phi)$$

where ϕ is the phase angle.

Furthermore the alternating voltage $V = V_0\sin\omega t$ can also be represented by a complex exponential

$$V = V_0 e^{j\omega t} \qquad (1)$$

such that $e^{j\omega t} = \cos\omega t + j\sin\omega t$ and $j = \sqrt{-1}$. (2)

Current $I = I_0 \cos(\omega t+\phi)$ will be represented by

$$I = I_0 .\ e^{j\omega t}\, e^{j\phi} \qquad (3)$$

where I_0 gives magnitude information, $e^{j\omega t}$ is a rotating vector and $e^{j\phi}$ contains the phase information.

Any component in a circuit, such as R,C or L, can be defined as having an impedance Z which can be represented as a complex number. Since Z is analogous to a resistor in a dc circuit, it is given by :

$$Z=V/I$$

From equation (1) and (3) impedance is

$$Z = (V_0/I_0).\ e^{j\phi} = |Z|.e^{j\phi} = Z\angle\phi$$

where |Z|.is the magnitude and ϕ is the phase angle. In a complex plane Z can be represented as

$$Z = a + jb$$

such that $a = |Z|\cos\phi = Z'$ (real Z)

and $b = |Z|\sin\phi = Z''$ (Imaginary Z)

$$|Z| = \sqrt{Z'^2 + Z''^2}$$

$$\phi = \tan^{-1}\left(\frac{Z''}{Z'}\right)$$

Impedance can now be plotted in a complex plane as given below

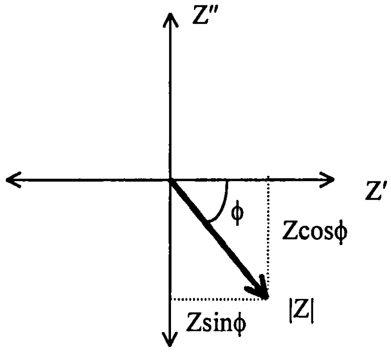

Impedance of various elements in an ac circuit will be given by:

for pure resistance $Z = R + j0 = R$

for pure capacitor $Z = 0 - j/\omega C = -j/\omega C$

and for inductor $Z = 0 + j\omega L = j\omega L$

Thus for a series RC network impedance is given by

$$Z = Z_R + Z_C = R - j/\omega C$$

giving the plot as in figure 2.3

Impedance for a parallel RC network will be

$$1/Z = 1/R + j\omega C$$

$$Z = R/(1+\omega^2R^2C^2) - \omega RC\,/\,(1+\omega^2R^2C^2),$$

which is the equation of a circle and gives the plot as in figure 2.4

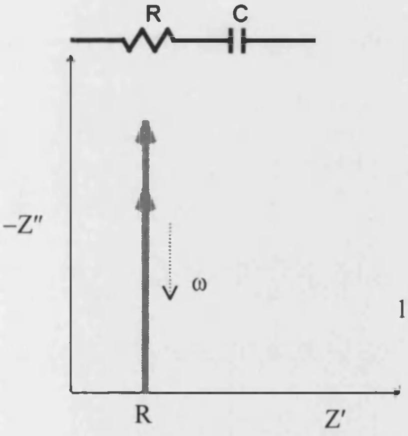

Figure 2.3

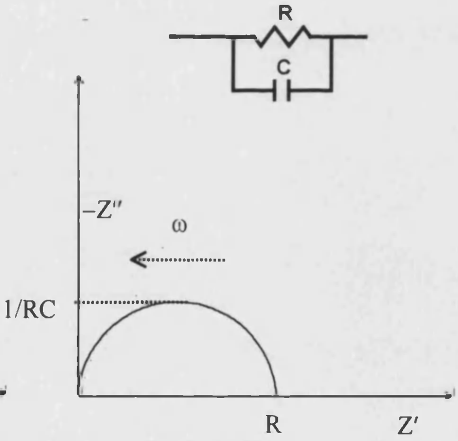

Figure 2.4

In a parallel RC circuit plot, the diameter of semicircle achieved will give the value of resistance and the top point of semicircle is used to calculate the value of capacitance.

The manner in which this theory is useful in determining the properties of materials is explained as follows. In many materials, especially those which are not necessarily conductors of electricity, the impedance varies as the frequency of the applied voltage changes. The variation is a function of the physical or chemical properties of the material. Thus, if a measurement of impedance over a frequency range is made, and the results are plotted on an axes, it is possible to relate the results to the physical and chemical properties of the material. This is done by representing the electrochemical system in the form of an electrical equivalent circuit, where the manner in which various conducting elements of the circuit are connected will determine the physical nature and chemical processes within the electrochemical system. Considering an example of solid electrolyte {170} where the total conductivity will be a summation of the conductivity from intra grain, grain boundary and electrode-electrolyte interface. The three components can be represented in the form of an equivalent circuit as below:

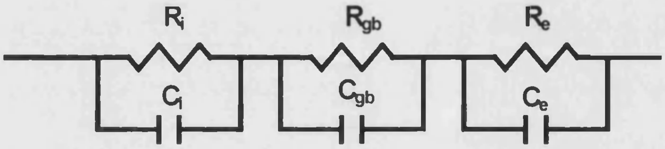

Figure 2.5: Equivalent circuit for a solid electrolyte

where i, gb and e refer to the intragrain, grain boundary and electrode-electrolyte interface components respectively of the material. The impedance plot from such a material will then be as shown in figure 2.6.

Other representations used for displaying data are admittance, permittivity and modulus given by:

Admittance $Y = 1/Z$

Permittivity $\varepsilon = Y/j\omega C_0 = \varepsilon_R - j\varepsilon_I$

C_0 = Vacuum capacitance of measuring cell.

Modulus $M = 1/\varepsilon$

Y and Z spectra are used for analysing response for a solid electrolyte system where the time constants of various processes differ as a result of different capacitances.

ε and M spectra are used for analysing the dielectric response of systems.

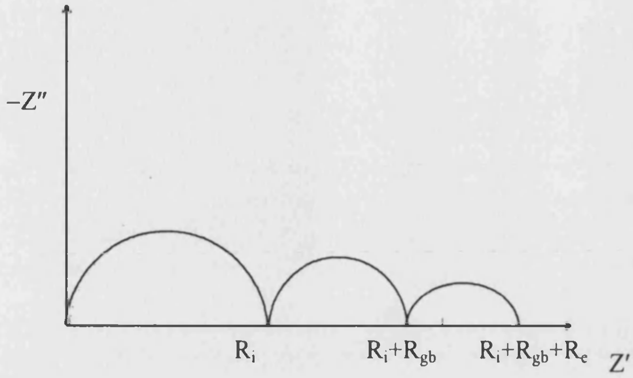

Figure 2.6: Impedance spectra for a solid electrolyte

2.5.2 *Application of Impedance Spectroscopy in Ceramics*

Impedance spectroscopy as a technique for studying bulk electrical properties has been utilised for some ionic conductors such as ZrO_2, β-Al_2O_3 and other solid state materials. There is no significant work available on its use in high insulation and primarily electronic conducting materials such as Al_2O_3. Earlier Miranzo et al{60} have reported using impedance spectroscopy for studying the electrical properties of alumina. However due to the equipment limitations in respect to maximum resistance, these authors were unable to study alumina properties below 800°C.

The explanation given by Bonanos et al{171} can be of use in studying the application of impedance spectroscopy to alumina. The authors explain how impedance spectroscopy and electron microscopy in unison can be utilised to understand the transport properties of materials. They considered a two phase material with one being a majority phase and the other a minority. In terms of complex conductivity ψ_i the electrical conductivity of a two phase mixture is given by

$$\psi_i = \sigma_i + j\omega\varepsilon_i$$

where σ_i is dc conductivity and ε_i is permittivity of phase i.

An equivalent circuit for such a two phase mixture will be:

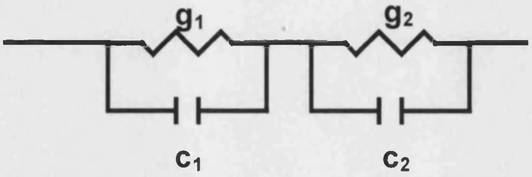

Figure 2.7: Equivalent circuit for a two phase mixture

where g_i is the conductive component and c_i is the capacitive component.

In a complex impedance plane, values of g_i can be calculated from the semicircles. c_i^{-1} can be calculated from the semicircles in a modulus spectra.

This circuit is compared with a microstructure using an effective medium model where two phases are considered in such a way that:

Case I :- there is a dilute distribution of spheres of minor phase 2 in the major phase 1(figure 2.8 (a))-similar to porosity in the ceramic.

Case II :- a small amount of minority phase surrounding majority phase 1 (figure 2.8 (b))-similar to glassy phase around a grain.

(a) *(b)*

Figure 2.8:Microstructure model

In case I the conductivity of porosity is very much lower than that of the grain interior or the grain boundary. The presence of pores will modify the impedance plots by altering the diameter of grain interior arc for intragranular pores and grain boundary arc for intergranular porosity. In niether case will the pores introduce an additional arc in an impedance plot. However they might introduce additional arcs in the modulus plot. Thus for case I, a complex modulus plot will give a better resolution rather than the impedance plot.

The grain boundary in case II will not introduce an additional semicircle to that of grain interior in a modulus plot. Thus an impedance plot will give better resolution for case II.

For a microstructure with ellipsoidal particles or anisotropic grains, a case similar to liquid phase sintered alumina, both Z and M spectra will give non ideal arcs, i.e. a semicircle with centre below the axis.

Summary of section 2.5

Impedance spectroscopy as a technique to characterise the bulk electrical properties of materials has been discussed. It is based on the concept that if an electrochemical system is introduced in an ac circuit, its impedance varies with the change in frequency of the applied voltage. The variation depends on the physical or chemical properties of material. These properties can be analysed by representing the electrochemical system in the form of an AC equivalent circuit, consisting of resistors and capacitors joined in series or parallel depending on the processes prevalent within the system. As in the case of a solid electrolyte, the conductivity contribution to the bulk will be a summation of conductivity due to grain interior, grain boundary or electrode. The three components will result in three semicircles in a complex impedance plane which can be used to calculate the electric components and relate them to material properties. Other representations such as admittance, permittivity or modulus plots can be utilised depending on the microstructure of the material. Impedance plots are useful where grain interior-grain boundary effects are dominant and modulus plots result in a better resolution for other regions.

CHAPTER III

MATERIAL PREPARATION

This chapter gives the details on:

- ✓ *the characterisation procedures and results for the reference material*
- ✓ *development of the base and the doped compositions*
- ✓ *the procedures and the results of physical testing.*

3. MATERIAL PREPARATION

Material preparation involves following steps:

(1) Analysis of the reference material and preparation of the base composition

This involves the analysis of the reference insulator which is a 94% alumina ceramic manufactured by Seagoe. This information is used to prepare the composition that is the base composition, and would be used for the further work.

(2) Preparation of the TiO_2 doped compositions

Controlled addition of TiO_2 to the base composition.

(3) Study of the effect of other dopants

The other dopants namely Cr_2O_3 and V_2O_5, that could affect the conductivity of alumina have also been tried, in conjunction with TiO_2.

(4) Physical characterisation.

The physical testing is limited to testing density, porosity and fracture strength on some compositions. The electrical characterisation, shrinkage studies and microstructure evaluation, which are important for this study, have been described in subsequent chapters.

3.1. Study of Seagoe Alumina Insulator.

The reference ceramic for this study is the 94% pure alumina insulator used in klystrons. Seagoe is one of the manufacturers of these insulators. These insulators are to be emulated, as near as possible, in regard to the composition. With this aim in mind, the following studies have been carried out on the insulator.

3.1.1. Microstructure

A microstructural examination has been undertaken to characterise the grain size using SEM and a study of the glass phase in SEM and TEM.

3.1.1.1. Grain Size

For the measurement of grain size, the samples were cut from the original insulator, polished and etched according to the following procedure:

3.1.1.1.1. Procedure

Sample preparation involves

a) Cutting approximately 5mmx5mm pieces from the Seagoe ceramic insulator using:

Table 3.1

Equipment	Buehler Isomet 2000
Blade type	Bueller 15LC [15μm diamond-low concentration]
Cutting Speed	2900 rpm
Load	600 g
Cutting time	approx. 1-2 minutes
Post Cutting Cleaning	Ultrasonic in 50% water, 50% ethanol and detergent. Cleaned in running water Dipped in alcohol for 15minutes and Dried

b) Mounting in cold setting resin using:

Table 3.2

Resin Used	6 parts Epoxide + 1 part Epoxide hardener(Requiring two parts per mount)
Procedure	Weighed resin and reduced viscosity by keeping at 40°C for 15 minutes before mixing with hardener. Poured in to the mould and evacuated till the resin boils Kept in pressure chamber for 2 hours to reduce resin shrinkage. Cured at 40°C overnight. Stripped the mounts from the mould

c) A suitable polishing procedure chosen to get a smooth and reflecting surface with no defects such as diamond inclusions and grain pull out is in table 3.3 below:

Table 3.3

Wheel/Cloth	Polishing Medium	RPM	Pressure (lb/in^2)	Time
Grinding Wheel	Resin bonded-45μm	120	5	30secs or till levelled
Metlap-10	15μm water based diamond	120	5	4min
Ultrapad	9μm water base diamond	120	5	5min
Texmat	3μm water based diamond	120	5	4min
Texmat	0.06μm colloidal silica	120	10	5min

In all cases the direction of polishing is same as the direction of the wheel. After each operation the surface of the sample is cleaned with detergent and water, followed by spraying with ethanol and drying with a hot air blower.

d) Etching is carried out to remove the glassy phase from the surface and till the grains are platy. To choose a suitable etching procedure such that sharp grain boundaries can be observed, three types of etching procedures have been tried. These are

   i. Orthophosphoric Acid, 85ml+15ml distilled water→boiling for 15 minutes (total time in acid -approx. 30mins)
   ii. Thermal Etching at 1300-1450°C for 2hours
   iii. 40% Hydrofluoric acid-110ml +10ml Distilled water →heated in water bath to 80°C for10mins (total time in acid- 20mins)

   SEM pictures showed sample etched in Orthophosphoric Acid as the optimum etching procedure.

e) Gold coating for SEM

   Etched samples are cleaned with acetone to remove any surface grease to avoid the problem of surface charging and coated using an Edwards Sputter coater-S150B. Coating time is kept at 3 minutes.

f) Microstructural examination under SEM.

   Microstructure is studied in secondary electron mode and back-scattered mode using a Scanning Electron Microscope, model JEOL-6310 and JEOL-T330.

3.1.1.1.2. Grain size analysis.

The grain size distribution in the Seagoe alumina insulator is shown in figure 3.1. SEM studies show that the samples have undergone abnormal grain growth with:

- Average grain size approx. 30μm.
- Smaller grains are ~ 10μm and larger are ~ 50μm

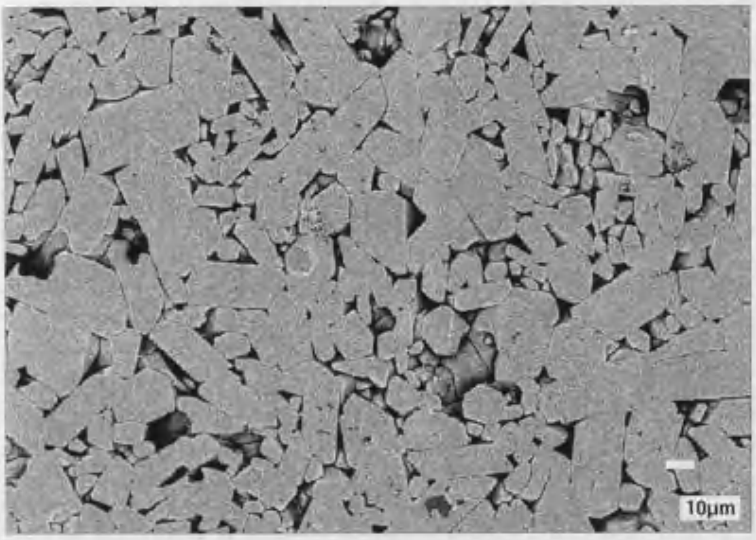

*Figure 3.1:
SEM micrograph of
Seagoe alumina*

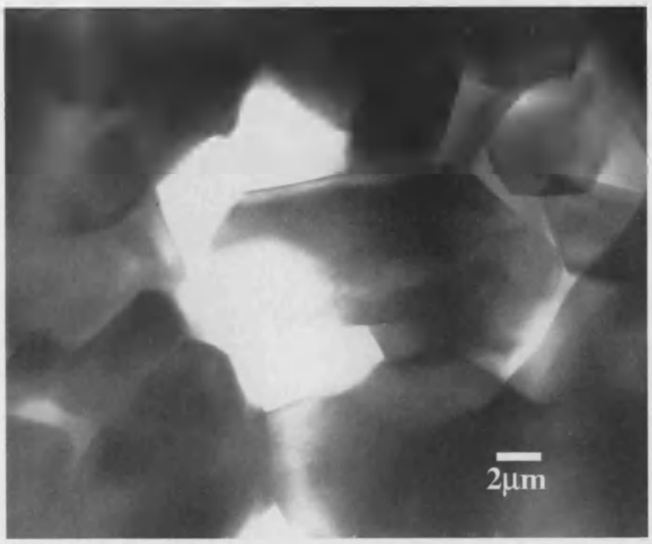

*Figure 3.2: TEM micrograph of
Seagoe alumina*

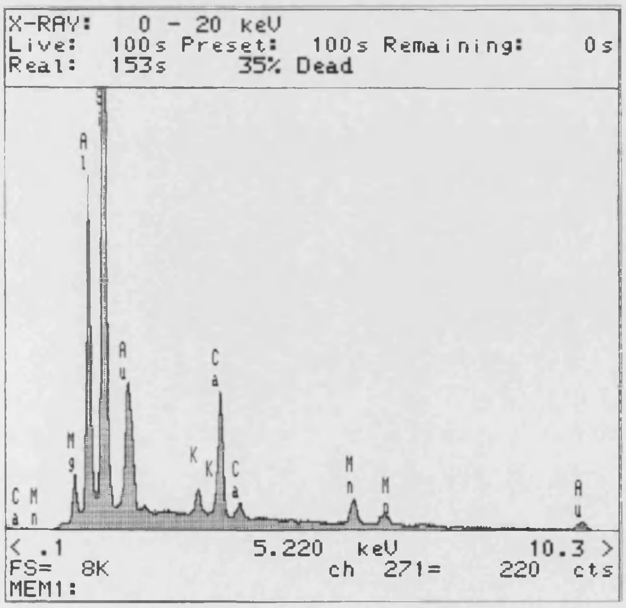

```
X-RAY:    0 - 20 keV
Live:   100s Preset:   100s Remaining:    0s
Real:   153s      35% Dead
```

```
< .1               5.220  keV           10.3 >
FS=  8K                 ch  271=     220  cts
MEM1:
```

*Figure 3.3: EDX Spectrum of
Seagoe alumina at the glass phase*

Two possible reasons can be identified for the abnormal grain growth:

1. the presence of liquid phase at the grain boundaries.{143}.
2. multiple firings for metallizing (in a reducing atmosphere){172}.
3. large grains facilitate the metallizing process and could have been generated by the choice of an alumina powder of an appropriate starting particle size. {172}

3.1.1.2. Glass Phase

3.1.1.2.1. Procedure

The glassy phase has been studied by EDX in SEM and TEM.

a) Samples for SEM are those of section 3.1.1.1 before etching. The gold coating time is reduced to 1 minute in order to obtain a lower thickness coating so as to generate a higher intensity of X-rays. The EDX used is a 'JEOL 5943' attached to an 'SEM JEOL 6310'. The glass phase is identified in the back-scattered mode and X-rays were generated at spot size '12' ensuring that *dead time** X-rays do not exceed 50%.

b) The TEM sample is prepared using the following procedure

   i. A thin section is cut from the insulator using a 'Buehler Isomet 2000' and 'Buehler 15LC' low concentration diamond saw.

   ii. The thickness of the section is further reduced to less than 0.1mm by grinding on emery paper.

   iii. A 3mm diameter section is cut from the sample using a 'Servo Drill-Model 7110'.

   iv. This section is stuck to the dimpling sample holder using a wax.

   v. The actual thickness of sample is checked and the dimple diameter fixed so as to give a centre of less than 10μm thickness when dimpled on both sides, using the 'Dimpler-Model D500'.

---

* *Dead Time: If the intensity of X-rays approaching the detector are too high then it is unable to process an X-ray before the new one arises leading to dead time.*

vi. The sample is then mounted on an ion milling holder and milled in a 'Gatan 600DIF Ion Thinner' at a voltage of 4kV and current of 1mA. Milling is carried out at a gun angle of 14° for sufficient time so as to produce a hole in the centre. After this, the gun angle is reduced to 11° and milling carried out for one more hour.

vii. The sample is carbon coated using an 'Edwards Speedivac 1226'.

viii. The TEM used was a 'JEOL 2000FX'. An area is identified and a X-ray spectrum generated using the EDX JEOL 5943.

3.1.1.2.2. Analysis of glassy phase

Insulators contain 94% alumina nominal, and ~ 8-10% by weight (~12% by volume) glass phase. A TEM showing grains and glass is shown in figure 3.2.

The EDX spectra is shown in figure 3.3. The spectrum gives a qualitative analysis of the possible components present. These components are discussed below:

- A large Si and small Al peak shows the glass to be rich in SiO_2 with a small quantity of dissolved Al_2O_3. SiO_2 is a glass former. The presence of an Al peak smaller than SiO_2 will mean it is present in a lower concentration and the absence of any visible crystals indicates it is dissolved in glass. There could be two alternate sources of dissolved Al_2O_3, one could be dissolution from the main grain in the body, and secondly it might have come from a raw material such as clay, which is often used in 94% alumina compositions.
- The presence of a Ca peak shows CaO to be a major additive. CaO is one of the major causes of abnormal grain growth in alumina ceramics {144,147}. However it is added to most of the alumina compositions. The reason for its addition may be attributed to the theory of glass forming additives, where CaO is used to aid the chemical stability of glass.
- A minor peak for Mg may be interpreted as indicating a presence of MgO in small quantities in the glassy phase. However it is well known that MgO is added to most alumina compositions for control of grain growth and sintering rate, to allow a high sintered density {147}. It is also known that it is normally added in

quantities if not higher, at least equal to that of CaO {155}. The possible reason for the presence of the small Mg peak may be the absorption of low energy X-rays, since Mg peak lies in the low energy area due to its low atomic number. A counter argument may be raised stating that the presence of platelike abnormal grains may support the fact that only a small quantity of MgO is present in the Seagoe composition. This argument can be explained by Park's{144} report that, in the presence of a liquid phase, MgO is unable to eliminate completely the anisotropy in the alumina grains.

- A small K peak may hint at the presence of minor amounts of K_2O. This may have come about due to the possible addition of KOH to alumina slurry in order to control the pH of the slurry. This is a normal industrial practice.
- The Mn peak has been noticed in the spectrum. Normally MnO, if present in a glass composition, is known to give a red colour to alumina. The pure white colour of Seagoe insulator shows it is not present in the glass phase but could have been deposited during metallizing firing as it is the part of the moly-manganese metallizing composition.
- The Au peak is from the gold coating. A carbon coating could not be used as the back scattered or secondary electron image could not differentiate the glassy phase from alumina due to the small difference in their average atomic numbers.

3.2. Preparation of Base Composition

The objective here is to prepare a 94% alumina composition that may be close to the composition of the Seagoe alumina insulator. From the discussion in Section 3.1.1.1.4 it can be interpreted that the base composition should have:

a) 94% alumina grains

b) SiO_2 as the major glass former.

c) Approximately equal quantities of CaO and MgO.

d) A very small quantity of K_2O present in Seagoe insulator, due to the processing requirements can be ignored, especially since its only and accidental impurity.

3.2.1. Composition

Based on the above analysis the following composition has been proposed:

Al_2O_3	94%
SiO_2	4%
MgO	1%
CaO	1%

3.2.2. Raw Materials

The raw materials used are all high purity grades to prevent the unknown complication that may arise from the presence of impurities. For the major raw material Al_2O_3, three alternate grades are tried. These are Alcoa's CT3000SG and Alcan's RA45 and LS2. All these three grades are of low soda alumina. CT3000SG and RA45 are reactive powders and LS2 has a larger crystallite size. For choosing the appropriate grade, the attainable degree of densification is chosen as a simple test. The following density values are achieved:

CT3000SG	99% of theoretical
RA45	98.5% of theoretical
LS2	94% of theoretical

CT3000SG is thus chosen for use in these experiments. The SEM micrograph of powder is shown in figure 3.4 and the particle size distribution measured using the 'Malvern particle size analyser' is given in Appendix A. The average particle size of this alumina is around 0.8μm.

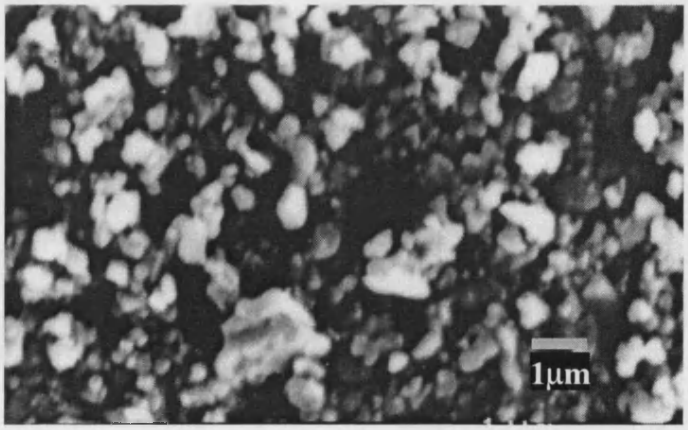

Figure 3.4: Particle size distribution of CT300SG

A complete list of raw materials used is given below:

Table 3.4

Compound	Supplier	Grade	Purity
Al_2O_3	Alcoa	CT3000SG	>99.5
SiO_2	BDH Ltd	Silica precipitated	>99.99%
MgO	BDH Chemicals	MgO heavy	LR-Grade; LOI=5%
CaO	Rectapure	$CaCO_3$ precipitated	>99%

The organic additives used are:

Dispex A40 by Allied Colloids as a dispersant

Polyethelene Glycol(PEG) of molecular weight 1500 as a binder.

Mixing medium is water.

3.2.3. Fabrication Procedure

3.2.3.1. Formulation

a) A 100g mix containing the following raw materials is weighed within an accuracy of 0.001g on a Sumitomo electronic balance (0.0001g accuracy).

CT3000SG	94g
SiO_2	4g
MgO	1.02g
$CaCO_3$	1.80g
Dispex	1.5g of dry mix
Water	80ml of dry mix

b) Raw materials are mixed for 24 hours in a plastic jar using zirconia grinding media followed by the addition of 2g PEG-1500 dissolved in 2ml water by heating and then mixed for 2 more hours.

c) The mix is discharged into a glass bowl, filtering through a 125 mesh brass screen.

d) It is then dried under the IR Lamp for ~ 6 hours.

e) The dried mix is ground in a mortar and pestle and passed through a 15mesh screen for granulation.

3.2.3.2. Pressing

a) The mix is dry pressed in a uniaxial hand press into a cylinder using a 20mm diameter die with the following parameters:

Powder weight = 7.5gm(to achieve a height of ~12mm at a green density of 2.3g/cc)

Dry pressing pressure = 20 bars for 1 minute to give enough strength for ejection and handling.

b) Iso pressing:

Uniaxial pressed samples are inserted into a latex tube keeping a distance of at least 20mm between samples. The tube is sealed from one end and evacuated using a rotary pump from the other end and then sealed.

The pellet is iso-pressed in ‘Iso Lab’ manufactured by Standard Fluid Power Ltd at different pressures to determine the optimum iso-pressing pressure.

Green Density values (dimension method) from the powder prepared as in section 3.2.3.1 at different pressing pressures are:

Uniaxial pressing: 1.73g/cc

Iso-Pressing:

50 MPa	2.01g/cc
100 MPa	2.10g/cc
120MPa	2.16g/cc
150 MPa	2.17g/cc

Based on green density values, 130MPa is considered as the right pressing pressure.

3.2.3.3. Firing

Samples are fired in a 'Vecstar' Super Kanthal furnace, in an air atmosphere heated with molybdenum disilicide elements. The following firing schedule is used:

Firing Schedule- A

RT to 650°C	@	120°C/hr
Soak at 650°C	for	0.5 hr
650 to 1450°C	@	180°C/hr
1450 to 1500°C	@	120°C/hr
Soak at 1500°C	for	2 hr
1500 to 1200°C	@	300°C/hr
1200 to RT	Natural Cooling	

This composition will be henceforth referred to as the 'Base Composition'.

3.2.3.4. Characterisation

a) Sintered samples are tested for bulk density and apparent porosity by the water absorption method. The procedure followed is as given by the British Standard number EN 623-2 : 1993 {173}

b) Microstructural analysis is carried out using procedure 3.1.1 for samples chemically etched in ortho-phosphoric acid (procedure 3.1.1.1 (d) (i)).

However SEM micrographs showed that this was not the best etching procedure in this case. Instead, thermal etching, was tried at temperatures 1350°C, 1400°C and 1450°C. It was found that etching at 1450°C is ideal.

3.2.4. Analysis of Base Composition

a) Bulk Density = 3.67g/cc

Apparent porosity = nil

Bulk density of Seagoe alumina insulator by same method = 3.64g/cc

b) Microstructure: The SEM micrograph for this composition is shown in figure 3.5. Comparing it with the microstructure of Seagoe alumina, the following inferences have been made:

i) The average grain size of the base composition is approximately 3μm, with the smallest grain being of about 1μm and largest ~ 5μm. This size is significantly smaller than that of Seagoe alumina described in section 3.1.1.1. This may be due to the choice of starting powder, lower firing temperature or lack of multiple firing as occurs in metallizing, as would have happened with Seagoe alumina.

ii) A fair degree of anisotropy results from grain growth. The reason for this is also same as explained in section 3.1.1.1.4.

Overall the structure of the base composition is a fully dense ceramic with a few scattered inter-granular pores. Most of the hollow portions visible in the micrograph are due to etching out of the glass from the grain boundaries. To get a microstructure with a larger grain size so as to resemble the Seagoe grain size, another set of samples was prepared using a higher firing temperature. The new firing schedule is:

Firing Schedule - B

RT to 650°C	@	120°C/hr
Soak at 650°C	for	0.5 hr
650 to 1550°C	@	180°C/hr
1550 to 1600°C	@	120°C/hr
Soak at 1600°C	for	2 hr
1600 to 1200°C	@	300°C/hr
1200 to RT	Natural Cooling	

The microstructure for this firing is shown in figure 3.6. Though the grain size has increased but this firing caused a decrease in density. The decrease in density could be due to the exaggerated grain growth and expansion of internal pores as a result of over-firing. Thus only the 1500°C fired samples are to be used for further work. Also since the electrical conductivity studies are to be carried out relative to this composition, the effect of difference in grain size can be ignored.

3.3. Doping the Base Composition

TiO_2 is being used to alter the resistivity of alumina. Watanabe et al {100} reported that Cr_2O_3 in combination with TiO_2 had a significantly greater influence on the resistivity of alumina, as explained in section 2.2.2.4 of literature review. Based on this information compositions doped with both TiO_2 and Cr_2O_3, have also been prepared. Also V_2O_5 has been tried as an alternative dopant that may contribute to the fall in resistivity of alumina.

3.3.1. Composition

TiO_2 is doped to levels ranging from 0.25% to 10% by weight of base composition. Preliminary trials and literature has suggested that Cr_2O_3 and V_2O_5 are other dopants that together with TiO_2 can affect alumina conductivity. Thus compositions containing TiO_2 and Cr_2O_3, TiO_2 and V_2O_5 and TiO_2, Cr_2O_3 and V_2O_5 have been fabricated and tested.

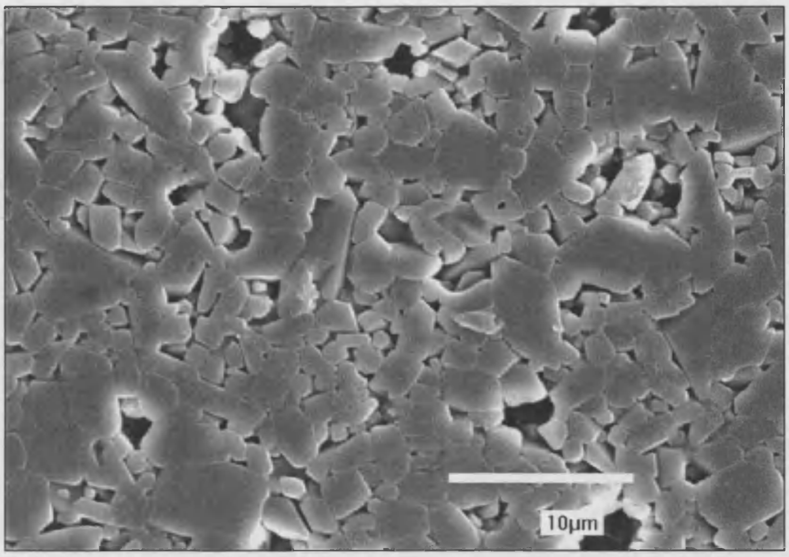

Figure 3.5: Grain size distribution in Base Composition fired at 1500 °C

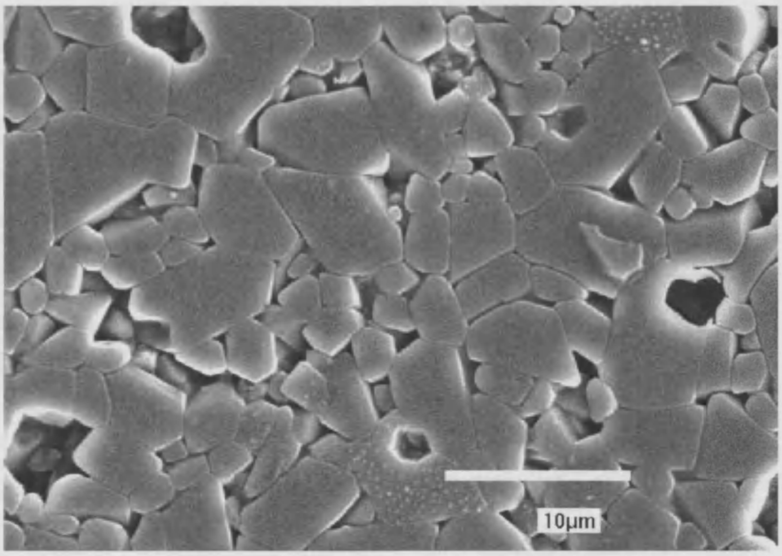

Figure 3.6: Grain size distribution in Base Composition fired at 1600 °C

3.3.2. Raw Materials

As was done for the base composition, pure sources of the raw materials have been utilised.

Table 3.5

Compound	Supplier	Grade	Purity
TiO_2	SCM	TiONA	>99.9
Cr_2O_3	BDH Chemicals	AR	>99.99%
V_2O_5	BDH Chemicals	LR	>98.5%

The V_2O_5 powder was coarse and was ground using zirconia grinding media, then dried and ground again. This has been done to improve the distribution of V_2O_5 in the composition.

3.3.3. Fabrication Procedure

Formulation, pressing and firing procedures are the same as described in section 3.2.3.1 to 3.2.3.3. Additional samples fired at 1600°C, according to the schedule in section 3.2.4 were also prepared for some of the compositions. However this was discontinued since in addition to the problem of decrease in density, they showed inconsistent results during electrical characterisation. The TiO_2 doped formulations produced are given in Table 3.6 and formulations containing TiO_2 with other Cr_2O_3 and V_2O_5 dopants are shown in Table 3.7.

Table 3.6

Raw Material	BC	T01	T02	T05	T07	T1	T2	T2.5	T3	T4	T5	T10
Al_2O_3	94	94	94	94	94	94	94	94	94	94	94	94
SiO_2	4	4	4	4	4	4	4	4	4	4	4	4
MgO	1.02	1.02	1.02	1.02	1.02	1.02	1.02	1.02	1.02	1.02	1.02	1.02
$CaCO_3$	1.8	1.8	1.8	1.8	1.8	1.8	1.8	1.8	1.8	1.8	1.8	1.8
TiO_2	-	0.1	0.25	0.5	0.75	1	2	2.5	3	4	5	10

BC: Base Composition

Table 3.7

Raw Material	BC	TC1	TC2	TC3	TC4	TV1	TV2	TV3	TV4	TV5	TCV1	TCV2
Al_2O_3	94	94	94	94	94	94	94	94	94	94	94	94
SiO_2	4	4	4	4	4	4	4	4	4	4	4	4
MgO	1.02	1.02	1.02	1.02	1.02	1.02	1.02	1.02	1.02	1.02	1.02	1.02
$CaCO_3$	1.8	1.8	1.8	1.8	1.8	1.8	1.8	1.8	1.8	1.8	1.8	1.8
TiO_2	-	0.5	1	2	1	0.25	1	1	1	3	0.25	1
Cr_2O_3	-	0.5	1	1	2	-	-	-	-	-	0.5	0.5
V_2O_5	-	-	-	-	-	0.5	0.25g	0.5	0.75	0.5	0.5	0.5

Further compositions were prepared by altering the percentage of glass forming additives, namely MgO, CaO and SiO_2. These compositions are also necessary for shrinkage control, as will be explained in Chapter 7 on shrinkage studies.

Table 3.8

Raw Material	M1	M2	M3	M4
Al_2O_3	94	94	94	94
SiO_2	4	4	4	2.7
MgO	-	0.1	0.1	0.7
$CaCO_3$	-	-	0.1	1.2
TiO_2	2	2	2	2

3.3.4. Characterisation

The green density of isostatically pressed samples is determined by the dimension measurement method and the fired bulk density is checked using procedure given by BS EN 623-2 : 1993. Linear shrinkage is calculated using green and fired dimensions and the formula

%Shrinkage in lateral direction $$S_L = \frac{d_g - d_f}{d_f} \times 100$$

%Shrinkage in perpendicular direction $$S_t = \frac{t_g - t_f}{t_f} \times 100$$

where d_g is green diameter; t_g is green thickness
and d_f is fired diameter; t_f is the fired thickness of the solid cylinders.

Shrinkage data is of paramount importance for the development of functional gradient material. To get a complete temperature v/s shrinkage curve, a dilatometer has been utilised. The details are in chapter 7.

Fracture strength is measured using polished circular disc samples and the procedure defined by ASTM F394-78 {174} and rig design similar to that used by Shetty et al for the piston-on-3-ball test {175}.

3.3.5. Results

Green, fired density, apparent porosity and shrinkage values achieved for these compositions are given below in table 3.9:

Table 3.9

Composition	Green Density (g/cc)	Fired Density (g/cc)	Apparent Porosity (%)	Linear Shrinkage (%)	
				S_L	S_t
BC	2.15	3.59	0.11	20.68	19.96
T01	2.15	3.60	0.06	20.32	20.11
T02	2.14	3.59	0.03	19.91	20.38
T05	2.13	3.55	0.02	20.10	19.94
T07	2.16	3.57	0.08	20.34	18.75
T1	2.14	3.53	0.03	19.52	20.23
T2	2.14	3.56	0.31	20.13	20.65
T2.5	2.10	3.46	0.00	19.72	20.18
T3	2.14	3.47	0.07	19.41	19.36
T4	2.11	3.53	0.02	19.91	19.18
T5	2.08	3.38	0.06	18.91	17.69
T10	2.09	3.40	0.00	19.21	19.29

Table 3.10

Composition	Green Density (g/cc)	Fired Density (g/cc)	Apparent Porosity (%)	Linear Shrinkage(%)	
				S_L	S_t
TC1	2.15	3.53	0.14	20.68	19.96
TC2	2.15	3.55	0.07	20.32	20.11
TC3	2.14	3.53	0.11	19.91	20.38
TC4	2.13	3.53	0.01	20.10	19.94
TV1	2.16	3.47	2.78	20.34	18.75
TV2	2.14	3.52	0.09	19.52	20.23
TV3	2.14	3.43	0.60	20.13	20.65
TV4	2.10	3.40	3.47	18.69	17.64
TV5	2.14	3.36	0.03	19.41	19.36
TCV1	2.13	3.48	0.86	20.20	20.43
TCV2	2.14	3.39	0.53	20.76	20.29

Table 3.11

Composition	Green Density (g/cc)	Fired Density (g/cc)	Apparent Porosity (%)	Linear Shrinkage(%)	
				S_L	S_t
M1	2.24	3.47	0.08	17.90	18.41
M2	2.18	3.44	0.03	17.12	17.81
M3	2.19	3.44	0.08	17.25	18.36
M4	2.13	3.61	0.08	19.04	19.50

Figures 3.7 (a), (b) and (c) show the variation of fired density and apparent porosity for various compositions.

From the tables 3.9-3.11, it can be seen that the green density values for all the compositions, iso-pressed at same pressure, are the same within experimental error. The only deviation is in the case of composition M1, M2 and M3. This can be attributed to the absence of MgO or presence of an MgO content significantly lower than other compositions. This follows from the work of Ferreira et al {176} on slip cast bodies, who noticed lower green densities with higher amounts of MgO due to a higher volume of pores and pore size distribution in the green body as an increase in critical moisture content and drying shrinkage.

Addition of TiO_2 reduces the fired density. This was expected as has been discussed by Ikegami et al {158}, in that MgO doping gave a final density of 99% while TiO_2 doping gave a density up to 97-98% of true density. Nevertheless more importantly the open porosity is nearly zero. Addition of Cr_2O_3 to TiO_2 doped compositions does not alter the density or porosity significantly. However addition of V_2O_5 caused a substantial lowering in density and increase in porosity. In composition TV5, containing 3%TiO_2, and 0.5% V_2O_5, additional TiO_2 offsets the deleterious effect of V_2O_5 resulting in a very low porosity, though still lower density. Similarly comparing composition TV1 (0.25%TiO_2 + 0.5%V_2O_5),

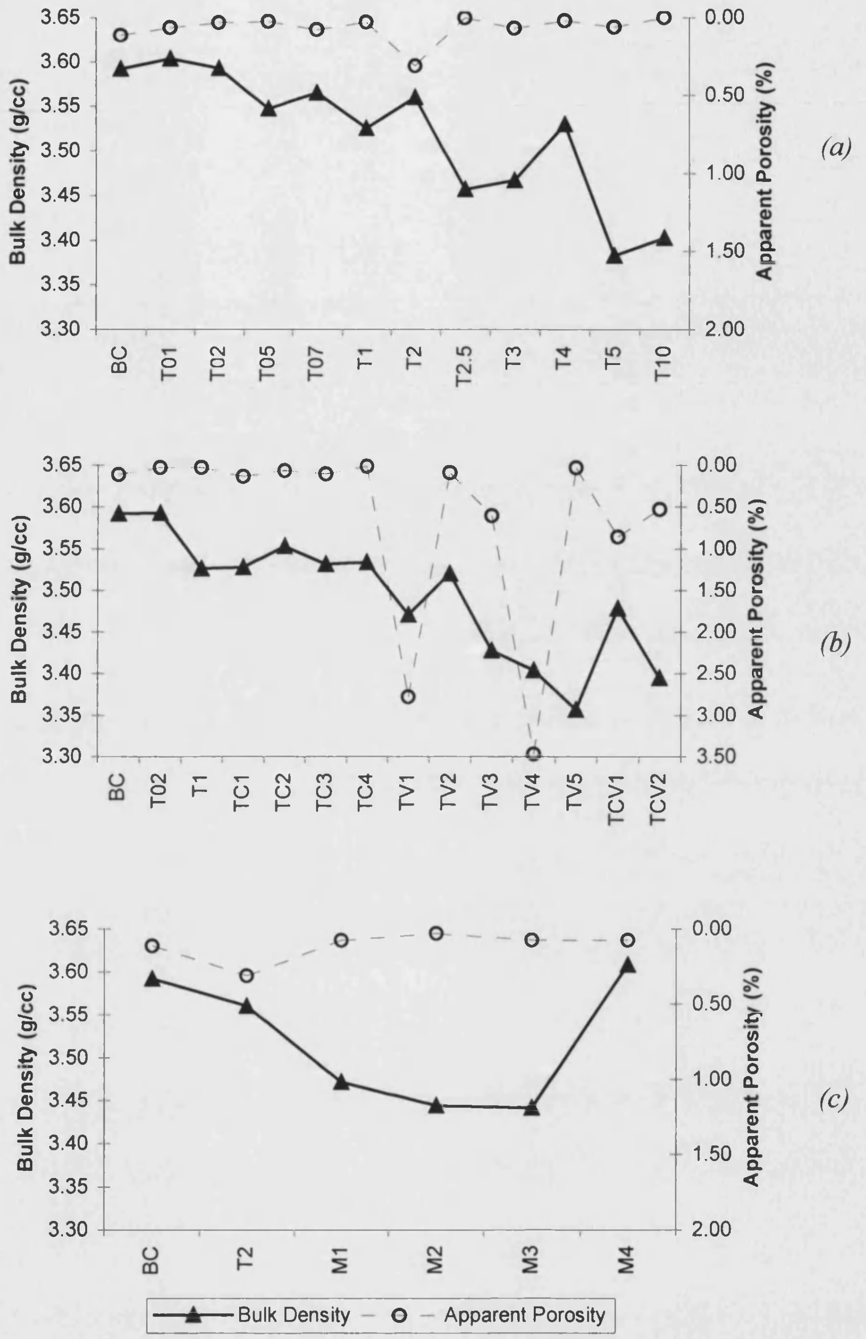

Figure 3.7 Density v/s porosity for(a) TiO_2 doped compositions (b) TiO_2 plus Cr_2O_3 &/or V_2O_5 doped compositions (c) with reduced glass content

TC1:0.5%TiO_2+0.5%Cr_2O_3

TC2:1%TiO_2+1%Cr_2O_3

TC3: 2%TiO_2+1%Cr_2O_3

TC4: 1%TiO_2+2%Cr_2O_3

TV1:0.25%TiO_2+0.5%V_2O_5

TV2:1%TiO_2+0.25%V_2O_5

TV3:1%TiO_2+0.5%V_2O_5

TV3:1%TiO_2+0.5%V_2O_5

TV4:1%TiO_2+0.75%V_2O_5

TV5:3%TiO_2+0.5%V_2O_5

TCV1:0.25%TiO_2 +0.5%Cr_2O_3+0.5%V_2O_5

TCV1:1%TiO_2 +0.5%Cr_2O_3+0.5%V_2O_5

TV2 (1%TiO_2 + 0.25%V_2O_5), TV3 (1%TiO_2 + 0.5%V_2O_5) and TV4 (1%TiO_2 + 0.75%V_2O_5) there seems to be a balance of the addition of TiO_2 and V_2O_5 that will give the best possible density and porosity. Better porosity values for compositions TCV1 and TCV2 show that the addition of Cr_2O_3 to the V_2O_5 and TiO_2 compositions helps in reducing porosity. High density values for the compositions with lowered glass content i.e. total alumina content equal to that in base composition, gives a density equal to that of the base composition. This can be used to deduce that addition of TiO_2 does not reduce the density but it is rather the decreased percentage of total alumina in the composition that causes a fall in density.

The shrinkage values show that the final shrinkage for all the compositions is very close except for compositions with lowered MgO and CaO. (M1, M2 and M3). However in order to determine the shrinkage profile during the heating cycle, dilatometer studies were necessary. These are discussed in chapter 6.

Fracture strength is measured on base composition and some TiO_2 doped compositions are shown in figure 3.8. The flexural strength of the base composition is within the acceptable limits. However the value reduces on doping with TiO_2 and for compositions with no MgO and CaO additives. The reasons for this will be discussed later in chapter 5.

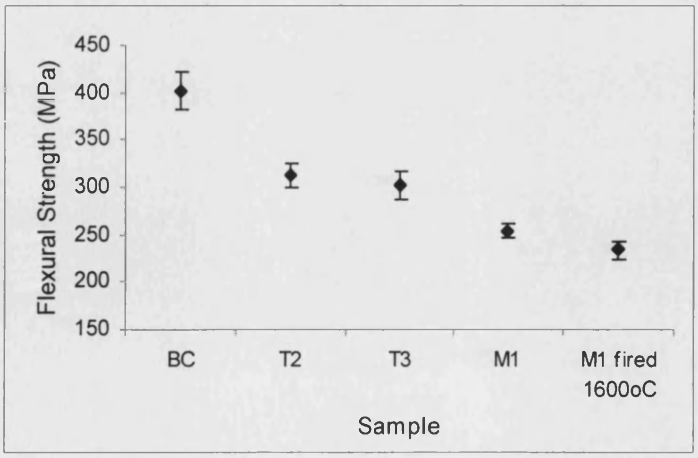

Figure 3.8 Flexural Strength for some compositions

CHAPTER IV

ELECTRICAL CHARACTERISATION

This chapter explains the testing procedure, and discusses the results from testing the resistivity of various compositions using impedance spectroscopy.

4. ELECTRICAL CHARACTERISATION

Most of the earlier studies on electrical conductivity of alumina were carried out using dc techniques, by measuring electrochemical-cell emf, and high voltage impulse breakdown. The former technique was popular for measuring the transport properties and the latter was used for studying the dielectric breakdown strength of alumina. Both the techniques require the use of a high voltage input to generate the results from high resistivity alumina. Electrical properties in this project have been studied mainly by using the impedance spectroscopy technique.

4.1. Impedance spectroscopy

Impedance spectroscopy uses a small ac voltage impulse (<2-3volts) to measure the bulk conductivity of material by frequency response analysis. Since a very small voltage is applied, there is no chance of an error arising due to flashover breakdown or diffusion of any species under high voltages. However this technique has been used for studying materials showing ionic conductivity and has not been very popular for material such as Al_2O_3, where the largest contribution to bulk conductivity is from electronic carriers. Also, earlier impedance measurement equipment did not have the capability to measure the conductivity of high resistivity materials such as alumina. The maximum possible resistivity material that could be measured was $10^8\Omega$cm. The equipment used for present study is the Solartron Dielectric Test System. This consists of a Frequency Response Analyser Solartron FRA model 1260 coupled with Solartron Dielectric Interface 1296 and a PC running 'Solartron Impedance Measurement Software Version 2.0.0'. With such equipment it is possible to measure the resistivity as high as 10^{14} Ωcm. The figure 4.1 gives the assembly of the Dielectric Test System {177}.

The 1296 Dielectric Interface is an ultra high sensitivity multi-range current to voltage converter, has an attenuator for noise free low level stimulus of the sample, DC rejection circuit, and high precision reference capacitors. The 1296 software automatically controls range and reference switching, if required by the test.

The current to voltage converter is able to resolve femto amp signals and operates over a wide bandwidth from 10μHz to 10MHz. This allows extremely high impedance sample to be measured (>100Tohms), which in turn allows meaningful measurements to be made on insulators. The 1296 contain a number of high precision reference capacitors which are used to make the high accuracy measurements of the sample (particularly at high frequency). Figure 4.2 shows the accuracy range of this system {178}

4.2. High Temperature Testing

The high temperature measurements are carried out using a high temperature rig similar to that shown in figure 4.3 based on the design by Bonanos et al {171}. The rig is place in a Pyrotherm 1200°C tubular furnace. The sample is connected to the sample port of system 1296 using the prescribed cables and platinum wires. Platinum wires were used towards the sample end of connection, to enable the system to make measurements at high temperature. The platinum wires are held to the surface of sample using a spring loaded device.

Testing was also carried out on a second set of samples from the same batch that were annealed in H_2 atmosphere. This was done in a metallising furnace at the Marconi Applied Technologies. The annealing temperature was 1460°C for 40minutes in 10:90 mixture of H_2 and N_2, bubbled through water at 25°C.

4.3. Electroding

For the connection between the platinum wire and sample, it is necessary to apply a conducting electrode to the sample surfaces, which are electroded using platinum paste. The discs are cleaned using a solution of 50% distilled water, 50% ethanol and detergent, using ultrasonic for 5 minutes. This is followed by dipping the specimens in ethanol and drying at 80°C for 10minutes. A thin layer of

platinum paste is painted on one face of the disc and dried in an oven at 120°C for 8 hours. Similarly a second face of the disc is painted and dried. The coated disc is then fired to 1000°C using the following schedule:
RT to 1000°C @ 300°C/hour
soak at 1000°C for 0.5 hour, followed by
natural cooling to room temperature.

For the samples annealed in H_2 atmosphere, a silver paint manufactured by Electrolube Ltd[✫] is used, to prevent oxidation of the alumina samples during electroding firing. This paint requires drying at 50°C for 2 hours. However these samples were tested only up to a temperature of 600°C to avoid oxidation during testing. This is because the test rig is designed to take the measurements only under ambient conditions. It was confirmed that there is no visible difference between the resistivity values for sample coated with platinum from those coated with silver. This was done by using the samples from same batch, one electroded with platinum and other with silver, and tested for electrical resistivity from room temperature to 600°C.

4.4. Overcoming Gas Phase Conduction

It is known that the conductivity measurement in high resistivity materials can result in an error, especially at high temperatures, due to the gas phase conduction {37,38}. Various techniques were applied to get over this problem.

Three different sample morphologies and experiment set ups were tried. The first sample shown in figure 4.4 (a) is 12mm dia and 3-3.5 mm thickness with opposite surfaces electroded. The resistivity values seemed very low. Probably the gas phase conduction effects resulted in a significant reduction in resistivity. The sample shown in figure 4.4 (b) is 20mm diameter and about 0.8 to 1mm thick, with 7x7mm electrode in the middle of each face. The sample in figure 4.4 (c) is similar to the former but with a surface guard to earth the surface

---

[✫] *Silver Conductive Paint, Catalogue no. 101-5621, Manufacturer: Electrolube Ltd, Berkshire*

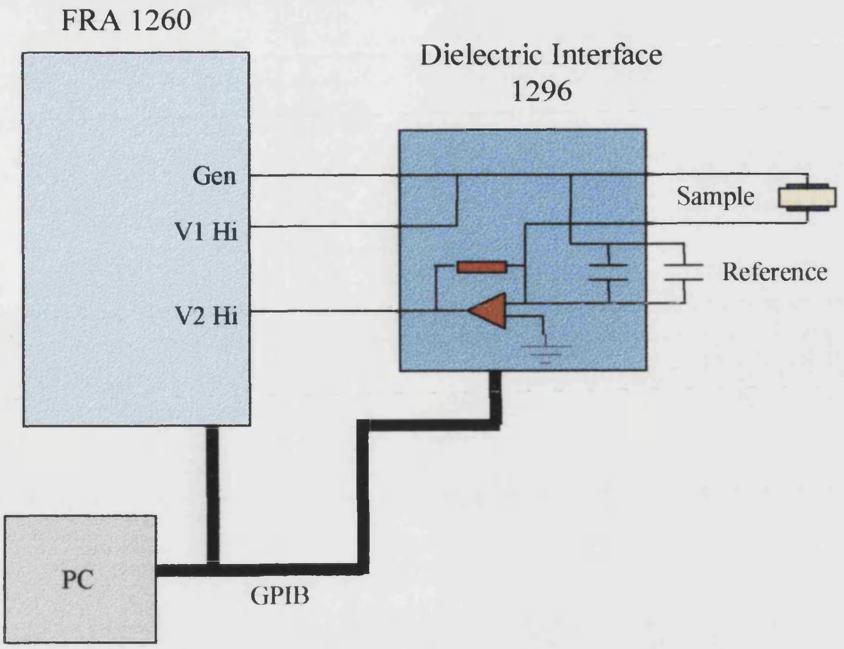

Figure 4.1: Dielectric Test System by Solartron

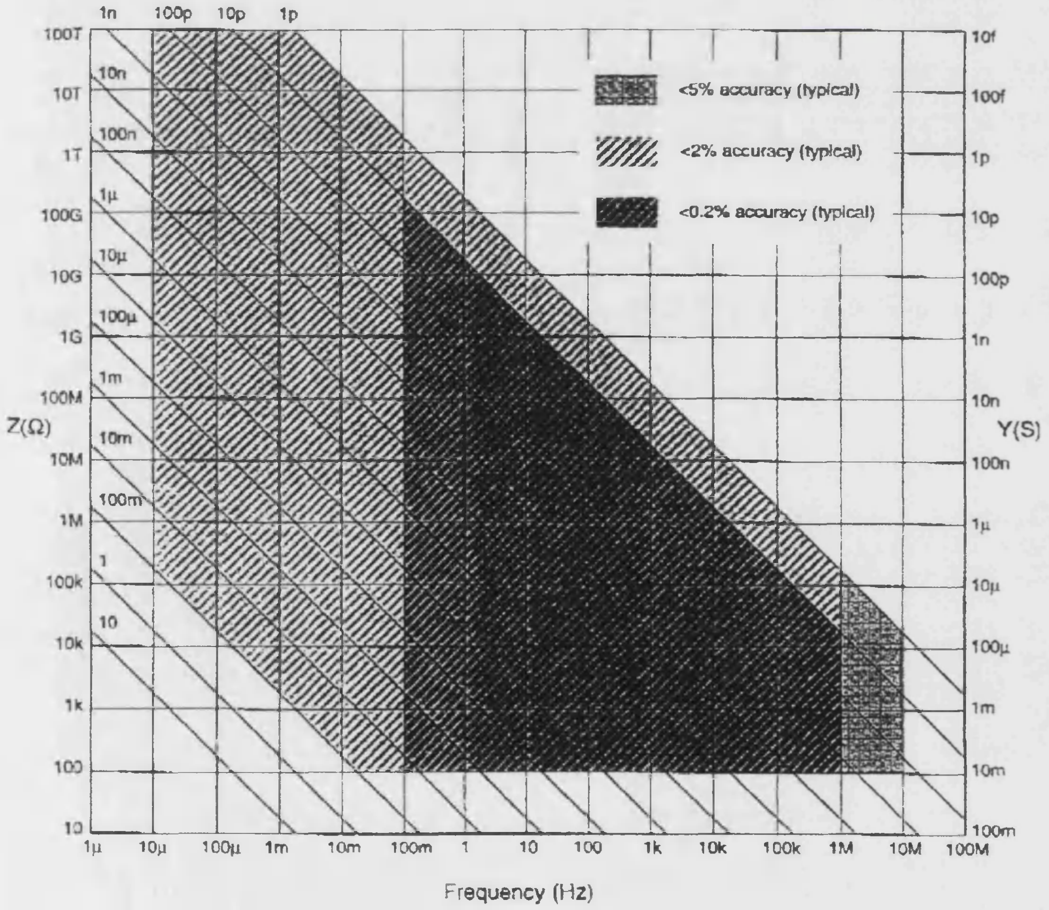

Figure 4.2: Accuracy of real capacitance values (typical), measured in reference mode

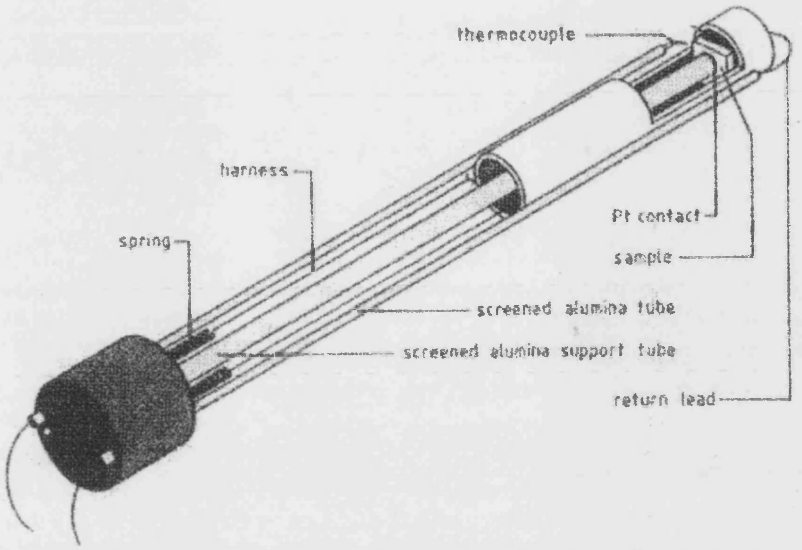

Figure 4.3- High Temperature Rig for Impedance measurements

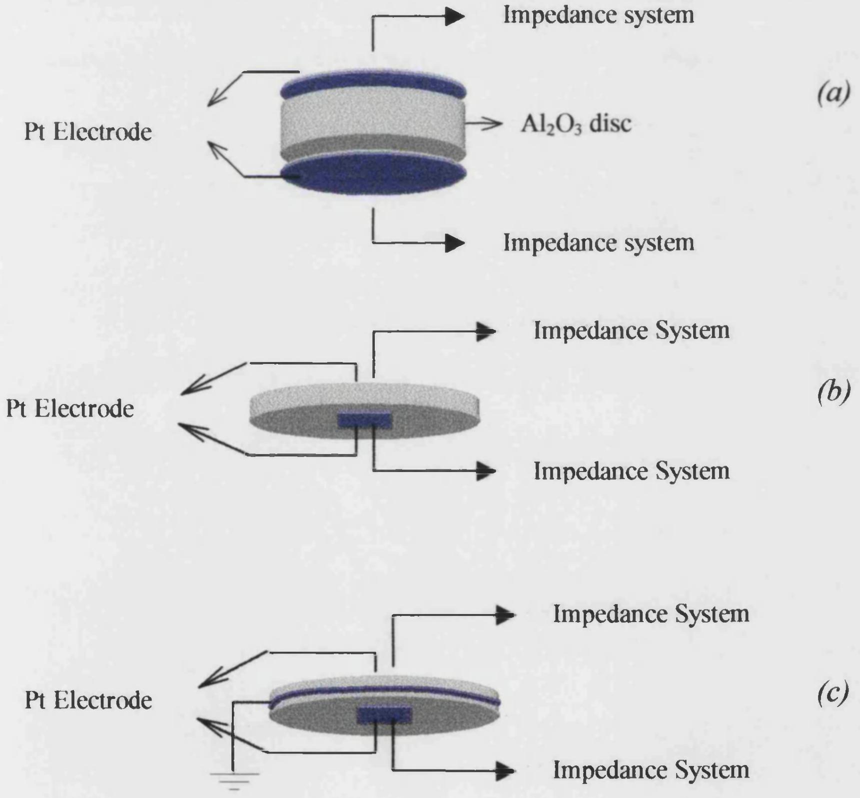

Figure 4.4: Sample Morphologies for Impedance Test (a) 12mm diameter, ~3mm thick with 12mm electrode area (b)20mm diameter 0 8-1mm thick, with 7x7mm electrode and (c) same as 'b' with surface gaurd

conduction. The resistivity values were similar for both these morphologies (figure 4.4(b) and (c)), for temperatures 100 to 900°C, confirming that the latter sample results are not affected by the gas phase conduction. Thus the morphology used for further electrical studies is same as that shown in figure 4.4 (b).

4.5. Impedance measurements

The frequency analyser 1260, the dielectric interface 1296 and a PC were connected as recommended by the manufacturers operating manual.

The sample was loaded in the sample holder ensuring that both the platinum leads have made a good contact with the electroded surfaces. The fixture is inserted in the furnace. Measurements are to be made at 40° and 100 to 900°C at 100°C intervals. For samples annealed in H_2 atmosphere, the maximum measurement temperature is 600°C.

Once the fixture is set and connections are complete, 'Solartron Impedance Measurement Software Version 2.0.0' on Microsoft Windows is used to perform the experiment in the following steps:

1. Instrument Set-up : The instrument set-up and the communications test is carried out as specified by Solartrons 1296 Operating Manual. The communication addresses are as given below:

Impedance Interface		
	Type	1296
	Address	2
Frequency Response Analyser		
	Type	SI1260
	Address	12

2. Experiment and Measurement Setup: After the communications test is passed the experiment set-up is carried out as explained by the operating manual. The following set-up is utilised:

Constants

Parameter	Value	Settling Delay
Temperature (°C)	40	0
DC Bias (Vdc)	0	0
AC Level (Vrms)	2	0

Measument Sequence

Parameter	Start	End	Steps
Frequency(Hz)	1e7	0.005	29

Frequency Sweep Steps/decade: 5

Measurement Setup

Method

Reference	none

Analyser

Auto Integration	off
Integration Period	0 seconds

The program automatically runs the frequency sweep and collects the impedance values. The sweep is repeated at each of the temperatures, after giving a temperature stabilisation time of one hour.

4.6. Analysing Data

The data received from the instrument is exported to 'Z-View Version 2.1a' software of Scribner Associates, Inc. Data is utilised to plot complex plane impedance plots (imaginary v/s real impedance) and bode plots (magnitude impedance and phase angle v/s frequency). The curve fitting software of Z-View is utilised for defining an equivalent circuit and determining the resistance values of the ceramic. The choice of frequency range is based on a dummy test carried out on the base composition for a range of 10MHz to 100μHz . The results showed material behaving as a near pure capacitor at the very low frequency range. Overall the range of 10MHz to 0.005Hz is found most suitable.

Typical as received complex and Bode plane plots for one of the compositions is shown in the figure 4.5.

4.6.1. Calculation of Sample Resistance

Calculation of resistance from the complex impedance graphs has been done using the following two steps :

1. Identifying an equivalent circuit
2. Fitting the complex plane graph to this circuit and identifying the values of resistance and capacitance using the circle fit option in the Z-View program.

4.6.2. Identifying an equivalent circuit

It was difficult to identify an appropriate equivalent circuit using the room temperature graph. Thus a high temperature graph such as the plot at 700°C for the base composition was used to study the equivalent circuit. The plot showed a single semi-circle which originates at a value slightly higher than zero on the Y - axis, indicating a capacitance effect. However this capacitance could be a result of the capacitative effect shown by an AC circuit at high frequencies.

Two conductivity mechanisms are possible:

(a) the ionic conductivity as shown by a solid electrolyte and

(b) the electronic conductivity probably by electron hopping.

There could be four components in glass phase sintered alumina contributing to the conductivity. These have been represented in figure 4.6. These are grain interior, glass interior, grain boundary and electrode interface components.

First assumption: If we assume that ionic conductivity is the primary mechanism of conductivity, an equivalent circuit similar to that of solid electrolyte {170} but with 4 components, can be used (figure 4.7). The four components are alumina grain interior, grain boundary, glass interior and platinum-alumina ceramic interface. However a single semi-circle in the complex plot (figure 4.5 (a)) indicates that four components have either very similar R and C values or the RxC product for two components is too close to resolve into separate curves for each component. Nevertheless we know that the platinum-ceramic interface resistance has a very high capacitance and very low resistance when compared with the other three components, hence it can be ignored. Thus the complex curve gives the value of bulk resistance, i.e. alumina grain interior plus grain boundary plus glass interior. The new equivalent circuit now can be defined as shown in figure 4.8.

There is a flaw in this assumption. For ionic carriers grain boundary capacitance would be significantly higher than the grain or glass interior capacitance, a feature which is not visible in the complex curve received (figure 4.5 (a)). This gives a doubt as to whether ionic carrier contribute to the conductivity. This observation is also in line with the published literature so far. However the existence of ionic conductivity cannot be ruled out for the case of doped ceramics, which will be discussed later. In the meantime, a second assumption, that of the electronic conductivity being responsible for this curve, is worthy of discussion.

Second assumption: If the electronic carriers are dominating the conductivity in alumina, then:

- ✓ Capacitance due to the electronic carriers is low for grain and glass interior and grain boundary.
- ✓ The electrode interface will have a high capacitance but the resistance is very low
- ✓ In such a situation carriers will take the path of minimum resistance and the total resistivity will be equal to the lower resistance element in the material.
- ✓ The equivalent circuit will then be as shown in figure 4.9.

Once again the interface resistance can be ignored, and the bulk resistance this time will be the minimum of R_a, R_{gb} and R_{gl}, giving an equivalent circuit similar to figure 4.8. Here R_b will be the minimum of three values.

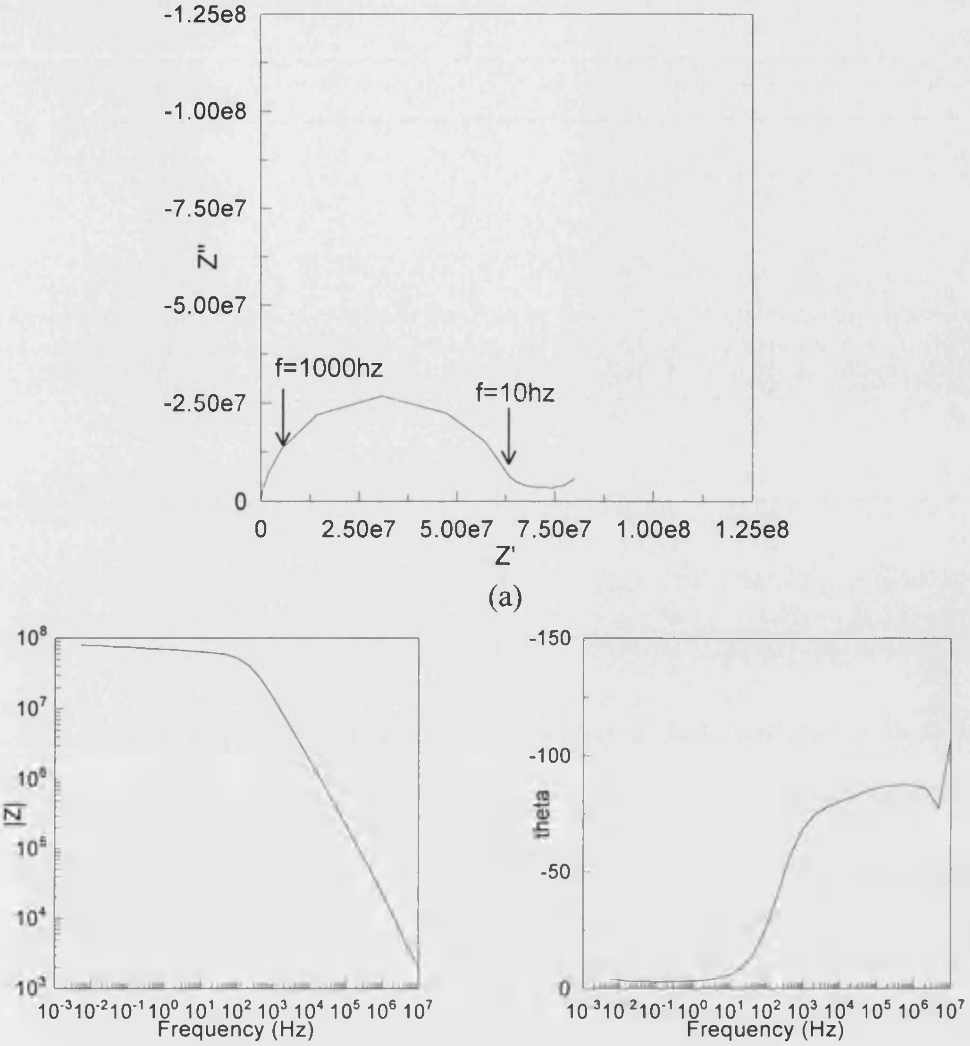

(a)

(b)

Figure 4.5- Complex (a) and Bode (b) plots for as received results from Dielectric Test System

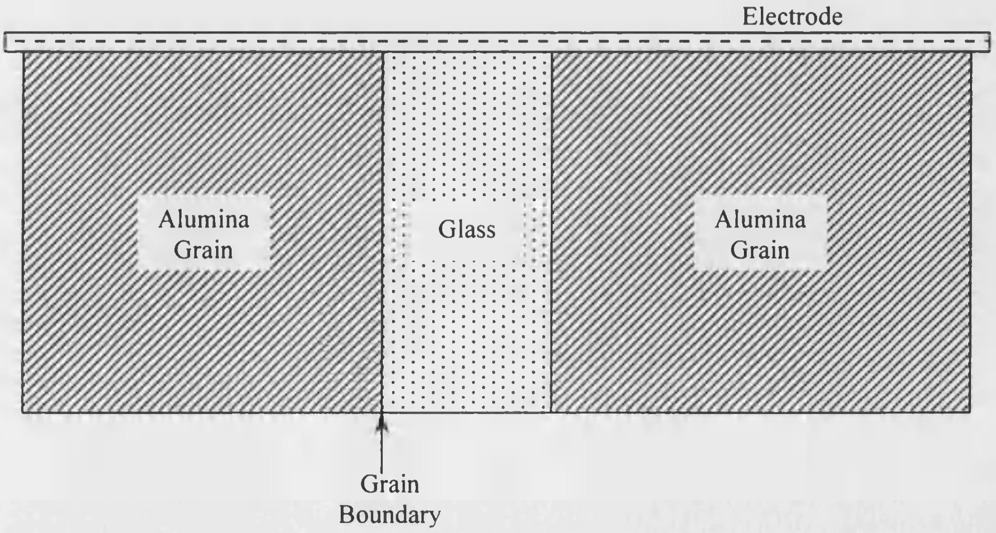

Figure 4.6: Representation of the components of alumina microstructure

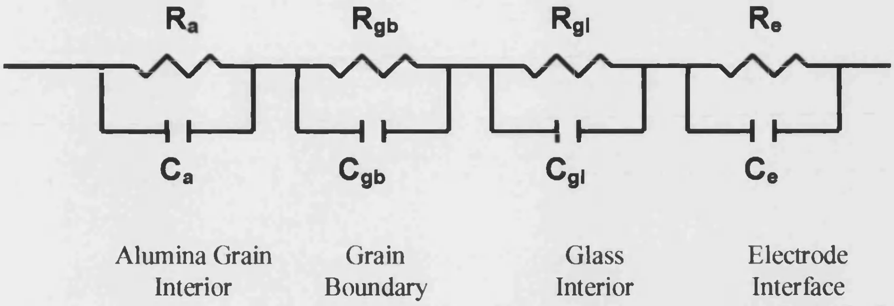

Figure 4.7: Conducting elements in alumina if assumed ionic conductor

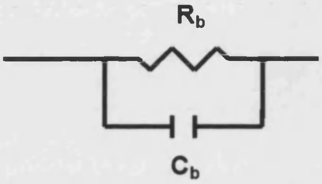

Figure 4.8: Probable equivalent circuit for bulk alumina resistance

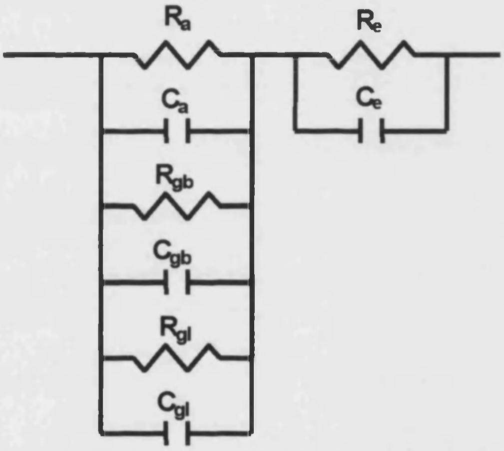

Figure 4.9: Conducting elements in alumina if assumed electronic conductor

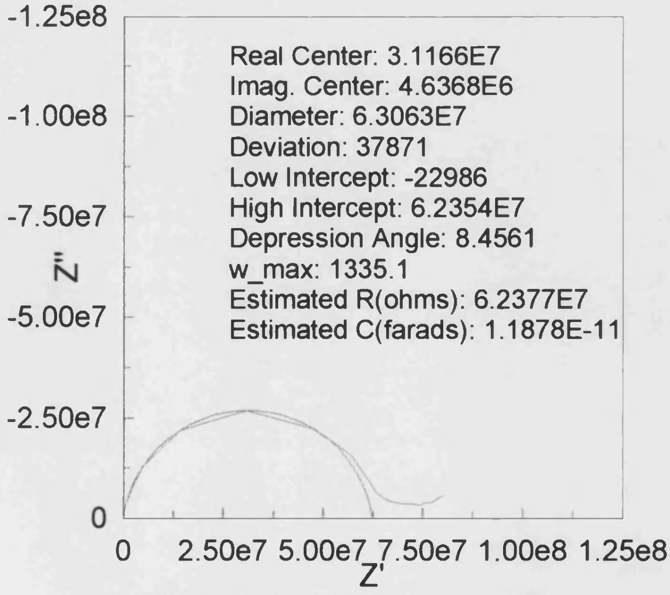

Real Center: 3.1166E7
Imag. Center: 4.6368E6
Diameter: 6.3063E7
Deviation: 37871
Low Intercept: -22986
High Intercept: 6.2354E7
Depression Angle: 8.4561
w_max: 1335.1
Estimated R(ohms): 6.2377E7
Estimated C(farads): 1.1878E-11

Figure 4.10: Circle fitting results

4.6.3. *Fitting the complex plane graph to circuit in figure 4.8*

Circle fit from the Z-View program can be used to fit the graph employing the circuit of figure 4.8. This resistance could either be the bulk resistance, as in assumption 1, or could be that of the lowest resistivity component in the alumina. The fitting results are as shown in figure 4.10.

However for low temperature results, it has been assumed that this curve is a part of larger semi-circle and the curve is extrapolated, to get the resistance values. There is a possibility that some of these values may not be very accurate. However it may be possible to use them for comparative purposes. In most of the cases it was found that high frequency data (> 1000Hz) could be ignored when carrying out the curve fitting.

Furthermore the resistance values thus estimated may not be ideal for comparative purposes, since resistance in addition to material characteristics, is also a function of the thickness and the area of cross-section of specimen. Instead resistivity being a fundamental property of a material, is used when comparing doped and undoped compositions. It is calculated using the formula:

$$\rho = R\frac{a}{\ell}$$

where ρ= Resistivity in ohm-cm, R= Resistance calculated from the fitting in ohms, a = area of cross-section and ℓ = thickness of specimen without electrode.

4.7. Results

As discussed before all the room temperature resistance results have been ignored due to the possibility of adsorbed surface moisture. The resistivity with various doping percent of TiO_2 has been compared at different temperatures in fig 4.11. For the samples subsequently annealed in an H_2 atmosphere the resistivity is shown in figure 4.15. Similarly the resistivity at various temperatures for compositions doped with TiO_2 plus Cr_2O_3 and or V_2O_5 has been shown in figure 4.12-4.14 and figure 4.16.

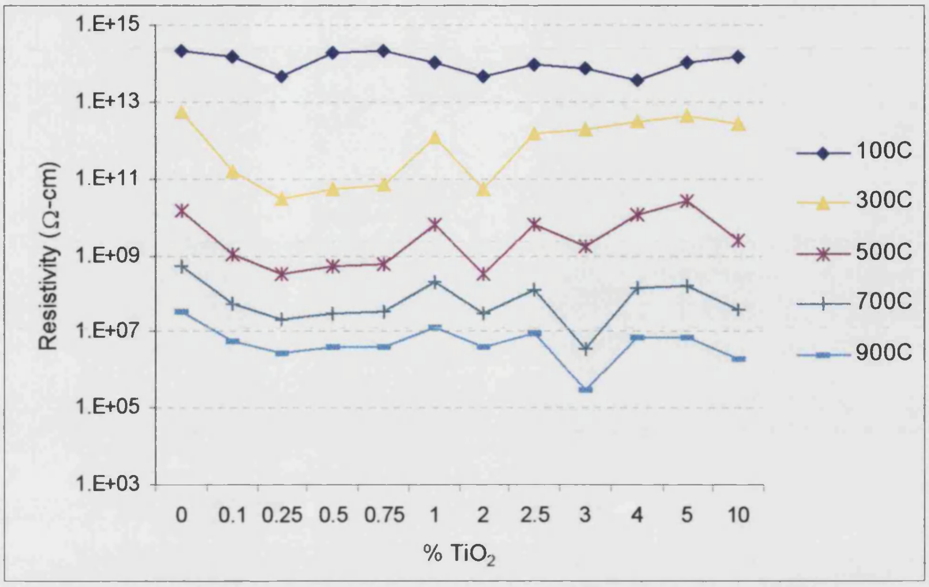

Figure 4.11: Graph of resistivity v/s TiO_2 percentages- as fired

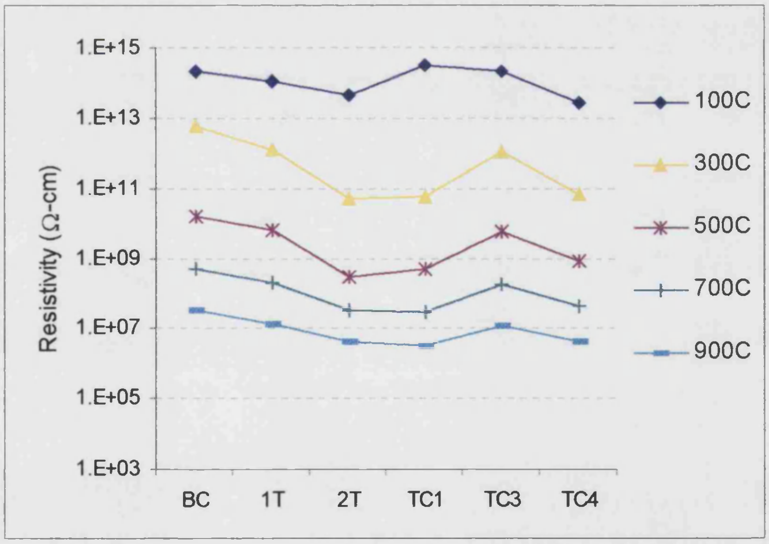

Figure 4.12: Graph of resistivity v/s compositions with TiO_2 plus Cr_2O_3 as fired

TC1: 0.5%TiO_2 +0.5%Cr_2O_3 TC3: 2%TiO_2 +1%Cr_2O_3 TC4: 1%TiO_2 +2%Cr_2O_3

4.7.1. Electrical Properties for samples fired in air

The resistivity values of alumina with various percentages of TiO_2 have been compared in figure 4.11. No specific trend is visible for all the temperatures. However 0.25%TiO_2 shows a fall in resistivity by 2 orders of magnitude at temperatures of 300°C and above. A similar trend is also visible for 3%TiO_2 composition for temperatures above 500°C.

TiO_2 doped compositions, with Cr_2O_3 added have been compared in figure 4.12. It can be safely confirmed that, in the as fired condition, doping the TiO_2 composition with Cr_2O_3, does not have any significant change in the resistivity.

The effect of the addition of V_2O_5 to the 1% TiO_2 doped composition is shown in figure 4.13. With the addition of V_2O_5, resistivity falls, up to 2 orders of magnitude, for 0.5% V_2O_5. Resistivity increases again on increasing V_2O_5 above this level. Addition of 0.5%V_2O_5 to the 0.25%TiO_2, and 3%TiO_2 composition also results in a resistivity drop of about 2 orders of magnitude (figure 4.14). Adding Cr_2O_3 to TiO_2 + V_2O_5 compositions was not useful.

A larger drop in resistivity (about 3 orders of magnitude) is seen in composition M1, which has 2%TiO_2 with no MgO and CaO (figure 4.14).

Thus none of the as fired samples were successful in reducing the conductivity to the extent required for the application of klystrons, which is at least 5 orders of magnitude. The samples from these compositions were annealed in reducing atmosphere in the continuous metallising furnace at Marconi Applied Technologies (formerly EEV Ltd). The conditions of firing were:

Temperature: 1460°C
Soak Time: 40minutes
Atmosphere: 10%H_2 and 90%N_2 bubbled through water at 25°C.

4.7.2. Effect of H_2 Annealing

The result of H_2 annealing on compositions with various percentages of TiO_2 are shown in figure 4.15. The fall in resistivity, as compared with base composition, is steeper than for the as fired composition. The best results are achieved in 3%TiO_2 composition, which has a drop in resistivity of 9 orders of magnitude. It shows a low temperature resistivity of $1x10^5\Omega cm$ as compared to base composition resistivity of $2x10^{14}$. At 300°C it drops to 7000Ω-cm, against base composition value of $7x10^{11}$-cm. Above this temperature the resistivity of the base composition falls to $3x10^9\Omega$-cm, while that for the 3 % TiO_2 composition drops marginally to 2000Ω-cm. Overall the fall in resistivity is much higher than the minimum required value of $10^9\Omega$-cm. This trend is confirmed on three different samples of 3%TiO_2 annealed at Marconi for two different times.

An increase in TiO_2 doping by just 1% above the 3% level, resulted in a steep increase in resistivity. The decrease in resistivity took place again only at the 10%TiO_2 composition but still only to $2x10^7\Omega$-cm, about 2 orders of magnitude above the 3%TiO_2 composition. The reason for this unusual trend has been studied in detail and the results discussed in the following chapters.

TiO_2 + Cr_2O_3 compositions show some improvement in resistivity drop results on annealing in H_2. However this effect may be more due to the TiO_2 rather than due to Cr_2O_3. The presence of V_2O_5 in the TiO_2 doped composition is not of help in this case, as the resistivity drop is to the same level as in the TiO_2 +V_2O_5 as-fired compositions. 3%TiO_2 composition with V_2O_5 also shows steep fall in resistivity, but the drop is nearly 2 orders less than the composition with only 3%TiO_2. This may suggest that the presence of V_2O_5 reduces the extent of the drop in resistivity of TiO_2 doped compositions in the case off H_2 annealed samples. This will be discussed later.

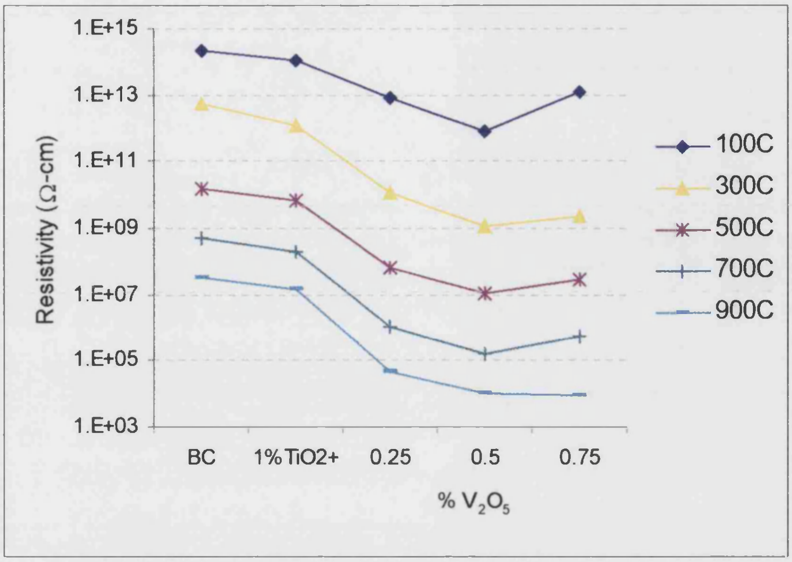

Figure 4.13: Graph of resistivity v/s compositions with TiO_2 plus V_2O_5 as fired

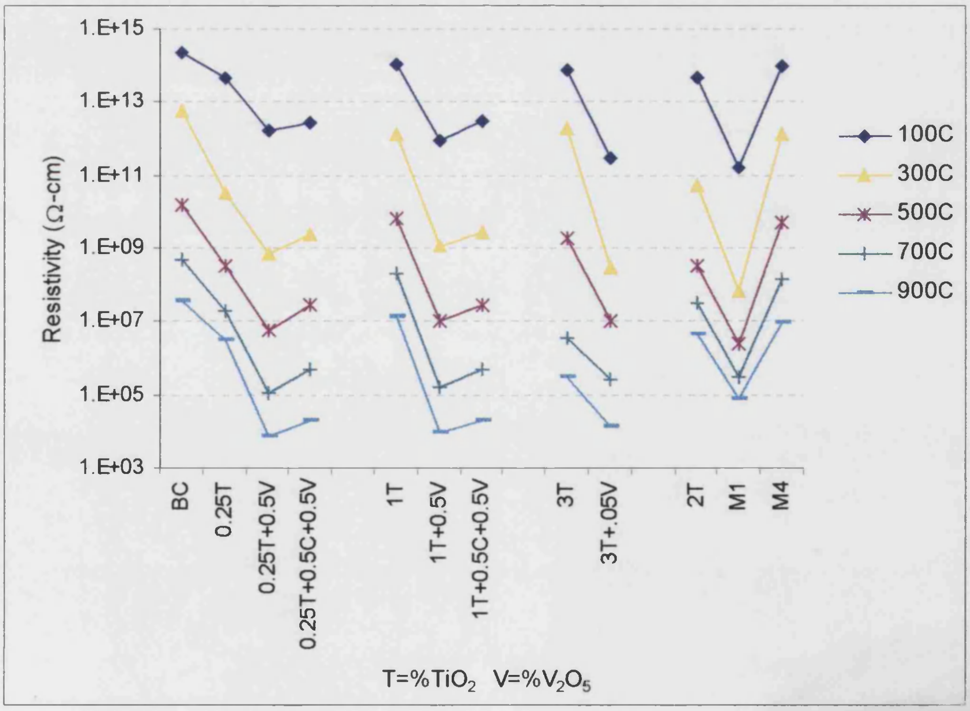

Figure 4.14: Graph of resistivity v/s compositions with TiO_2 V_2O_5 & Cr_2O_3 as fired

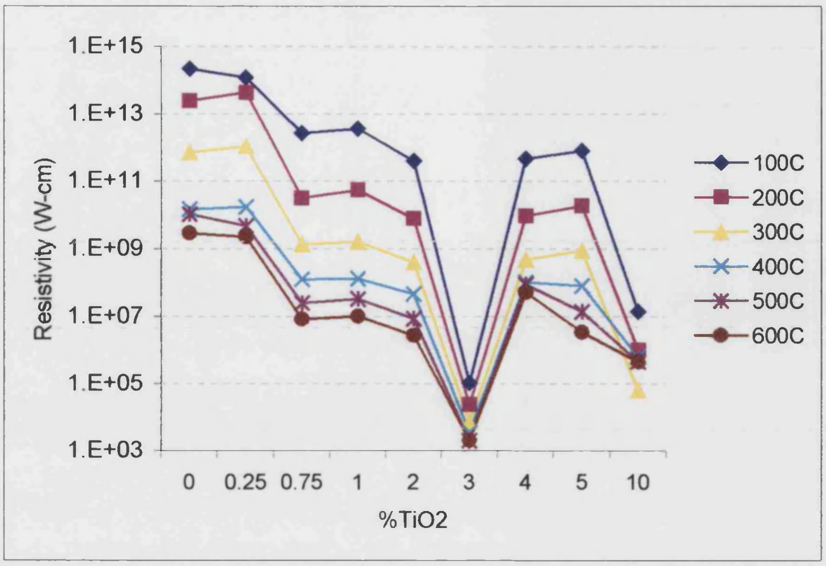

Figure 4.15: Graph of resistivity v/s TiO_2 percentages-H_2 annealed

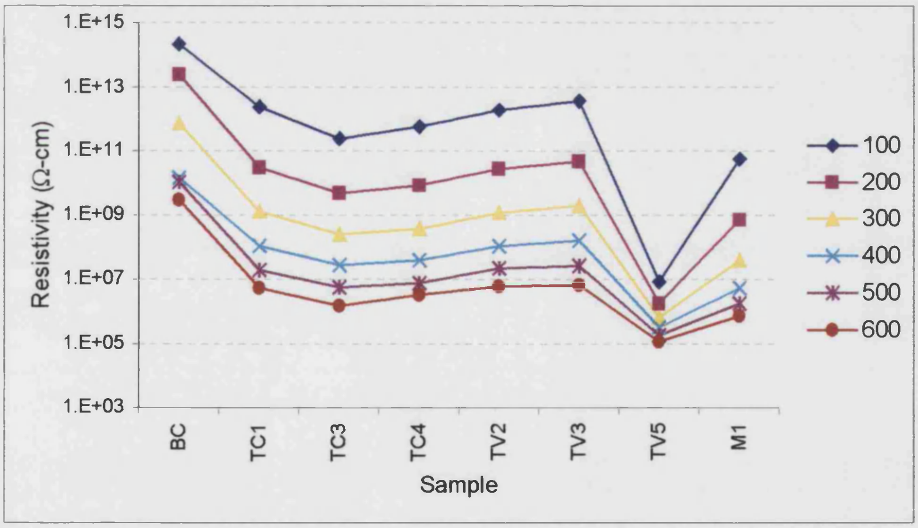

Figure 4.16: Graph of resistivity v/s compositions with TiO_2 plus Cr_2O_3 V_2O_5 - H_2 annealed

TC1: 0.5%TiO_2 +0.5%Cr_2O_3	TC3: 2%TiO_2 +1%Cr_2O_3	TC4: 1%TiO_2 +2%Cr_2O_3
TV2: 1%TiO_2 +0.25%V_2O_5	TV3: 1%TiO_2 +0.5%V_2O_5	TV5: 3%TiO_2 +0.5%V_2O_5

4.7.3. Activation Energy

Activation energy gives an indication of the barrier a charge carrier has to overcome to move to the next site and thus take part in conduction. The material with a lower activation energy will thus conduct easily. Activation energy can be calculated using the equation below.

For dilute solid solutions (low dopant concentration), activation energy is related to conductivity by the following expression {73}:

$$\sigma T = \frac{[V_o]N_0(Ze)^2}{k} J_d^2 f_0 \gamma \cdot \exp(\Delta S_m / k) \exp[-\Delta H / (kT)]$$

Where σ is conductivity, V_o the concentration of vacancies, N_0 the number of anion sites per unit volume, Ze is charge per particle, J_d is the particle density, f_0 is a factor signifying number of equivalent sites between which a charge particle jumps, γ is lattice vibrational frequency, ΔS_m is the entropy for jump and ΔH_m is the enthalpy for conduction, also called activation energy for conduction.

This expression can be simplified into

$\sigma T = A \exp[-\Delta H / (kT)]$ where A is a constant

this is equal to

$\ln(\sigma T) = \ln A + [-\Delta H / k](1/T)$

and matches the equation for a straight line:

$y \quad = c \quad + \quad mx$

Thus a plot of $\ln(\sigma T)$ vs. 1/T is linear, and the slope is equal to $\Delta H/k$. Where k is the Boltzman constant and is equal of $1.38\text{x}10^{-23}$ Joules/Kelvin, and ΔH is the activation energy. ΔH can be calculated in eV using the conversion,

1Joule=$6.24\text{x}10^{18}$ eV

The activation energy for various samples has been calculated from the Arrhenius plots in figures 4.17-4.18 for as fired and H_2 annealed samples.

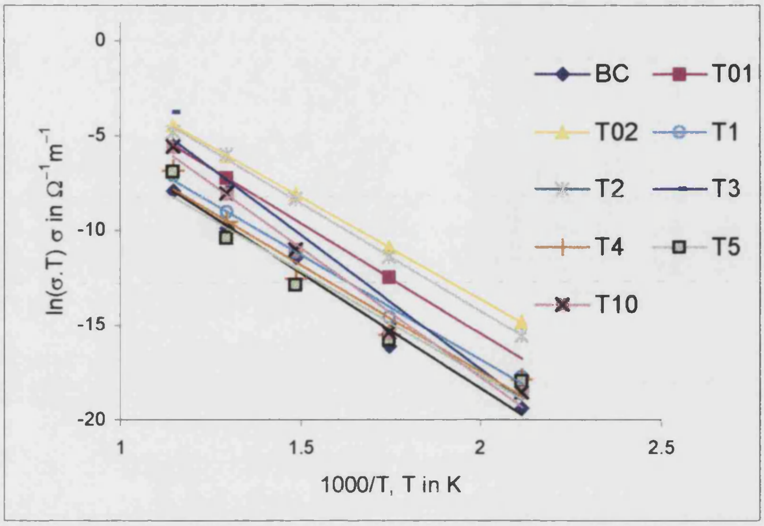

(a)

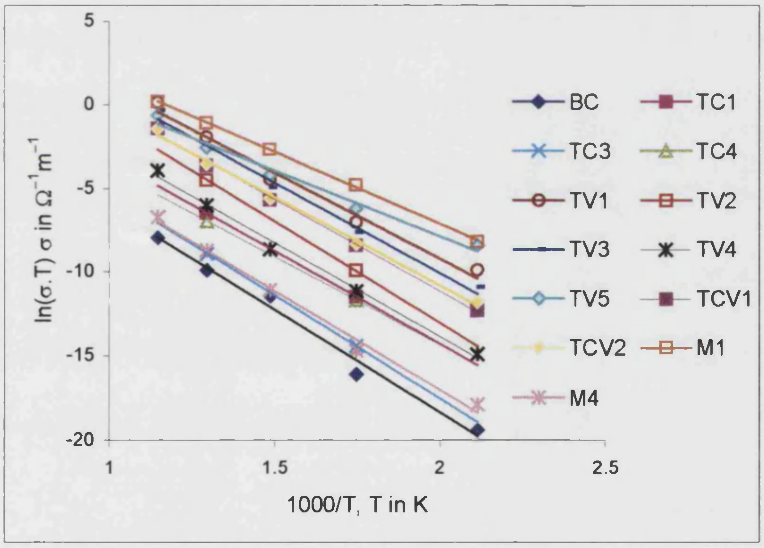

(b)

Figure 4.17: Trendline graph in 200-600 ℃ range for as fired (a) TiO_2 doped compositions and (b) TiO_2 +Cr_2O_3.V_2O_5 compositions

TC1: 0.5%TiO_2 +0.5%Cr_2O_3 TC3: 2%TiO_2 +1%Cr_2O_3 TC4: 1%TiO_2 +2%Cr_2O_3

TV1: 0.25%TiO_2 +0.25%V_2O_5 TV2: 1%TiO_2 +0.25%V_2O_5 TV3: 1%TiO_2 +0.5%V_2O_5

TV4: 1%TiO_2 +0.75%V_2O_5 TV5: 3%TiO_2 +0.5%V_2O_5

TCV1: 0.25%TiO_2 +0.5%Cr_2O_3 +0.25%V_2O_5 TCV1: 1%TiO_2 +0.5%Cr_2O_3 +0.25%V_2O_5

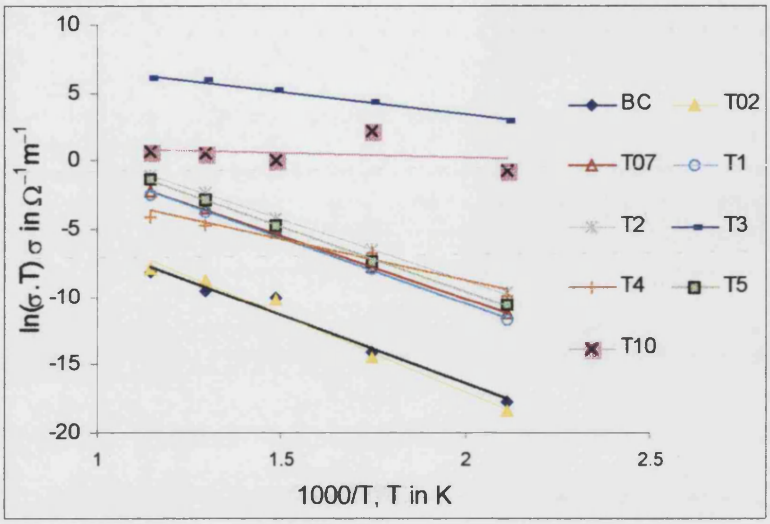

(a)

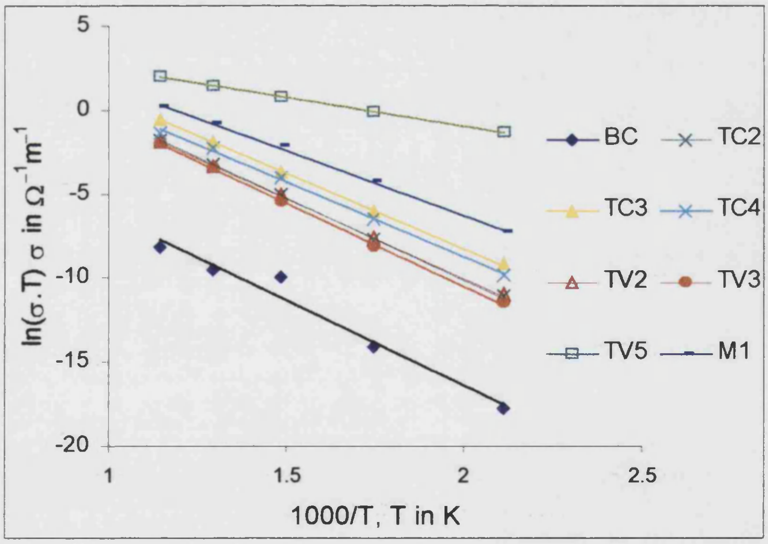

(b)

Figure 4.18: Trendline graph in 200-600 ℃ range for H_2 annealed (a) TiO_2 doped compositions and (b) TiO_2 + Cr_2O_3 / V_2O_5 compositions

The activation energy for each sample in the range of 200-600°C is calculated from the slope of the linear trendline. The values have been compared in figure 4.19. A possible scatter in these values was calculated by approximately determining the experimental uncertainity at various measuring stages (~5%) and adding "1–correlation coefficient" of the best fit data on straight line.

For the as fired TiO_2 doped compositions the activation energy is the same within a reasonable error, except for the 3% and 10% TiO_2 composition, where slightly higher values are attained. Compositions containing Cr_2O_3 with TiO_2 also do not show any definite trend. 3%TiO_2 composition containing 0.5%V_2O_5 did have a lower activation energy, indicating V_2O_5 playing some role in reducing the resistivity of alumina.

For the H_2 annealed case, significantly lower activation energy resulted in the 3%TiO_2 composition (sample T3) showing a steep fall in resistivity. Similar activation energy values were found for the 3%TiO_2 + 0.5%V_2O_5 (sample TV5) composition, though having 2 orders higher resistivity than 3%TiO_2 composition. This might indicate similarity of mechanisms of conductivity in both these composition. Further the large difference between the activation energy for the T3 and TV5 compositions compared with other compositions indicates different current carriers to be operative in the former compositions relative to the latter. Increased activation energy is noticed in samples with higher or lower percentages of TiO_2 than the 3% composition. The activation energy of the 10%TiO_2 composition (sample T10) showed a very high error in measurement due to the non-linear trend of resistivity v/s temperature. This could be due to too many different factors/charge carriers contributing to the conductivity of the 10%TiO_2 composition.

The results of electrical characterisation have been discussed in detail, in light of the microstructure of these compositions set out in the following chapters.

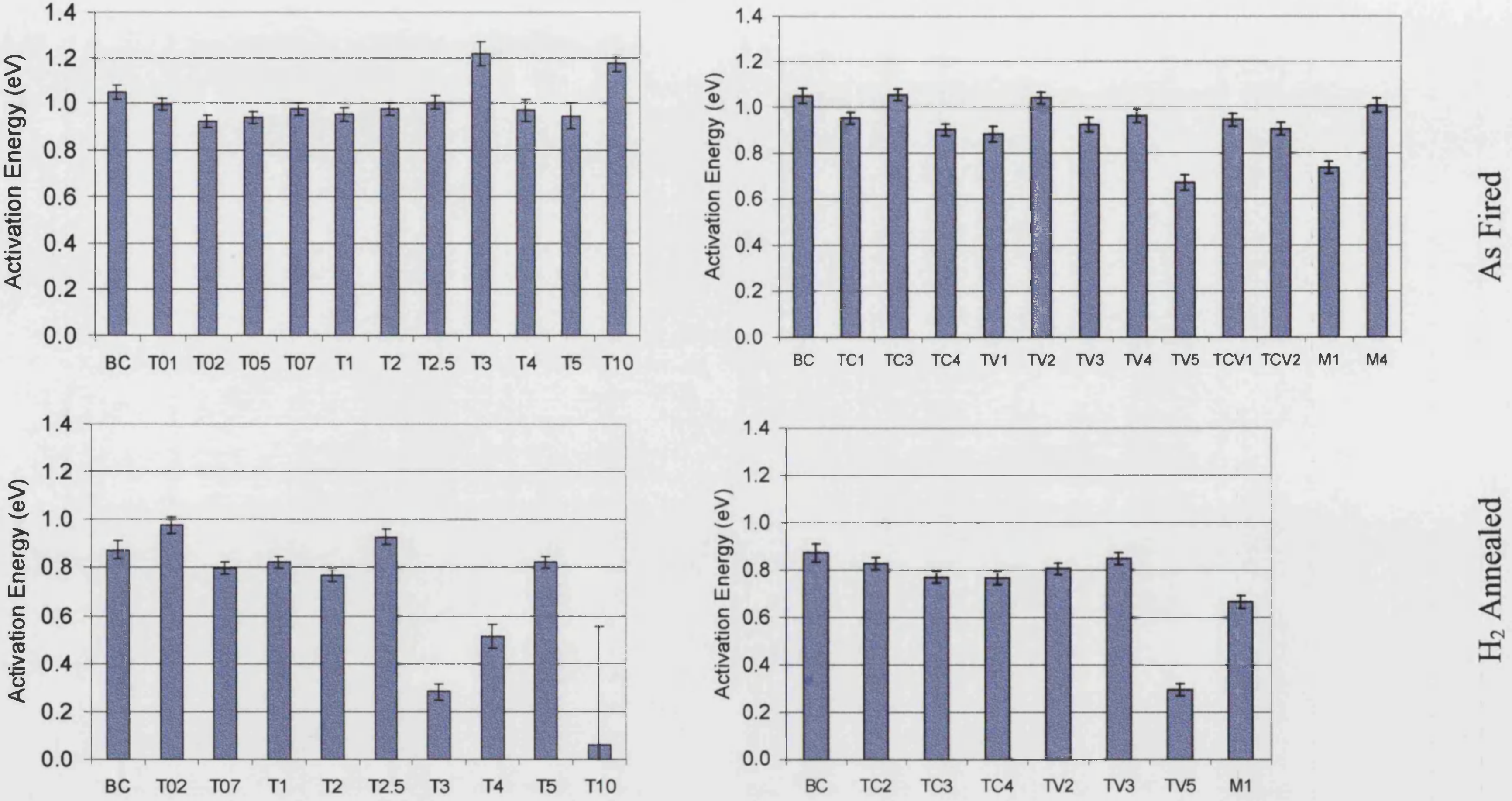

Figure 4.19: Activation Energy for various samples

CHAPTER V

MICROSTRUCTURE EVALUATION

Chapter covers the results from SEM, TEM, EPMA and XRD studies on the compositions that have shown interesting characteristics in the electrical testing.

5. MICROSTRUCTURE EVALUATION

The previous chapter has described how TiO_2 V_2O_5 and Cr_2O_3 have influenced the electrical properties of alumina. Some of the results are also unusual. In this chapter a study has been done to identify where these additives are located in the alumina network, what phases they are forming and then relate the results to the electrical characteristics shown by alumina. This will help determine the reasons for the electrical behaviour shown by alumina under the influence of these additives. The microstructure of exaggerated grain growth in liquid phase sintered alumina is well known, and has been shown in figure 3.1. The literature has suggested that TiO_2 addition increases the grain size of alumina. This will be discussed in the section following the phase distribution.

5.1.Phase Distribution

The distribution of various phases in TiO_2 and Cr_2O_3 /V_2O_5 doped alumina have been studied using SEM, TEM and Electron Probe Micro Analysis (EPMA) in conjunction with X-ray Diffraction and Energy Dispersive X-rays (EDX). The glass forming additives i.e. SiO_2, MgO, and CaO will also influence the alumina microstructure and will affect the distribution of TiO_2. Their distribution also holds importance for a complete understanding. The study has been carried out in 3 steps. These are:

(a) Study the distribution of various additives within the alumina network using qualitative analysis with EPMA, and SEM in the back scattered mode
(b) Identification of various phases being formed using XRD and TEM
(c) Carry out the quantitative analysis for the distribution of TiO_2 in the alumina network.

5.1.1. Distribution of Additives

Sample preparation for SEM and TEM studies is the same as explained in chapter 3. The samples used for EPMA were the same as those used for SEM. The EPMA instrument was a 'JEOL JXA-8600 Superprobe'. The standards used for setting the crystal positions to identify various materials are as listed in table 5.1:

Table 5.1

Material	Element	Standard
Al_2O_3	Al	pure aluminium metal
SiO_2	Si	pure silicon metal
MgO	Mg	$MgAl_2O_4$
CaO	Ca	$CaCO_3$
TiO_2	Ti	pure titanium metal
V_2O_5	V	pure vanadium metal
Cr_2O_3	Cr	pure chromium metal
	O	$MgAl_2O_4$

It is well know that SiO_2 is a glass forming oxide and is located mainly in the glass phase. Other additives have been mapped for composition TCV2, which contains all the three dopants, TiO_2, V_2O_5 and Cr_2O_3. Figure 5.1 shows the microstructure of the composition with mapped additives. The microstructure consists of abnormal alumina grains with intermediate glass (marked G). This mapping shows CaO is present primarily in the glass region. The bright area in the microstructure is TiO_2 rich. The TiO_2 rich area is near some of the grain boundaries, and V_2O_5 is also present in the same place. Cr_2O_3 is distributed uniformly over the entire area. From this mapping, it is difficult to predict the specific position of the MgO, although it can be said that the areas where MgO is present in excess, a cluster of small grains is evident.

The distribution of TiO_2 and V_2O_5 is clearer from the mapping in the $3\%TiO_2+0.5\%V_2O_5$ composition (figure 5.2). Again both are present in the same location in alumina microstructure.

5.1.1.1. TiO_2 Distribution in Alumina Microstructure

In a composition containing only 0.25% TiO_2, a slightly higher concentration of TiO_2 seems to exist within the glassy area, than exists in the alumina (figure 5.3). This suggests that TiO_2 even at very small concentrations has a tendency to dissolve into the glass. Nevertheless it is known that its solubility in Al_2O_3 is limited to 500ppm {103} and most of it is retained in the grain boundary {50}.

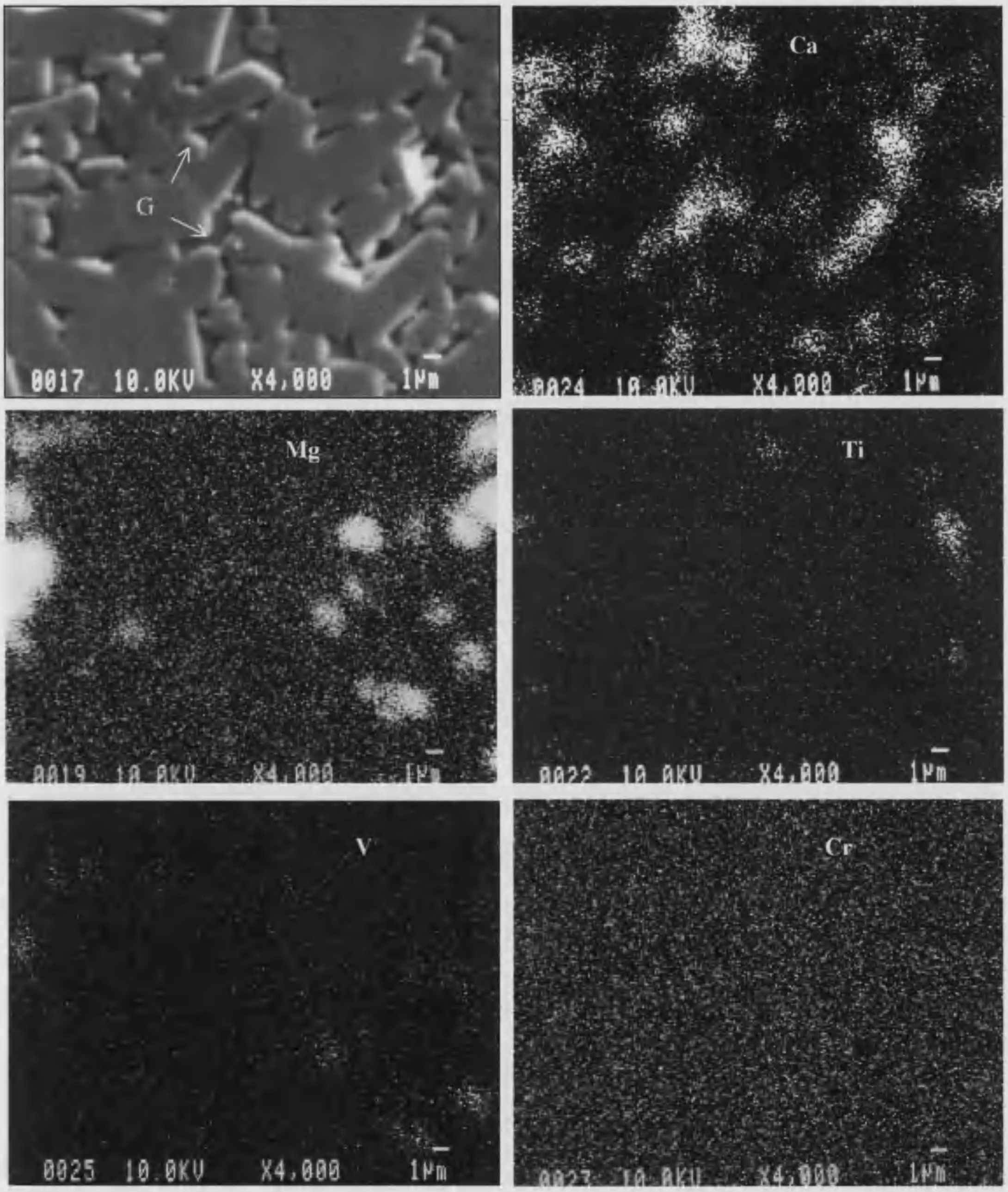

Figure 5.1: Mapped additives, showing their position in the alumina network in composition TCV2, containing 1%TiO_2 +0.5%V_2O_5 +0.5%Cr_2O_3

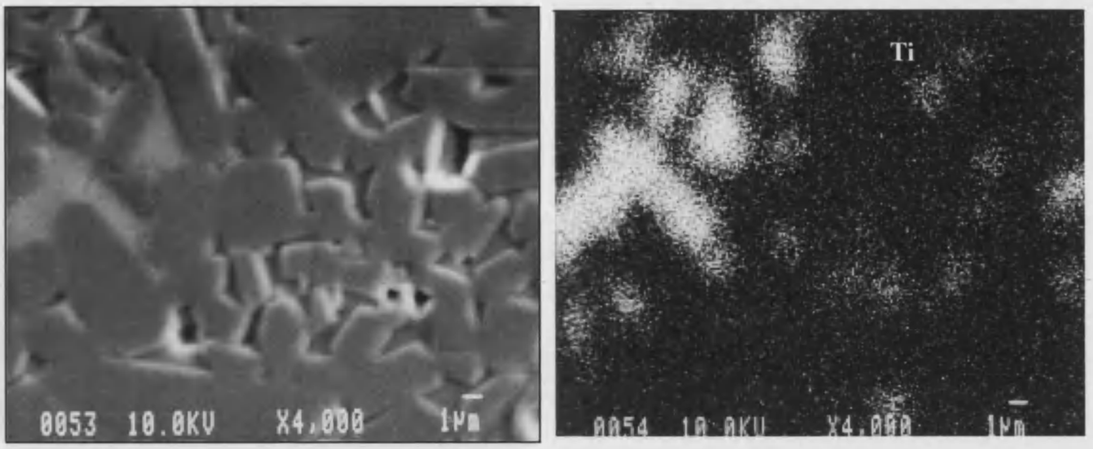

Figure 5.2: Mapped TiO_2 and V_2O_5 in 3%TiO_2+0.5%V_2O_5 composition

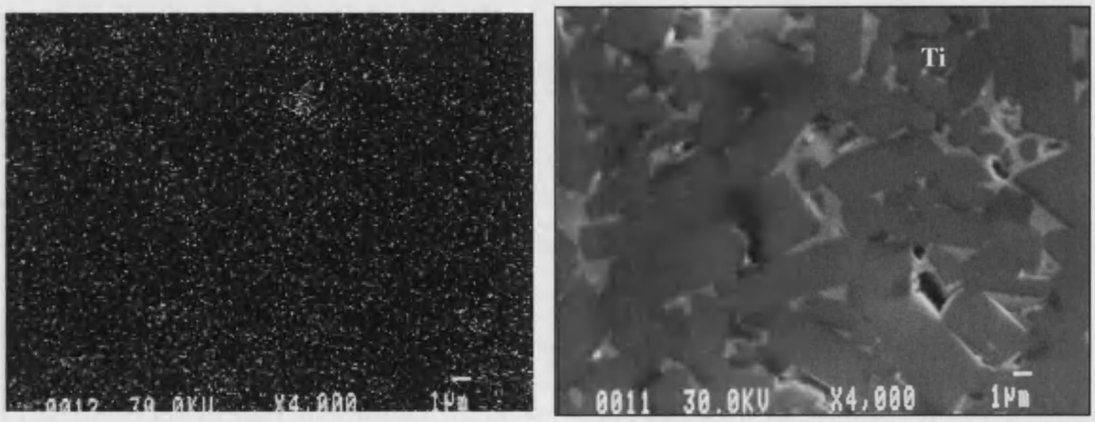

Figure 5.3: Ti map in composition containing 0.25%TiO_2

What happens if the TiO_2 concentration is increased significantly as in 3%TiO_2? Figure 5.4 (a) shows the secondary electron image and figure 5.4 (b) shows the back scattered image for same area. The alumina grains are very clear (marked by black arrow). The darker portions, marked ① is the glass area as shown by the EDX spectrum in figure 5.5 (a). The bright portion marked ② is the Ti rich area as shown in the EDX spectrum in figure 5.5 (b). The excess Ti forms a Ti rich precipitate at the grain boundary. The composition of this phase and the compounds therein will be discussed later in this chapter. As the TiO_2 percentage is reduced the distinct Ti precipitates reduce considerably in 2.5% composition (figure 5.6(a)), are around same level for 2% (figure 5.6(b)), and are nearly eliminated at 1%TiO_2 (figure 5.6(c)). Thus below 1%TiO_2 it can be assumed that all the TiO_2 present is either in glass phase or dissolved in the Al_2O_3 grains. No visible difference existed between the back scattered images of the as fired and the H_2 annealed sample.

5.1.1.2. V_2O_5 Distribution in Alumina Microstructure

As discussed earlier, V_2O_5 is present at the same place as TiO_2 exists. Thus the V_2O_5 is present in Ti rich precipitates (white bright areas). The TiO_2 is also dissolved in alumina and glass even in very small percentage compositions. To study if V_2O_5 also goes into the alumina and glass the TV1 composition, containing just 0.25%TiO_2 and 0.5%V_2O_5 has been studied. No Ti rich precipitates, as were present in high TiO_2 compositions, are present here. In contrast to the statement in the previous section regarding the non-existence of Ti precipitates in low percentage TiO_2 compositions, TiO_2 +V_2O_5 precipitates have been seen in the TV1 composition. The bright area at the edge of the grain marked ③ in figure 5.7 has a fairly high TiO_2 and V_2O_5 content (EDX- figure 5.8(a)) while another glass area marked ④ has none (EDX-figure 5.8(b)), as also is the case for the alumina grain. At a different point in this sample (figure 5.9) the EDX at glass, point ⑤, did have small amount of V_2O_5 (figure 5.10) but TiO_2 could not be detected. A small amount of TiO_2 and V_2O_5 in the glass is visible in the 1%TiO_2 + 0.7%V_2O_5 sample (EDX figure 5.12 at point ⑥ in figure 5.11). The high alumina peak in glass is due to the stray X-rays from surrounding alumina grains, which could not be isolated, due to the small size of glass area. This

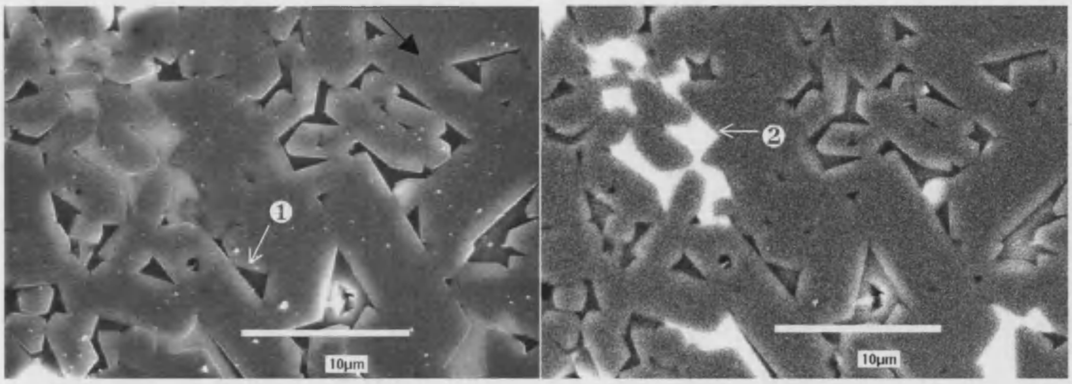

(a) (b)

Figure 5.4: 3%TiO_2 sample in (a) secondary electron mode (b) Back scattered mode

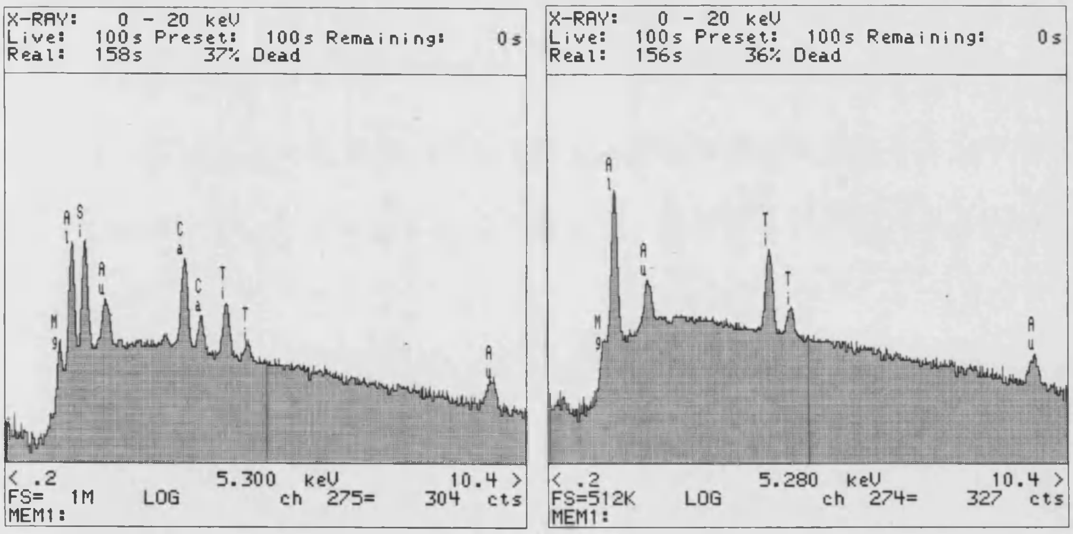

```
X-RAY:    0 - 20 keV
Live:  100s Preset:  100s Remaining:    0s
Real:  158s      37% Dead
```

```
< .2             5.300  keV          10.4 >
FS=  1M    LOG         ch  275=      304  cts
MEM1:
```

```
X-RAY:    0 - 20 keV
Live:  100s Preset:  100s Remaining:    0s
Real:  156s      36% Dead
```

```
< .2             5.280  keV          10.4 >
FS=512K    LOG         ch  274=      327  cts
MEM1:
```

(a) (b)

Figure 5.5: EDX spectrum for 3%TiO_2 sample at (a) point ① (b) point ②

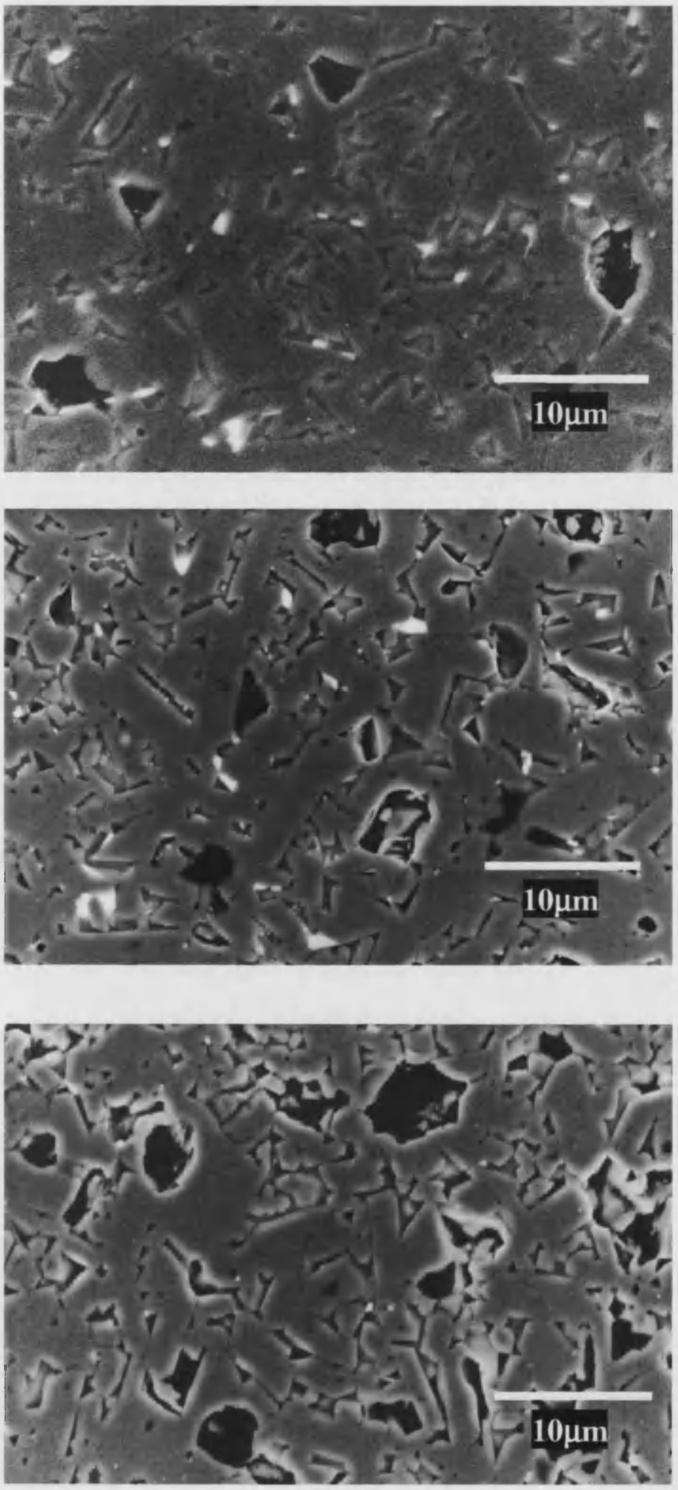

(a) 2.5%TiO_2

(b) 2%TiO_2

(c) 1%TiO_2

Figure 5.6: Back scattered images showing the Ti rich precipitates (white bright spots)

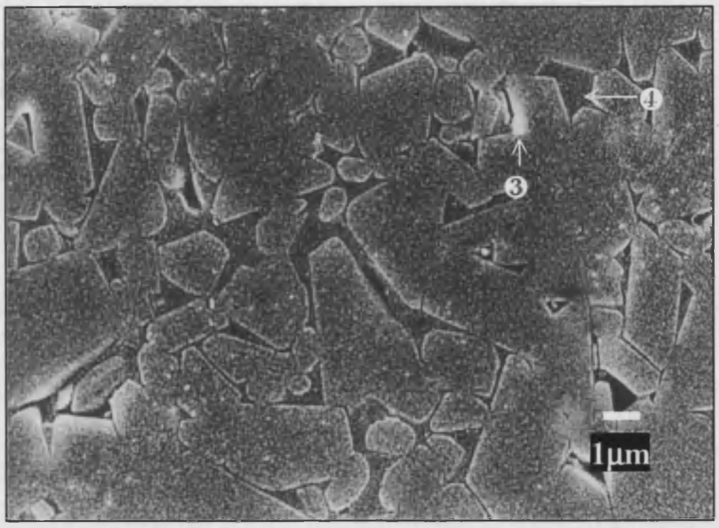

Figure 5.7: Back scattered image for 0.25%TiO_2 +0.5%V_2O_5 sample

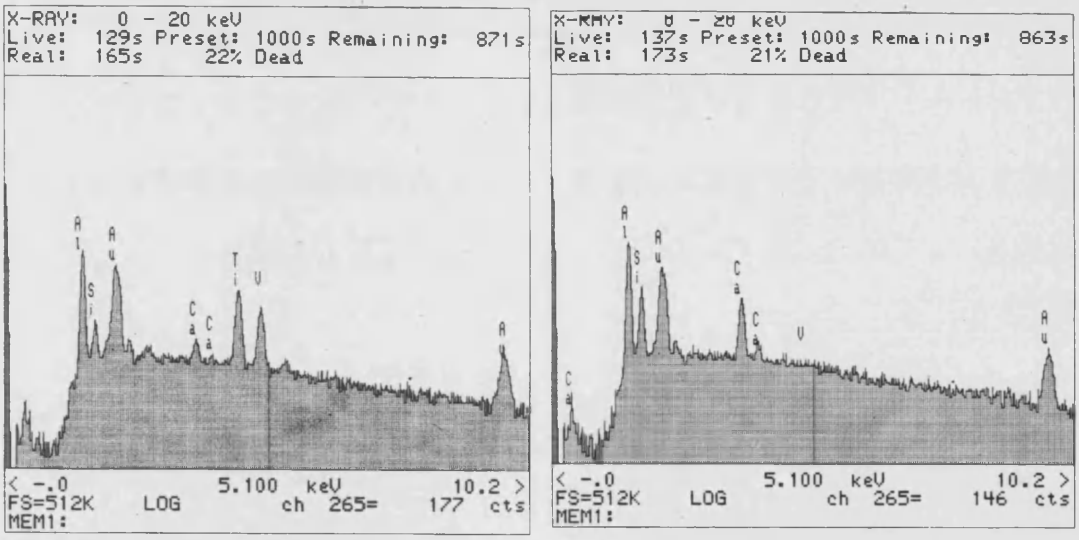

```
X-RAY:    0 - 20 keV
Live:   129s Preset: 1000s Remaining:   871s
Real:   165s        22% Dead

< -.0               5.100   keV          10.2 >
FS=512K     LOG          ch  265=      177  cts
MEM1:
```

```
X-RAY:    0 - 20 keV
Live:   137s Preset: 1000s Remaining:   863s
Real:   173s        21% Dead

< -.0               5.100   keV          10.2 >
FS=512K     LOG          ch  265=      146  cts
MEM1:
```

(a) (b)

Figure 5.8: EDX spectrum for 0.25%TiO_2 +0.5%V_2O_5 sample at (a) point ③ (b) point ④

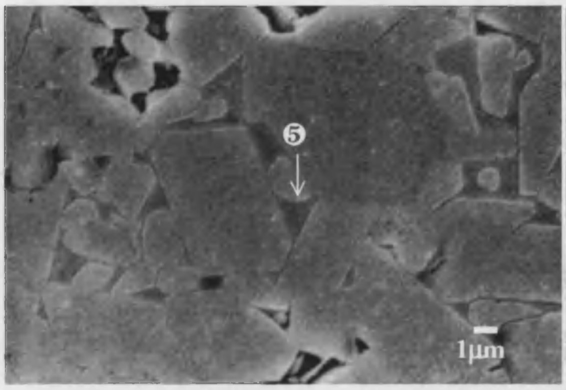

Figure 5.9: Back scattered image for 0.25%TiO_2 +0.5%V_2O_5 sample

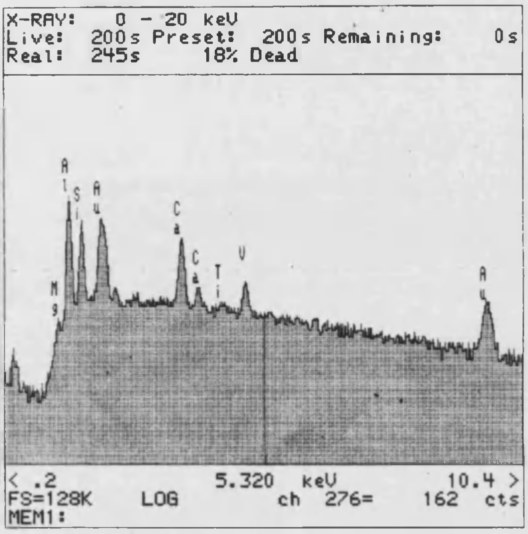

```
X-RAY:    0 - 20 keV
Live:  200s Preset:  200s Remaining:     0s
Real:  245s      18% Dead
```

```
< .2              5.320  keV         10.4 >
FS=128K    LOG          ch  276=      162  cts
MEM1:
```

Figure 5.10: EDX image at point ⑤

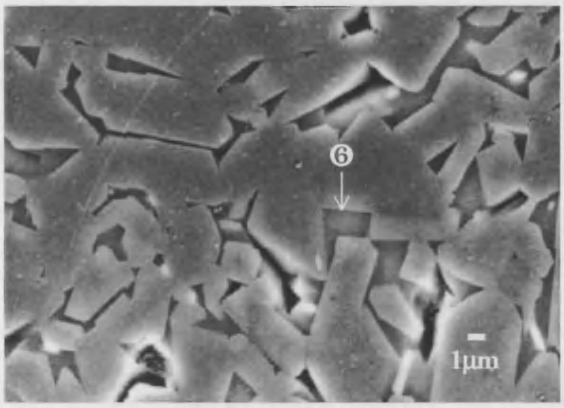

Figure 5.11: Back scattered image for 1%TiO_2 +0.7%V_2O_5 sample

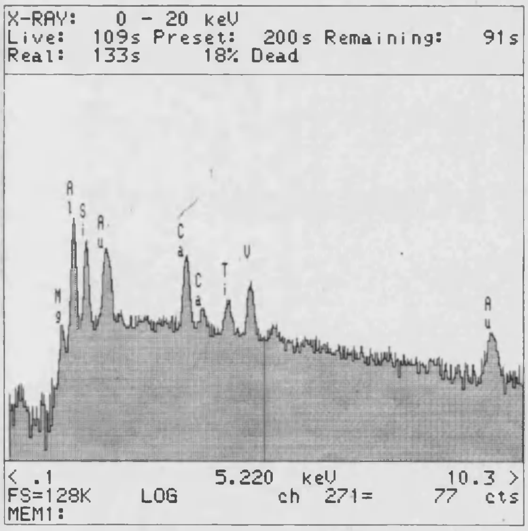

```
X-RAY:    0 - 20 keV
Live:  109s Preset:  200s Remaining:    91s
Real:  133s      18% Dead
```

```
< .1              5.220  keV         10.3 >
FS=128K    LOG          ch  271=       77  cts
MEM1:
```

Figure 5.12: EDX image at point ⑥

discussion suggests that V_2O_5 is more soluble than TiO_2 in the glass and can be present, apart from inTi rich precipitates, in glass even if TiO_2 is absent. The V_2O_5 in glass might be responsible for marginally reducing the resistivity of alumina (figure 4.13). Looking at the phase diagrams of Al_2O_3 - V_2O_5 , $CaO-TiO_2-V_2O_5$ and $CaO-MgO-SiO_2$ -V_2O_5 , no high temperature phase was found forming between any of V_2O_5 and any of the other additives. Most compounds of V_2O_5 existed as liquid above 900°C. In fact it is known to vaporise to an extent of 5.5% above 1450°C (as described in the explanation for the phase diagram. This indicates the V_2O_5 should exist only in the glass, or as recrystallised form in the alumina microstructure. Nevertheless its preferential presence along with TiO_2 indicates the formation of some TiO_2 -V_2O_5 compound which could not be identified due to lack of any more published information in this area.

Cr_2O_3 is distributed uniformly over the entire alumina microstructure (figure 5.1), and the distribution is independent of the presence of TiO_2. Thus Cr_2O_3 which together with TiO_2 could have reduced the conductivity of Al_2O_3, as was reported by Watanabe et al {100}, forms no specific phase or compound with TiO_2 and has no influence on the conductivity of alumina (figure 4.12). The $Cr_2O_3-TiO_2$ -Fe_2O_3 phase diagram, indicates the formation of Ti-Cr compounds like $Ti_7Cr_2O_{17}$, $Ti_6Cr_2O_{15}$, $Ti_2Cr_2O_7$, however most of these compounds are unstable above 1300°C. This could be the reason why the Cr_2O_3 does not form a phase with TiO_2 in this work.

5.1.1.3. TiO_2 dissolution in Al_2O_3

Earlier studies have shown the dissolution of TiO_2 in the alumina grain occurs up to 500ppm {103} and have observed that the dissolution goes up in low p_{O2} due to the higher dissolution of Ti^{3+} {50}. Also, higher dissolution of Ti in Al_2O_3 should reduce the conductivity, based on the theory of Tsaur and Kröger {50}. However in the present study, the annealing at low p_{O2} has led to a steep increase in conductivity. To study the amount of TiO_2 that dissolves into Al_2O_3, quantitative analysis on EPMA was carried out on samples fired in air and compared with the results from samples annealed in H_2. The standards used were same as shown in table 5.1. The crystal and peak positions used for each element and the weight percent of each element in the standard, as detected by the probe, are as in table 5.2. The voltage used was 10kV to prevent detecting X-rays from deeper levels in the sample, i.e. to determine only the surface information {179}.

Table 5.2

Element	Standard	Wt%	Crystal	Peak
Al	Al	100.00	TAP*	90.650
Si	Si	100.00	LIF*	77.440
O	$MgAl_2O_4$	44.95	LDE*	110.225
Ti	Ti	100.00	LIF	191.115
Mg	$MgAl_2O_4$	17.09	TAP	107.490
Ca	$CaCO_3$	40.04	PET*	107.435
Cr	Cr	100.00	LIF	159.260
V	V	100.00	LIF	174.105

* *TAP = Thallium Acid Phthalate LIF = Lithium Fluoride PET = Pentaerythritol ($C_5H_{12}O_4$)*
LDE = Tungsten-Silicon combination with 2d=60.9

The atomic percent ratio of Ti/Al elements for 3%TiO_2 composition in as-fired samples and H_2 annealed samples is shown in figure 5.13. The chart might be interpreted as showing a marginally higher dissolution of titanium oxide in Al_2O_3 for the H_2 annealed sample. However, looking at the degree of scatter over 5 different readings, it may be safer to predict that there is no significant increase in the dissolution of TiO_2 in Al_2O_3 with H_2 annealing in this sample. Thus, the results from these samples disagree with the argument of Tsaur and Kröger {50} and also Watanabe et al {106} regarding increased dissolution of titanium oxide in alumina grain on annealing in H_2. In other words most of the TiO_2 in >1% compositions is forming the Ti rich precipitates irrespective of whether the samples are as fired or H_2 annealed. Identification of components formed on TiO_2 doping has been carried out using XRD and TEM.

5.1.2. *Identification of Phases*

Individual phases have been identified using X-ray diffraction (XRD). The XRD equipment used is 'Philips Analytical model PW1720/00' with 'Philips PW1877 PC-APD' version 3.5b diffraction software. The anode is Cu and the scan rate 1 degree per minute. The X-ray data for 3%TiO_2 composition shows (figure 5.14) mainly Al_2O_3 peaks. To identify the lower concentration phases such as the Ti based compounds, a batch a scan set up with scan rate of 0.02 degree per minute

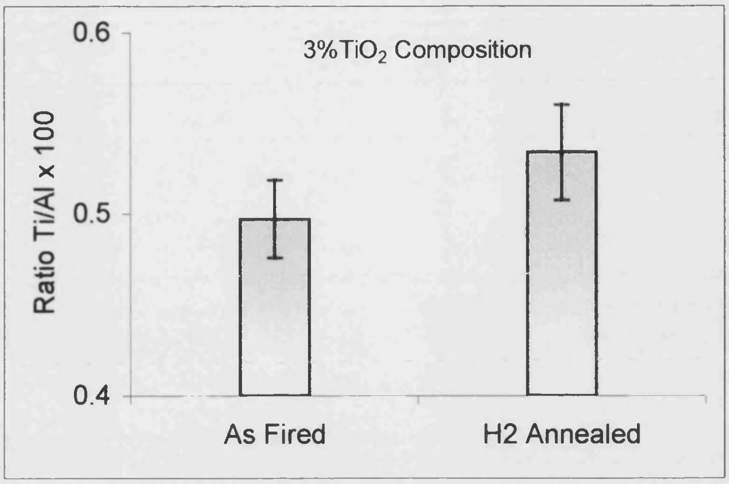

Figure 5.13: Ti dissolution in Al_2O_3 grain

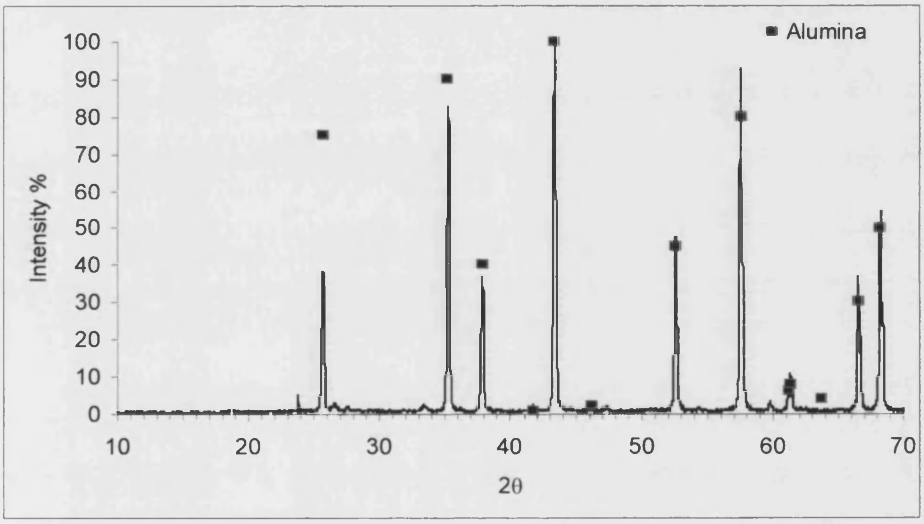

Figure 5.14: X-ray Diffraction pattern for $3\%TiO_2$ composition - short scan

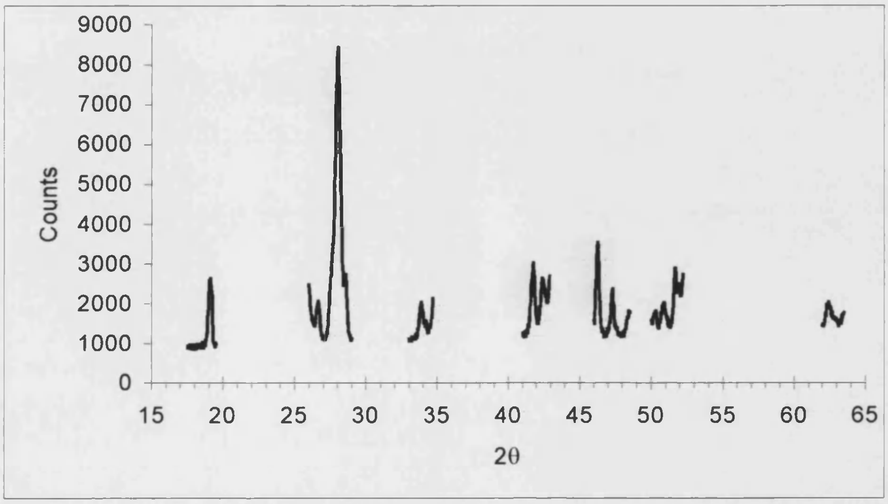

Figure 5.15: X-ray Diffraction pattern for $3\%TiO_2$ composition - long scan

was tried. The 2θ ranges were chosen to include mainly non-alumina peaks. This was carried out based on a set of x-ray data taken in a short scan, on base composition and TiO_2 doped compositions, and identifying the 2θ values in which Ti based phases could have been detected. The new data for 3%TiO_2 is as seen in figure 5.15. This is a combined graph of five different 2θ ranges, 17.5-19.5, 26-29, 33-34.7, 41-43.5, 46-48.5, 50-52.5 and 62-63.5. To compare the type and content of each phase formed for the different compositions, quantitative analysis is necessary.

For quantitative analysis the 'Direct Comparison Method', as explained by Cullity {180}, has been utilised. The peaks from each phase are normalised against the Al_2O_3 peak at d=1.601, for each sample, by taking a ratio of the counts on the specified peak to the counts on Al_2O_3 peak. This ratio is represented in form of a percent peak height relative to the height of Al_2O_3 peak, on the Y-axis, such that higher the number, the higher the intensity of X-rays and the greater the quantity of that phase. This factor will be called as the quantity factor (QF). The possible degree of scatter was calculated by taking 4 scans from two different 3%TiO_2 samples. The approximate error in the peak height is ~12%.

5.1.2.1. Phases in as fired composition

The possible phases formed and their concentration, have been compared for different TiO_2 concentration (figure 5.16), taking the XRD from the base composition as the reference. Due to large number of elements present in the composition, many different phases may be present and the peaks from one phase may be interfering with other phases. To avoid the complexities from such a situation, only a few major peaks comprising of Ti^{4+} phases are compared and discussed.

In the base composition (figure 5.16(a)), the major peak at 2θ = 28.02° is the $CaAl_2Si_2O_8$ (anorthite) peak. With the addition of 3%TiO_2 to this composition, Al_2TiO_5 is formed (figure 5.16(c)). With a further increase in TiO_2 added to the sample, the concentration of Al_2TiO_5 increases considerably and additional titanium oxide peaks are formed. From d values this peak can be construed as from Ti_2O and Ti_3O_5, a form of $Ti_2O_3!TiO_2$. Although it is unlikely that the reduced state of TiO_2, Ti_2O_3 can form in an as fired material, for the time being we can call them as the titanium oxide phases. The concentration of these Al_2TiO_5 and titanium oxide increases considerably at 10%TiO_2. Thus on addition of 3%TiO_2 to the base composition, the Al_2TiO_5 peak increase by a factor of 1. With increase in TiO_2 by another 1%, the Al_2TiO_5 peak increases by a factor of 4 and other titanium oxide peak increase by 1.5. When the TiO_2 concentration increases a further 6 percent, at 10% TiO_2, the Al_2TiO_5 concentration has increased by a factor of 12. This indicates that above 3%TiO_2 there is an exponential increase in Ti containing phases with increase in TiO_2 content.

5.1.2.2. Phases in H_2 annealed composition

Figure 5.17 shows the XRD patterns for the 3%, 4% and 10%TiO_2 compositions. The Al_2TiO_5 peak for 3%TiO_2 sample (figure 5.17(a)), seems to have become shorter as compared with the as fired peak (figure 5.16(b)). However within the degree of error (~12%) we can safely say that it has stayed unchanged, except that it has shifted marginally. The fall in Al_2TiO_5 peak is more obvious in 4% and 10%TiO_2 patterns (figures 5.17 (b) and (c)). Notably, the 10%TiO_2 peak height has decreased by 50%. Surprisingly, the $2\theta = 28°$ (d=3.18) peak has increased. Though it was stated earlier (for base composition) that this is an anorthite peak, here it may well be due to a Ti based phase having d values close to anorthite, for example, TiO_2 -rutile (d=3.25, I=100). Furthermore the Ti_2O peak seems to have been eliminated, though there is a greater likelihood of this phase being formed in H_2 annealed sample. Possibly it might have just shifted.

Nevertheless one clear conclusion that can come out of this study is that the concentration of Al_2TiO_5 reduces on annealing in H_2. The compound might be converting into TiO_2 +Al_2O_3. However theoretically it is known that the conductivity increases with the Ti reducing from the 4+ state to the 3+ state, resulting in the formation of Ti_2O_3. The exclusive Ti_2O_3 peaks are mainly at d =1.7 (2θ = 53.8) which might be masked by the 45%Al_2O_3 peak at d = 1.74. A 60%Ti_2O_3 peak is at d = 2.57 (2θ = 34.85) which might combine with the 60%

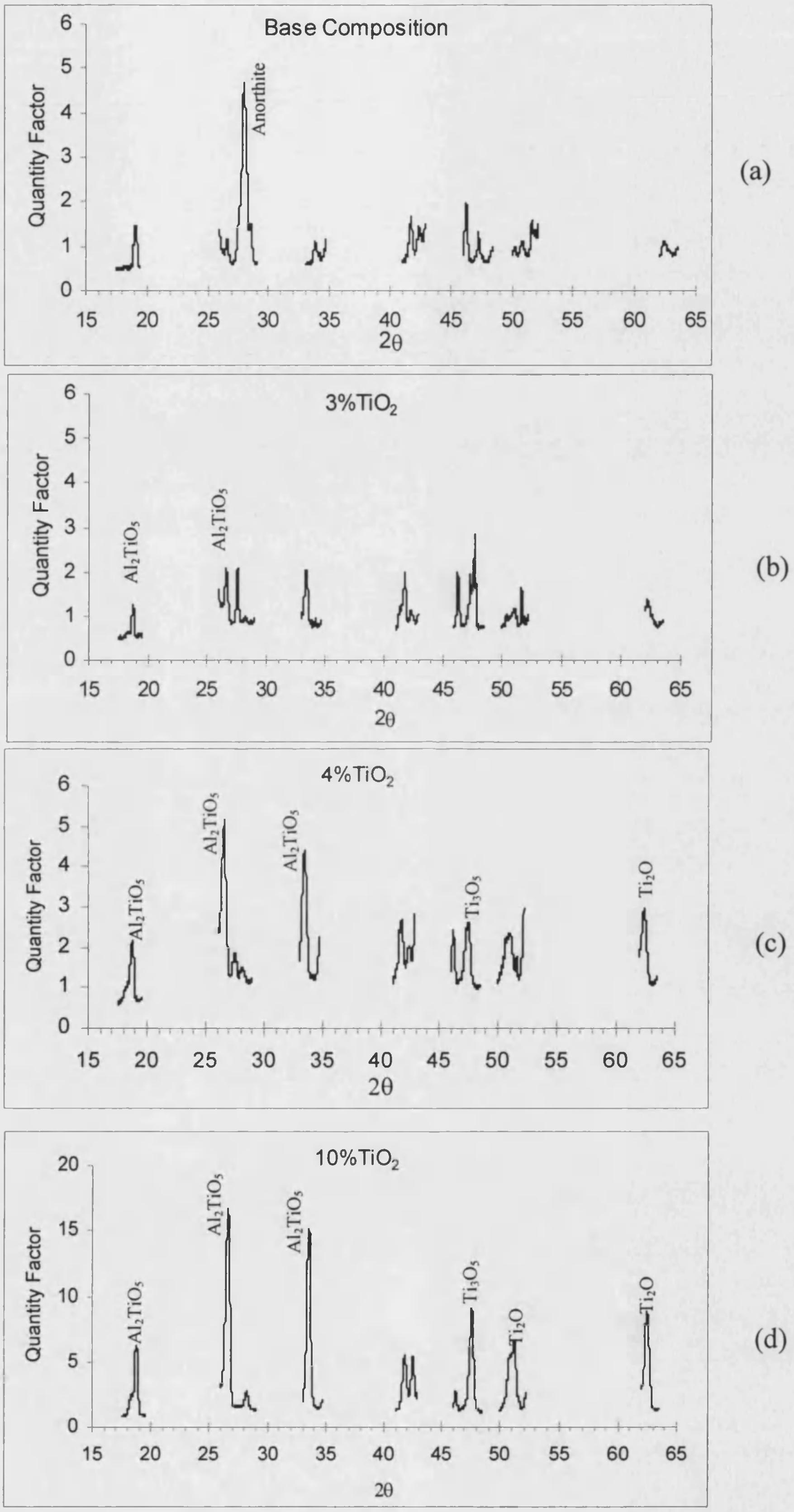

Figure 5.16: Normalised XRD patterns for as fired samples

OF ~ 1.

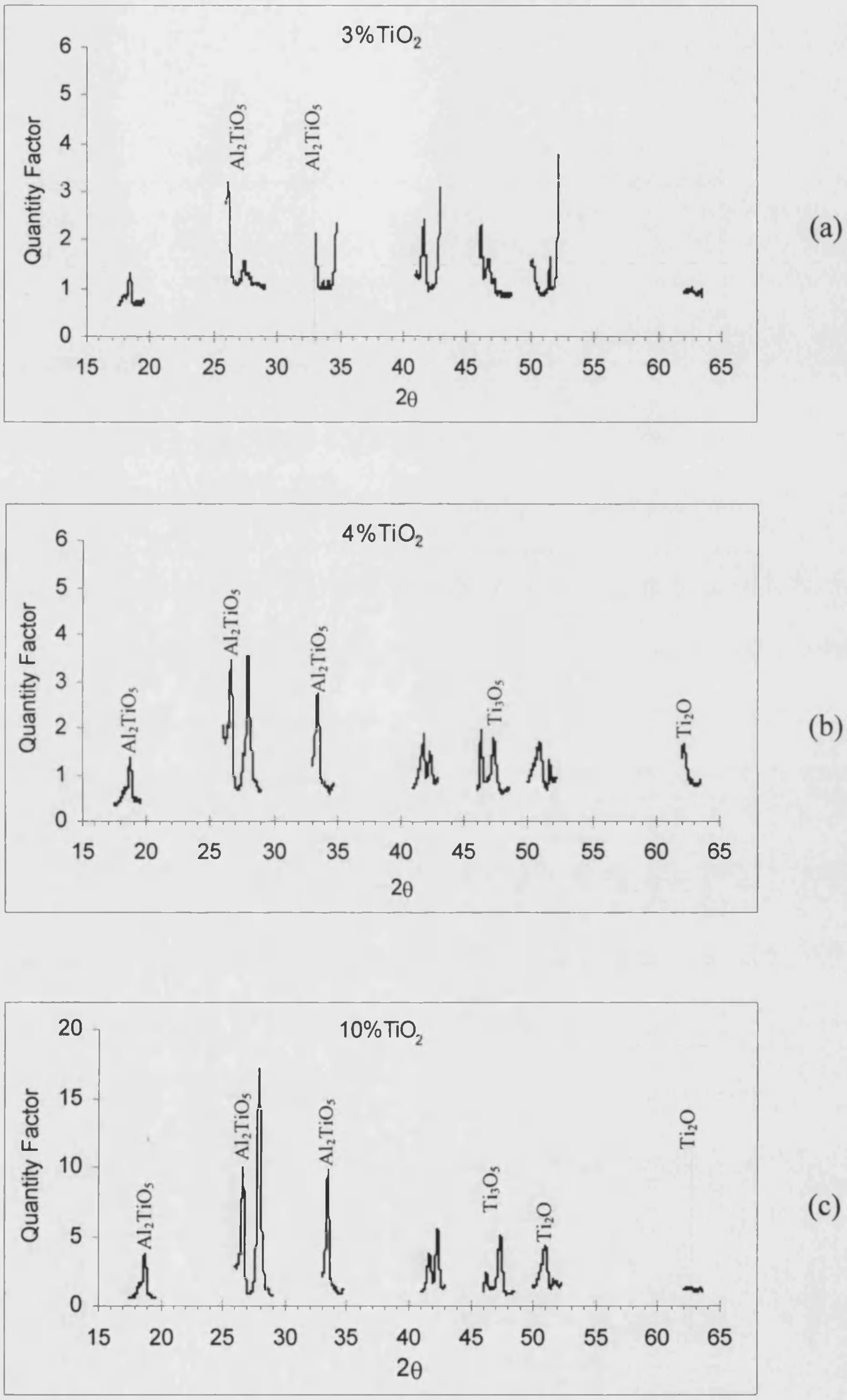

Figure 5.17: XRD patterns for H_2 annealed samples

Al_2TiO_5 peak at d = 2.65 or is more probably masked by the 90% Al_2O_3 peak (d = 2.55). However the existence of a Ti_2O_3-TiO_2 as a Ti_3O_5 peak was observed in 4% and 10%TiO_2 composition X-ray diffraction patterns. A closer look at the formation of these phases is possible in the TEM study.

5.1.2.3. TEM studies on as fired samples

The TEM sections studied were mainly the as fired T3 and T10 sample composition. In the T3 sample, few grains were pure Al_2O_3, as shown in figure 5.18. The diffraction pattern (figure 5.19) was indexed for corundum. However most of the grains contained a small amount of dissolved Ti. Al_2O_3 grains in the 10%TiO_2 composition had similar EDX traces, a typical example is shown in figure 5.20. The diffraction pattern in figure 5.21, from this grain could not be indexed directly for α-Al_2O_3. This might be due to the changes to the Al_2O_3 lattice on dissolution of TiO_2.

A very few grains in the 3% TiO_2 sample and a large number of grains in the 10%TiO_2 composition have nearly equal intensity of Al and Ti peaks. Figure 5.22(a) shows an example for one such crystal from the 3%TiO_2 sample with the EDX pattern in figure 5.22(b). This could be some form of aluminium titanate crystal. The diffraction pattern from this sample is shown in figure 5.23 (a). The d values calculated are shown in figure 5.23(b). The d values resemble those for $Al_2Ti_7O_{15}$, but, these could not be indexed. An aluminium titanate crystal in the 10%TiO_2 sample, shown in figure 5.24(a) with its associated EDX trace in figure 5.24(b) had a diffraction pattern as shown in figure 5.25(a). This was indexed to the Al_2TiO_5 -orthorhombic form with unit cell parameters as :

a = 9.439, b = 9.647 and c = 3.593

The pattern was indexed to this crystal as shown in figure 5.25(b). At a different orientation for the same sample, the diffraction pattern (figure 5.25(c)) with d values as in figure 5.25(d), could not be easily indexed.

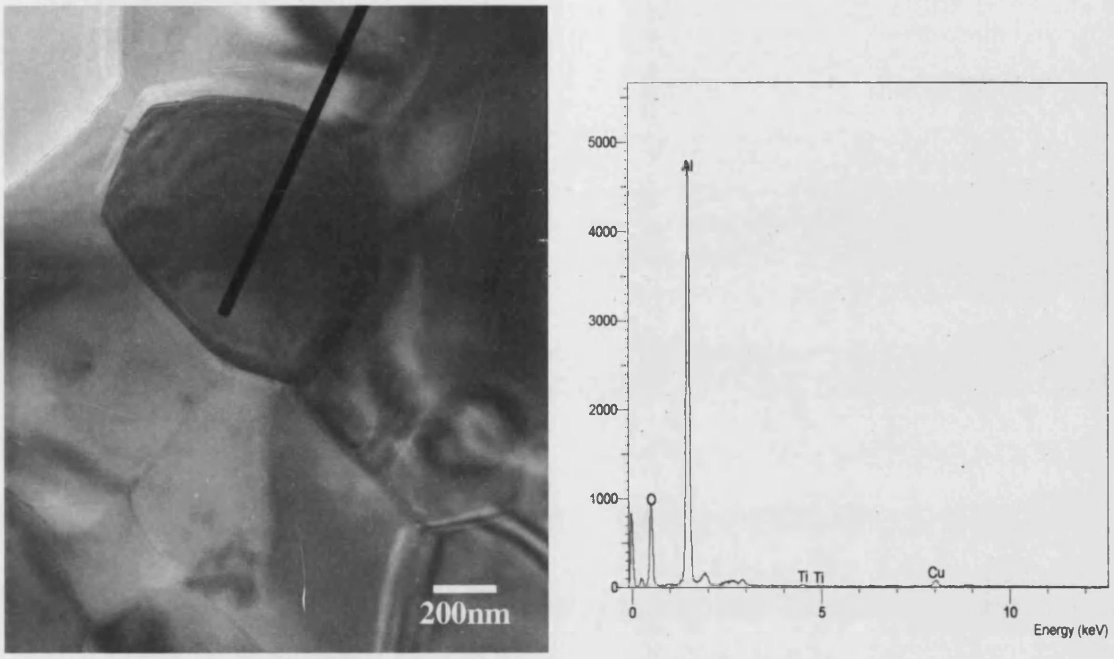

(a) (b)

Figure 5.18: (a) Marked Al_2O_3 grain giving the (b)EDX pattern

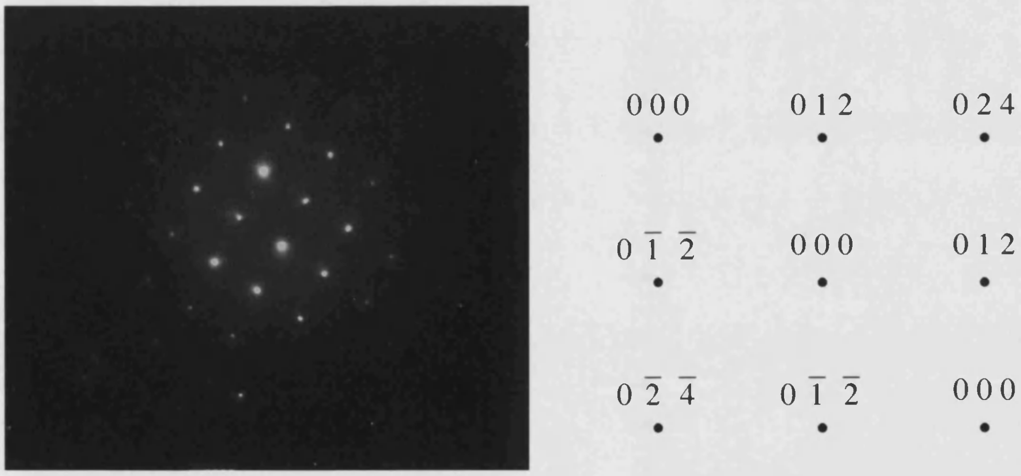

(a) (b)

Figure 5.19: (a) Diffraction pattern from Al_2O_3 grain and (b) indexing for corundum

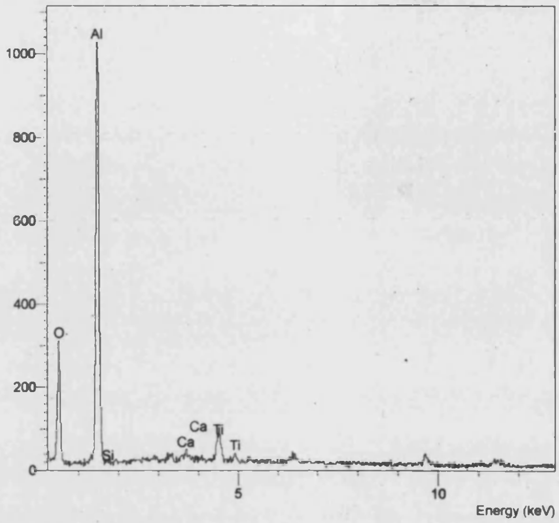

Figure 5.20: EDX at an Al_2O_3 grain in 10%TiO_2 sample

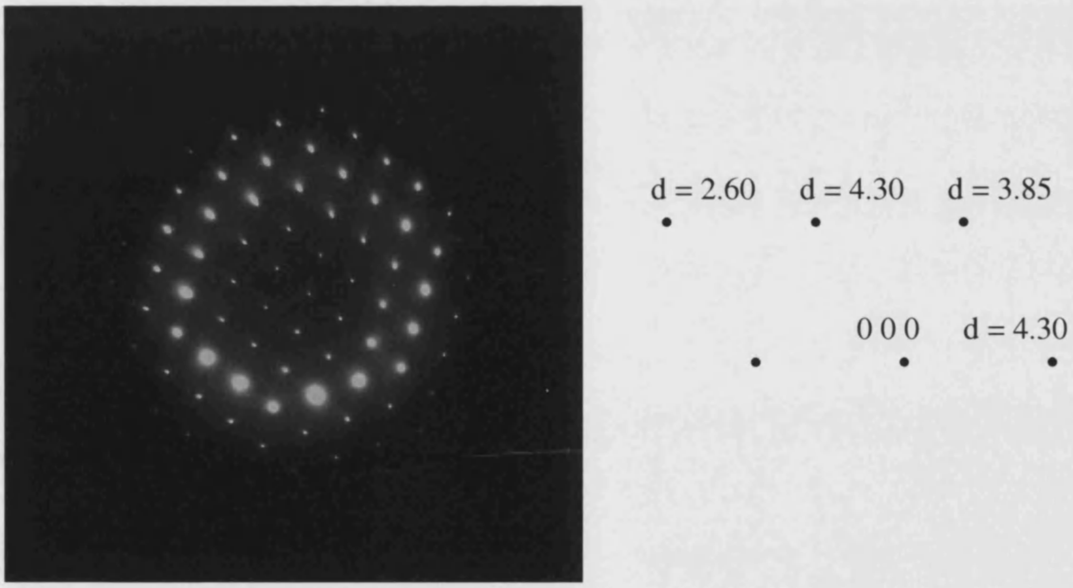

(a) (b)

Figure 5.21: (a) Diffraction pattern at an Al_2O_3 grain in 10%TiO_2 sample and (b) d values

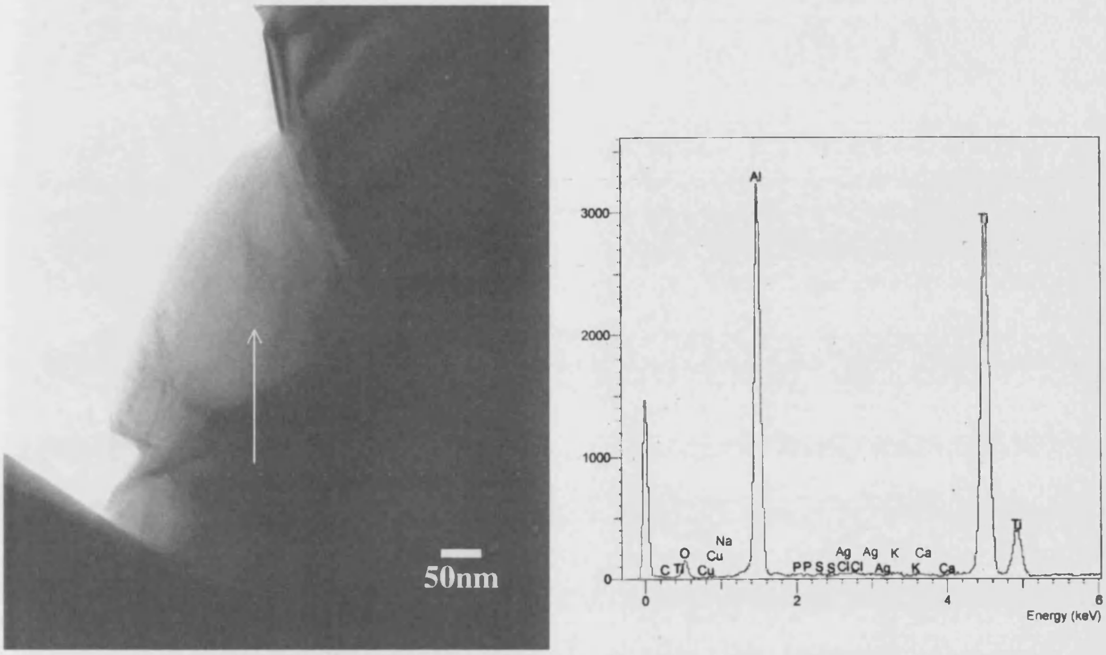

(a) (b)

Figure 5.22: (a) Marked Al-Ti grain giving the (b)EDX pattern

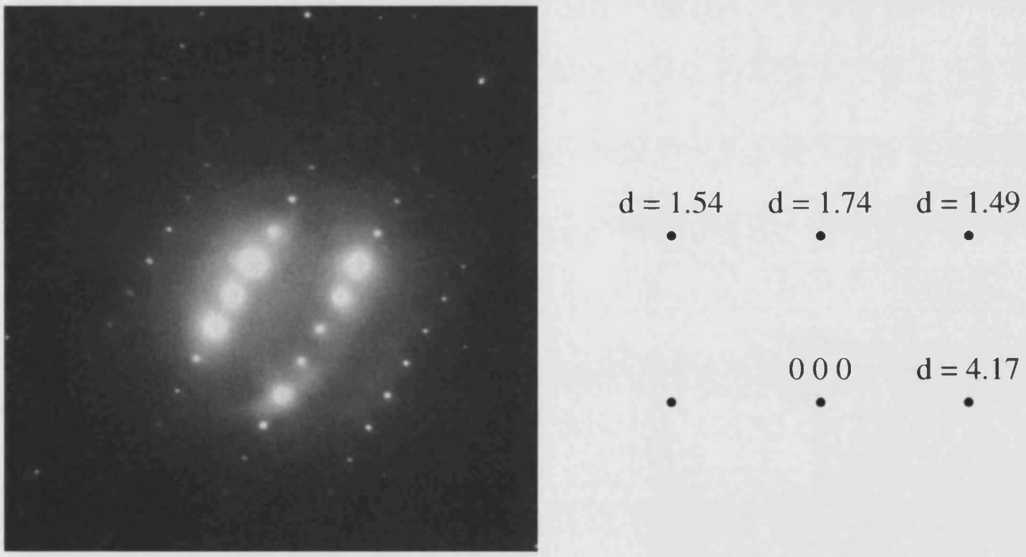

(a) (b)

Figure 5.23: (a) Diffraction pattern for an Al-Ti grain in the 3%TiO_2 sample and (b) d values

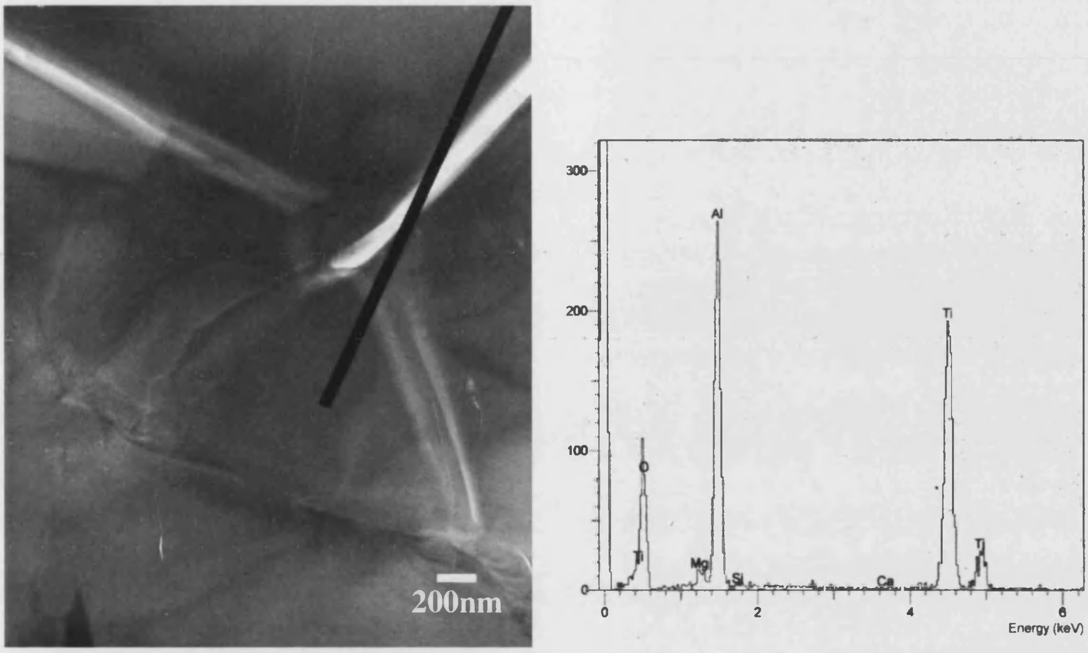

(a) (b)

Figure 5.24: (a) Marked Al-Ti grain in 10%TiO_2 sample giving the (b)EDX pattern

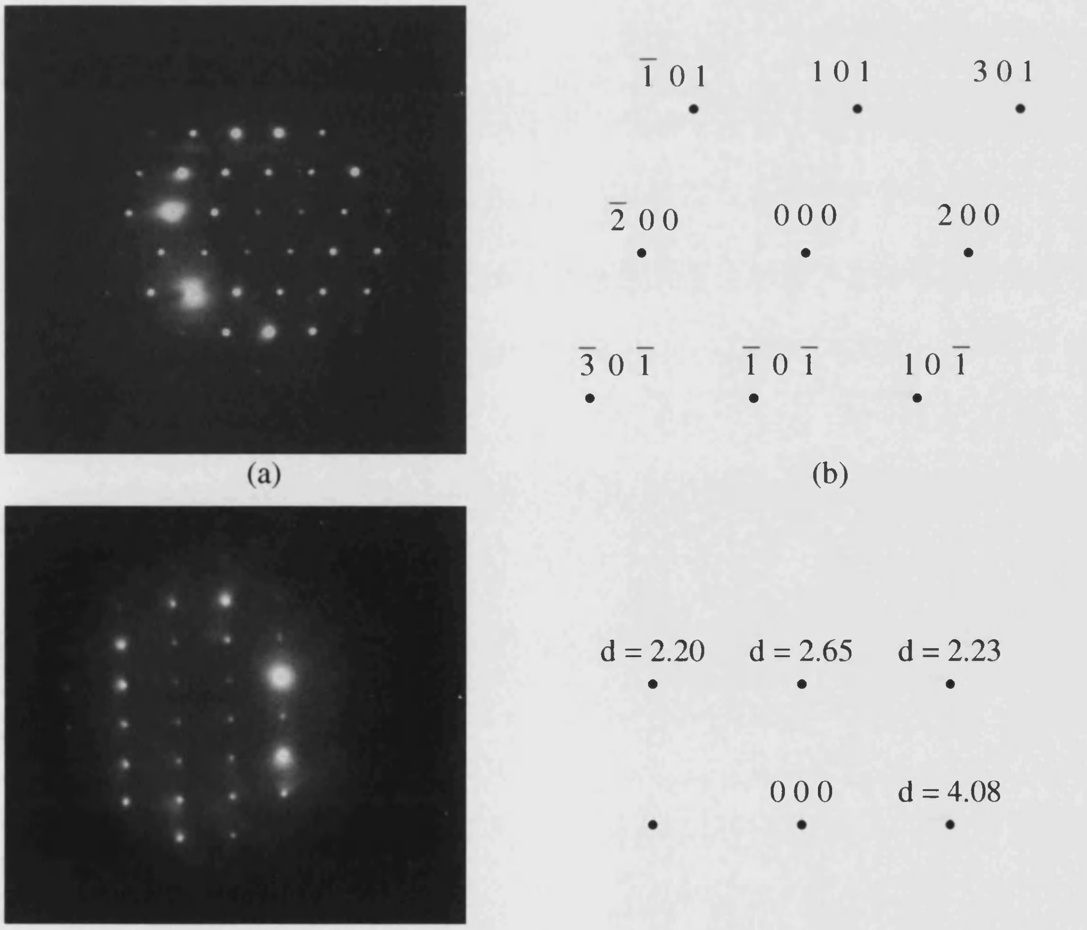

(a) (b)

(c) (d)

Figure 5.25: (a) Diffraction pattern from Al_2TiO_5 grain for 10%TiO_2, (b) indexing for Al_2TiO_5 (c) Diffraction pattern for different orientation and (d) d values

A few grains with high Ti content were seen in both the 3% and 10% TiO_2 samples. These are probably titanium oxide grains. Figure 5.26(a) shows the Ti rich grain (figure 5.26(b)) in 3%TiO_2 sample. The diffraction pattern for this sample is as shown in figure 5.27(a). The calculated d values, shown in figure 5.27(b) are close to TiO_2 - Brookite structure. However this could not be indexed and thus this structure of TiO_2 could not be confirmed.

The Ti rich crystal in the 10%TiO_2 sample is shown in figure 5.28. The d values calculated from the diffraction pattern from this crystal (figure 5.29(a)) matched Ti_3O_5 a form of Ti_2O_3!TiO_2, but could not be indexed to this. However it could be indexed to Ti_2O_3 -Rhombohedral (figure 5.29(b)) with unit cell dimensions:

$a = 4.758 = b, c = 12.991$

The formation of this reduced form of TiO_2, in as fired sample is really doubtful, even though some peaks of this material were visible in X-ray diffraction data as well. (Section 5.1.2.2). Perhaps the Ti^{3+} is formed in the high vacuum atmosphere during ion beam thinning operation. The formation of TiO_2 -Brookite structure, low temperature form of TiO_2, is also doubtful. The starting powder is TiO_2 - anatase (XRD values in appendix B) which on heating normally will be expected to convert to TiO_2 -rutile. However here under the influence of various other materials it might be stabilising into the Brookite structure of TiO_2.

5.1.2.4. Formation of Glass and other compounds from additives

The three components of the microstructure are the Al_2O_3 grains, TiO_2 rich areas, which have been discussed earlier, and the intermediate glass between the grains. The distribution of these phases in the 10%TiO_2 composition can be seen from figure 5.30. The glass forming additives are SiO_2, CaO and MgO. The objective of this section is to identify the distribution of these additives and the components of the glass. Glass in its base composition and EDX pattern are shown in figure 5.31 (a) and (b) respectively. It is known that in liquid phase sintered alumina, the calcium aluminate glass is amorphous {181}.)

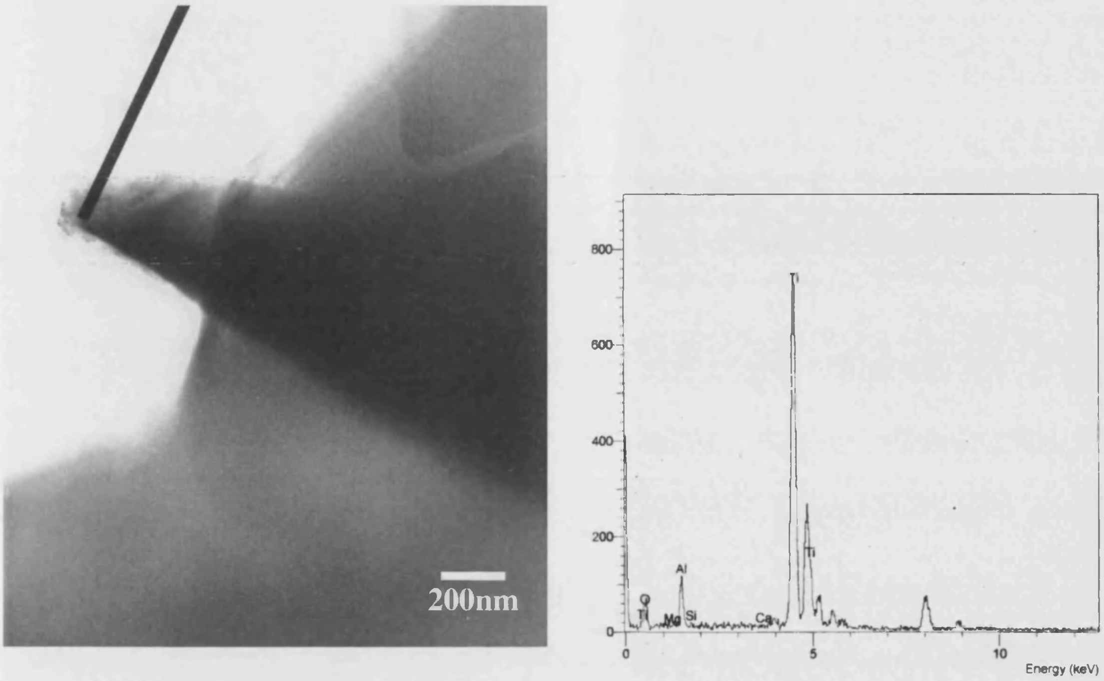

(a) (b)

Figure 5.26: (a) Marked Ti-rich grain in 3%TiO_2 sample giving the (b)EDX pattern

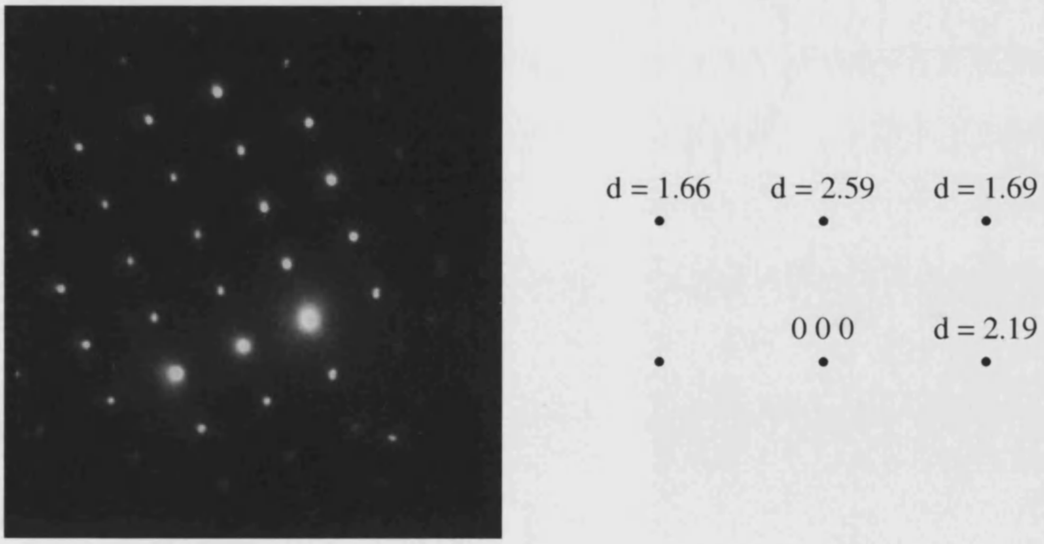

(a) (b)

Figure 5.27: (a) Diffraction pattern at Ti-rich grain in 3%TiO_2 sample and (b) d values

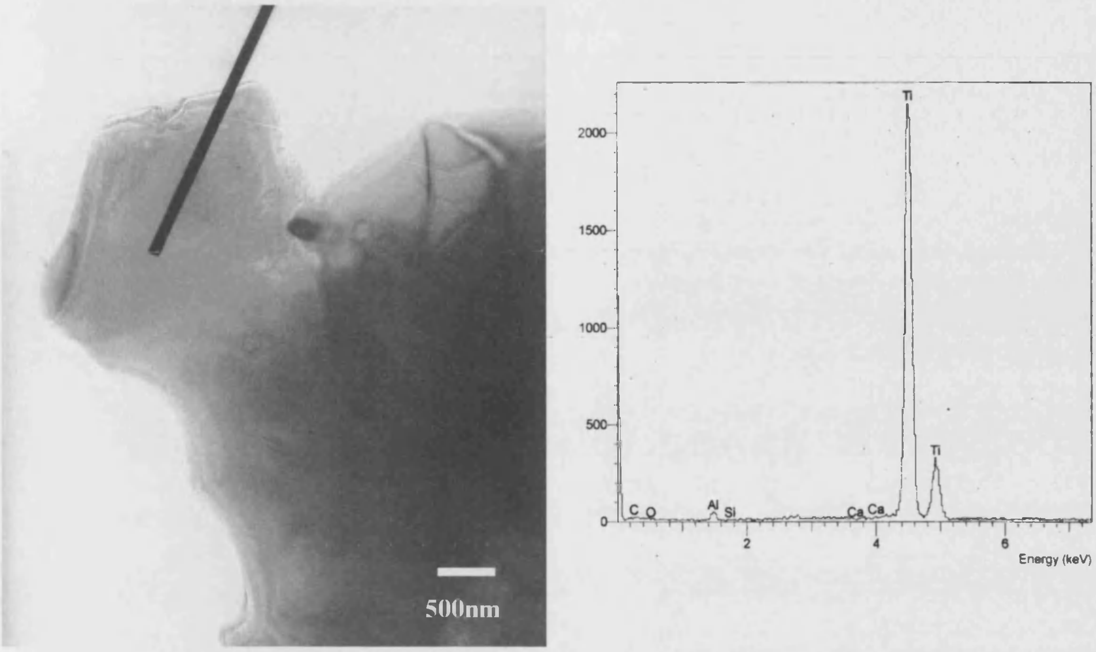

(a) (b)

Figure 5.28: (a) Marked Ti-rich grain in 10%TiO_2 sample giving the (b)EDX pattern

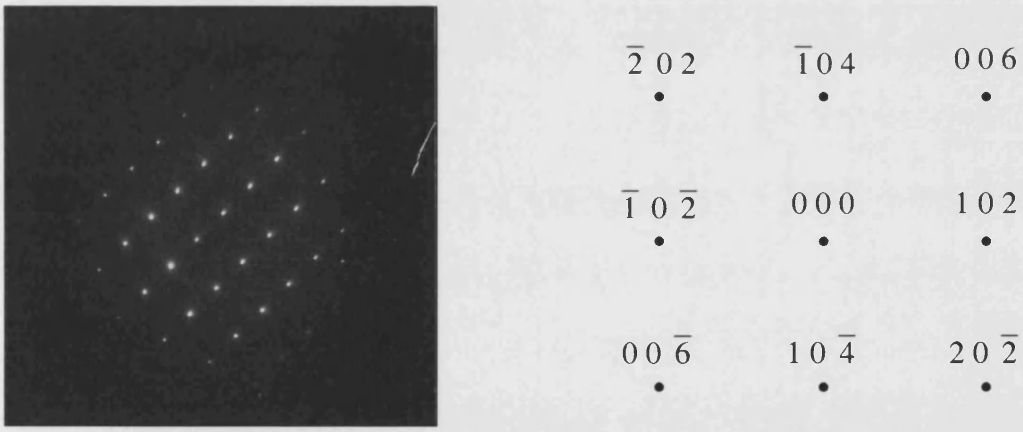

(a) (b)

Figure 5.29: (a) Diffraction pattern from Ti-rich grain in 10%TiO_2
(b) indexing for Ti_2O_3

A TEM micrograph taken from the glass in the as fired 3%TiO_2 sample is shown in figure 5.32(a). The EDX trace is shown in figure 5.32 (b) and the diffraction pattern in figure 5.33. Another TEM picture from glass shows its rough surface (figure 5.34). This might be due to the preferential ion milling. A similar EDX for glass, figure 5.35(b) in the 10%TiO_2 composition (figure 5.35(a) also shows a similar degree of dissolution of Ti in the glass. From the diffraction pattern of 3%TiO_2 its is clear that in TiO_2 doping, there is no secondary crystalline phase in the glass and it remains amorphous. Thus TiO_2 is dissolving into the glass and becoming a part of the liquid. The question as to whether the TiO_2 in the glass increases its conductivity will be discussed in the next chapter. The Al peak in glass would be due to dissolved Al_2O_3. This has been reported by Brydson et al {181}.

From the results discussed above, it is clear that the SiO_2 is present exclusively in glass. However CaO and MgO were found at other places as well, as explained below. A Ca rich area was found within the Al_2O_3 grain in the 3%TiO_2 composition (figure 5.36). Also the diffraction pattern (figure 5.38 (a)) from a similar Ca rich area (figure 5.37) shows a ring pattern. The d values calculated (figure 5.38(b)) could not be matched with any calcium aluminate compound. The EDX pattern taken from a grain boundary in the 10%TiO_2 sample (figure 5.39), indicates the presence of a compound containing mainly calcium and titanium. The diffraction pattern (figure 5.40) showed it to be amorphous. Some weak rings on the outside of this pattern are evidence of the presence of very fine precipitates.

Magnesium aluminium titanate crystals were observed in the 10%TiO_2 sample. All the crystals marked ⊗ in figure 5.41 (a) had very similar EDX pattern (figure 5.41(b)). The glass nearby marked ⊕ had negligible Mg (figure 5.41(c)). Individual crystals showed relatively high amounts of Mg along with Al and Ti. The diffraction pattern in figure 5.42 did match some of the Mg-Al-Ti compounds namely $Mg_{0.3}Al_{1.4}Ti_{1.3}O_5$ and $Mg_{0.6}Al_{0.8}Ti_{1.6}O_5$, but could not be confidently indexed. Nevertheless the first compound could be formed from a solid solution of Al_2TiO_5 and $MgTiO_5$ {182}. This crystal may be a mixture of both these compounds. The surrounding grains were aluminium titanate (marked 'x') or pure Al_2O_3 (marked '+').

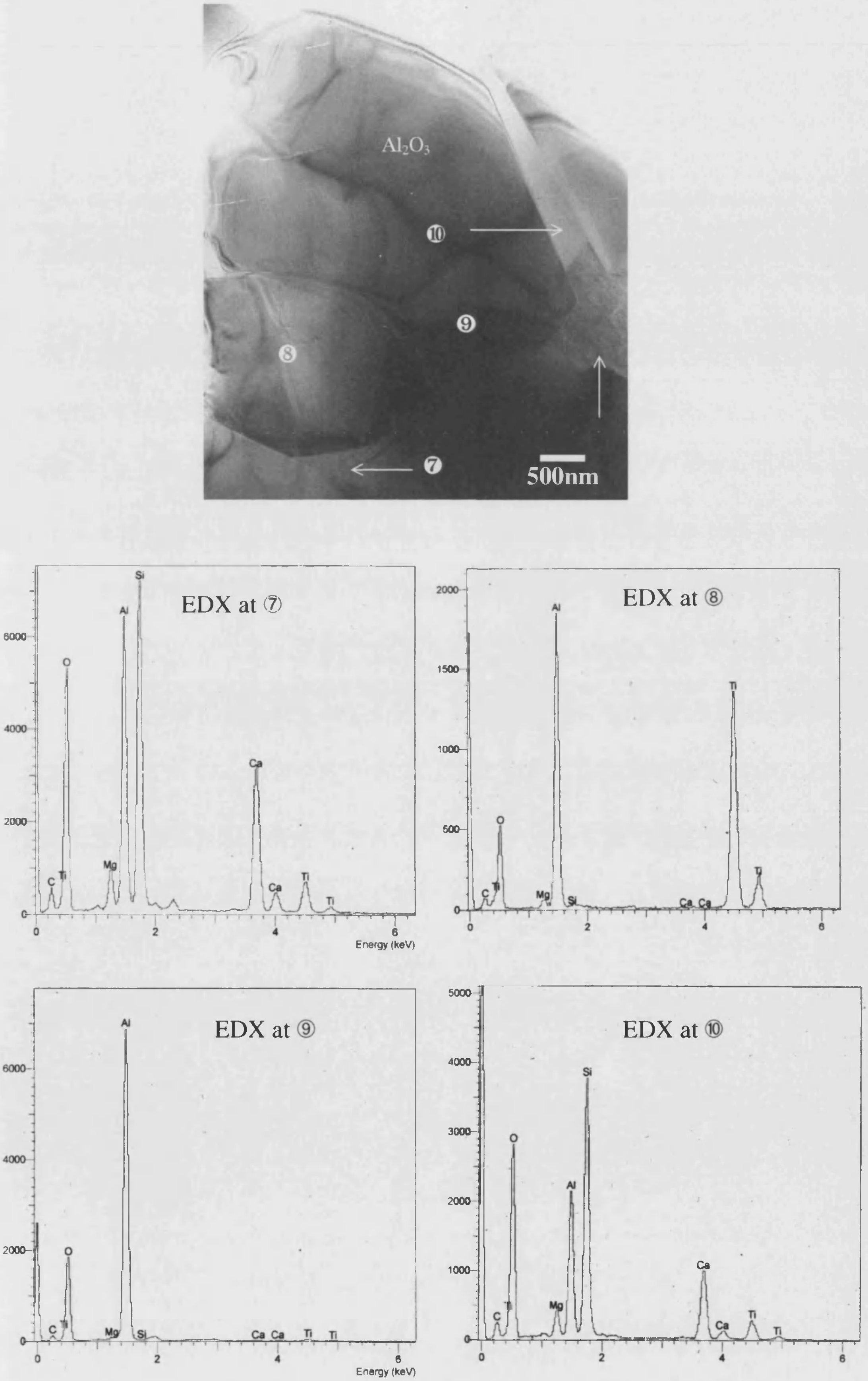

Figure 5.30: Distribution of glass and other grains in 10%TiO_2 sample

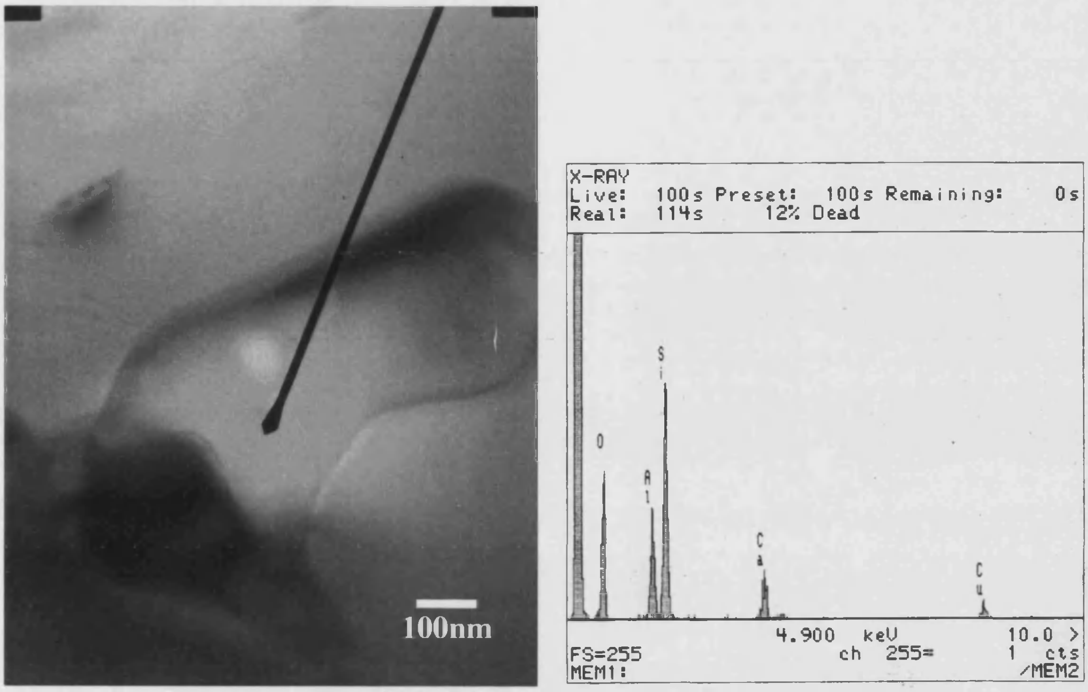

(a) (b)

Figure 5.31: (a) Marked glass in base composition sample giving the (b)EDX pattern

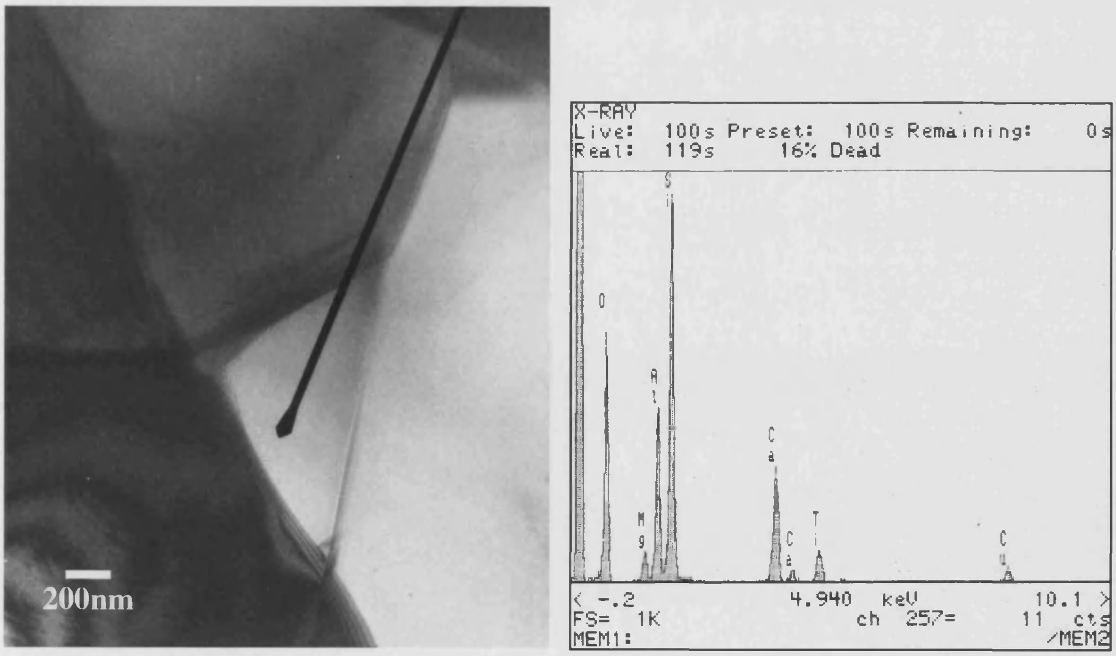

(a) (b)

Figure 5.32: (a) Marked glass in 3%TiO_2 sample giving the (b)EDX pattern

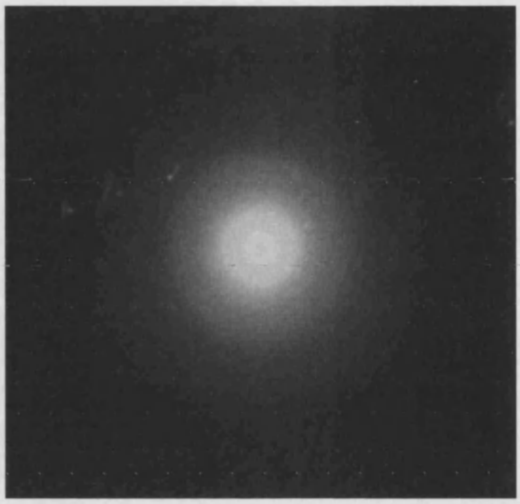

Figure 5.33: Diffraction pattern of glass in the 3%TiO_2 sample

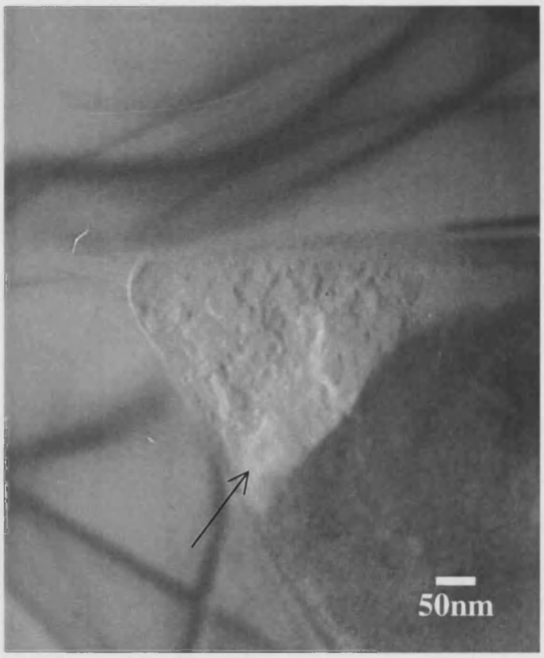

Figure 5.34: Glass in the 3%TiO_2 sample

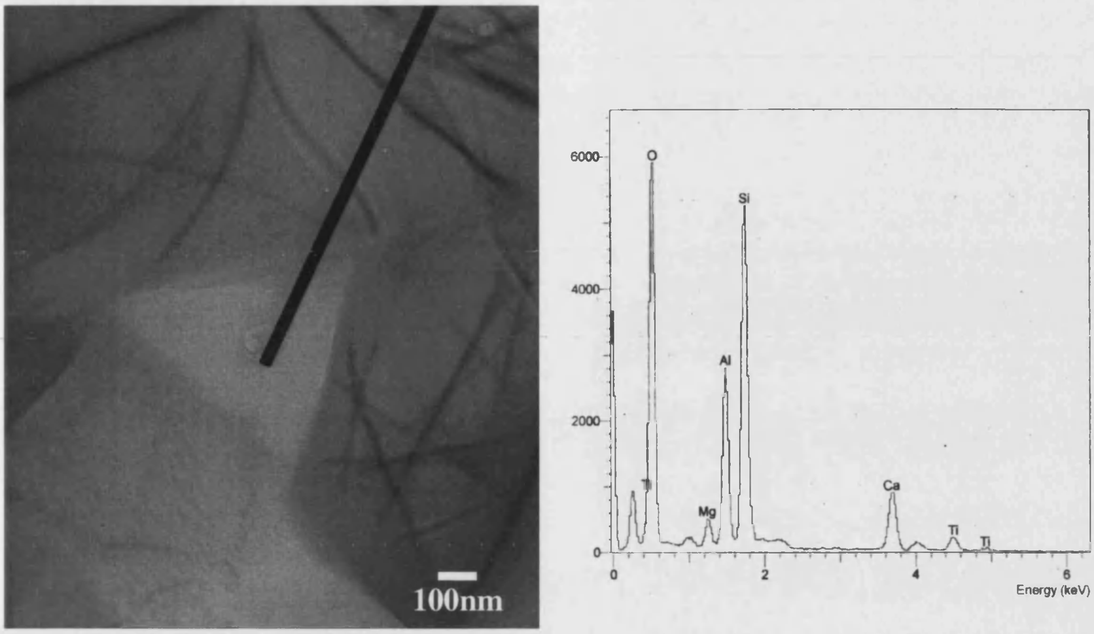

(a) (b)

Figure 5.35: (a) Marked glass in 10%TiO_2 sample giving the (b)EDX pattern

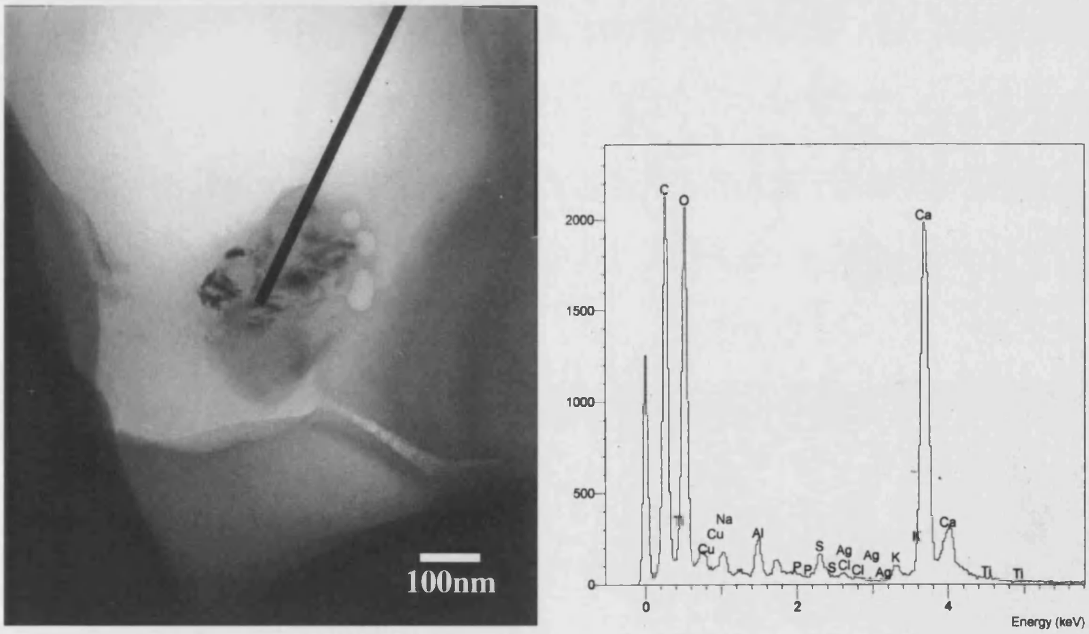

(a) (b)

Figure 5.36: (a) Marked Ca rich area in 3%TiO_2 sample giving the (b)EDX pattern

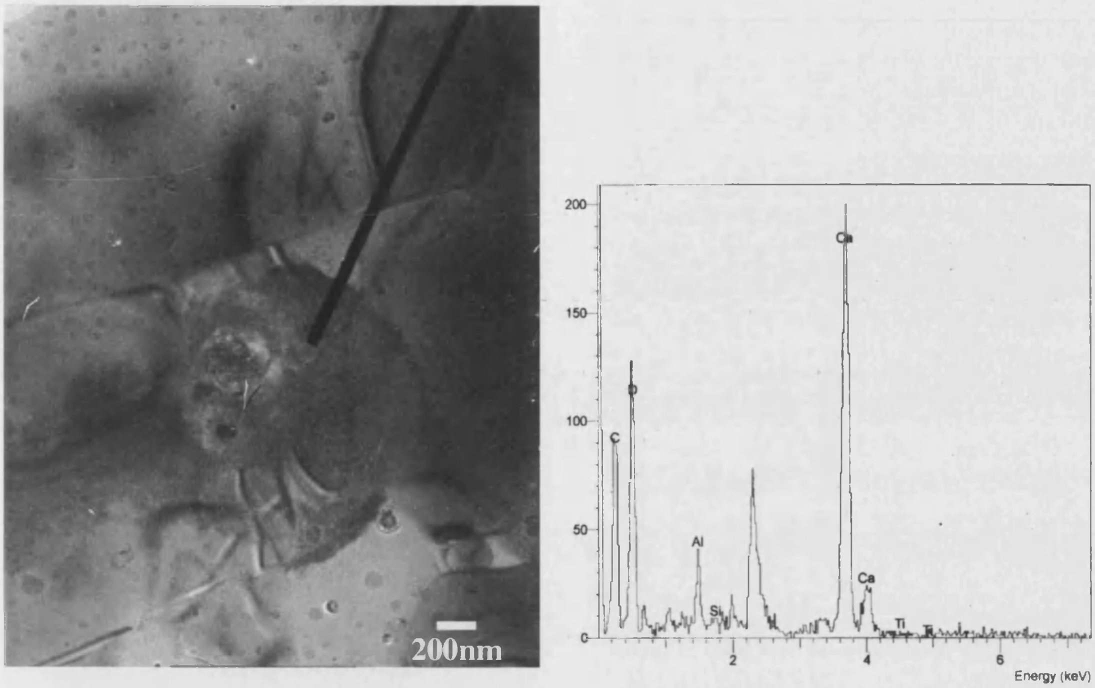

(a) (b)

Figure 5.37: (a) Marked Ca rich area in 3%TiO_2 sample giving the (b)EDX pattern

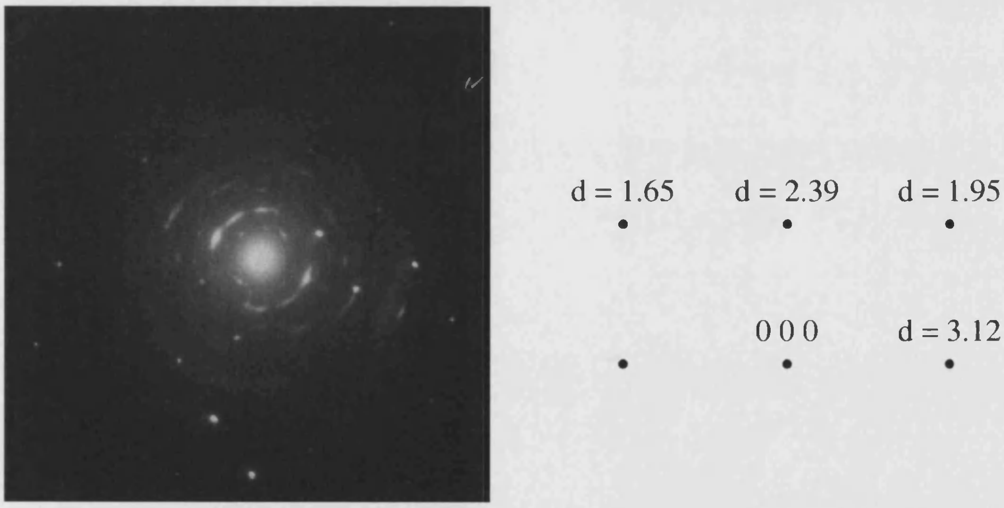

(a) (b)

Figure 5.38: (a) Diffraction pattern at Ca-rich grain in 3%TiO_2 sample and (b) calculated d values

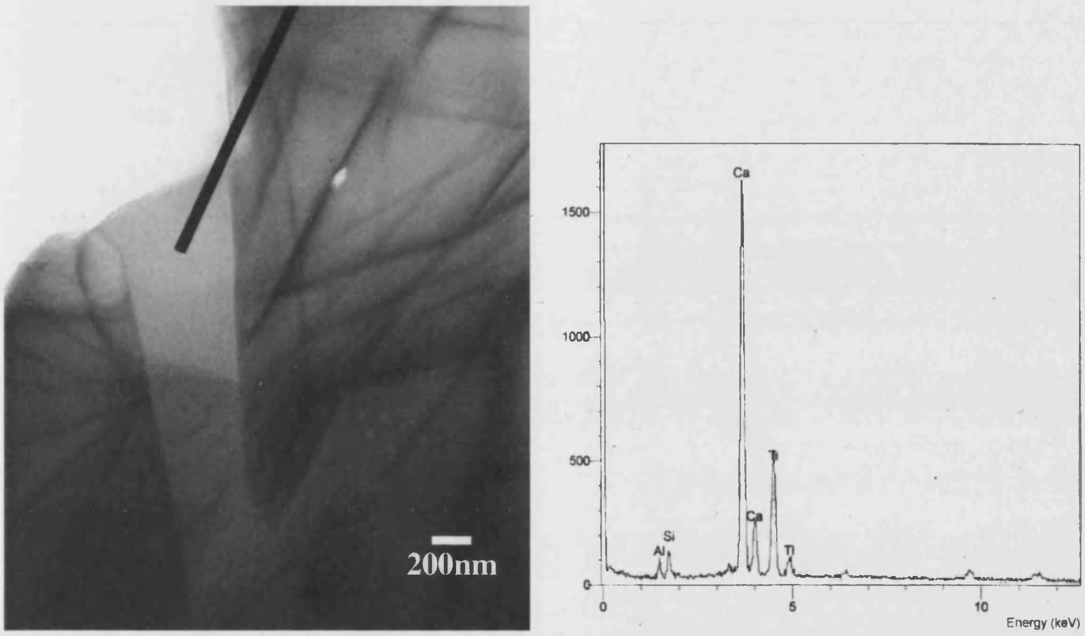

(a) (b)

Figure 5.39: (a) Marked Ca-Ti area in 10%TiO_2 sample giving the (b)EDX pattern

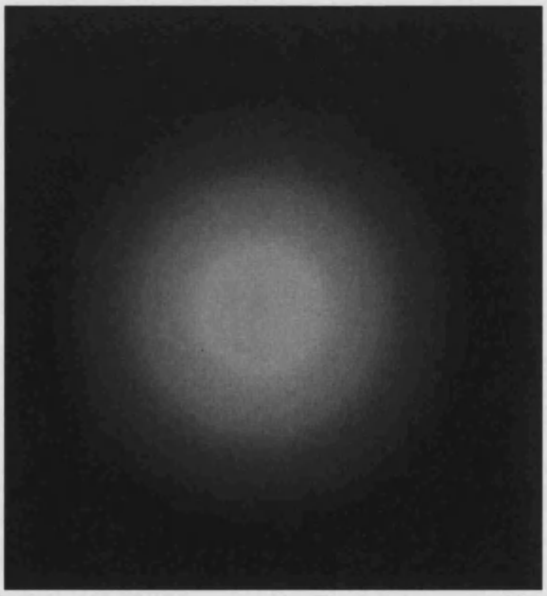

Figure 5.40: Diffraction pattern at Ca-Ti rich area in 10%TiO_2 sample

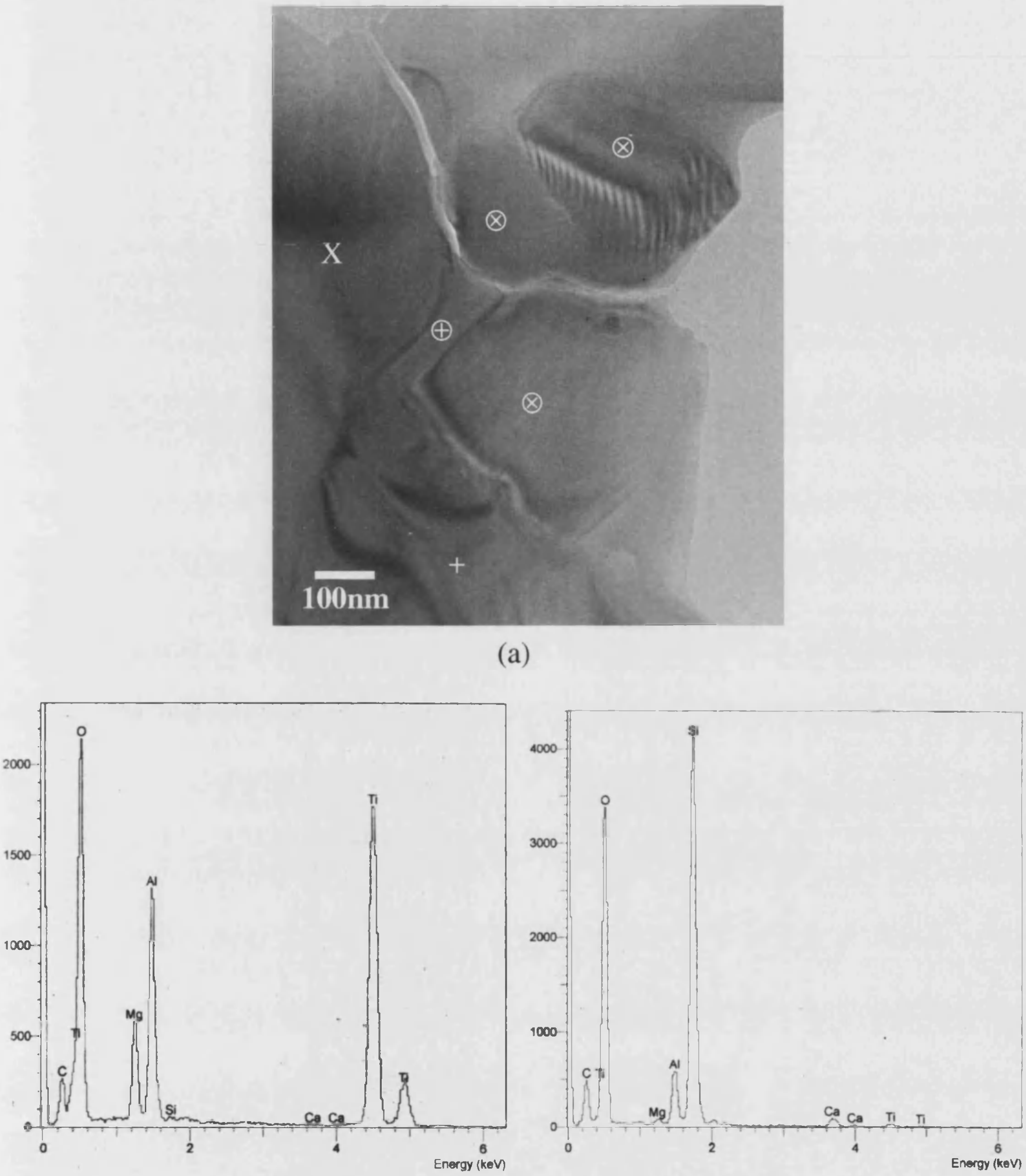

(a)

(b) (c)

Figure 5.41: (a) Mg rich area with (b) EDX pattern at ⊗ and (c) EDX pattern at ⊕

Figure 5.42: Diffraction pattern at Mg-Al-Ti crystal

5.1.3. Quantitative Analysis for Distribution of TiO_2 in Al_2O_3.

The objective of this study was to identify the percentage of Ti rich precipitates formed in the network. For this the image analysis on the 1000-X magnification back-scattered images has be carried out. The image is assumed as consisting of two phases, the bright Ti rich phase and the dark phase that includes alumina, glass and porosity. The software used was developed by Optimas Corporation 'Version 6.1'.

The analysis involved the following steps:

(a) Area identification: Area on which image analysis is carried out is shown within the dotted line box in figure 5.43 (2%TiO_2 picture) The area chosen for all other images was similar, i.e. not including the marker.

(b) Binarise: The image is converted into two-colour format by converting into 8bit grey. Thus the image is now converted into two phases, the bright phase as the Ti rich precipitates and the dark as all other phases.

(c) Filter: Some images show a very high number of white spots due to the noise in the back-scattered picture, the 4%TiO_2 picture is special example. A filter "Gaussian 5x5" was found to be the most appropriate method to isolate this noise and measure only the genuine Ti rich precipitates.

(d) Area measurement: The area of each of these phases is measured automatically and the percent of each calculated. The values for various TiO_2 compositions is shown against their picture in figure 5.43.

The percent area of Ti rich phases shows an increase from 2% to 3%TiO_2 and this then decreases in the 4% and 5% TiO_2 and increases again in the 10%TiO_2 image. The trend is similar to that of the activation energy (figures 4.19) and resistivity (figure 4.15) for these compositions.

The Ti rich area in the 3%TiO_2 + 0.5%V_2O_5 composition is:

Ti rich area = 28%

Dark Area = 82%

which is similar to that of the 3% TiO_2 as is also the trend for its resistivity, i.e. dropping sharply (figure 4.16). However the reasons for the difference between the resistivity values of the two compositions, are discussed in the next chapter.

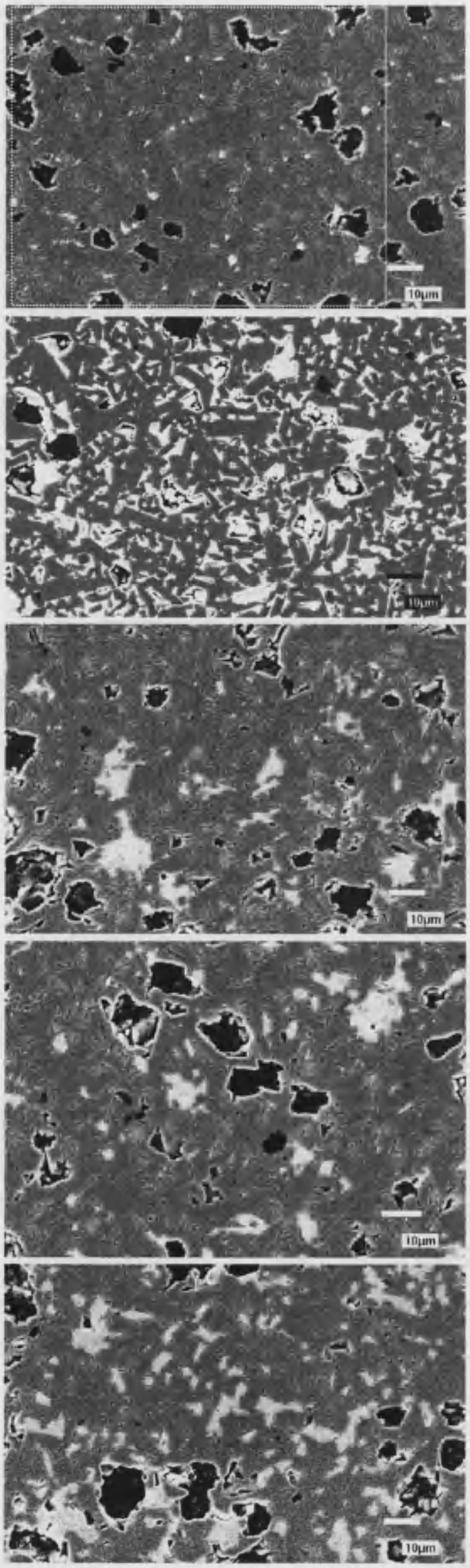

2%TiO_2

Ti Rich Area = 4%

Dark Area = 96%

3%TiO_2

Ti Rich Area = 26%

Dark Area = 74%

4%TiO_2

Ti Rich Area = 15%

Dark Area = 85%

5%TiO_2

Ti Rich Area = 13%

Dark Area = 87%

10%TiO_2

Ti Rich Area = 24%

Dark Area = 76%

Figure 5.43: Results of image analysis

At a first stage a simplistic explanation could be that the percent Ti rich area and the activation energy of the sample are related. However, a more clear reasoning may arise from describing the structure in terms of two-dimensional Voronoi networks.

The microstructure in figure 5.43 has been modelled using the Voronoi network model as was done by Bartkowiak et al {183} for ZnO varistors. The Ti rich bright spots in 1%TiO_2 are assumed to be the randomly distributed Ti sites, which grow with the addition of TiO_2 to the network. The steep fall in resistivity can be related to these Ti sites reaching a level and becoming connected in the 3%TiO_2 sample i.e. reaching a near percolation threshold. The percolation threshold in 2D as discussed by Jerauld et al {184} was 33%. In a 3D network the average number of neighbours in the lattice increases and the bond percolation threshold varies from 10% to 17% depending on the structure of the network {185}. Though the values for 2D do not agree with the percentages calculated from image analysis in figure 5.43, previous works have shown that the factors that govern this value are many and were calculated for a specific network under the appropriate assumptions.

From an examination of the microstructures, the transition in the growth of Ti sites from 1% to 3%TiO_2 can be considered to reach a state of percolation threshold. In 4% TiO_2 though, the growth of Ti rich area is still fairly high but the number of Ti sites has reduced resulting in a pre-percolation threshold. Again at 10%TiO_2 the number of these sites has increased to reach a percolation threshold. Thus for Ti in Al_2O_3 the percolation threshold can be considered to be ~25% in a 2D network.

5.2.Grain Size

The grain size of the base composition, as discussed earlier, is one of exaggerated grain growth (figure 5.44). With the addition of 1%TiO_2 the grain size nearly doubles (figure 5.45) and increases further at 3%TiO_2 with greater numbers of abnormally large grains (figure 5.46). Exaggerated grain growth may be the reason for the lowering of the density (figure 3.7(a)) and flexural strength (figure 3.8) with increase in TiO_2 content. The grain size in 4% (figure 5.47) and 10% TiO_2 (figure 5.48) is similar to the 1% composition. This could be due to the reduced distribution of TiO_2 in the compositions above the 3%TiO_2 compositions (section 5.1.3). The TiO_2 agglomeration is visible in figure 5.49 in a 4%TiO_2 sample.

The composition M1 containing no MgO and CaO in the glass, shows a structure of fairly uniform and small grain size, ~ 2-3μm (figure 5.50). This seems contrary to the accepted wisdom that MgO addition to alumina is responsible for a controlled grain growth and small grain size, while TiO_2 causes exaggerated growth. However the reason for the small grain size here is the lack of formation of glass at the sintering temperature due to the absence of glass forming aids such as CaO and MgO. This is obvious from the lower density, high porosity (figure 3.7 (c)) and lowered flexural strength (figure 3.8). The steep fall in resistivity of this composition in the as-fired condition could be related to the small grain size. The alumina grain being a very high resistivity material, most of the conduction would be expected to take place through the grain boundaries, that are now larger in number.

It has been concluded by many authors that CaO is responsible for exaggerated grain growth in alumina {147-150}. The small grain size in the M1 composition could be the cause of the absence of CaO. This is apparent through the example of 3%TiO_2 +0.5%V_2O_5 sample (figure 5.51(a)), where a larger grain had some Ca dissolved in it (figure 5.51(b)) while the smaller grain had none (figure 5.51(c)). Thus removal of CaO might help in reducing the grain size and consequently the resistivity. However this would have an effect on the physical properties particularly the density (figure 3.7 (c)). Thus this method of reducing the resistivity is not recommended.

The grains in the base composition showed hexagonal arrays of dislocations defects in form of sub-boundaries (figure 5.52). The dislocations in the grain were also seen in the 3%TiO_2 composition (figure 5.53). Dislocations can affect electrical properties as they can be potential barriers for current carriers, or can be charge traps. Nevertheless they may not influence the conductivity if the major conductivity path is the grain boundary rather than the grain interior. The predominant type of conductivity in alumina will become clear from the discussion in next chapter.

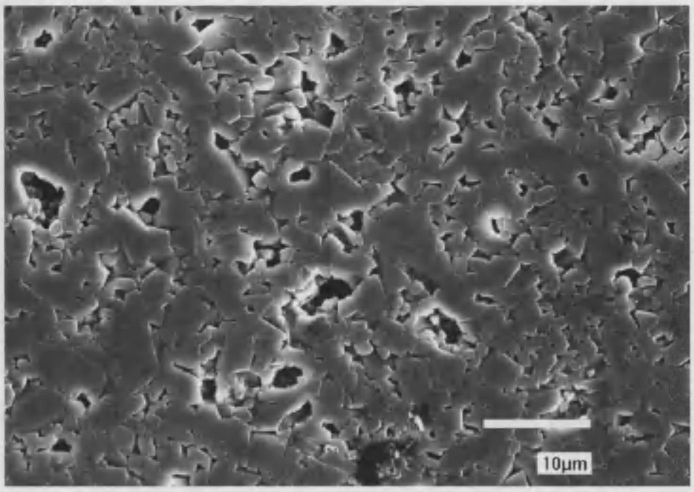

Figure 5.44: Grain size distribution in base composition sample

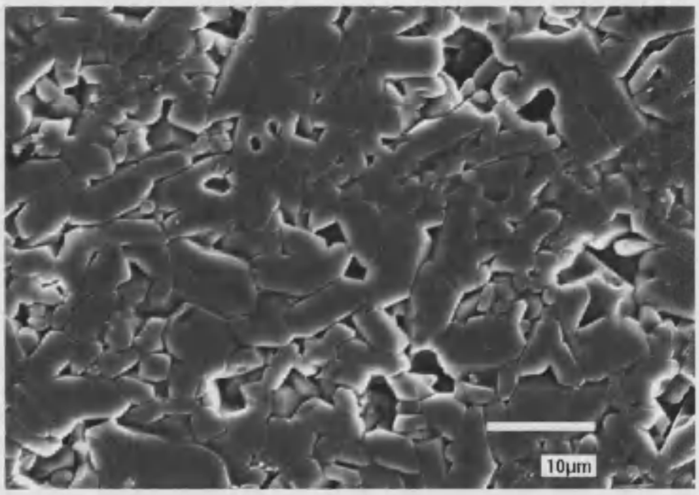

Figure 5.45: Grain size distribution in 1%TiO_2 sample

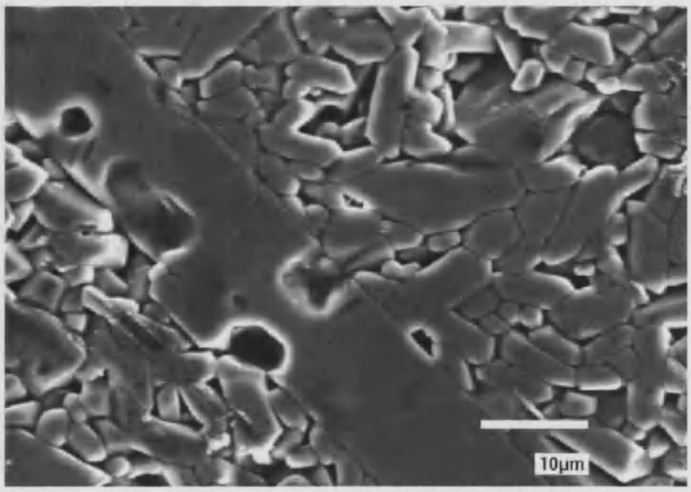

Figure 5.46: Grain size distribution in 3%TiO_2 sample

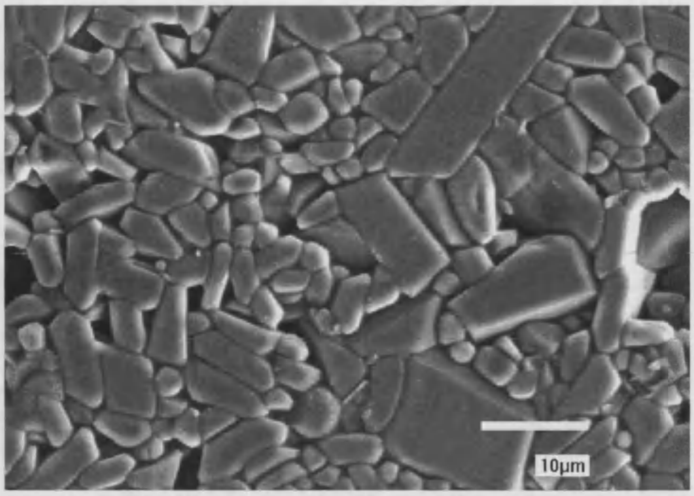

Figure 5.47: Grain size distribution in 4%TiO_2 sample

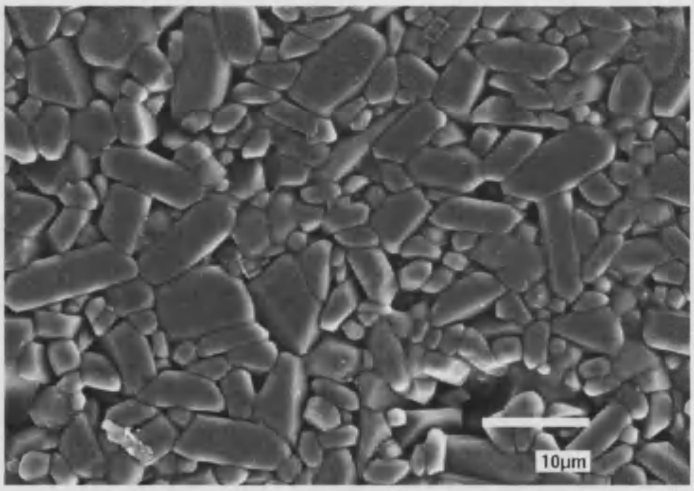

Figure 5.48: Grain size distribution in 10%TiO_2 sample

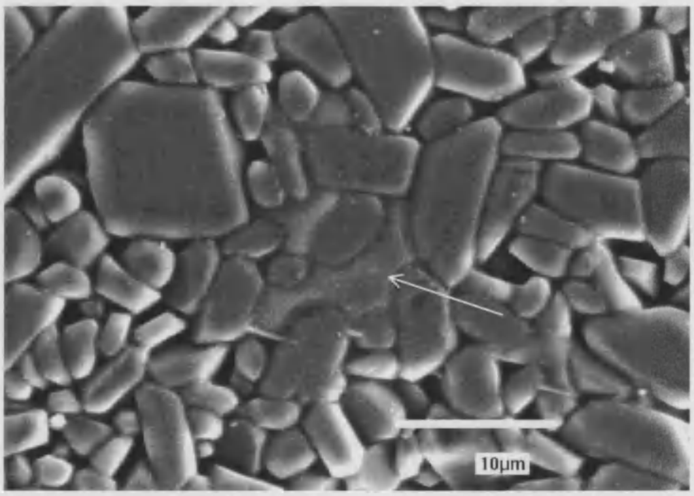

Figure 5.49: 4%TiO_2 grain structure showing Ti agglomeration

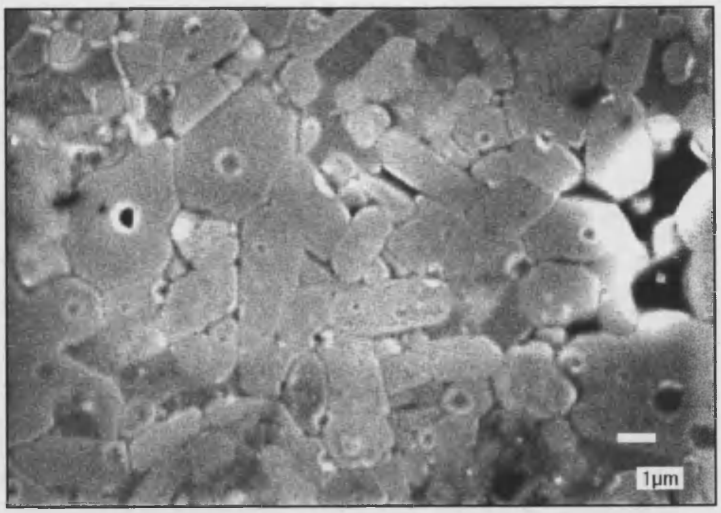

Figure 5.50: Grain size distribution in M1 sample

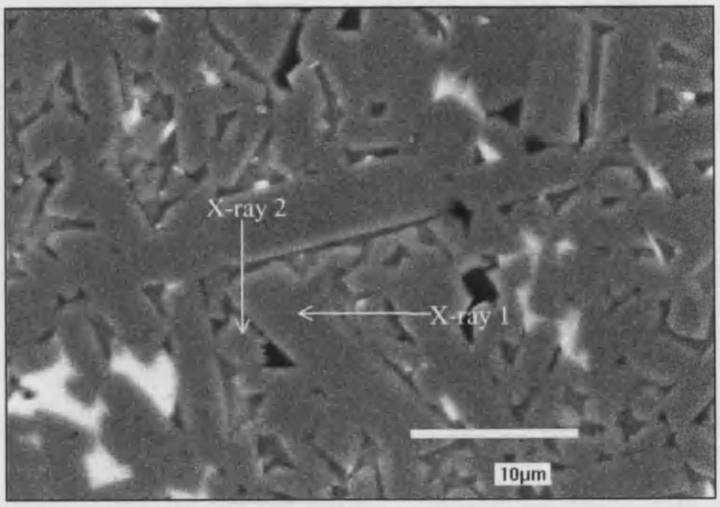

(a)

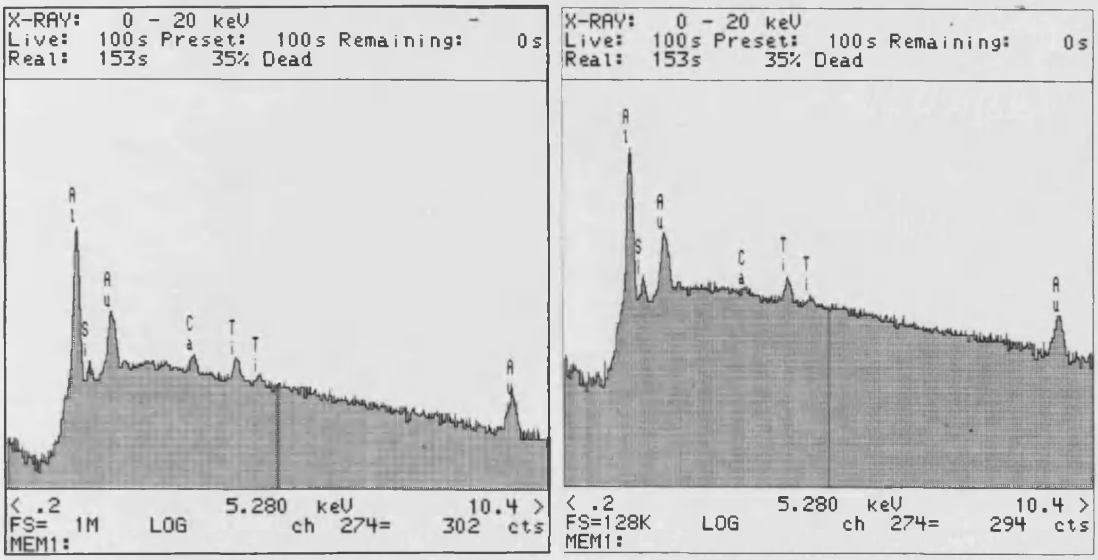

```
X-RAY:   0 - 20 keV
Live:   100s Preset:   100s Remaining:     0s
Real:   153s      35% Dead

< .2              5.280   keV           10.4 >
FS=  1M     LOG         ch  274=       302  cts
MEM1:
```

```
X-RAY:   0 - 20 keV
Live:   100s Preset:   100s Remaining:     0s
Real:   153s      35% Dead

< .2              5.280   keV           10.4 >
FS=128K     LOG         ch  274=       294  cts
MEM1:
```

(b) (c)

Figure 5.51: (a)3%TiO_2 +0.5%V_2O_5 sample with
(b) X-ray-1 at large grain and (c) X-ray-2 at small grain

Figure 5.52: Dislocations in the grains in Base composition

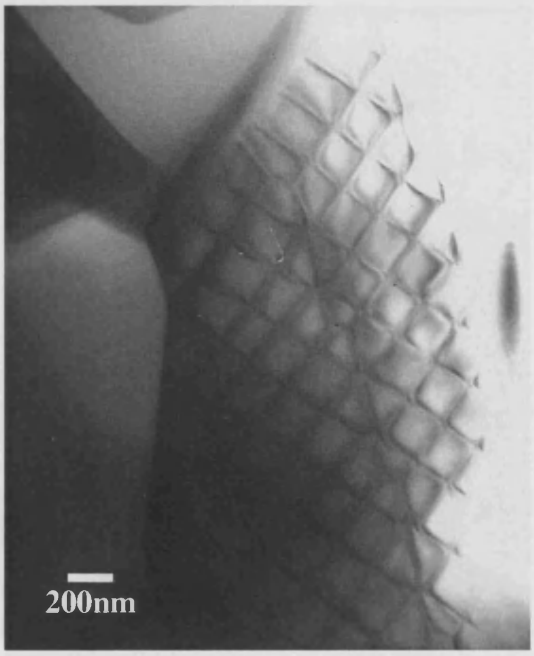

Figure 5.53: Dislocations in the grains in 3%TiO_2 sample

CHAPTER VI

DISCUSSION

This chapter covers

- ✓ *the interpretation of electrical resistivity results in the light of microstructure*
- ✓ *discusses the probable charge carriers in T3, TV5 and T10 samples*

6. DISCUSSION

The summary of the results of electrical characterisation is as follows.
The compositions used were made up of the base composition, which is 94% Al_2O_3 containing no TiO_2, and compositions with 0.1% to 10%TiO_2 added. Two sets of samples for each composition were tested, these were as-fired and annealing the fired samples in H_2. In the as-fired sample, addition of TiO_2, even as low as 0.1%, resulted in a drop of up to 2 orders of magnitude in resistivity and stayed unchanged with further increase in TiO_2 addition. The resistivity dropped further, up to 2 orders with the addition of V_2O_5 to the TiO_2 doped composition. Annealing in H_2 resulted in no major change in resistivity for the samples up to 2%TiO_2. However, on increasing the TiO_2 doping to 3% (sample T3) the resistivity decreased by nearly 9 orders of magnitude. A similar steep drop of ~10^7 was also visible in 3%TiO_2 +0.5%V_2O_5 composition (sample TV5). The resistivity increased again by 10^6 at 4% TiO_2 (sample T4 and T5)) and decreased again at a TiO_2 concentration of 10% (sample T10).

It is apparent that the trend of change in resistivity, especially the steep decrease for sample T3, TV5 and T10) is affected by the distribution of TiO_2 and V_2O_5 in the Al_2O_3 network. This has been studied in the following section. Furthermore the wide difference in the results of as-fired and H_2 annealed samples is due to the different charge carriers operative in the two samples. The nature of the possible charge carriers have also been discussed.

6.1. Decrease in resistivity with the addition of TiO_2

On addition of a small amount of TiO_2 to the base composition, it was found to dissolve into the Al_2O_3 grain, dissolve in the glass and also precipitate in the form of isolated pockets in the Al_2O_3 matrix. In the base composition, it can be safely assumed that the conduction is through the glass phase and not through the high resistivity Al_2O_3 grain. With the addition of TiO_2 to the glass, the conduction increases marginally and remains unchanged with a further increase in TiO_2 concentration (figure 4.11). This is in line with the discussion in section 5.1.2.4 where the dissolution of TiO_2 in the glass remains constant with increase in TiO_2 addition to the base composition.

A similar reasoning is possible if Al_2O_3 is the conducting medium. Though Al_2O_3 in the base composition would have carried no current, in a doped composition, the modified lattice, due to Ti incorporation, can become another charge carrying medium. It might be possible that the conductive medium has changed from the glass to alumina grains in the doped compositions. This is more likely because the glass is isolated to some extent, unlike the Al_2O_3 grains which are all interconnected. This could be the reason for the sudden fall in resistivity at 0.25%TiO_2 shown in figure 4.11. Nevertheless, since the dissolution in Al_2O_3 reaches a saturation limit even at this low concentration of TiO_2, any additional TiO_2 forms precipitates at the grain boundary and this does not contribute to the conductivity of the alumina. As a result the resistivity remains unchanged. At 3% TiO_2 the Ti precipitates have become numerous and are now blocking the conduction through Al_2O_3 resulting in a marginal increase in resistivity.

However, this trend takes place only in the as-fired compositions. The H_2 annealed samples have shown an interesting trend in the change in their resistivity. Especially of interest are the 3%TiO_2, 3%TiO_2 + 0.5%V_2O_5 and 10%TiO_2 compositions, which have shown very low resistivity compared to other compositions. The first assumption made here is that the Ti rich precipitate has now become conductive. This transition of the Ti rich precipitate from being insulating to conducting will be discussed later in this chapter. In the meantime the fall in resistivity in the 3%TiO_2 composition is considered to be related to the Voronoi network discussed in the last chapter.

6.1.1. *The Percolation Effect*

A steep increase in the Ti rich white area in the 3% TiO_2 has been discussed as demonstrating a *percolation effect*† (section 5.1.3). The steep fall in resistivity (figure 4.15) is considered a result of this percolation. The trend can be explained based on Stauffer's {187} theory that the current now flows only through the

---

† *Percolation theory deals with clusters of neighbouring sites such that each site of a very large lattice is occupied randomly with probability p, independent of its neighbours. A concentration p when an infinite network gets formed in an infinite lattice, such that the cluster extends from one side of the system to other, is defined as a percolation threshold. Below this threshold the connectivity in the lattice does not exist.{186}*

conducting Ti rich phases rather than through the insulating alumina or glass. Thus the conductivity network in the 3%TiO_2 has changed to the Ti rich regions, from the alumina/glass regions in ≤2%TiO_2 compositions. This can explain the fall in activation energy from ~0.9eV to 0.3eV, i.e. the former is the activation energy of alumina/glass network while the latter is that of the Ti network. Similar activation energy values (figure 4.19) and microstructure of the 3%TiO_2+0.5%V_2O_5 system, indicates that the conducting species is similar to the 3%TiO_2 composition.

Furthermore, in a percolating network, one would expect that the conductivity of the system would be proportional to the volume fraction of conducting Ti rich phases. However earlier experiments on metal conductors have shown that this is not the case {188}. This is because the *"dead end" clusters*[Ж] formed due to the additional volume fraction, contribute to the additional mass of the percolating network, but not to the electrical current carrying capacity of the system. Thus we can expect that any additional TiO_2 added to this system should result in the conductivity being no more than the threshold value seen for 3%TiO_2. However the results for 4%TiO_2 (figure 4.15) unexpectedly show that the resistivity has increased steeply to the level it was at in the 2%TiO_2 composition.

6.1.2. Increased Resistivity at High TiO_2 Percentage

Looking at the microstructure of the 4%TiO_2 sample in figure 5.43, we can see that the percolating network has broken down and the Ti rich phases have agglomerated. Similar agglomeration is also visible in the 5% and 10%TiO_2 compositions, although in the 10% composition the Ti rich agglomerates have become more numerous and formed a near percolation path again resulting in a steep drop in resistivity, though to a lesser extent than for the 3%TiO_2. It can be interpreted that in compositions containing >4%TiO_2, the agglomeration of the Ti is the reason for its lack of dispersion in the alumina network, and the conducting phase reverting to the Al_2O_3/glass. This is suggested as the reason for the increased activation energy, resulting in an increase in the resistivity.

[Ж] *Dead end clusters are the conducting areas not attached to the percolation/conducting path.*

The possible explanation for this agglomeration could be inadequate mixing leading to improper distribution of TiO_2. To overcome this the material was again prepared and the mixing time doubled and subsequently tripled. An adequate quantity of dispersant (Dispex) was also used. The processing and firing conditions were kept exactly the same. The resulting microstructure for the double (figure 6.1(b)) and triple (figure 6.1(c)) mixing time showed no improvement with the agglomeration of Ti phases when compared with the original 4%TiO_2 sample (figure 6.1(a)). Additionally the electrical resistivity values for as-fired and H_2 annealed samples were similar for all the three cases. This led to the conclusion that there was a deeper explanation for this difference.

6.1.2.1. Reasons for agglomeration of TiO_2 rich phases

6.1.2.1.1. Role of MgO

The composition of Ti rich phases was studied using EPMA. Typical chemical composition data, as-received from the EPMA for the 3%TiO_2 mixture are:-

Element	Peak	Net (cps)	Atom %
Mg	107.450	1543.3	1.6263
Al	90.585	43678.6	29.6891
O	109.510	6467.8	23.765
Ti	191.080	1159.5	10.6039
Si	77.375	181.1	0.1254
Ca	107.420	61.9	0.0436

A ratio of Mg/Ti and Al/Ti for each result was calculated and the average for each composition plotted as in figure 6.2. It is clear that the T3 sample with 3%TiO_2 has a higher percentage of Mg at bright sites as compared to those with 4%, 5% and 10%. With increase in Ti, it is expected that the Mg/Ti ratio will decrease slightly, but the drop in the ratio from 3% to 4% TiO_2 in T3 to T4 sample is steep. Furthermore the ratio is similar with an increase in TiO_2 from 4% to 10%. This is sufficient reason to suggest the formation of a different phase in the >4% compositions as compared with the 3%TiO_2 composition. However no Mg-Ti compounds were seen in the XRD results in figure 5.16. This may not be sufficient explanation for the absence of Mg-Ti compounds, as most of the peaks

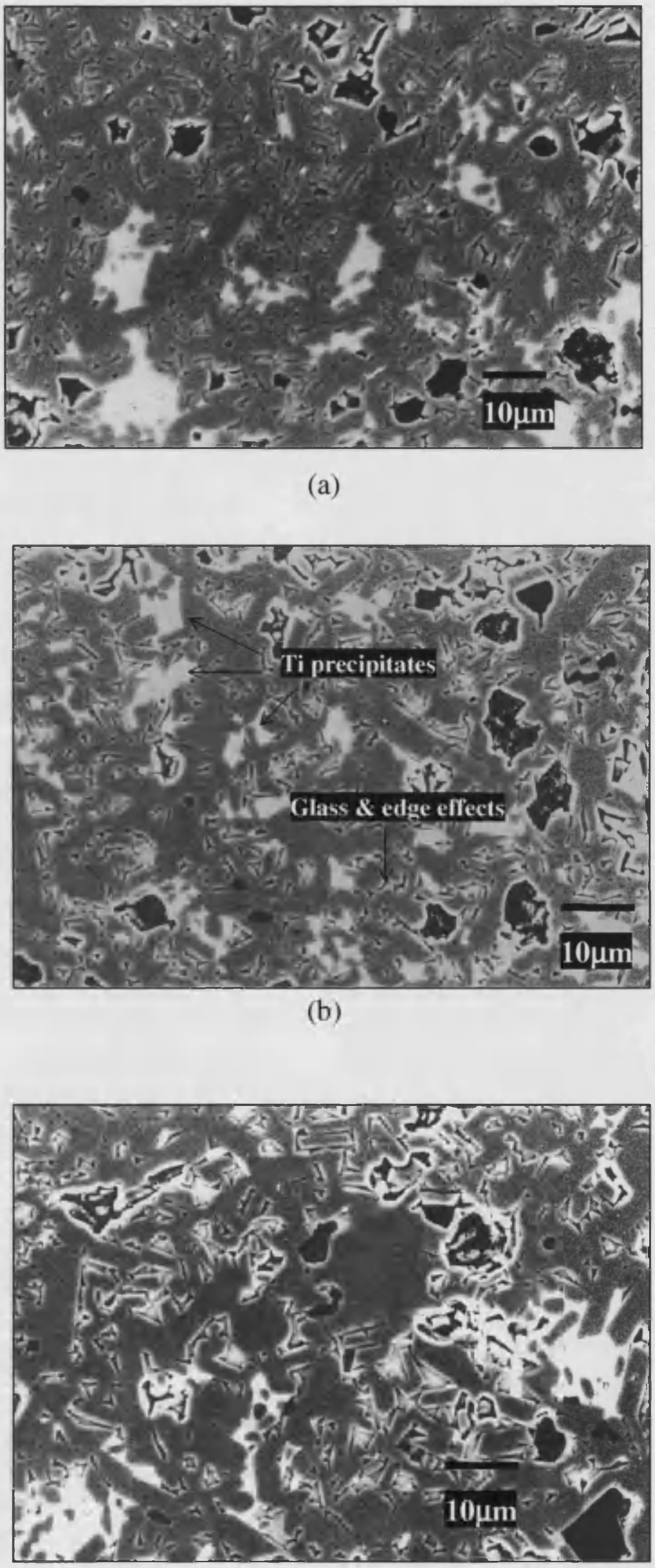

(a)

(b)

(c)

Figure 6.1: 4%TiO_2 composition (a) normal mixing time (b) double mixing time and (c) triple mixing time

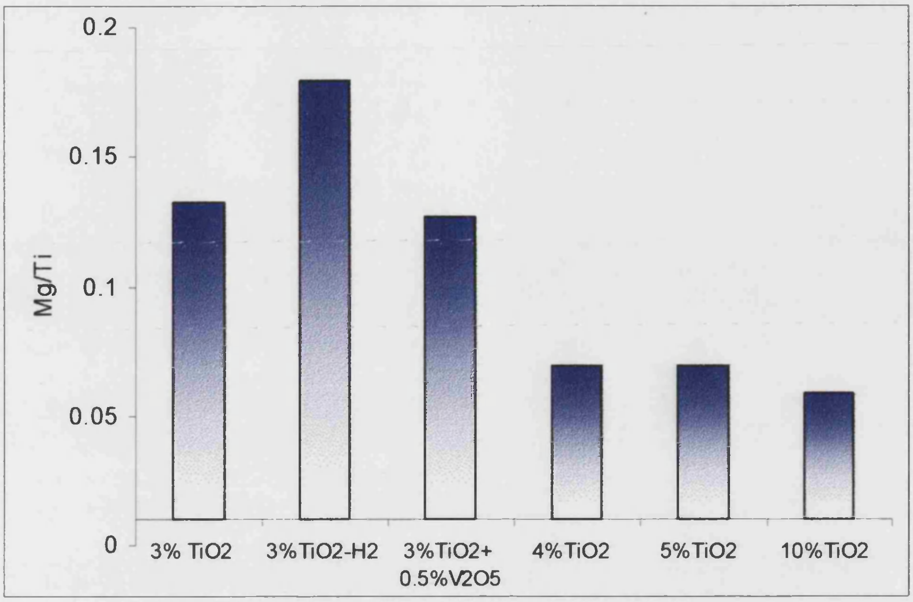

(a)

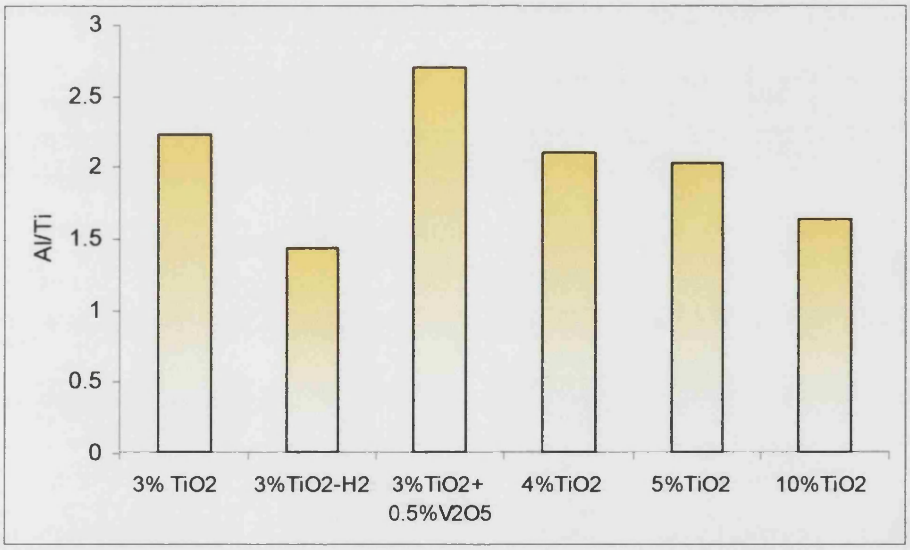

(b)

Figure 6.2: Ratio of atomic percent (a) Mg/Ti (b) Al/Ti calculated from EPMA results

of Mg-Ti or Mg-Al-Ti compounds coincide with Al_2O_3 peaks (figure 6.3). The latter being strong peaks will tend to mask the Mg-Ti peaks.

Since it was not possible to confirm the presence of Mg-Ti compounds from the XRD results directly, an indirect method was tried. A sample was prepared with 3%TiO_2 dopants but without the other glass forming additives. This composition is called 'pure alumina-3%TiO_2' composition and designated as PAT3. This composition will have negligible* Mg-Ti compounds as there is no MgO added to the composition. The peaks were normalised for the quantitative analysis of XRD data. Now the height of the peak, as discussed in section 5.1.2, is a quantity factor (QF) equal to the ratio of phase peak to the 80%Al_2O_3 peak from the same sample. The number on the y- axis is an arbitrary value signifying the quantity of a phase for relative comparison purpose only.

The quantity of Al_2TiO_5 in PAT3 sample composition is compared with the T3 and T4 samples in figure 6.4. It is clear that the pure alumina composition PAT3 shows a higher Al_2TiO_5 concentration than the T3 composition. This shows that absence of MgO in PAT3 has resulted in a higher concentration of Al_2TiO_5 while in the T3 sample the presence of MgO results in some TiO_2 going into the formation of Mg-Ti containing compounds and with a resultant decrease in Al_2TiO_5 concentration. Furthermore in the T4 composition the Al_2TiO_5 concentration increases to the same level as in the pure alumina (PAT3) composition. Based on the argument above the reason for Ti agglomeration could be explained as follows:

1% MgO presence in up to 3% TiO_2 may shift the kinetics towards the formation of Mg-Ti compounds rather than Ti rich compounds such as Al_2TiO_5. The formation of the former compounds will require a lesser amount of TiO_2, producing a greater distribution of Ti rich area. In this composition the ratio of Mg/Ti may be a threshold limit to promote the formation of Mg-Ti compounds. These compounds are present in sufficient quantity to form an interconnecting network when reaching the percolation threshold.

---

* *Even the pure alumina composition will have traces of MgO present, which might form a very small peak of Mg-Ti, that can be ignored when comparing with the peaks of samples where 1%MgO has been added i.e. T3 sample.*

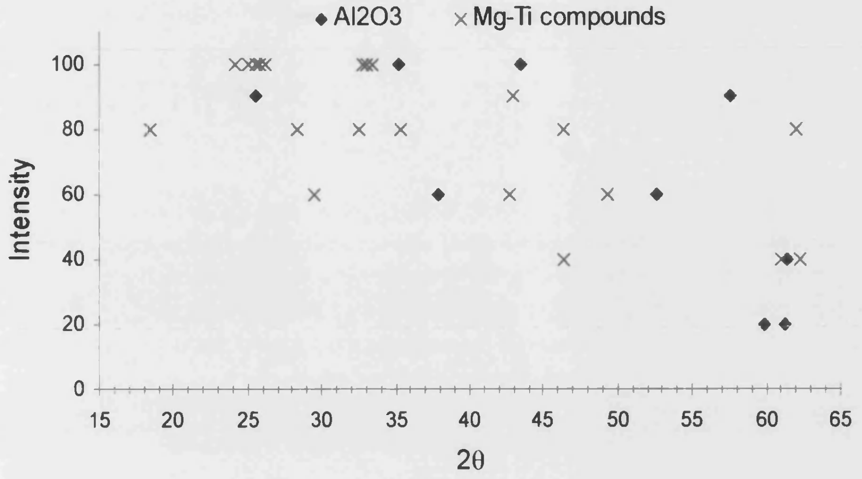

Figure 6.3: Positions of Al_2O_3 and Mg-Ti/Mg-Al-Ti compounds

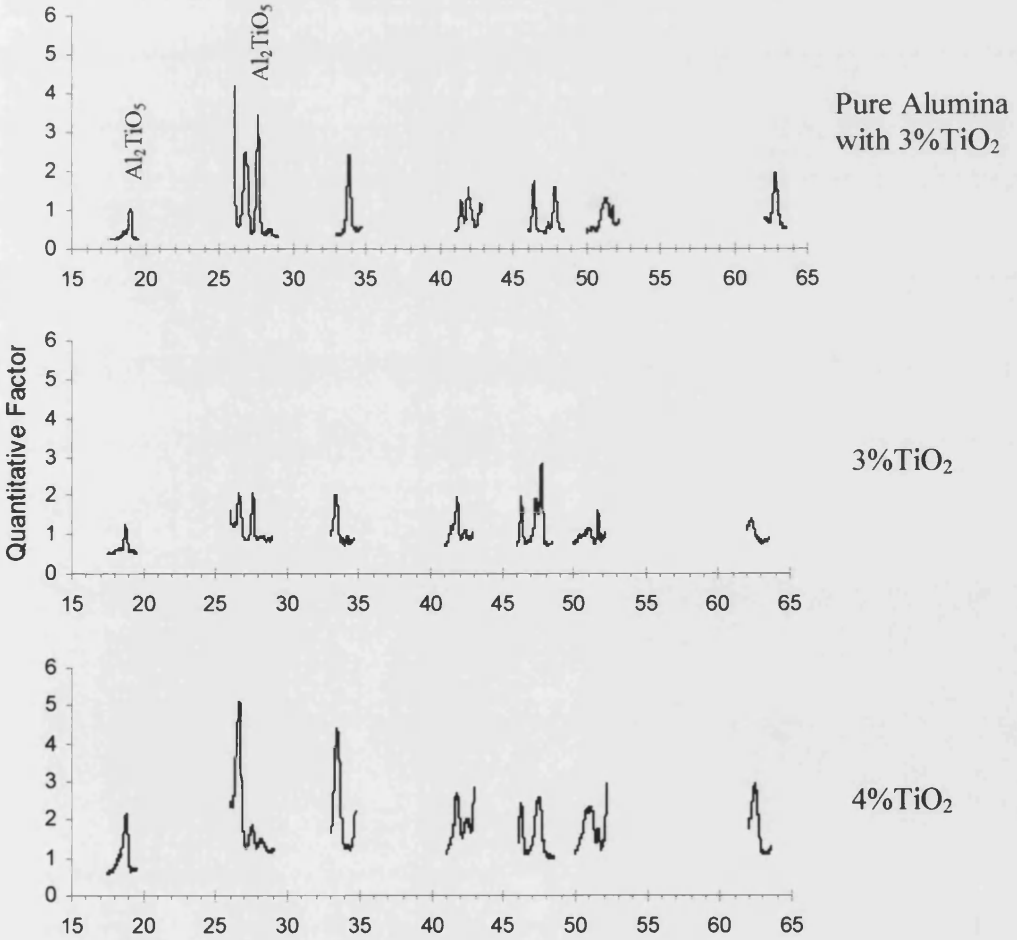

Figure 6.4: Normalised XRD peaks for quantitative comparison

At the 4% TiO_2 level, the Mg/Ti ratio is lower than the threshold and the kinetics of reaction shift towards the formation of a greater quantity of the Ti rich compounds. These compounds then require a higher quantity of TiO_2 causing a shortage of TiO_2 for wider distribution to form an interconnection and thus breaking the percolation network.

The importance of MgO for the wider distribution of Ti^{4+} compounds can be further supported from observations on the microstructure of the pure alumina compositions. The lack of Mg in pure Al_2O_3-TiO_2 compositions also results in the agglomeration of Ti rich areas in the 3 & 5%TiO_2, resulting in a microstructure (figure 6.5) similar to the T4 sample (figure 6.1).

The type of Mg-Ti compound formed may be same in all the TiO_2 doped compositions. As was shown by the TEM for the T10 sample, discussed in section 5.1.2.4, this may be a Al_2TiO_5 + $MgTiO_5$ phase.

6.1.2.1.2. Colloidal coagulation

Another explanation for the agglomeration of the Ti rich area in the T4 can be made based on colloidal theory. It is known that in colloids the collision between two similar particles can lead to a permanent contact between the colliding particles resulting in coagulation {189}. With increase in particle concentration the probability of collision increases and the probability of coagulation increases. Furthermore in the case of polymer adsorption on particles, if the polymer concentration is sufficiently low, such that the rate of particle collisions is faster than the rate of polymer adsorption, polymer chains can be co-adsorbed on more than one particle, forming polymer bridges. At a higher concentration, the bridges formed may be disrupted as polymer adsorption continues and bridging flocculation occurs, leading to open flocs {190}. A similar explanation may be relevant in the present system. If we assume TiO_2 is being absorbed on the surface of Al_2O_3 particles and forming a solid solution of Al_2O_3-TiO_2, then bridges are formed at the TiO_2 concentration of 3% which get disrupted at 4%, leading to coagulation of Ti rich agglomerates. Also the "Theory of sedimentation process" suggests that the rate of flocculation is directly proportional to the particle size and the concentration of particles {191}. This can be used to explain the possible

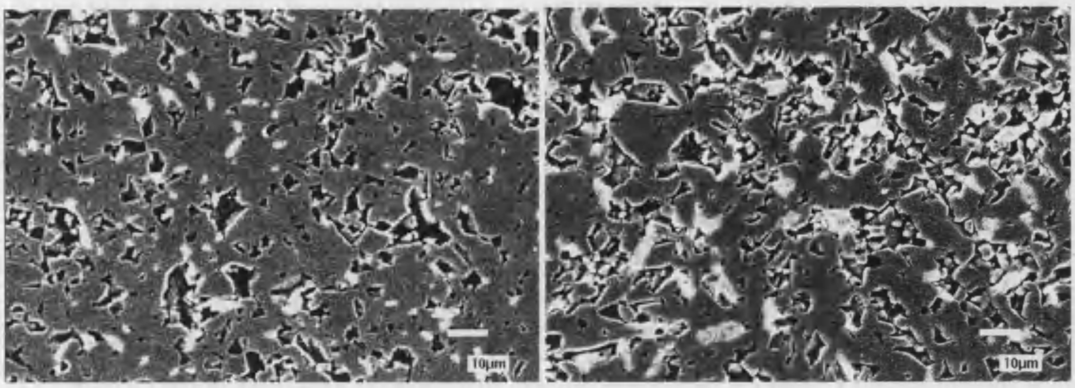

(a) (b)

Figure 6.5: Back scattered pictures from pure alumina compositions (a) 3%TiO_2 and (b) 5%TiO_2

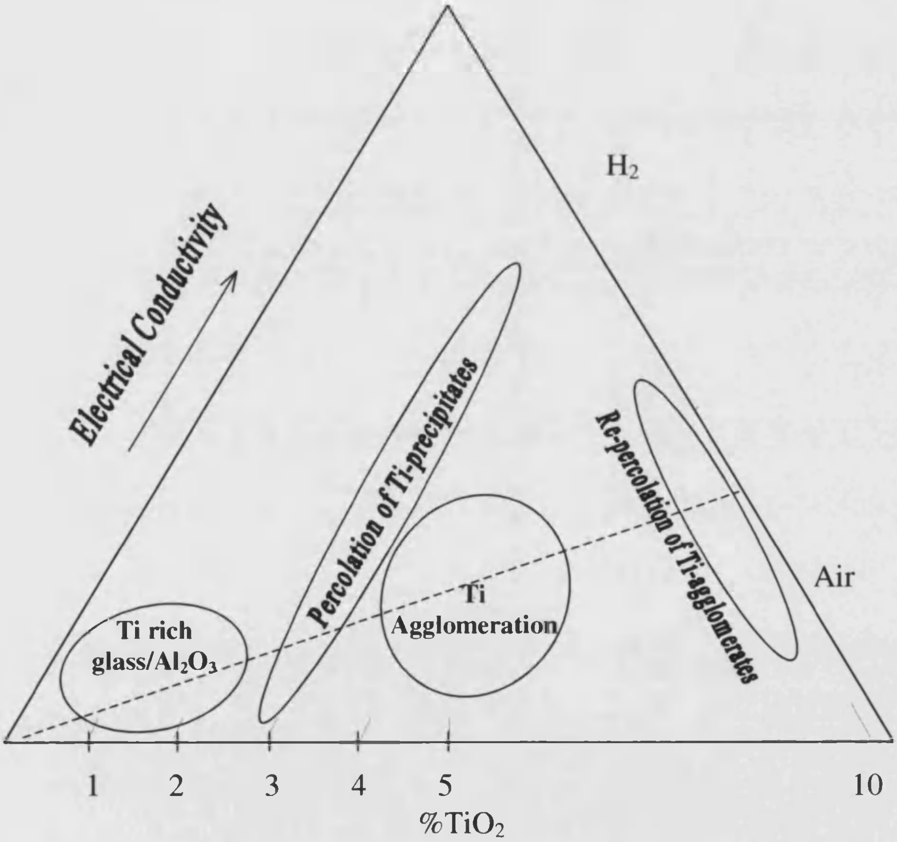

Figure 6.6: Conductivity map in TiO_2 doped Al_2O_3

flocculation with increased concentration of TiO_2 in the 4%TiO_2 composition. The likelihood of this happening during the mixing stage can be ruled out due to the presence of sufficient quantity of dispersant. In summary, at 4%TiO_2, the concentration has crossed a threshold to stay distributed and thus forms Ti rich agglomerates.

In conclusion, 3%TiO_2 is a threshold limit to form a percolation network of Ti rich compounds which lower the resistivity of Al_2O_3. At 4% the TiO_2 rich compounds have coagulated resulting in increased resistivity. The coagulation is possibly a result of TiO_2 concentration becoming too high either to stay distributed or due to the shift of kinetics towards the formation of compounds requiring a larger quantity of TiO_2. These coagulates again become interconnected at 10% TiO_2 concentration to reduce the resistivity. A map of conductivity, and the relevant microstructures on which the discussion above is based is shown in figure 6.6.

The formation of a percolation network of TiO_2 rich compounds has resulted in $>10^6$ reduction of resistivity only for samples annealed in a low p_{O2} (H_2) and not those fired in high p_{O2} (as-fired in air). The reasons for the transition in Ti rich compounds from being non-conducting in the as-fired state to conducting in the H_2 annealed state can be due to a change in charge carrying species. The possible charge carriers in various compositions are thus worthy of discussion. Also, the similar activation energy of the 3%TiO_2 composition and the 3%TiO_2 + 0.5%V_2O_5 composition could be explained based on the nature of the charge carriers.

6.2. Possible charge carrier

Possible charge carriers for the various compositions can be proposed based on the results in this study and on previous work on other TiO_2 based materials.

6.2.1. Charge Carrier in as-fired Samples

6.2.1.1. In base composition

In pure alumina, the conductivity as given by Endl and Hausner {192} could be due to Al^{3+} ions at low temperature, supplemented by a stronger electronic conductivity at high temperature. Additionally the presence of oxygen vacancies in alumina has been reported by many authors {9,18}. However the occurrence of any ionic conduction below 1200°C has been opposed by some authors {50,60}. Nevertheless $V_O^{\bullet\bullet}$ could be a carrier for ionic conductivity at low temperatures in alumina. Thus the high mobility electronic carriers are in a minority and the low mobility ionic carriers are the major current carriers at ambient conditions (room temperature and p_{O2}=1atm), that is why Al_2O_3 is such a good insulator at room temperature. Similarly in the presence of MgO, Al_2O_3 conductivity is governed by the Mg_{Al}' defect.

6.2.1.2. *In sample with 3%TiO₂*

In the case of Al_2O_3 doped with TiO_2, a proportion of the TiO_2 dissolves into the Al_2O_3, as was determined by the EPMA results (section 5.1.1.3). It has been postulated earlier that in the as-fired samples, the resistivity of the 3%TiO_2 sample is high. The conduction is mainly through the alumina grains as the TiO_2 rich areas are insulating in as fired samples. Based on the earlier publications, discussed in section 2.2.2, it is possible to assume that at the test temperatures of the samples in this project (100-900°C) the conduction through alumina is electronic. Furthermore, the conductivity will be governed by the electrons generated in Al_2O_3 by the incorporation reactions {193}:

$$Al_2O_3 \rightleftharpoons 2Al_{Ti}' + V_O^{\bullet\bullet} + 3O_O$$

$$Al_2O_3 \rightleftharpoons 2Al_i^{\bullet\bullet\bullet} + \tfrac{3}{2}O_2 + 6e'$$

$$2Al_2O_3 \rightleftharpoons 3Al_{Ti}' + Al_i^{\bullet\bullet\bullet} + 6O_O$$

The majority of ionic carriers produced from the above reactions will have too low a mobility to cause any steep increase in the conduction through the alumina grains, thus resulting in a high resistivity ceramic.

The reason why the TiO_2 rich areas do not contribute to the conductivity under these conditions is the high resistivity of rutile (10^{12} Ω-cm) at room temperature and high p_{O2} (=1atm). However TiO_2 has a near semi-conduction band gap of 3-3.5eV {73, 194} against a band gap 9eV for Al_2O_3 {10}. The conduction is still through alumina, because though TiO_2 has 10^8-10^{11} charges/cm^3 {195} their mobility is only 0.2cm^2/V.sec {196}, while Al_2O_3, which has a charge density of only 1electron/cm^3 has a higher mobility of 200cm^2/V sec {59}. TiO_2 which is also known to influence the conductivity of Al_2O_3 due to its tendency to become non-stoichiometric {102} has the nonstoichiometry of oxygen deficiency of only ~ 10^{-3}at% at these pressures even at temperatures of 1000°C {197}. That is why TiO_2 rich areas will have a higher resistivity than Al_2O_3, making them insulators and potential barriers to the conduction through alumina. Thus this material will have higher resistivity than the 2%TiO_2 sample. Thus in the as-fired T2 sample the activation energy is from the conduction through Al_2O_3 and in the as-fired T3 sample the activation energy is higher (figure 4.19) due the conduction through the high resistivity Al_2O_3 grains being further blocked by the TiO_2 rich precipitates. It is only in the H_2 annealed state that TiO_2 rich area is conducting. The charge carriers in this sample are discussed later in this chapter.

6.2.1.3. *In sample with 3%TiO_2 + 0.5%V_2O_5 (TV5)*

The TiO_2 in this sample formed a percolation path similar to that in the T3 sample. However unlike the T3 sample this composition had a lower activation energy and lower resistivity than 3%TiO_2 alone in the as-fired samples. It is suggested that his difference can be attributed to the presence of V_2O_5 in the composition.

Studies have shown that V_2O_5 dissolves into TiO_2 {198}, as was seen in the TV5 sample where TiO_2 and V_2O_5 are present at the same position, i.e. in the Ti rich bright areas (figure 5.2). Herrmann et al {199} have shown that the resistivity of TiO_2 is reduced when the concentration of V_2O_5 impurity in it is above the level of 4wt%, which coincides with the concentration level in this composition. This can be used to suggest that unlike in the T3 sample, the Ti rich area has now become more conducting than the Al_2O_3 grain. Thus the lower activation energy in the TV5 sample is due to the conducting species changing to the Ti rich bright phase rather than the Al_2O_3 grain in T3 sample (figure 4.19).

The importance of V_2O_5 causing this effect can be explained based on the results of the studies of the addition of a pentavalent oxide such as Nb^{5+} to TiO_2-rutile. On Nb^{5+} doping in rutile, the photocurrent density doubles {200} and electrical conductivity increases significantly {201}. TiO_2 shows n-type semiconduction with the predominant lattice defects present as Ti^{3+}. Similarly work on catalysts has shown that the addition of V^{5+} cations to TiO_2-anatase results in increased conductivity with an n-type doping effect {202}. Based on these studies it is possible to propose that on addition of a pentavalent oxide such as V_2O_5 to TiO_2, a similar increase in n-type conduction can result. This explanation also applies for the other TiO_2-V_2O_5 compositions (TV1 and TV3) which show a decrease in resistivity over the samples containing only TiO_2 (figure 4.13) even-though the existence of similar effects in Al_2O_3-TiO_2 system have not been reported.

Thus in conclusion, for the as-fired T3 sample (3%TiO_2) the activation energy increases over and above that of the 2%TiO_2 sample due to highly insulating Ti rich phases blocking the charge carriers through Al_2O_3 grains. On V_2O_5 dissolution into the percolating Ti phase, it becomes conducting and becomes the charge carrying path, resulting in a decrease in activation energy.

6.2.2. Charge Carrier in H_2 Annealed Samples

On annealing the T3 sample in H_2, the sharp fall in activation energy (figure 4.19) and resultant resistivity (figure 4.15) has been noticed. A similar sharp decrease in activation energy is also observed in the TV5 sample (figure 4.19). Though the latter sample has higher resistivity than the former (figure 4.16). The reasons for the overall decrease in activation energy and the difference in the resistivity of these two compositions can also be attributed to the change in charge carriers. This will be discussed further.

6.2.2.1. In 3%TiO_2 sample

The works published linking the p_{O2} with the change in conductivity of TiO_2 doped alumina have been of two types. Most of the publications cover the change in conductivity when the sample is processed in air and tested at low p_{O2}. Very few publications have studied the effect of firing the sample in low p_{O2} and then testing in air, as is the case in this project. However the conductivity behaviour at low p_{O2} has been found to be similar for both the cases i.e. increase in conductivity on testing in low p_{O2} or firing at low p_{O2}. Though no work exists on firing the sample in air and then annealing at low p_{O2}, previous work is useful in proposing the nature of the charge carriers in TiO_2 doped samples.

For TiO_2 doped Al_2O_3, a resistivity decrease in an argon atmosphere was noticed by Endl and Hausner {192}. They believe that this was due to the defect conductivity at low p_{O2} as a result of $Ti^{3+}{}_{Al}{}^{3+}$ substitution following the reaction:
$Ti^{4+} + e' \rightarrow Ti^{3+}$
However Mohapatra and Kröger believe {80}, that Ti^{3+} being iso-valent with Al^{3+}, should not contribute to an increase in conductivity while Ti^{4+} should result in the formation of substitutional defects ($Ti_{Al}^{\bullet}$) {107} and in this way cause an increase in conductivity. On the other hand Tsuar and Kröger {50} reported that the addition of TiO_2 increases the alumina conductivity only by the formation of aluminium titanate precipitates at the grain boundary. They also believe that Ti^{3+} has greater solubility in Al_2O_3 and will reduce the quantity of Al_2TiO_5 and would be less effective in increasing the conductivity than Ti^{4+}. Formation of some Al_2TiO_5 in the T3 sample has been discussed previously and if the latter statement were to be true, we should have seen a higher conductivity in the as-fired state as compared to the H_2 annealed state. Thus these latter analogies do not fit the results in this study. Also the greater solubility of TiO_2 in the Al_2O_3 grain is not apparent from the EPMA results in figure 5.13. Thus the explanation of Mohapatra and Kröger {80} and Tsaur and Kröger {50} do not agree with the results in this study. The explanation of Endl and Hausner {192} is more in line with the results seen here.

Nevertheless, a more accurate explanation for the steep fall in resistivity on H_2 annealing is possible from the work of Gruber and Krautz {108}. They reported that TiO_2, when annealed in a reducing atmosphere and when in contact with other metal oxides, readily reduces to lower valence oxides, such as Ti_2O_3, TiO and Magneli phases, Ti_nO_{2n-1} (n = 4-10) {194}. On oxygen depletion, when the TiO_2 composition approaches $TiO_{0.3\text{-}0.5}$, the crystal structure changes from hcp to fcc and there is an increase in the number of d-electrons in the d-band. This results in a sharp increase in its conductivity and titanium oxide becomes semiconducting {108}. The same mechanism may be responsible for reducing the resistivity of Ti rich phase in T3 material. Thus the "bright" area is now becoming conducting due to TiO_2 reduction and now is the main current carrying phase, rather than the

Al_2O_3 present in the as-fired material, making the T3 alumina composition nearly semiconducting on annealing in an oxygen depleted environment.

Defects operative in TiO_2 rich precipitate:

Predominant defects responsible for the TiO_2 conductivity have been identified as $V_O^{\bullet\bullet}$ with both n-type or p-type conductivity possible, depending on the temperature. {203}. Kim et al {204} added the possibility of the Ti_i^{4+} ion conducting, but only at temperatures above 1000°C. They agreed with $V_O^{\bullet\bullet}$ being the major defect below 1000°C. The mechanism of conductivity within TiO_2 has been reported as the small polaron hopping for both electrons and electron holes {203} with an activation energy of ~ 0.2eV {205} which is very close to the activation energy of 0.3eV for the T3 composition in this study.

The XRD and TEM studies discussed previously have shown the TiO_2 to be present in the form of Al_2TiO_5 and Mg-Ti compounds. It can be added that TiO_2 present as Al_2TiO_5 or as magnesium titanate will also have similar defect structure to that discussed in the previous paragraph. Furthermore it has been reported that magnesium titanate is also semiconducting at room temperature with an activation energy of 0.34eV {206}. This value is also similar to the activation energy value of 0.3eV for the 3%TiO_2 composition.

Additional charge carriers in H_2 annealed T3:

The discussion so far entails a single charge carrying species that is responsible for the conductivity in H_2 annealed 3%TiO_2 sample. However the complex impedance results show two separable curves (figure 6.7), unlike all other compositions that produce only single curve. This indicates that there is a possibility that a different species is also contributing to the conduction, especially because the activation energy is similar for both. One species is the semiconducting Ti^{3+}, as discussed above. The other could be an ionic species. This belief is based on the lower DC conductivity value (figure 6.8) as compared with the ac conductivity. The possible ionic carrier could be the hydrogen radical ($H_i^{\bullet}$) which could form as a result of heating in an H_2 atmosphere. Generation of

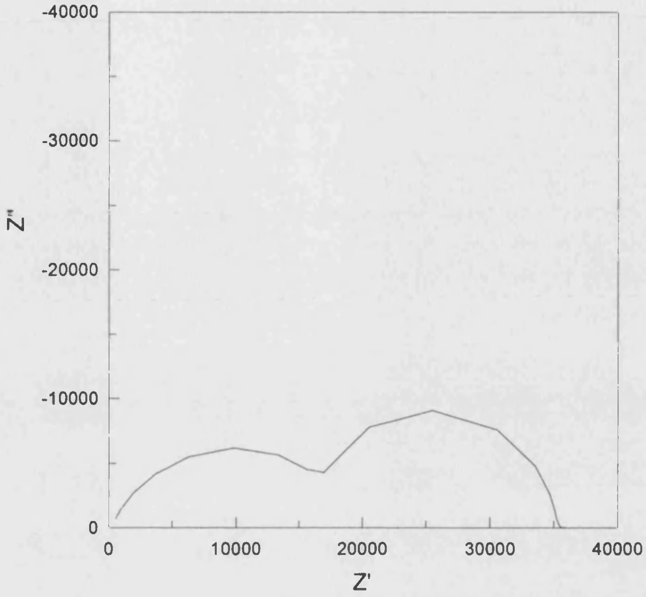

Figure 6.7: Complex Impedance graph for 3%TiO_2 composition at 100°C

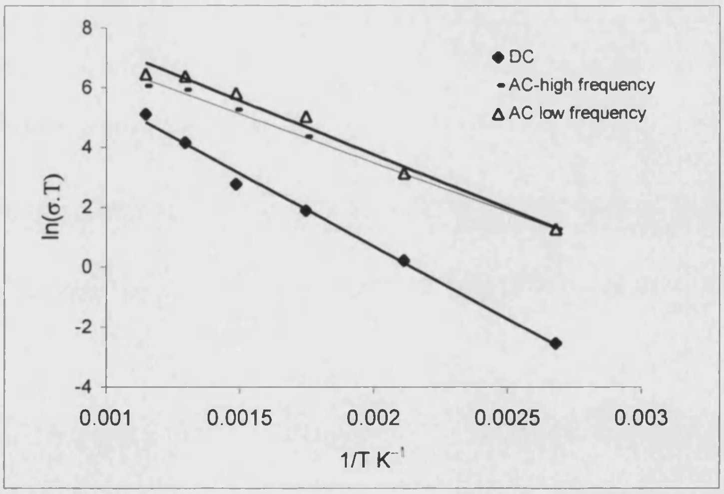

Figure 6.8: DC v/s AC conductivity for 3%TiO_2 composition

hydrogen donors following the H_2 injection into acceptor dominated Al_2O_3 {93} and TiO_2 film {208} has been reported. An increase in the ac conductivity as a result of H_2 donating an electron to the conduction band of TiO_2, as reported by Pyun and Kim {208}, might be taking place. To further support this contention, samples were annealed in low p_{O2} using helium rather than H_2. A marginal increase in conductivity on annealing in an He atmosphere, as compared with a steep increase after H_2 annealing (figure 6.9 (a)), could support this argument. As an alternate argument the two conducting species could be the Ti^{3+} at the grain boundary and in the grain interior.

To summarise this section, the increase in conductivity of T3 is due to the Ti^{4+}, becoming a semiconducting Ti^{3+}, or other reduced forms, and probably a hydrogen radical $H_i^{\bullet}$ both of which have similar activation energy of 0.3eV. This is irrespective of whether TiO_2 is present in free form or as Al_2TiO_5 or Mg-Ti phases.

6.2.2.2. Charge Carriers In 3%TiO_2 +0.5%V_2O_5 sample

The microstructure of the percolating bright TiO_2 rich areas is similar for the 3%TiO_2 + 0.5%V_2O_5 composition, which also has a low activation energy. Inspite of the similar activation energies of T3 and TV5 samples, the latter has higher resistivity. The similar activation energy indicates that the dominant effect on conductivity of this composition is the same as in the T3 composition i.e. the reduced form, semiconducting Ti^{3+} in the Ti rich bright area in figure 5.44. It is the vanadia which is playing the significant role in this change in resistivity from the 3%TiO_2 composition. Thus the operative mechanism here is based on a different reasoning.

Vanadium oxide is more easily reduced than TiO_2 {208}, and it may spontaneously transfer an electron to TiO_2, {202}.

$$e^- (V_2O_5) \Rightarrow e^- (TiO_2)$$

Thus V_2O_5 will increase the electrons available for conduction in the Ti rich phase. The increase in the electrons from V_2O_5 on reducing this composition in He

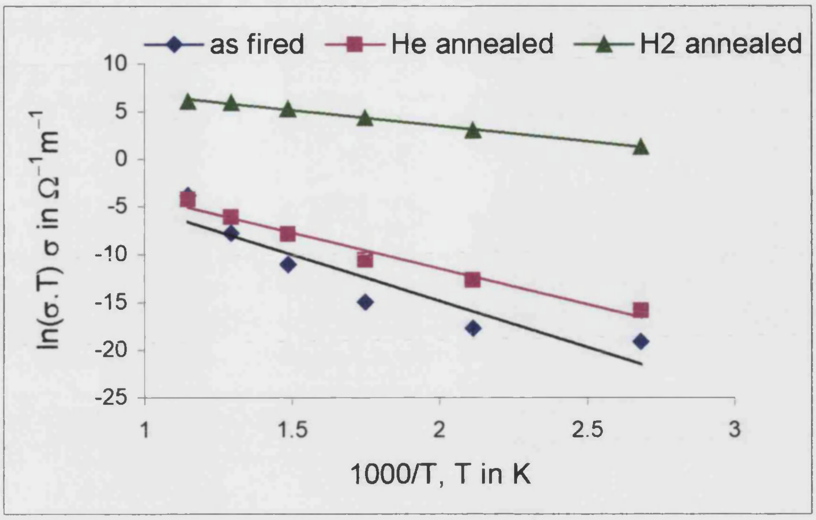

(a)

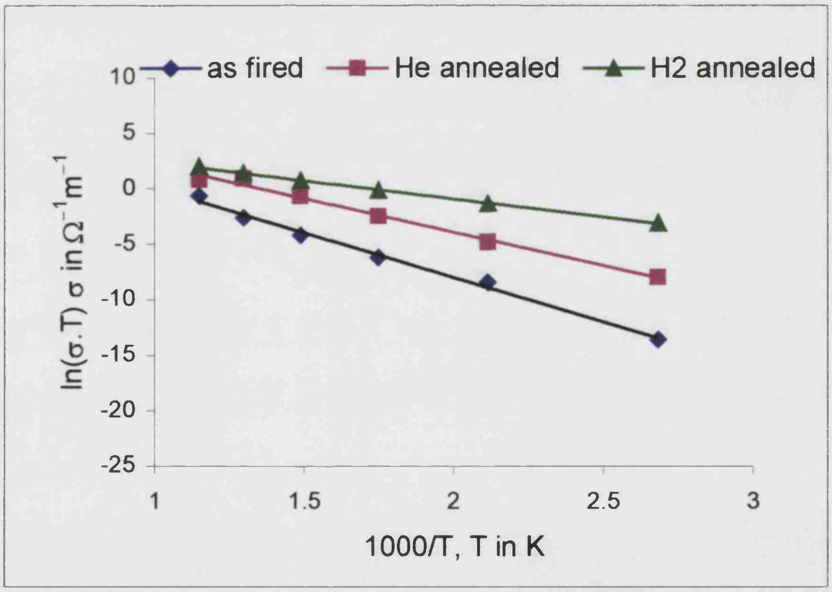

(b)

Figure 6.9: Effect of firing atmosphere on the Conductivity v/s Temperature for (a) 3%TiO_2 and (b) 3%TiO_2 +0.5%V_2O_5 composition

annealing is the reason for its steeper increase in conductivity than the T3 sample (figure 6.9).

However on reducing this composition in the H_2, the opposite trend of higher resistivity of the TV5 sample than the T3 sample is observed. This can be explained based on the work reported by Viparelli et al {202} and Sasaki et al{209}. The former found that vanadium oxide has a lesser effect on TiO_2 conductivity {202} when it reduces from V^{5+} to V^{3+} {209}. The trivalent state (V^{3+}) no longer has the same effect on TiO_2 as it had in the pentavalent state (V^{5+}){202}. In other words it does not transfer the electron, to the TiO_2 .The phase now acts as a barrier to the movement of charges. Thus even though Ti^{3+} will be the main species responsible for conduction, V^{3+} will be the barrier to this movement thus resulting in the lower conductivity.

In conclusion, in the TV5 sample, the Ti rich area, similar to that in T3 sample, is the charge carrying component. However it shows relatively higher conductivity in the He annealed sample due to the generation of access electrons from reduced V^{5+}, whereas it shows lower relative conductivity on H_2 annealing, due to the reduced V^{3+} acting as a barrier to the movement of Ti^{3+} carriers.

6.2.2.3. Charge Carriers in T10 composition

Conductivity in the 10%TiO_2 composition (figure 4.15) can be attributed to the reduced Ti^{3+}, present in Al_2TiO_5 agglomerates. Furthermore above 300°C the conductivity of the T10 sample starts decreasing rather than increasing. This might be due to the temperature coefficient of conductivity for titanium oxide becoming negative due to various factors of the experimental conditions {108}. This would explain the non-linear change in conductivity with increase in temperature above 300°C.

A map summarising the charge carriers in TiO_2 and TiO_2 -V_2O_5 composition is shown in figure 6.10.

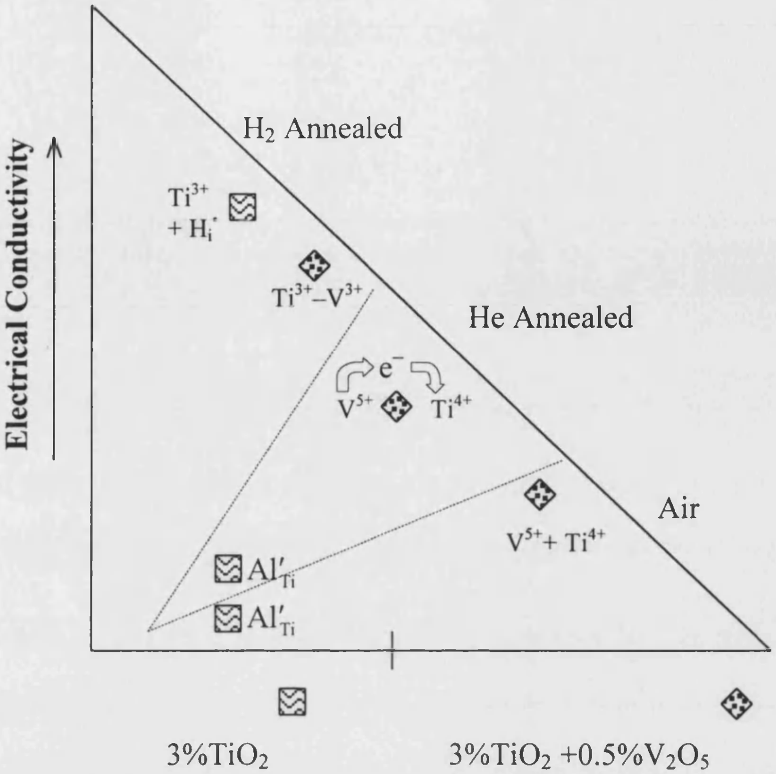

Figure 6.10: Charge carrier map in T3 and TV5 compositions

It is possible to relate the microstructures with conductivity v/s frequency response using a network of resistors and capacitors. This has been carried out in the following section.

6.3. RC Network Analysis for Impedance results

The electrical response of a material can be related mathematically to a combination of resistors and capacitors, arranged in an array of parallel and series connected components (figure 6.11), taken from the R-C network model as explained by Almond and Vainas {210}. The real (Z') and imaginary (Z'') components of impedance are converted into conductivity (σ) and relative permitivity (ε_r) for the 200°C measurements, using the equations:

$$\sigma = \frac{Z'}{Z'^2 + Z''^2} \frac{\ell}{A}$$

$$\varepsilon_r = -\frac{Z''}{Z'^2 + Z''^2} \frac{1}{\omega} \frac{1}{\varepsilon_0} \frac{\ell}{A}$$

where ℓ = thickness of sample, A = Area of cross-section, ω = angular frequency = $2\pi f$, and ε_0 = permitivity of vacuum

The derivation for this equation is explained in Appendix C.

The conductivity and permitivity v/s frequency response for the base composition and 2%TiO_2 composition is shown in figure 6.12 and 6.13 respectively.

The plots can be explained in terms of microstructure and RC network shown in figure 6.11. We can assume that the resistors act as the conducting phase, which in this case is the Ti rich phase, and capacitors signify the dielectric, which in this microstructure is the alumina grain or glass, whichever has the lower conductivity. As discussed previously glass has a higher conductivity than alumina in the base composition.

It is clear from figure 6.14, that the 2%TiO_2 composition will have a very large number of capacitors and few resistors. Such a situation has been described by Vainas et al {211} as analogous to a non-percolating conducting phase consisting of 60% capacitors and 40% resistors. The conductivity response from the sample (figure 6.13) shows the pure resistive component of impedance at frequencies

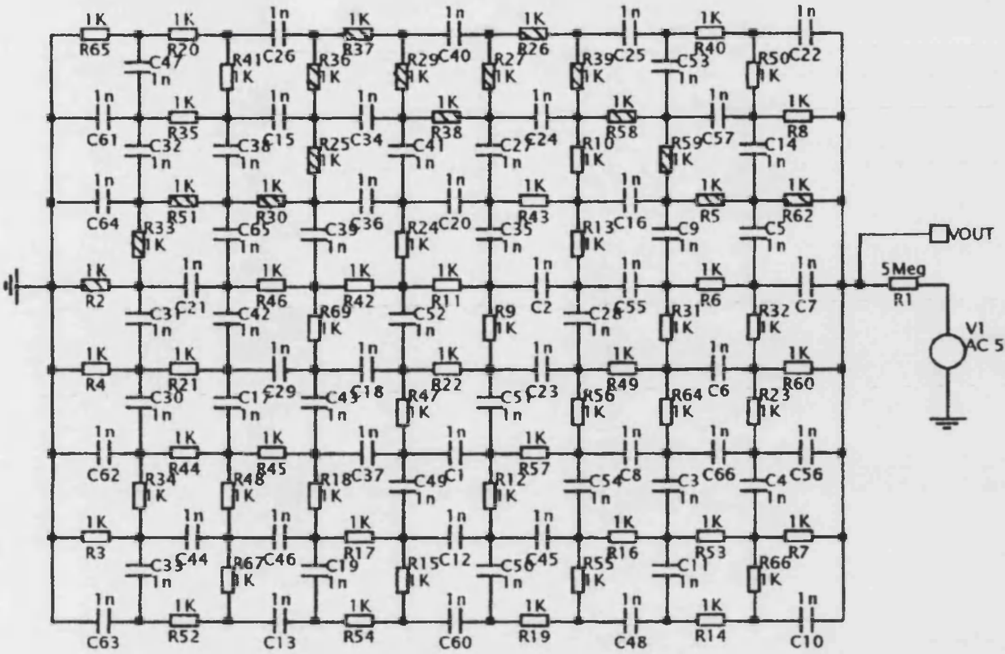

Figure 6.11: RC network model of Almond and Vainas {211}

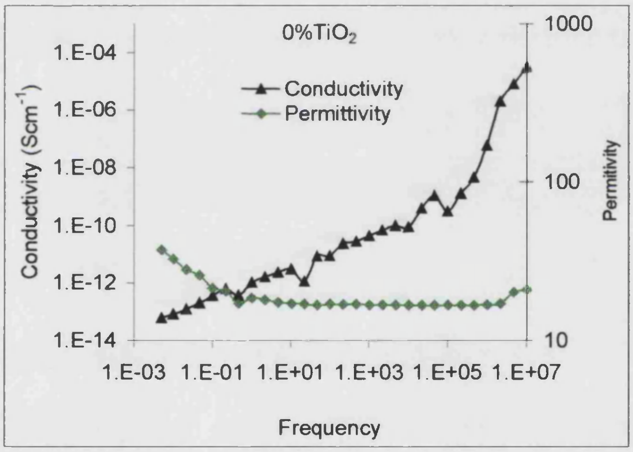

Figure 6.12: σ and ε v/s frequency response for base composition at 200°C

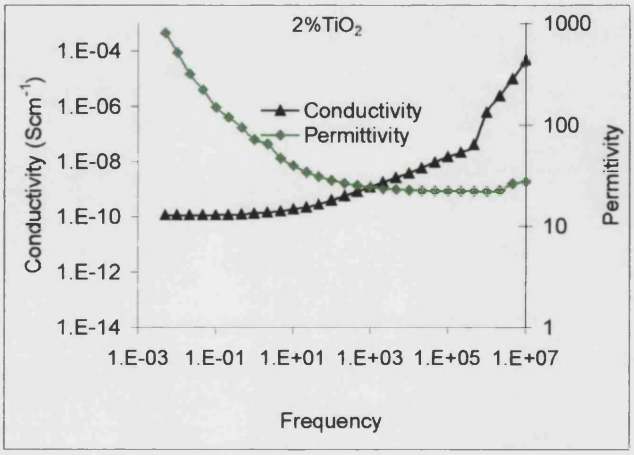

Figure 6.13: σ and ε v/s frequency response for 2%TiO_2 composition at 200°C

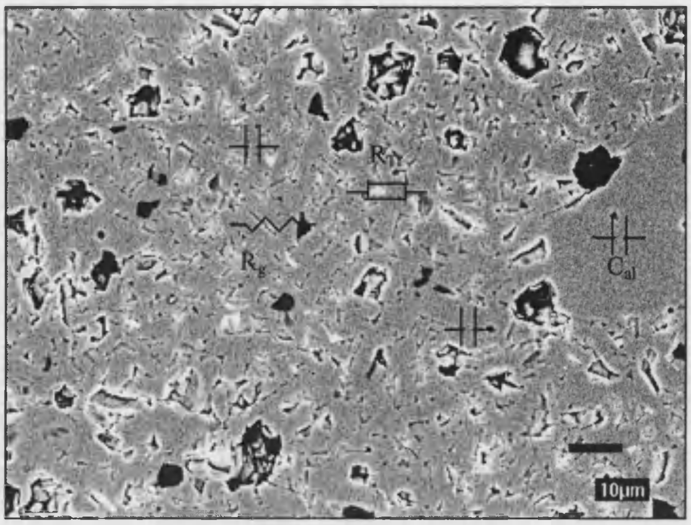

Figure 6.14: 2%TiO_2 microstructure with few conductive and many dielectric parts

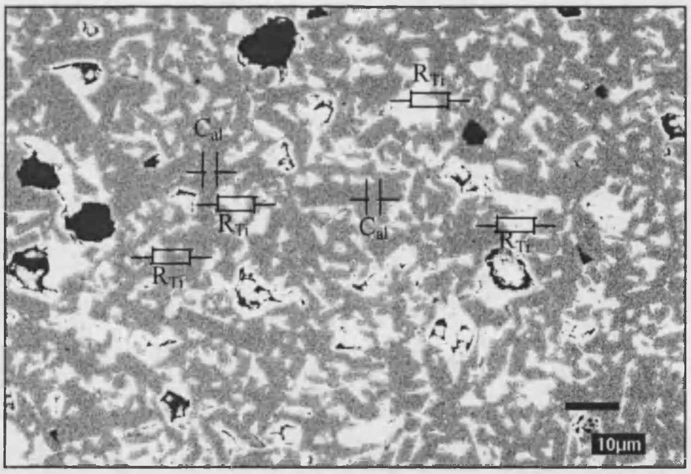

Figure 6.15: 3%TiO_2 microstructure with large number of conductive parts

below 1Hz. These are the glass resistors R_g. At frequencies of 1Hz to 500kHz, the resistance of the alumina capacitance (C_{al}) reduces to contribute towards the increasing conductivity of the system. The increase here follows a *power law*[¤], n ≃ 0.5. The same reasoning could be valid for the 0%TiO_2 composition. However due to no TiO_2 present in the glass, it has much lower conductivity. Thus the pure resistive region would be visible at a much lower frequency, as compared with 2%TiO_2. The small TiO_2 inclusions (bright areas) are the resistors (R_{Ti}) in series with the large glass resistors. Their conductivity will be much higher than that of alumina or glass. As a result the contribution of these resistors to the total resistivity of the system will be insignificant.

The > 5 orders of magnitude increase in conductivity at 3%TiO_2 is due to the change in mechanism of conductivity and activation energy. A microstructure consisting of percolating Ti rich area, resulting in high conductivity has been discussed in section 6.1.1. This microstructure now represents a large number of high conductivity resistors (R_{Ti}) and fewer high resistivity capacitors (C_{al} for alumina and C_g for glass) (figure 6.15). This situation is analogous to a percolating conducting phase equivalent to a network consisting to 60% resistors and 40% capacitors, as analysed by Almond and Vainas {210}. The new path for conduction is a Ti rich path due to the $R_{Ti} \ll R_{al}$ and R_g. The percolating path is indicated by the R_{Ti} at low frequency connected in series across both the electrodes resulting in the resistive region, at a frequency below 1kHz (figure 6.16). Furthermore, there may be other Ti rich areas which are not connected with the main percolating paths. Glass/alumina present here, are capacitors that are isolated and do not contribute to the conductivity at frequencies below 10kHz. At a frequency of 10kHz, the alumina/glass capacitors now start conducting and connect the unconnected TiO_2 rich paths with the main percolating path. This increases the strength of percolation and the overall conductivity. Due to the higher conductivity of the system, the alumina capacitors connect the conductivity networks at a higher frequency (5kHz) than in the 2%TiO_2 case (1kHz).

[¤] *Power law: It is widely found that {210} the ac conductivity (σ) increases as a power of frequency (ω) at high frequency i.e.* $\sigma \propto \omega^n$

The new network, now formed, also has a significantly lower capacitance than the percolating Ti rich network. This is reasoned on the basis that at the highest frequencies, the ωC conductance of the alumina/glass is far greater than the conductivity of the Ti rich islands. The high frequency conductance is dominated by a percolation path of capacitive Al_2O_3 regions while the resistive Ti islands are effective open circuits. As the frequency is reduced, the relative conductivities of the 2 regions converge and unconnected capacitive regions become bound by resistive regions to the percolation path of capacitors to result in an effective rise in network capacitance, shown by the high permitivity in figure 6.16.

In the case of the 4%TiO_2 composition (figure 6.17), the pure resistive component of impedance (at a frequency <1Hz) is due to the same resistor as was the case in the 2%TiO_2 composition i.e. glass. Also at a higher frequency the power law of $n \simeq 0.5$ is due the alumina capacitors joining in. However in this case a new power law ($n>1$) is apparent at a frequency higher than 10kHz. This may be due to the high conductivity TiO_2 islands now joining in the circuit of glass resistors and alumina capacitors. These Ti rich islands, having a higher conductivity, now join the conducting network and cause a sharper increase in conductivity.

At 10%TiO_2 the Ti rich islands have become significantly larger in number, reaching a near percolation state (figure 5.43). Here the higher conductivity is again due to the Ti rich resistors. The percolation is weaker, i.e fewer percolation paths, resulting in the conductivity being lower than the percolation conductivity of 3%TiO_2. Also, as for the case of the 4%TiO_2 composition, when the capacitors from the Ti rich areas join the capacitors from alumina/glass, the second power (>1) is valid, again above 10kHz (figure 6.18).

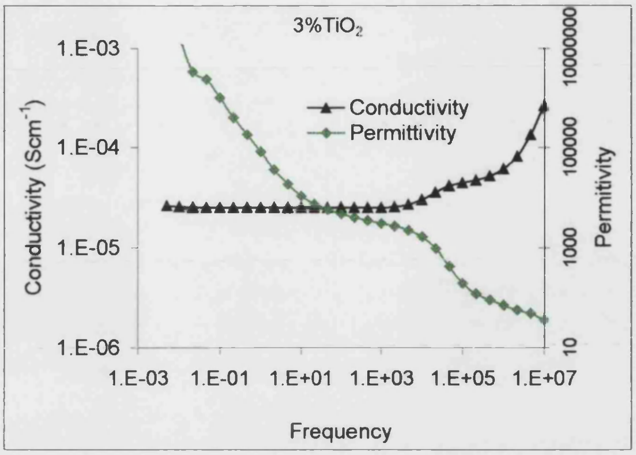

Figure 6.16: σ and ε v/s frequency response for 3%TiO_2 composition at 200°C

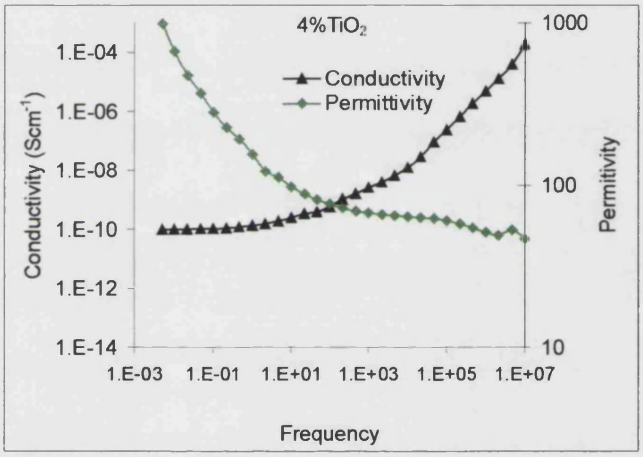

Figure 6.17: σ and ε v/s frequency response for 4%TiO_2 composition at 200°C

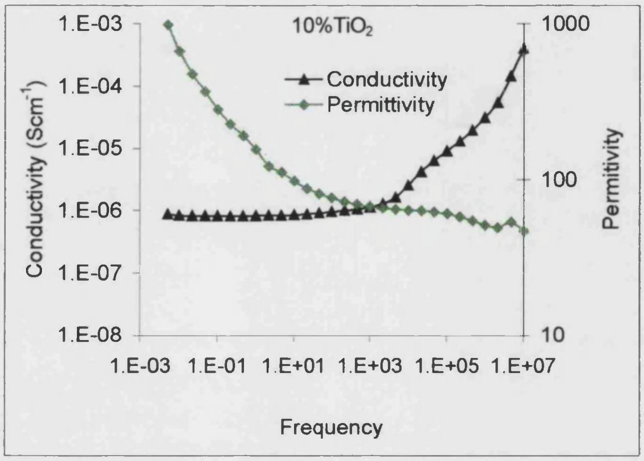

Figure 6.18: σ and ε v/s frequency response for 10%TiO_2 composition at 200°C

CHAPTER VII

FUNCTIONAL GRADIENT MATERIAL

An Investigation

This chapter covers a preliminary analysis regarding the feasibility of manufacturing a functional gradient material between the base composition and TiO_2 *doped composition*

7. FUNCTIONAL GRADIENT MATERIAL

An Investigation

The primary objective of this project was to identify an appropriate ceramic dielectric having a range of compositions with a lower resistivity than the base alumina composition. For the operational usefulness of this study, a detailed programme will be necessary to investigate the incorporation of this composition into the base composition. The method suggested for this to be successful is the preparation of a functional gradient material. The concept involves a monolithic material, with a property variation across the thickness of the component, the property in question here being the resistivity. The functional gradient insulator will have one surface at a lower resistivity, to use for bleeding excess charge to earth, and other surface high resistivity, to keep the voltage stand-off property. A brief introduction to the preparation of this material is given here. Two possible methods could be involved:-

(a) Pressing one layer base composition and second layer lower resistivity composition together in a mould so that they form a monolith 2 layered green compact. On firing the compact will have at one end the base composition and at the other end the lower resistivity composition with the resistivity variation across the thickness, thus forming a functional gradient material.

(b) Surface impregnation of TiO_2 into a base composition green compact. The idea here is that on firing, the TiO_2 will enter the compact and form a microstructure similar to that of the 3%TiO_2 composition. The surface will then have a lower resistivity due to the incorporation of TiO_2 yet the bulk still retaining the higher value.

The feasibility of each of these two methods has been studied.

7.1.Pressing the two compositions together

On pressing the two different compositions and firing, the first possible problem could be the development of differential stresses in the functional gradient compact due to different sintering kinetics of two compositions. The sintering kinetics have been studied by measuring the shrinkage of the compacts as a function of temperature. For a compact to be free of firing stresses it is necessary for the doped compositions to have a shrinkage curve very similar to that of base composition. Therefore it is necessary to obtain a complete shrinkage v/s temperature curve. This has been measured by firing the green sample in a 'Netsch Dilatometer'.

7.1.1. Measurement Method

A 'green' cylinder was prepared by using the procedure described in section 3.2.3.2 using a 10mm pressing die. Conditions of test were:

Atmosphere:	ambient
Maximum temperature at the sample:	1480°C
Firing schedule for furnace:	RT to 1500°C @ 5°C/min soaking 60 minutes 1500 to RT @5°C/min

Shrinkage data was collected automatically by a computer. The output was a graph of $^{\Delta L}/_{L}$ v/s temperature, where L is the green dimension of sample and ΔL is the change in dimension. This value is of shrinkage with respect to the green dimension. It was multiplied by the green dimension and then divided by the fired dimension to obtain a shrinkage value with respect to the fired dimension. This value was then plotted against temperature to generate a shrinkage curve

7.1.2. Shrinkage Data

The as received plot from the dilatometer data is shown in figure 7.1. The reference state is at the room temperature (point 'A'). As the temperature is raised, to ~ 1100°C, the compact expands, indicated by the negative shrinkage at point 'B'. This is due to the presence of the organic additives and air pockets in the compact which expand due to increase in temperature. Above this temperature the compact starts to sinter, and coagulation indicated by the increase in shrinkage is noticed (point 'C' onwards). The compact continues to shrink with increase in temperature, at a faster rate, till it reaches the ultimate possible density (point

'D'). Any increase in shrinkage with temperature beyond this will be reversible. The temperature at point 'D' is the sintering temperature of the compact. As the body is cooled from this state the shrinkage stays nearly the same reducing only marginally due to contraction on cooling ('F'), reaching the ultimate shrinkage at room temperature (at 'G').

A sudden drop in temperature by 100°C is noticed between 1425 to 1450°C (point 'H'). The data shows that exactly at 1426°C temperature drops to around 1350-1360°C and within a couple of minutes it rises back to original temperature. This temperature drop was noticed even when ZrO_2 was heated to above 1450°C in the dilatometer. This phenomenon does not seem to be taking place in most of the TiO_2 doped compositions (figure 7.2). However this is not the case since examination of the raw data in table 7.1 confirms that temperature does fall but since the graph has reached maximum shrinkage at this temperature, it is not visible in the plot. The phenomenon thus can be attributed to a dilatometer error.

Table 7.1

Base composition		1%TiO2		3%TiO2	
Temperature (°C)	Linear Shrinkage %	Temperature (°C)	Linear Shrinkage %	Temperature (°C)	Linear Shrinkage %
1421	12.55	1427	18.72	1418	19.46
1425	13.15	1427	18.77	1422	19.49
1429	13.74	1384	18.82	1426	19.53
1406	14.37	1352	18.86	1428	19.56
1366	14.98	1401	18.80	1389	19.63
1376	15.51	1447	18.74	1349	19.71
1419	15.94	1451	18.74	1396	19.68
1448	16.32	1454	18.74	1446	19.63
1451	16.67	1458	18.73	1451	19.65

The shrinkage plots, showing a comparison between the base composition and the TiO_2 doped compositions is shown in the figure 7.2. The final shrinkage for all the doped compositions is similar to that of the base composition. However the kinetics of sintering appear to be faster in most of the TiO_2 doped compositions

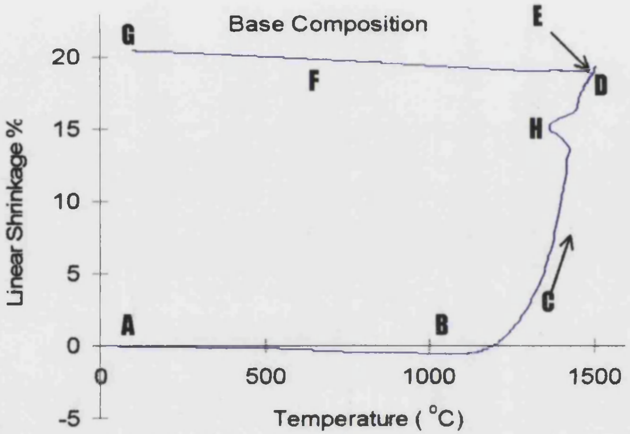

Figure 7.1: Shrinkage v/s temperature for base composition - as received data

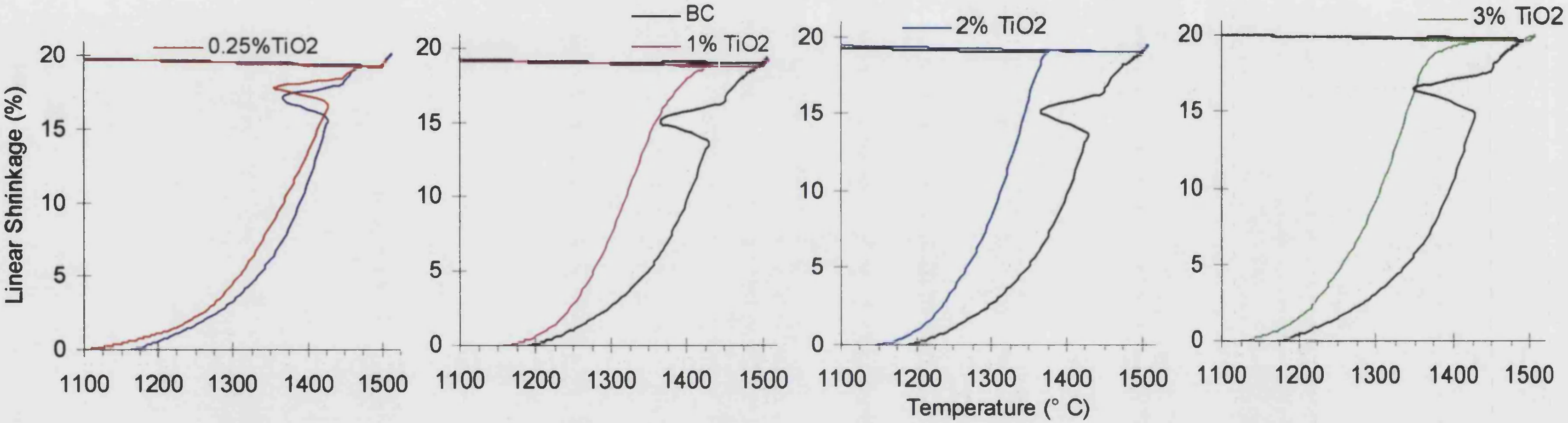

Figure 7.2: Shrinkage curves for different TiO_2 doped compositions compared with the base composition

when compared with the base composition. This can be explained on the basis of the work of Ikegami et al {158}, who reported that TiO_2 enhances densification in the initial and intermediate sintering stages of sintering. Addition of V_2O_5 to the composition makes the matters worse, as this composition has even higher kinetics than the composition doped with TiO_2 alone (figure 7.3). Addition of Cr_2O_3 does not have any affect on the sintering kinetics.

At this point an assumption is made that the increased kinetics is also a result of the increased volume fraction of glass phase in the doped composition as, unlike the base composition, the total percentage of alumina in the doped compositions has been reduced to less than 94%. On this basis, two compositions M1 and M4 are prepared where the percentage of alumina is held at 94% and compensation made for the TiO_2 addition by eliminating the MgO and CaO (M1) and reducing each component of the glass phase proportionately (M4). The sintering kinetics of the M1 composition is nearer to the base composition (figure 7.7), probably due to the increase in glass forming temperature in the absence of fluxes such as MgO and CaO. However this composition has a significantly lower density and also has a lower ultimate shrinkage, so is not useful. The proportionate decrease in glass volume fraction, i.e. maintaining the percent Al_2O_3 to 94, does not slow the sintering kinetics (figure 7.4).

The majority of these compositions could not form a direct gradient material with the base composition due to their very different sintering kinetics. The closest that could be obtained to successfully form the functional gradient material is the 0.25%TiO_2 composition. The effect is clearer on studying a compact of base composition with 1%TiO_2 + 0.5%V_2O_5, made by pressing and firing together the powders. From figure 7.5 its clear that this compact will have a difference in dimension from base composition end (A) to the doped end (B). More importantly cracks will be developed at the interface ‘C’ due to differential shrinkage. Radial cracks are seen on the surface (figure 7.6 (a)). On closer examination the crack is

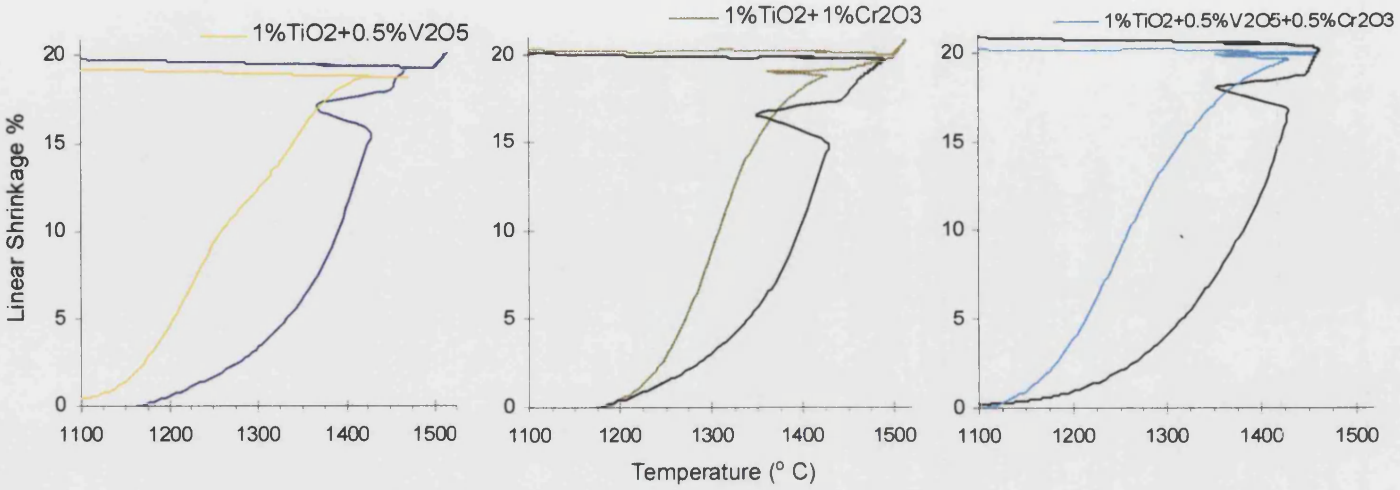

Figure 7.3: Comparison of Shrinkage curves for TiO_2 +V_2O_5 /Cr_2O_3 doped compositions with base composition

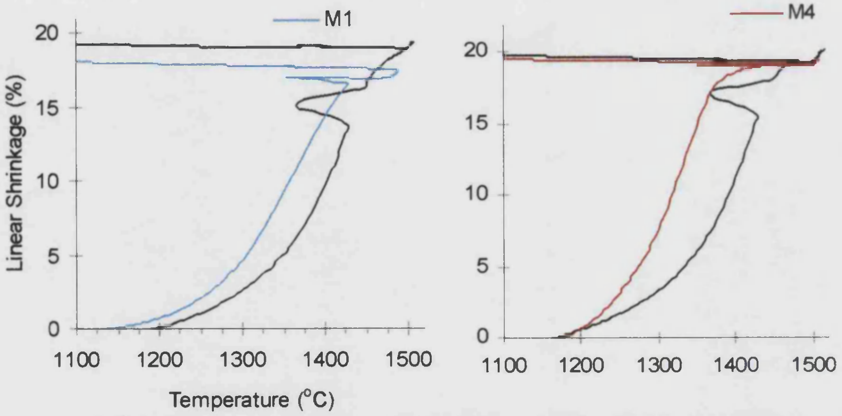

Figure 7.4: Comparison of Shrinkage curves for TiO_2 doped compositions with adjusted glass components

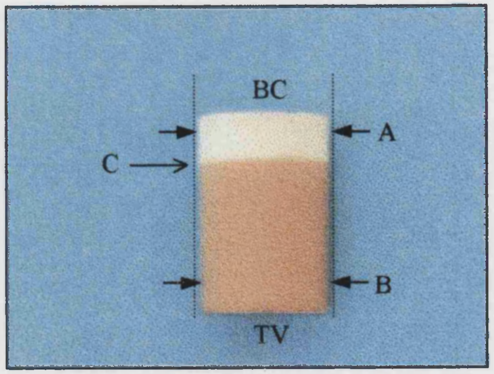

Figure 7.5: Pressing BC and 1%TiO_2 +0.5%V_2O_5 compact

fairly deep (figure 7.6(b)). However when this sample was sliced to look at the interface in the bulk, no such crack was visible (figure 7.7 (a)). The dark lines (figure 7.7 (b)) are the cutting marks. After cutting the samples were not polished as this removes any micro cracking. The crack free inner surface indicates that there is good compatibility between the two materials and if the shrinkage difference problem can be overcome, it would be possible to form a satisfactory functional gradient material.

To conclude this discussion it can be deduced that a single step pressed functional gradient material as in figure 7.4 is not practicable. Instead a multilayer compact may be worth trying. This will involve the first layer next to the base composition being 0.25%TiO_2, which may not develop stresses due to the small difference in its shrinkage to the BC. The next layer can be of 1%TiO_2 that has a shrinkage not very different from 0.25%TiO_2 and thus may not develop the stresses with the former. Similarly a layer of higher percentage TiO_2 can be build up successively till the required composition, say 3%TiO_2 is reached on the other surface. Thus though the total shrinkage difference between 3% TiO_2 and BC is large the relative difference between the individual layers is small enough not to cause any firing stresses and or cracking. However the dimensional difference will still exist between these layers, and a detailed programme of work will be necessary to find the solution. An alternate solution to the multilayer method could be incorporating TiO_2 at the surface. This should solve the problem of dimension difference between the base composition and TiO_2 rich end. Trials designed for this approach are discussed as follows.

7.2.Surface impregnation of TiO_2

The objective here was to impregnate sufficient TiO_2 into the surface to form a percolation path similar to the 3%TiO_2 composition, to get a lower resistivity surface. The first requirement for this was to prepare a solution of Ti based compound that could be painted on to the surface. The "paint" was prepared using

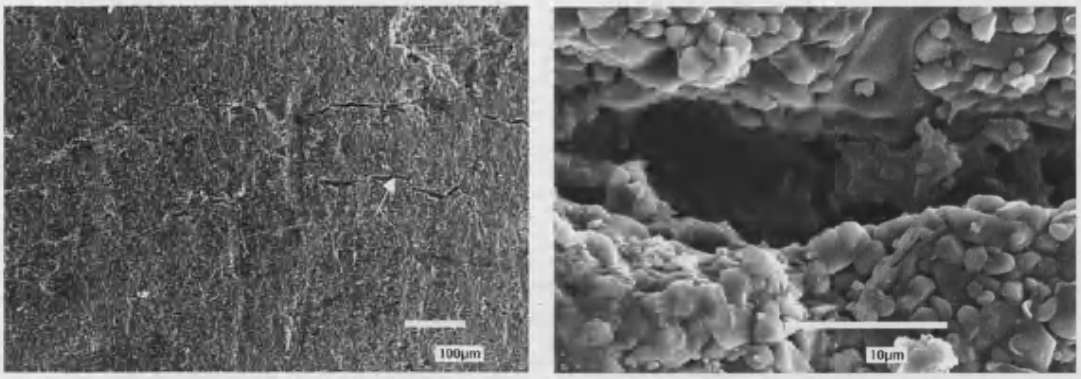

(a) (b)

Figure 7.6 : Cracks at the interface 'C' of figure 7.5-on surface

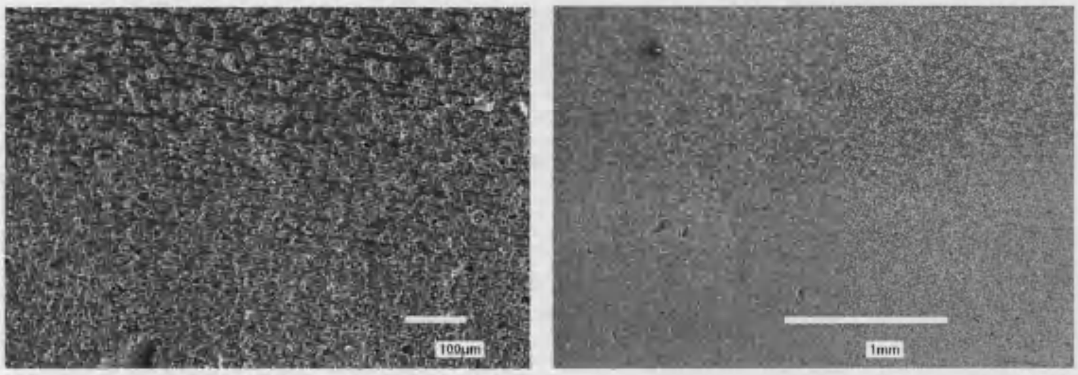

(a) (b)

Figure 7.7 (a): Interface 'C' of figure 7.5-in the bulk

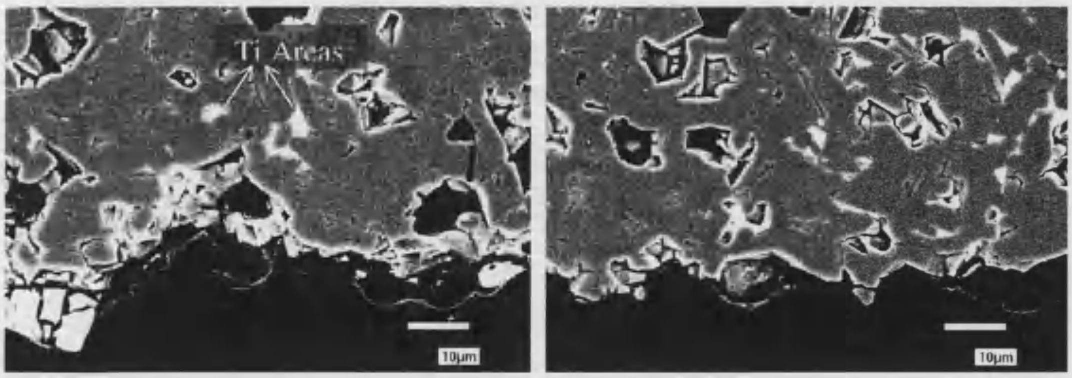

(a) (b)

Figure 7.8: Back Scattered image for surface impregnation of titanium ethoxide
(a) normal (b) vacuum impreganted

(a) titanium ethoxide ($Ti(OC_2H_5)_4$)
(b) titanium oxide in water
(c) titanium nitride in alcohol

The semi-fluid paint was coated on to a green compact. The compacts were fired as per the firing schedule of the base composition described in section 3.2.3.3. The compacts were cut along the thickness and polished to study the extent of Ti penetration into alumina. For the options (b) and (c), no Ti penetration was visible. However for titanium ethoxide a small amount of Ti did penetrate into the compact as shown in figure 7.8 (a). However the concentration of TiO_2 absorbed into the Al_2O_3 was too low to give the percolation effect of a 3%TiO_2 composition.

To improve the concentration, vacuum impregnation was tried. The green samples were evacuated (using rotary pump) for half an hour to remove any trapped air in the open pores. Then, with samples in vacuum, titanium ethoxide solution was poured into the petri-dish in which the green compact were lying. The samples were left in the solution with the vacuum running for about 15 minutes. They were then taken out and allowed to dry at room temperature for 24 hours. They were then fired and cut and polished as before. The result is as shown in figure 7.8(b). The quantity of TiO_2 absorbed has improved, though still not adequate enough to result in a percolation effect. Improvement in the absorption of TiO_2 into Al_2O_3 may be possible by using a pressure impregnation method. This would require design of an appropriate fixture and further detailed experiments.

For this part of the project the study is limited to this preliminary investigation. It is left to a future investigator to carry out more detailed work on development of a practical functional gradient material, its incorporation into the manufacturing process, and development of a method to test the resistivity across the composition gradient.

CHAPTER VIII

CONCLUSIONS

Suggestions for further work and conclusions to this project

8. CONCLUSIONS

8.1. Introduction

The main objective of taking up this work is to improve the performance of alumina insulators in the Super-Klystron environment. It has been established that alumina is the most popular material for applications involving high power, radio frequency and vacuum environment. Most of the competing materials used in high voltage applications do not have physical properties as good as alumina (Table 8.1). Furthermore, alumina with purity lower than 99% is a better choice due to its lower SEE coefficient (SEE = 4-5 at 1keV) than the ultra high purity or single crystal alumina (SEE = 6-8 at 1keV).

Table 8.1

Property Material	Tensile strength (MPa)	Thermal Conductivity (W/m°K)	Volume Resistivity (Ωcm)	Permittivity	tanδ (50-60hz)	Dielectric Strength (kV/mm)
Alumina*	190-300	22-39	>10^{14}	8-10	0.0001	25-35
Porcelain	30-100	1-4	10^{11}-10^{13}	5-7.5	0.02-0.04	10-20
Toughened Glass	100-120	1	10^{12}	7	0.015-0.05	>25
Polymer**	20-35	0.17-0.9	>10^{14}	2.3-5.5	0.0001-0.005	>25
RBGF***	2.1-2.2	0.2-1.2	10^{11}-10^{14}	2.5-6.5	0.005-0.02	3.0-20

*- *94-99.9%pure Al_2O_3*
**- *PTFE, silica filled epoxy and Silicon Elastomers, ethylene propylene diene monomer, and polyolefine filled with alumina trihydrate*
***- *Resin bonded Glass fibre*

However even the SEE yield of 4-5 is unacceptable for this application. Ways have been studied by various authors to reduce the SEE without affecting any of the physical properties. To enable this the first and foremost suggestion has been to lower the value of tanδ. This would require further studies into the improvement of microstructure, lowering of impurities especially the alkali metals and reduction in dislocation and point defects. The microstructure of alumina has been widely researched except for the liquid phase sintered, which has problems of abnormal grain growth and porosity. No one has yet been able to report a solution for improving the microstructure of liquid phase sintered alumina. A good microstructure will consist small size uniformly distributed alumina grains. However the insulators in the Super-Klystron application need to be metallized for formation of a hermetic bond with metal. The metallizing operation requires the alumina insulator to have a relatively large grain size. There is a need to carry out a modification to the metallizing process so that it can be carried out on a small grain ceramic.

The effect of additives such as TiO_2, which can help reduce the value of tanδ, have been studied and the past work needs to be integrated with the alumina used in this application. Reduction of defects would require linking the dislocation engineering to the charge localisation phenomena. The point defects that can cause an electron trapping and instant detrapping need further investigation.

However the proposed solution on which this project was undertaken is the modification of the insulator surface, provided there is the property gradient from the surface to the bulk, in order to prevent the development of an interface that might cause electron trapping. The idea was to have an additive at the surface that can generate a higher number of electrons, so as to increase the surface conductivity without affecting the bulk. A mechanism to bleed the increased charge to ground can be developed thereby reducing the change of electrical breakdown.

8.2. Conclusion to this Project

The dopants identified for this purpose were the TiO_2, V_2O_5 and Cr_2O_3. The controlled addition of these dopants to the base composition was carried out and their affect on the resistivity and the reasons thereof were studied. The base composition was designed based on the study on a sample of the 94%Al_2O_3 insulator from Seagoe. It can be said that the base composition was very close to the Seagoe insulator in terms of its density, porosity and grain structure. The flexural strength was very close to the values reported in literature for this material. The difference between their grain size however can be ignored in this project, as the study involves the relative difference in the resistivity values of various compositions with doping to the same base composition. Much of the variation in composition is taken up in the glass phase.

The effect of dopants on the resistivity of the base composition is as given below:

As-Fired Sample

- The base composition had a resistivity of >10^{14} Ω-cm, due to the high resistivity of alumina grains.
- Addition of 0.25%TiO_2 resulted in a resistivity decrease of ~10^2 Ω-cm, due to the TiO_2 dissolving into the Al_2O_3 grains. However this was the saturation limit for the resistivity as also for the limit for the dissolution of TiO_2 in the Al_2O_3 grain.
- 3%TiO_2 had a slightly higher resistivity than other TiO_2 doped compositions. This was considered due to the TiO_2 precipitates becoming inter-connected and probably breaking a conduction path between the Al_2O_3 grains.
- TiO_2 /Cr_2O_3 doping does not significantly affect the electrical resistivity
- Adding 0.5%V_2O_5 to TiO_2 doped alumina does reduce resistivity by 10^3 Ω-cm. This is in line with earlier work on resistivity increase in Ti^{4+} due to V^{5+}, as the microstructural investigation in this work had shown both the additives present at the same spot in the Al_2O_3 network.
- Removal of MgO and CaO from the glass phase also reduces the resistivity by 3 orders of magnitude due to the generation of a small grain size. However this composition is not suitable due to its poor physical properties

H_2 Annealing the Fired Samples

- 3%TiO_2 composition had a significant decrease in resistivity reaching a value of ~10^5 Ω-cm at room temperature and 1000 Ω-cm at 300°C. This was due to the TiO_2 reducing to semiconducting Ti^{3+} and the conduction path shifting from Al_2O_3 grains to the interconnected Ti rich precipitates. It is suggested that this was because the Ti precipitates reaching a percolation threshold, a value of 24% in 2D, in this study. The DC and AC conductivity tests indicated that the conductivity is due to mixed conduction i.e. both ionic and electronic carriers are operative.
- Similar results were also obtained for the 3%TiO_2 + 0.5%V_2O_5 composition. However, probably due to reduced V^{5+} to V^{3+}, it had slightly higher resistivity than the 3%TiO_2 composition.
- At 4%TiO_2 this percolation is broken due to the agglomeration of TiO_2 rich areas. The reasons for the agglomeration have been suggested as:

(a) the coagulation of TiO_2 at higher concentration
(b) the formation of compounds, such as Al_2TiO_5 and rutile, that require larger quantity of TiO_2 than the compounds in 3%TiO_2 composition, such as $MgTiO_5$, that require lesser concentration of TiO_2 and promoting greater distribution of TiO_2 rich phase.

- Re-percolation of TiO_2 agglomerates at 10%TiO_2 addition again resulted in a sharp decrease in resistivity, to reach 10^7 Ω-cm at room temperature and ~10^5 Ω-cm at 300°C.

Thus to achieve the desired results of low resistivity, the fired alumina ceramic sample will have to go through annealing in H_2 atmosphere. Nevertheless H_2 annealing would not necessarily have to be introduced as an additional step in the insulator manufacture. This is because as a part of normal manufacturing operation, H_2 firing is carried out on these insulators for metallizing purpose. This operation is necessary for any insulator used in the Klystron or other microwave applications and the reduction in resistance would take place accordingly.

The only additional process involved is the preparation of a functional gradient material. A preliminary investigation on the feasibility of making a bond between the base composition and TiO_2 doped composition has been carried out in this project. It has been demonstrated that it is feasible to form a functional gradient material.

APPENDIX

&

REFERENCES

Appendix A

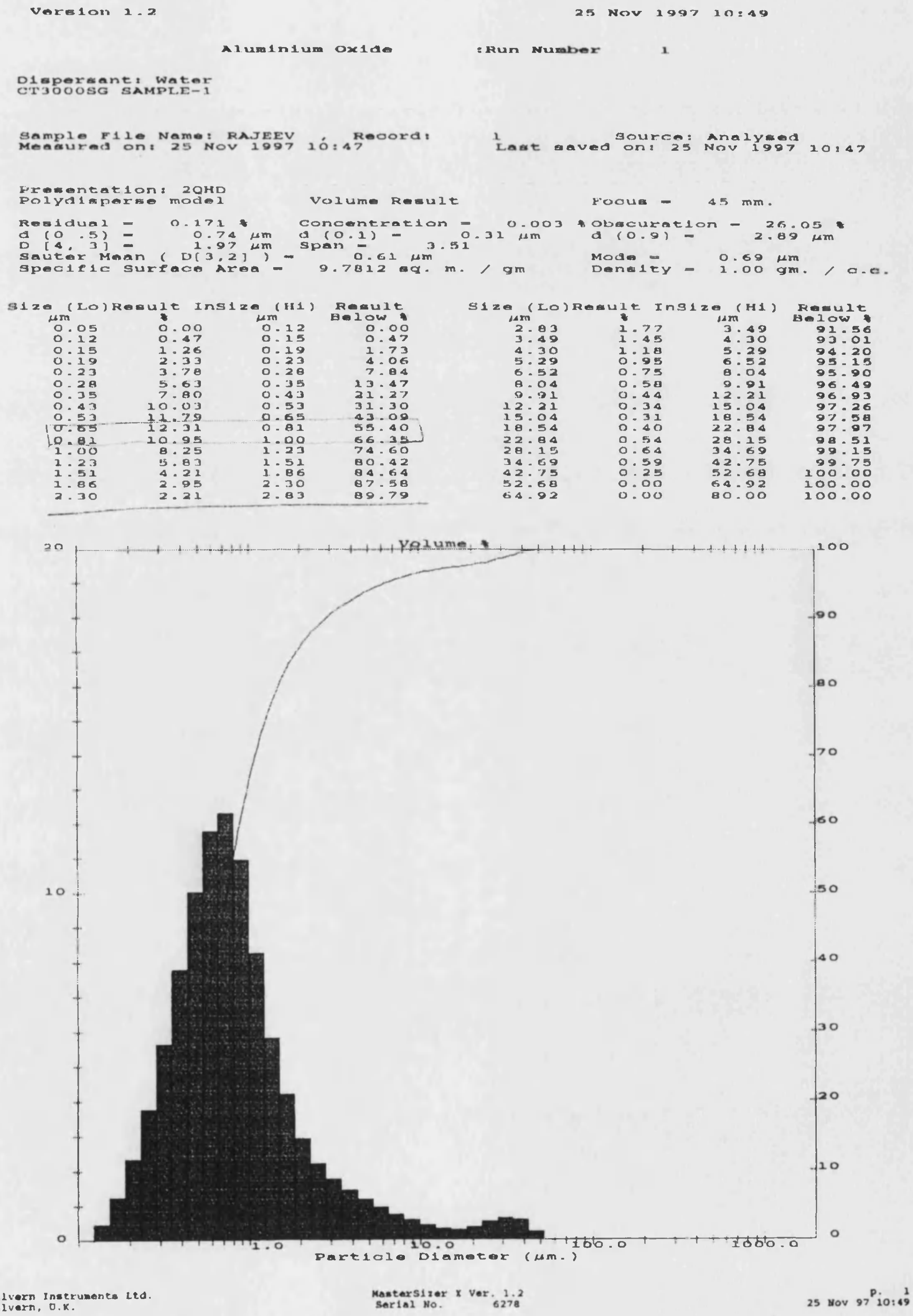

```
  Version 1.2                                              25 Nov 1997 10:49

                   Aluminium Oxide          :Run Number      1

 Dispersant: Water
 CT3000SG SAMPLE-1

 Sample File Name: RAJEEV    ,   Record:       1           Source: Analysed
 Measured on: 25 Nov 1997 10:47               Last saved on: 25 Nov 1997 10:47

 Presentation: 2QHD
 Polydisperse model          Volume Result               Focus =    45 mm.

 Residual =     0.171 %     Concentration =    0.003 %Obscuration =  26.05 %
 d (0 .5) =        0.74 µm  d (0.1) =       0.31 µm    d (0.9) =       2.89 µm
 D [4, 3] =        1.97 µm  Span =        3.51
 Sauter Mean ( D[3,2] ) =        0.61 µm               Mode =        0.69 µm
 Specific Surface Area =   9.7812 sq. m. / gm          Density =  1.00 gm. / c.c.

Size (Lo)Result InSize (Hi)  Result        Size (Lo)Result InSize (Hi)  Result
   µm          %          µm     Below %          µm          %          µm     Below %
   0.05      0.00       0.12      0.00           2.83       1.77       3.49     91.56
   0.12      0.47       0.15      0.47           3.49       1.45       4.30     93.01
   0.15      1.26       0.19      1.73           4.30       1.18       5.29     94.20
   0.19      2.33       0.23      4.06           5.29       0.95       6.52     95.15
   0.23      3.78       0.28      7.84           6.52       0.75       8.04     95.90
   0.28      5.63       0.35     13.47           8.04       0.58       9.91     96.49
   0.35      7.80       0.43     21.27           9.91       0.44      12.21     96.93
   0.43     10.03       0.53     31.30          12.21       0.34      15.04     97.26
   0.53     11.79       0.65     43.09          15.04       0.31      18.54     97.58
   0.65     12.31       0.81     55.40          18.54       0.40      22.84     97.97
   0.81     10.95       1.00     66.35          22.84       0.54      28.15     98.51
   1.00      8.25       1.23     74.60          28.15       0.64      34.69     99.15
   1.23      5.83       1.51     80.42          34.69       0.59      42.75     99.75
   1.51      4.21       1.86     84.64          42.75       0.25      52.68    100.00
   1.86      2.95       2.30     87.58          52.68       0.00      64.92    100.00
   2.30      2.21       2.83     89.79          64.92       0.00      80.00    100.00
```

```
Malvern Instruments Ltd.             MasterSizer X Ver. 1.2                     P.  1
Malvern, U.K.                        Serial No.     6278              25 Nov 97 10:49
```

Appendix B

XRD Data for Titanium Oxide Powder

```
Philips Analytical                              PC-APD, Diffraction software

                        Start angle [°2θ]:   5.005
                          End angle [°2θ]:  89.985
                          Step size [°2θ]:   0.010
                        Maximum intensity: 812.2500
                        Time per step [s]:   0.400
                             Type of scan: CONTINUOUS

                 Peak positions defined by: Top of smoothed peak
                    Minimum peak tip width:    0.10
                    Maximum peak tip width:    1.00
                           Peak base width:    2.00
                      Minimum significance:    1.00
                           Number of peaks:      29


   Angle  d-value  d-value  Peak width  Peak int  Back. int  Rel. int  Signif.
   [°2θ]  α1  [Å]  α2  [Å]    [°2θ]     [counts]  [counts]     [%]

  16.895   5.2436   5.2565    0.480          1          3       0.1      1.10
  25.275   3.5209   3.5295    0.100        590          3      72.7      1.96
  25.405   3.5031   3.5118    0.180        812          3     100.0     18.52
  27.510   3.2397   3.2476    0.200         22          3       2.7      2.46
  36.160   2.4821   2.4882    0.240         10          3       1.3      2.39
  37.025   2.4261   2.4320    0.120         61          2       7.5      1.77
  37.895   2.3723   2.3782    0.140        234          2      28.8      4.93
  38.655   2.3274   2.3331    0.280         74          2       9.1      9.21
  41.285   2.1850   2.1904    0.240          6          2       0.8      2.36
  43.265   2.0895   2.0946    0.240          2          2       0.3      1.64
  44.685   2.0263   2.0313    0.240         12          2       1.5      2.18
  48.125   1.8892   1.8939    0.200        372          3      45.9     14.76
  53.955   1.6980   1.7022    0.100        237          3      29.2      2.79
  55.145   1.6642   1.6683    0.160        216          3      26.6      6.99
  56.675   1.6228   1.6268    0.160          6          3       0.8      1.66
  62.170   1.4919   1.4956    0.120         38          2       4.7      5.25
  62.755   1.4794   1.4831    0.140        169          2      20.8      4.23
  64.145   1.4507   1.4542    0.240          3          2       0.4      1.16
  65.070   1.4323   1.4358    0.480          2          2       0.2      1.07
  68.815   1.3632   1.3665    0.180         74          2       9.1      4.88
  69.025   1.3595   1.3629    0.120         44          2       5.4      1.44

  70.335   1.3374   1.3407    0.140         81          2      10.0      3.91
  70.545   1.3339   1.3372    0.100         44          2       5.4      1.24
  74.175   1.2774   1.2805    0.320          6          2       0.7      1.24
  75.100   1.2639   1.2670    0.200        114          2      14.1      9.44
  75.335   1.2606   1.2637    0.120         58          2       7.1      2.35
  76.090   1.2499   1.2530    0.160         30          2       3.7      1.83
  80.820   1.1883   1.1912    0.240          4          2       0.5      1.80
  82.715   1.1658   1.1687    0.140         53          2       6.6      2.97
```

Appendix C

Calculation of Conductivity and Permitivity from Impedance results

Assume a fitting an impedance result into a simple RC network as below.

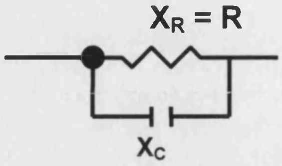

For impedance semi-circle

$$X_C = \frac{1}{i\omega C}$$

$$Z^* = \frac{X_R X_C}{X_R + X_C} = \frac{R}{i\omega CR + 1}$$

$$= \frac{R(1 - i\omega CR)}{1 + \omega^2 C^2 R^2}$$

$\omega = 2\pi f$, f = ac frequency

Z^* is a complex impedance function and in terms of real (Z') and imaginary (Z'') impedance is given by the equation:

$$Z' + iZ'' = \frac{R}{1 + \omega^2 C^2 R^2} - i\frac{\omega C R^2}{1 + \omega^2 C^2 R^2}$$

Thus

$$Z' = \frac{R}{1 + \omega^2 C^2 R^2}$$

$$Z'' = -\frac{\omega C R^2}{1 + \omega^2 C^2 R^2}$$

Then

$$Z'^2 + Z''^2 = \frac{R^2 + (\omega C R^2)^2}{(1 + \omega^2 C^2 R^2)^2} = \frac{R^2}{1 + \omega^2 C^2 R^2} = R \times Z'$$

$\therefore \rho = \frac{Z'^2 + Z''^2}{Z'} \frac{A}{\ell}$ where ρ is the resistivity, A is the area of crossection of sample and ℓ is the thickness.

Conductivity then is given by:

$$\sigma = \frac{Z'}{Z'^2 + Z''^2}\frac{\ell}{A}$$

Since capacitance:

$$C = \frac{\varepsilon_r \varepsilon_0 A}{\ell}$$

where ε_r is the relative permitivity and ε_0 is the permitivity of vacuum

$$\varepsilon_r = \frac{C}{\varepsilon_0}\frac{\ell}{A}$$

$$Z'^2 + Z''^2 = \frac{R^2}{1 + \omega^2 C^2 R^2}$$

$$\frac{Z''}{Z'^2 + Z''^2} = \frac{1 + \omega^2 C^2 R^2}{R^2}\frac{-\omega C R^2}{1 + \omega^2 C^2 R^2}$$

$$C = -\frac{Z''}{Z'^2 + Z''^2}\frac{1}{\omega}$$

$$\varepsilon_r = -\frac{Z''}{Z'^2 + Z''^2}\frac{1}{\omega}\frac{1}{\varepsilon_0}\frac{\ell}{A}$$

REFERENCES

{1} Private communication with Prof. R. Stevens.

{2} Vlieks, A.E., Allen, M.A., Callin, R.S., Fowkes, W.R., Hoyt, E.W., Lebacqz, J.V.,and Lee, T.G.; Breakdown phenomena in high power Klystrons; IEEE Transactions on Electrical Insulation 1989, Vol.24, No.6, pp1023-28

{3} Saito, Y.; Surface Breakdown Phenomena in Alumina rf Windows; IEEE Transactions on Dielectrics and electrical insulation, 1995, Vol.2, No.2, pp.243-50

{4} Watanabe, T., Kitabayashi, T., Nakayama, C.; Electrostatic force and absorption current Of Alumina Electrostatic Chuck; Japanese Journal of Applied Physics Part 1-Regular Papers Short Notes & Review Papers, 1992, Vol.31, No.7, pp.2145-2150

{5} Jardin, C., Durupt, P., Robert, D., Michel, P., and Gressus, Le; Behaviour of α-Al_2O_3 Insulator surfaces under electron Irradiation; Journal of Materials Science, 1991, Vol. 26, pp3019-24

{6} Saito, Y., Matuda, N., Anami, S., Baba, H., Kinbara, A. and Horikoshi; G.; Breakdown of Alumina rf Window; Rev. Science. Instrum., Vol. 60, pp. 1736-39, 1989

{7} Saito, Y.; Surface Breakdown Phenomena in Alumina rf Windows; IEEE Transactions on Dielectrics and electrical insulation, 1995, Vol.2, No.2, pp.243-50

{8} Lee, K.H. and Crawford Jr, J.H.; luminescence of the F-Centre in Sapphire; Physical Review, 1979, Vol. B19, pp 3217-3221

{9} Michizono, S., Saito, Y., Yamaguchi, S., Anami, S., Matuda, N., and Kinbara, A.; Dielectric materials for use as output window in high-power Klystrons; IEEE Transactions on Electrical Insulation, 1993, Vol.28, No.4, pp.692-699

{10} Vallayer, J., Treheux, D.; Electromagnetic radiation effect on Sapphire charge trapping Properties; Proceedings Third International Conference on Electric Charge, 1998, pp 527-530

{11} Saito, Y., Yamaguchi, S., Anami, S., Matuda, N., Kinbara, A., Horikoshi, J., and Tanaka, J.; Breakdown of Alumina Rf Windows; IEEE Transactions on Electrical Insulation, 1989, Vol.24, pp.692-699

{12} Michizono, S., Saito, Y., Fukuda, S., Hayashi, K., and Anami, S.; RF windows used at S-band pulsed klystrons in the KEK Linac; Vacuum, 1996, Vol.47, No.6-8, pp.625-628

{13} Saito, Y., Matuda, N., Anami, S., Baba, H., Kinbara, A., Horikoshi, G., and Tanaka, J.; Breakdown of Alumina RF Windows; IEEE Transactions on Electrical Insulation, 1989, Vol.24, pp.1029-32

{14} Saito, Y., Michizono, S., Anami, S., and Kobayashi, S.; surface flashover on alumina RF windows for high-power use; IEEE Transactions on Electrical Insulation, 1993, Vol.28, No.4, pp.566-573

{15} Asokan, T. and Sudarshan, T.S.; Dependence of the surface flashover properties of Alumina on the polishing abrasive parameters; IEEE Transactions on Electrical Insulation, 1993, Vol.28, pp535-44

{16} Gressus, C.Le, Maire, Ph, and Duraud, J.P.; The influence of surface phenomena on the initiation of Discharge in Vacuum; IEEE Transactions On Electrical Insulation, 1989, Vol.24, pp.967-77

{17} Stoneham, A.M.; Linking the Atomic-Scale Processes to degradation and Breakdown: Energy localisation and Charge Localisation; Proceedings Third International Conference on Electric Charge, 1998, pp 1-9

{18} Martinez L., Durand, A.J. and Jardin, C.; Alumina Klystron Window Characterisation; Proceedings Third International Conference on Electric Charge, 1998, pp 562-566

{19} Saito, Y., Michizono, S., Sato, T., Kobayashi, S., Jardin, C.; Annealing Effects of Secondary Emission and Charging of Alumina Ceramics, Proceedings Third International Conference on Electric Charge, 1998, pp 382-90

{20} Blaise, G. and Legressus, C.; Charging and flashover induced by Surface Polarisation and Relaxation Process; Journal of Applied Physics, 1991, Vol. 69, No.9, pp 6334-9

{21} Sudarshan, T.S., and Cros, J. D.; The effect of chromium oxide coatings on surface flashover of Alumina spacers in vacuum; IEEE Transactions On Electrical Insulation, 1976, Vol.EI-11, pp.32-5

{22} Michizono, S., Kinbara, A., Saito, Y., Yamaguchi, S., Anami, S., Matuda, N.; TiN film coatings on Al_2O_3 Radiation Frequency window; Journal of Vacuum Science. and Technology A-Vacuum Surfaces and Films, 1992, Vol. 10, No.4 Pt1, pp 1180-1184

{23} Nyaiesh, A.R., Garwin, E.L., King, F.K., and Kirby, R.E.; Properties of thin multipactor TiN and Cr_2O_3 coatings for klystron widows; Journal of Vacuum Science and Technology, 1986, Vol.A4, No.5, pp2356-63

{24} Miller, H.C. and Furno, G.A.; The effect of Mn/Ti surface treatment on voltage-hold-off performance of alumina insulators in vacuum; Journal of Applied Physics, 1978, Vol.49, pp 5416-20

{25} Miller, H.C.; Improving the voltage hold-off performance of alumina insulators in vacuum through quasi-metallizing; IEEE Transactions on Electrical Insulation, 1980, Vol.EI-15, No.5, pp 419-28

{26} Anderson, R.A. and Brainard, J.P.; Mechanism of pulsed surface Flashover involving electron stimulated desoption; Journal of Applied Physics, 1980, Vol. 51, pp 1414-21

{27} DeTourreil, C.H. and Srivastava, K.D.; Mechanisms of surface charging of high-voltage insulators in vacuum; IEEE Transactions on Electrical Insulation, 1973, Vol. EI-8, pp 17-21

{28} Heldt, K. & Haase, G., Electrical Resistance of pure, Vacuum Sintered Aluminium Oxide, Z. Angew. Phys.; 1954, Vol. 6, No. 4, pp 157-60,

{29} F.A. Kroger in Advances in Ceramics, Vol 10, Edited by W.D. Kingery, Published by American Ceramic Society, Westerville, OH, 1984, p 1

{30} Wang, C.C., Akbar, S.A., Chen, w., and Patton, V.D.; Electrical-properties of high-temperature oxides, borides, carbides and nitrides; Journal of Materials Science, 1995, Vol. 30, No.7, pp 1627-41

{31} Tiku, S.K. and Kröger, F.A.; Energy levels of Donor and Acceptor Dopants and electronic and hole mobility in α-Al_2O_3 ;Journal of American Ceramic Society; 1980, Vol. 63, No. 1-2, pp 31-32

{32} Dutt, B.V., Hurrell, J.V., and Kröger, F.A.; High Temperature Defect Structure of Cobalt doped α-Al_2O_3 ; Journal of American Ceramic Society, 1975,Vol. 58, pp 421

{33} Dörre, E. and Hübner, H.;Alumina, Processing, properties and Applications; Materials Research and Engineering, ,Publ. by Springer-Verlag, 1984.

{34} Tiku, S.K. and Kröger, F.A.; Energy levels of Donor and Acceptor Dopants and electronic and hole mobility in α-Al_2O_3; Journal of American Ceramic Society , 1980, Vol. 63, No. 1-2, pp 31-32

{35} ASTM Standard ASTM - D 1829-66

{36} Petot-Ervas, G., Deweirder, D., Loudjani, M., Lesage, B. and Huntz, A. M. , The influence of microstructure on the transport properties of yttrium doped alumina, Advances in Ceramic, 1987, Vol. 23, pp 125-35

{37} J.P. Loup and A.M. Anthony, Influence, Starting from 1500°C, of Thermionic Emission on the measurement of resistivity of Oxides, Rev. Hautes Temp Refract., 1964, Vol. 1, No.1, pp 15-20

{38} Brook, R.J., Yee, J. and Kröger, F.A.; Electrochemical Cells and Electrical conduction od pure and doped Al_2O_3; Journal of American Ceramic Society, 1971, Vol. 54, No. 9, pp 444-51,

{39} Peters, D.W., Feinstein, L. and Peltzer, C.; On the high temperature conductivity of alumina; Journal of Chemical Physics, 1965, Vol.42, pp 2345-46

{40} Özkan, O.T. and Moulson, A.J.; The Electrical Conductivity of Single crystal and Polycrystalline Aluminium Oxide; British Journal of Applied Physics-D, 1970, Vol. 3, pp 983-87

{41} Moulson, A.J. and Popper, P; Problems associated with the measurement of volume resistivity of insulating ceramics at high temperature; Proceedings of the British Ceramic Society, Electrical and Magnetic Ceramics, No.10, March, 1968, pp 41

{42} Kitzawa, K. and Coble, R.L.; Electrical conduction in single crystal and Polycrystalline Al_2O_3 at High Temperatures; Journal of American Ceramic Society , 1974, Vol. 57, No. 6, pp 245-50

{43} S.P. Mitoff, Bulk Verses Surface Conductivity of MgO Crystals, Journal of Chemical Physics, 1964, Vol.41, No.8, pp 2561-62,

{44} Harmer, M.P. and Brook, R.J.; Effect of MgO additions on the kinetics of Hot pressing in Al_2O_3; Journal of Materials Science, 1980, Vol.15, pp 3017

{45} Will, F.G. and Janora, K.H. , Minimisation of Parasitic currents in High Temperature Conductivity measurements in High-resistivity Insulators, Journal of American Ceramic Society; 1992, Vol. 75, No. 10, pp 2795-802

{46} Pappis, J.; and Kingery, W.D.; Electrical properties of single crystal and polycrystalline alumina at high temperatures; Journal of American Ceramic Society, 1961, Vol. 44, No. 9, pp 459-64

{47} Kizilyalli, H.M., and Mason , P.R., DC and AC electrical conduction in single crystal alumina., Physica Status Solidi, 1976, Vol.36, No.2, pp 499-508

{48} Cohen ,J., Electrical conductivity of alumina, American Ceramic Society Bulletin, 1959, Vol.38, No. 9, pp 441-46

{49} Kröger, F.A.; Defect related properties in Doped Alumina; Solid State Ionics, 1984, Vol. 12, pp189-99

{50} Tsaur, J.M. and Kröger, F.A.; Electrical conductivity and Creep of polycrystalline α-Al_2O_3 doped with titanium or iron plus titanium; Journal of Materials Science, 1987, Vol.22, pp 2332-40

{51} Harrop, P.J.and Creamer, R.H.; High temperature electrical conductivity of Single-Crystal Alumina; British Journal of Applied Physics, 1963, Vol. 14, No. 6, pp335-39

{52} Geschwind, S. and Remeika, J.P.; Journal of Applied Physics, 1962, Vol.33, 370

{53} Lloyd, I.K., Pollock, T.M. and Bowen, H.K.; Conductivity of Iron doped polycrystalline alumina at high temperatures; Journal of American Ceramic Society, 1984, Vol. 67, No. 12, pp 810-14

{54} Yee, J. and Kröger, F.A.; Measurement of electromotive force in Al_2O_3 -Pitfalls and results; Journal of American Ceramic Society , 1973, Vol. 56, No.4 , pp 189-91

{55} Matsumura, T, The Electrical Properties of Alumina at High Temperature,. Canadian Journal of Physics, 1966, Vol. 44, pp 1685-98

{56} Hartmann, W. , Electrical Investigation of Oxide Semiconductors, Z.Physik, 1936, Vol.102, No.11/12, pp 709-33,

{57} Dutt, B.V., Hurrell J.P., and Kröger, F.A.; Electrical conduction in single crystal and polycrystalline alumina at high temperatures; Journal of American Ceramic Society, 1974, Vol. 57, pp 245-50.

{58} W.J. Lackey, Effect of temperature on the electrical conductivity and Transport mechanisms in Sapphire, Materials Science Research; 1971, Vol. 5, pp 489-91

{59} Will, F.G., deLorenzi, H.G. and Janora, K.H.; Conduction mechanism of Single Crystal Alumina; Journal of American Ceramic Society, 1992, Vol.75, No.2, pp 295-304,

{60} Miranzo, P., Tabernero, L , Moya, J.S.and Jurado, J.R.; Effect of Sintering Atmosphere on the densification and electrical Properties of Alumina; Journal of American Ceramic Society; 1990, Vol.73, No. 7, pp 2119-21,

{61} Paladino, A.E. and Kingery W.D., Aluminium ion Diffusion in Aluminium oxide; Journal of Chemical Physics, 1962, Vol.37, pp 957

{62} Oishi, Y. and Kingery, W.D.; Self diffusion of Oxygen in single crystal and polycrystalline Al_2O_3; Journal of Chemical Physics, 1960, Vol. 33, No.2, pp 480-86

{63} Y. Oishi, K. Ando and Y. Kubota; Self-diffusion of oxygen in single crystal alumina; Journal of Chemical Physics; 1980, Vol.73, No. 3, pp 1410-12

{64} El-Aiat, MM, Hou, L.D., Tiku, S.K., Wang, H.A. and Kröger, F.A.; High Temperature Conductivity and Creep of Polycrystalline Al_2O_3 doped with Fe and /or Ti; Journal of American Ceramic Society, 1981, Vol. 64, No.3, pp 174-82

{65} Mill, J.J., Non-stoichiometric defects in sapphire, Journal of .Physics and Chemistry of Solids, 1970, Vol. 31, pp2577-70

{66} Champion, J.A., Electrical conductivity of Sapphire and Ruby crystals, Proceedings of the British Ceramic Society, 1968, Vol 10, pp 51

{67} Dasgupta, S., Hart, J., Themoelectric Power of Sapphire Single Crystals, British Journal of Applied Physics, 1965, Vol.16, pp 725

{68} Peters, D.W.; Thermoelectric Power of single crystal Aluminium Oxide; J. Phys. Chem. Solids, 27,1560, 1966

{69} Stulov, G M. and Shalabutov, Y.K.; Investigations of the electrical and Optical Properties of Synthetic Sapphire at High Temperatures; Sov Phys; 1968, Vol.1, pp 996

{70} Dasgupta, S., Hall effect and Magneto-resistance of alumina single crystals, Journal of Applied Physics. D. App Phys, 1975, Vol. 8, pp 1822

{71} Hughes, R.C.; Generation Transport and Trapping of Excess Charge carriers in Czochralski-Grown Sapphire; Physics Review, B, 1979, Vol. 19, pp 5318

{72} Mohapatra, S.K. and Kröger,F.A., The dominant Type of Disorder in α-Al_2O_3 , Journal of American Ceramic Society, 1978, Vol.61 No.3-4, pp 106-9

{73} Kingery, W.D., Bowen, H.K., and Uhlmann, D.R.; Introduction to Ceramics; Chapter 17-18 , pp 913-974, John & sons Inc, New York

{74} Hou, L.D., Tiku, S.K., Wang, H.A., and Kröger, F.A.; Conductivity and creep in acceptor dominated polycrystalline alumina; Journal of Materials Science, 1979, Vol. 14, pp 1877-8

{75} Barta R., Bartuska, M., Hlavac, J. and Prochazka, S., Electrical Resistance of Sintered alumina. Silikaty, 1957, Vol.1, No.1, pp: 77-83

{76} Tiku, S.K. and Kröger, F.A.; Effects of Space Charge, Grain boundary Segregation and mobility differences between grain boundary and bulk on the Conductivity of Polycrystalline Al_2O_3; Journal of American Ceramic Society, 1980, Vol. 63, No. 3-4, pp 183-189

{77} H.L. Tuller, Nonstoichiometric Oxides , edited by O.T.Sørensen, Published by Academic Press, New York 1981, p271

{78} Deleauney, D., Huntz, A.M. and Lacombe, P., The influence of Yttrium in Sintering of Al_2O_3 , Journal of Less Common Materials, 1980, Vol.70, No.1, pp 115-17

{79} El-aiat, M.M. and Kröger, F.A.; Yttrium as iso-electric donor in α-Al_2O_3; Journal of American Ceramic Society, 1982, Vol.65, No. 6, pp 280-85

{80} Mohapatra, S.K and Kröger, F.A.; Defect Structure of α-Al_2O_3 doped with Ti, Journal of American Ceramic Society, 1977, Vol. 60, No. 9-10, pp 381-87

{81} Lessing, P.A. and Gordon, R.S.; Creep of Polycrystalline Alumina, pure and doped with Transition Metal impurities; Journal of Materials Science, 1977, Vol. 12, pp 2291

{82} Vest R.W., Electrical Behaviour of Refractory Oxides, AD-255079, 8pp.illus.; US Government Research Reports, 1961, Vol.36, No.1, pp 64,

{83} G.W. Hollenber and R.S. Gordon, Effect of Oxygen Partial Pressure on the Creep of Polycrystalline Al_2O_3 Doped with Cr, Fe and Ti, Journal of American Ceramic Society, 1973, Vol. 56, No.3, pp 140-47

{84} S.K. Mohapatra, S.K. Tikku and F.A. Kröger, The defect structure of unintentionally doped α-Al_2O_3 crystals, Journal of American Ceramic Society, 62, 1-2, 1979, 50-57

{85} Dienes, G. J., Welch, D.O. , Fishcer, C.R. , Hatcher, R.D., Lazareth, O. and Samberg, M.; Shell Model Calculations of some Point-Defect Properties in α-Al_2O_3 , Phys Rev. B, 1975, Vol. 11 No.8, pp 3060-70,

{86} Hammer, M., Roberts, E.W. and Brook, R.J.; Rapid Sintering of pure and doped α-Al_2O_3; Transactions and Journal of the British Ceramic Society, 1979, Vol. 78, pp 22-25

{87} Kröger, F.A.; Defect Models for Sintering and Densification of Al_2O_3:Ti and Al_2O_3:Zr; Journal of American Ceramic Society , 1984, Vol. 67, No. 6, pp 390-92

{88} Lee, C.H. and Kröger, F.A.; Electrical conductivity of polycrystalline Al_2O_3 doped Silicon; Journal of American Ceramic Society, 1985, Vol.68, No. 2, pp 92-99

{89} Brook, R.J.; Effect of TiO_2 on initial Sintering of Al_2O_3; Journal of American Ceramic Society, 1972, Vol. 55, No.2, pp 114-5,

{90} Mohapatra, S.K and Kröger F.A.; Defect Structure of α-Al_2O_3 doped with Magnesium; Journal of American Ceramic Society, 1977, Vol. 60, No. 9-10, pp 141-8

{91} Molla, J., Moreno, R. and Ibarra, A.; Effect of Mg doping on dielectric properties of alumina; Journal of Applied Physics, 1996, Vol.80, No.2, pp.1028-1032

{92} H.A. Wang, C.H. Lee and F.A. Kröger, Point defects in α-Al_2O_3:Mg studied by electrical conductivity, optical absorption and ESR, Physical Review B, 1983, Vol.27, No.6, pp 3821-41

{93} M.M. El-Aiat and F.A. Kröger, Hydrogen donors in α-Al_2O_3, Journal of Applied Physics, 1982, Vol.53, No.5, pp 3658-67

{94} Ahmed, A.S. Gontier-Moya, E.G.; On the Effect of dopants on the Charging Properties of Sintered α-Alumina; Proceedings of the Third International Conference on Electric Charge, 1998, pp 567-70

{95} Yamaouchi T. and Kondo, R. , Electrical Resistance of Alumina Porcelain, J of Ceramic Association, Japan, 1950, Vol.58, No.645, pp 82-7

{96} B.V. Dutt and F.A. Kröger , High temperature defect structure of Iron Doped α-alumina, Journal of American Ceramic Society , 1975, Vol.58, No.11-12, pp 474-6

{97} F.G.Will, H.G. deLorenzi and K.H. Janora, Effect of crystal orientation on conductivity and elctron mobility in Single-Crystal alumina. , Journal of American Ceramic Society, 1992, Vol.75, No.10. pp 2790-94

{98} Schmalzried, Z.;Ionic and electronic conduction in binary oxides and there investigation by emf measurement; Journal of Physics and Chemistry., 1963, Vol. 38, No. 1-2, pp 87-102,

{99} Hensler, J.R. ,Henry, E.C. , Electrical resistance of Some Refractory Oxides and Their Mixtures in the Temperature Range 600°C to 1500°C, Journal of American Ceramic Society 1953, Vol.36, No.3, pp 76-83

{100} Watanabe, T., Aso, Y., Nakayama, C.; Ozone generation of bipolar-type ceramic Ozonizer Module with Semiconductor Ceramic Discharge Electrode; Japanese Journal of Applied Physics Part 1-Regular Papers Short Notes & Review Papers, 1993, Vol.32, No.3A, pp.1229-1235

{101} Dilger, H.H.; Untersuchungen Der Mechanischen Und Elektrischen Eigenschaften Von Al_2O_3 Mit ZnO- Und NiO-Zusaetzen Bei Hohen Temperaturen -2. Elektrische Eigenschaften. (Investigations of the Mechanical and Electrical Properties of Al_2O_3 with ZnO and NiO additives at High Temperatures - 2. Electrical Properties); Ber Dtsch Keram Ges., 1974, Vol. 51, No. 5, pp 123-126

{102} Marucco, J., Gautron, J. and Lemasson, P.; Thermogravimetric and electrical Study of Non-stoichiometric Titanium Dioxide (TiO_{2-x}) between 800 and 1100°C; Journal of Physics and Chemistry of Solids, 1981, Vol. 42, pp 363-67

{103} Petot-Ervas, G., Saadi, B., Petot, C. and Loudjani, M.; Transport properties of titanium-doped alpha-alumina: Experimental results; Journal of The European Ceramic Society, 1997, Vol.17, No.7, pp 943-950

{104} Mckee, W.D. Jr. and Aleshin, E.; Aluminium Oxide-Titanium oxide solid solution; Journal of American Ceramic Society , 1963, Vol. 46, No. 1, pp 54-58

{105} Roy, S.K. and Coble, R.L.; Solubilities of magnesia, titania and magnesium titanate in Al_2O_3; Journal of American Ceramic Society , 1968, Vol. 51, No. 1, pp 1-6

{106} Watanabe,T., Aoshima, T., Kitabayashi, T. and Nakayama, C.; Resistivity and Microstructure of Alumina Ceramics added with TiO_2 fired In reducing atmosphere; Nippon Seramikkusu Kyokai Gakujutsu Ronbunshi-Journal Of The Ceramic Society Of Japan, 1993, Vol.101,No.10,pp.1107-14

{107} Grimes, R.W.; Solution of MgO, CaO and TiO_2 in α-Al_2O_3; Journal of American Ceramic Society, 1994, Vol. 77, No.2, pp 378-84

{108} Gruber, H., Krautz, E.; Electrical-Conductivity, Thermopower, Hall-Coefficient and Magneto-resistance of Titanium-Oxides With Different Oxygen-Content; Zeitschrift Fur Metallkunde, 1986, Vol.77, No.4, pp.203-206

{109} Liu,M, Ota,.T, Yamai,.I ; Synthesis Of Low Thermal Expansive Ceramics in the System Nb2O5- TiO2 and Electrical-Conductivity of the Reduced Ceramics , Yogyo-Kyokai-Shi, 1987, Vol.95, No.6, pp 583-589

{110} Shibagaki,.S, Ito,.K, Haneda,.H, Tanaka,.J, Shirasaki,.S, Phase and Microstructure of $MgTiO_3$ Ceramic Fired in Reducing Atmosphere, Journal of The Ceramic Society of Japan, 1992, Vol.100, No.10, pp 1261-1265

{111} Catlow, C.R.A., James, R., Mackrodt, W.C. and Stewart, R.F., Defect Energies in α-Al_2O_3 and rutile TiO_2 . Physical Review B-Condensed Matter, 1982, Vol.25, No.2, pp 1006-26

{112} Kofstad, P., Diffusional transport in MnO, Solid State Ionics, 1984, Vol. 12, No. 3, pp101-11

{113} Kathrein, H. and Freud, F., Electrical-Conductivity of Magnesium-Oxide Single-Crystal below 1200K; J Phys. Chem. of Solids, 1983, Vol. 44, No.3, pp177-86

{114} Jimenez, M., Castaing, J., Rodriguez, A. and Marquez, R., Influence of Carbon on Creep of NiO Polycrystals Journal of Physics and Chemistry of Solids, 1986, Vol. 47, No. 3, pp 331-34

{115} Wang, H.A. and Kröger, F.A.; Chemical Diffusion in Polycrystalline Al_2O_3; Journal of American Ceramic Society, Vol. 63, No. 11-12, 1980, pp 613-19

{116} Arashi, H. and Naito, L.H.; Oxygen permeability in ZrO_2-TiO_2-Y_2O_3 system; Solid State Ionics, 1992, Vol. 53-56, Pt 1, pp 431-35

{117} Mazen, S.A., Elfalaky,A.and Hashem,H.A.; Charge-Carriers and Mobility of Cu-Ti Ferrite; Applied Physics A-Materials Science & Processing, 1995, Vol.61, No.5, pp 559-563

{118} Miller, H. C., in ; High Voltage Vacuum Insulation; Basic concepts and Technology Practice, Edited by R.V. Latham (Academic Press, London, 1995), chapter 8.

{119} Published literature, Saphikon Inc

{120} Published literature Coors Ceramics Company

{121} Penn, S.J., Alford, N.M., Templeton, A., Wang, X.R., Xu, M.S., Reece, M. and Schrapel, K.; Effect of porosity and grain size on the microwave dielectric properties of sintered alumina; Journal of American Ceramic Society, 1997, Vol.80, No.7, pp1885-88

{122} Thorp, J.S., Akhtaruzzaman, M.And Evans, D.; The Dielectric-Properties of Alumina Substrates for Microelectronic Packaging; Journal of Materials Science, 1990, Vol.25, No.9, pp 4143-4149

{123} Molla, J., Heidinger, R. and Ibarra,A.; Alumina Ceramics for Heating Systems; Journal of Nuclear Materials, 1994, Vol.212-215, pp 1029-1034

{124} Atlas, L.M. Nagao, H. & and Nakamura, H.H., Control of Dielectric constant & Loss in Alumina Ceramics. , Journal of American Ceramic Society, 1962, Vol.45, No. 10, pp 464-71

{125} Hippel A.R. von, table of Dielectric Materials, Vol IV. Tech. Rept. 57 (Jan 1953), Vol. VI Tech Rept. 126 (June 1959) MIT Laboratory for Insulation Research.

{126} Gibbs, P. , Kinetics of High Temperature Processes, John Wiley & Sons, New York, 21-37, (1959)

{127} Alford, N.M. and Penn, S.J.; Sintered Alumina With Low Dielectric Loss; Journal Of Applied Physics, 1996, Vol.80, No.10, pp 5895-98

{128} Cahoon, H.P.and Christensen, C.J.; Sintering and grain growth of α-Al_2O_3; Journal of American Ceramic Society, 1956, Vol.39, pp 337-44

{129} Baei, Si. and Baik, S; Critical Concentration of MgO for the Prevention of Abnormal Grain-Growth in Alumina; Journal Of The American Ceramic Society, 1994, Vol.77, No.10, pp 2499-2504

{130} Buckley, S.N. and Agnew, P.; Radiation-Induced Changes in The Dielectric-Properties of Insulating Ceramics at ICRH Frequencies, Journal of Nuclear Materials, 1988, Vol.155, PtA, pp 361-365

{131} Ibarra, A., Heidinger, R. And Molla, J.; New Potentials for High Mechanical Strength Grades of Polycrystalline Alumina for EC Waves Windows; Journal of Nuclear Materials, 1992, Vol.191, PtA, pp.530-534

{132} Rao, K.V. and Samkula, A; Dielectric Properties of Cobalt Oxide, Nickel oxide and their Mixed Crystals; Journal of Applied Physics, 1965, Vol. 36, pp2031

{133} Yoshimura, M.Y. and Bowen, H.K.; Electrical breakdown strength of Alumina at high temperatures; Journal of American Ceramic Society , 1981, Vol. 64, No. 7, pp 404-10,

{134} Britt, E.J. and Davis, M.V.; Dielectric Breakdown in electrical Insulators used in thermionic converters; IEEE Thermionic conversion specialists conference, San Diego California, 1971, October 4-7, pp 137-46

{135} Bunag, M.M. and Koenig, J.H.; Ultra low loss Ceramic Dielectrics; Journal of American Ceramic Society, 1959, Vol. 42, pp 442-47,

{136} Owate, I.O., AC Breakdown Characteristics of Ceramic Materials, Journal of Applied physics, 1992, Vol.72, No.6, pp 2418-22

{137} Hibma, T. and Zeller, H.R.; Direct Measurement of Space-Charge Injection from a Needle Electrode into Dielectrics; Journal of Applied Physics, 1986, Vol.59, No.5, pp.1614-1620

{138} Zeller, H.R. and Schneider, W.R.; Electrofracture Mechanics of Dielectric Ageing; Journal of Applied Physics, 1984, Vol.56, No.2, pp.455-459

{139} German, R.M.; The microstructures of Liquid Phase Sintered Materials; Sintering Technology, Edited by R.M. German, G.L. Messing, R.G. Cornwall Published Marcel Dekker, Inc, 1996, pp 213-20

{140} Ives, F.JA.,.Cahn, H.M and Harmer, M.P.; Coarsening behaviour of an Alumina- Zirconia composite; Sintering Technology, Edited by R.M. German, G.L. Messing, R.G. Cornwall Published Marcel Dekker, Inc, 1996, pp 341-48

{141} Taruta, S., Takano, T., Takusagawa, N., Okada, K. and Otsuka, N.; Liquid phase sintering of bimodal size distributed alumina powder mixtures; Journal of Materials Science, 1996, Vol.31, No.3, pp.573-79

{142} Kwon, O.H. and Messing, G.L.; Kinetic Analysis of Solution Precipitation during Liquid Phase Sintering of Alumina; Journal of American Ceramic Society, 1990, Vol. 64, No. 2, pp 275-81

{143} Song, H. and Coble, R.L.; Origin and growth of Platelike Abnormal grains in Liquid phase sintered Alumina; Journal of American Ceramic Society, 1990, Vol. 73, No. 7, pp 2077-85.

{144} Park, S.Y.; Influence of a liquid phase on the microstructure development of Al_2O_3 ; Journal of Materials Science Letters, 1996, Vol.15, No.10, pp.878-880

{145} Bennison, S.J. and Harmer, M.P.; Grain growth kinetics for Alumina in the Absence of a liquid phase; Journal of American Ceramic Society, Vol.68, 1985, No.1, C-22-24

{146} Seabaugh, M., Horn, D., Kerscht, I., Hong, S.H. and Messing, G.L.; Anisotropic Grain Growth in Alumina Ceramics; Sintering Technology, Edited by R.M. German, G.L. Messing, R.G. Cornwall Published Marcel Dekker, Inc, 1996, pp 341-48

{147} Kaysser, W.A., Sprisseler, M., Handwerker, C.A. and Blendell, J.E.; Effect of Liquid Phase on Morphology of Grain Growth in Alumina; Journal of American Ceramic Society , 1987, Vol. 70, No. 5, pp 339-43

{148} Funkenbusch, A.W. and Smith, D.W.; Influence of Calcium on the Fracture Strength of Polycrystalline Alumina; Metallurgy Transactions, 1975, Vol. 64, No.12, pp 2229-301

{149} Jupp, R.S., Stein, D.F. and Smith D.W ; Observations on the effect of calcium segregation on the fracture behaviour of polycrystalline alumina; Journal of Materials Science, Vol. 15, , 1980, pp 96

{150} Sinharoy, S., Levenson, L.L. and Ray, D.E.; Influence of Calcium Migration on the Strength reduction of Dense Alumina exposed to steam; American Ceramic Society Bulletin, Vol. 58,No.4, 1979, pp 464-66

{151} DeWith, G.; Fracture of translucent Alumina : Temperature dependence and influence of CaO; Journal of Materials Science, Vol. 19, No. 7 , 1989, pp 2195-2202

{152} Bae, S.I. and Baik, S.; Determination of critical concentrations of SiO_2 and CaO for Abnormal Grain Growth; Journal of American Ceramic Society , Vol. 76, No. 4, 1993, 1065-67

{153} Brook, RJ.; Controlled grain growth; Ceramic Fabrication Processes, Treatise on Materials Science and Technology-Vol. 9, Edited by F.F.Y. Wang, Academic Press, 1976, pp 331-64

{154} Thompson, A.M., Harmer, M.P., Williams, D.P., Soni, K.K., Chabala, J.M. and Levi-Setti, R.; Direct observation of Mg and Ca Segregation in Al_2O_3; Sintering Technology, Edited by R.M. German, G.L. Messing, R.G. Cornwall Published Marcel Dekker, Inc, 1996, pp 309-16

{155} Baik, S. and Moon, J.H.; Effects of MgO on grain Boundary segregation of Ca during sintering of alumina; Journal of American Ceramic Society , Vol. 74, No. 4, 1991, pp 819-22

{156} Stearns, L.C. and. Harmer; Grain Boundary Pinning in Al_2O_3 - SiC; Sintering Technology, Edited by R.M. German, G.L. Messing, R.G. Cornwall Published Marcel Dekker, Inc, 1996, pp 325-32

{157} Taruta, S., Kitajima, K., Takusagawa, N., Okada, K. and Otsuka, N.; Influence of coarse particle-size on packing and sintering behavior of bimodal size distributed alumina powder mixtures; Nippon Seramikkusu Kyokai Gakujutsu Ronbunshi-Journal of the Ceramic Society of Japan, 1993, Vol.101, No.5, pp.583-588

{158} Ikegami T., Kotani,K. and Eguchi, K.; Some roles of MgO and TiO_2 in densification of sinterable Al_2O_3; Journal of American Ceramic Society, 1987, Vol-70, No. 12, pp 885-890

{159} Bagley, R.D., Cutler, I.B. and Johnson, D.L.; Effect of TiO_2 on initial sintering of Al_2O_3; Journal of American Ceramic Society, 1970, Vol. 53, No. 3, pp 136-41

{160} Winkler, E.R., Sarvar, J.S. and Cutler, I.B.; Solid Solution of Titanium Dioxide in Aluminium oxide; Journal of American Ceramic Society , 1966, Vol. 49, No. 12, pp 634-37

{161} Powers, J.D. and Glaeser, A.M.; Titanium effects on Sintering and Grain Growth of Alumina; Sintering Technology, Edited by R.M. German, G.L. Messing, R.G. Cornwall Published Marcel Dekker, Inc, 1996, pp 333-40

{162} Morgan, PED and Koutsoutis, MS; Phase studies concerning Sintering In Aluminas Doped with Ti^{4+} plus ; Journal of the American Ceramic Society, Jun 1985, Vol.68, No.6, pp.156-158

{163} Kebbede, A., Messing, G.L. and Carim, A.H.; Grain Boundaries in Titania doped α-Alumina with Anisotropic Microstructure; Journal of American Ceramic Society, 1997, Vol.80, No.11, pp 2814-20

{164} Horn, D.S. and Messing, G.L; Anisotropic Grain Growth in TiO_2 -Doped alumina; Materials Science and Engineering, 1995, Vol. A195, pp169-78

{165} Lange, F.F.; Relation between Strength, Fracture Energy and Microstructure of Hot-Pressed Si_3N_4; Journal of American Ceramic Society, 1973, Vol. 56, No. 10, pp 518-22

{166} Lange, F.F.; Fracture toughness of Si_3N_4 as a function of Initial α-phase content; Journal of American Ceramic Society, 1979, Vol. 62, No. 7-8, pp C-428-30

{167} Lange, F.F.; Fabrication and properties of dence polyphase silicon nitride; American Ceramic Society Bulletin , 1983, Vol. 62, No.12, pp 1369-74

{168} Stough, M.A., Hellmann, J.R. and Conway, J.C.; The effect of grain-boundary devitrification on the wear of glass-bonded alumina ceramics; Journal of Materials Science, 1994, Vol.29, No.14, pp.3665-3672

{169} Techniques and mechanisms in Electrochemistry by P.A. Christenen and A Hammet; Publisher: Blackie Academic and Professional

{170} Jiang, S.P., Love, J.G. and Badwal, S.P.S.; Electrochemical Techniques in Studies of Solid Ionic Conductors; Electrical Properties of Oxide materials, Key Engineering materials Vols: 125-126 Edited by J.Nowotny nad C.C. Sorrell

{171} Bonanos, N., Steele, B.C.H,. Butler, E.P., Johnson, W.B., Worrell, W.L., Macdonald, D.D., and McKubre, M.C.H.; Applications of Impedance Spectroscopy; Impedance Spectroscopy-Emphasizing Solid Materials and Systems, Edited by J.Ross Macdonald, Publisher: John Wiley & Sons

{172} Joining of ceramics edited by M.G. Nicholas; Published for The Institute of Ceramics by Chapman and Hall; Advanced Ceramic Reviews

{173} Part 2. Determination of density and porosity; Advanced Technical ceramics-Monolithic ceramics-General and textural Properties; British Standard BS EN 623-2:1993

{174} Standard Test Method for Biaxial Flexure Strength (Modulus of Rupture) of Ceramic Substrates, ASTM Designation F394-78, 1991, American Society for Testing and Materials

{175} Biaxial Flexure Tests for Ceramics; Shetty D.K., Rosenfield, A.R., McGuire, P., Bansal, G.K., and Duckworth, W.H.; American Ceramic Society Bulletin, Vol 59, No. 12, 1980

{176} Ferreira, JMF, Tari, G, and Lyckfeldt; O; Influence of magnesia on drying-shrinkage behaviour of alumina; Key Engineering Materials, 1997, Vol.132-136, No.Pt 1, pp 358-361

{177} Personal communication with Dr. Andrew Hinton, of Solartron

{178} Solartron 1296 Operating Manual

{179} Discussions with Dr. Glenn Love

{180} Cullity, B.D.; Chemical Analysis by X-ray Diffraction; Chapter 14 in, Elements of X-Ray Diffraction, ssecond addition, publ. Addison-Wesley Publishing company Inc, pp411-415

{181} Brydson, R., Chen, Sc., Riley, F.L., Milney, S.J., Pan, X, and Rühle, M; Microstructure and Chemistry of Intergranular Glassy ilms in Liquid Phase Sintered Alumina; Journal of American Ceramic Society, 1998, Vol. 81, No. 2, pp 369-79

{182} JCPDS-1995, PDF no. 33-854 and 34-1062

{183} Bartkowiak, M, Mahan, GD, Modine, FA, Alim, MA, Lauf, R, McMillan, A; Voronoi network model of ZnO varistors with different types of grain boundaries; Journal of Applied Physics, 1996, Vol.80, No.11, pp.6516-6522 IS: 0021-8979

{184} Jerauld, G.R., Hatfield, J.C., Scriven, L.E., Davis, H.T.; Percolation and Conduction on Voronoi and Triangular Networks - A Case-Study in Topological Disorder; Journal of Physics C-Solid State Physics, 1984, Vol.17, No.9, pp.1519-1529

{185} Jerauld, G.R., Scriven, L.E., Davis, H.T.; Percolation And Conduction on the 3D Voronoi and Regular Networks - A 2nd Case-Study in Topological Disorder; Journal of Physics C-Solid State Physics, 1984, Vol.17, No.19, pp.3429-3439

{186} Stauffer, D.; Introduction to Percolation Theory; Chapter 1-2, Publ. Taylor & Francis, London and Philadelphia, 1985

{187} ibid, Chapter 5

{188} Last, B.J. and Thouless, D.J., Physics Review Letters, 1971, Vol. 27, pp 1719

{189} Hiemenz, P.C. and Rajagopalan, R.; Principles of Colloid and Surface Chemistry-3rd Addition; Chapter 13, pp 592, Publ. Marcel Dekker, Inc., New York, 1997

{190} Milling A and Vincent, B.; in Collodal Polymer Interactions-From Fundamentals to Practice, Edited by R.S.Farinato and P.L. Dubin, Chapter 6, pp 147-173, Publ. John Wiley & Sons, Inc, 1999.

{191} Rich, L.G., Chapter 11, Processes used in Gross Particulate Removal Trains; Environmental Systems Engineering; Publ. Mc-Graw Hill Book Company1973

{192} Endl H. and Hausner, H.; The influence of Impurities and Sintering Atmosphere on Optical and electrical properties of aluminium oxide, II: Electrical Properties; Ber Dtsh. Keram. Ges., 1980, Vol 57, No. 6-8, pp 128-134

{193} Hwang C.S. and Kim H.J.; Electrical conductivity of TiO_2 thin Film Deposited on Al_2O_3 Substrates by CVD; Korean Journal of Ceramics, 1995, Vol.1, No. 1, pp 21-28

{194} Engineering Properties of Single Oxides; Engineered Materials Handbook, Volume 4-Ceramics and Glasses, Publ. ASM International, 1991; pp 754-755.

{195} Blaise, G.; Fields and Polarisation, Conduction and Charge Trapping in Insulating Materials; Proceedings Third International Conference on Electric Charge, 1998, pp 25-37

{196} Bluementhal, R.N., Coburn, J., Baukus, J. and Hirthe, W.M.; Electrical conductivity of Nonstoichiometric Rutile single crystals from 1000°C to 1500°C,; Journal of Physics and Chemistry of Solids, 1966, Vol. 27, pp 643

{197} Kofstad, P., Oxides of Group IVA Elements in Nonstoichiometry , Diffusion, and Electrical Conductivity in Binary Metal Oxides, pp 143, A Wiley Interscience Co., NY, 1972

{198} Disdier J., Herrmann J.M.; Electrical properties of V_2O_5-WO_3/TiO_2 EUROCAT catalysts evidence for redox process in selective catalytic reduction (SCR) deNOx reaction; Catalysis Today, 2000, Vol. 56, No. 4, pp. 389-401

{199} Herrmann, J.M.,Disdier, J., Deo, G., and Wachs, I.E.; Semiconductive and redox properties of V_2O_5 /TiO_2 Catalysts; Journal of Chemical Society-Faraday Transactions, 1997, Vol.93, No.8, pp 1655-60.

{200} Yokoyama S., Ishikawa S., Fukuta S., Murata Y.; Photoelectrochemical properties of TiO_2 rutile microalloyed with 4d and 5d transition elements; Solar Energy Materials and Solar Cells, 2000, Vol. 62, No. 1, pp. 157-165

{201} Rusu G.I., Mardare D.; Structural and electrical properties of TiO_2 RF sputtered thin films; Materials Science and Engineering: B, 2000, Vol. 75, No. 1, pp. 68

{202} Viparelli, P., Ciambelli, P., Volta, Jean-C, Herrmann, Jean-M; In-situ electrical Conductivity study of Titania-supported Vanadium-Niobium oxide Catalysts used in Oxidative Dehydrogenation of Propane; Applied Catalysis A:General, 1999, Vol. 182, pp 165-73

{203} Rekas M.,, Radecka M., Nowotny J; Semiconducting Properties Of Undoped TiO_2 . Journal of Physics and Chemistry of Solids, 1997, Vol. 58, No. 6, pp. 927-937

{204} Kim,M.H., Baek,S.B., Paik,U., Nam,S., Byun,J.D..; Electrical conductivity and oxygen diffusion in nonstoichiometric TiO2-x; Journal of the Korean Physical Society, 1998, Vol.32, No.Pt3 SS, pp S1127-S1130

{205} Frederikse, H.P.R.; Recent studies on Tutile (TiO_2); Journal of Applied Physics Supplement, 1961, Vol. 32 No. 10, pp 2211-15

{206} Isawa, K., Sugiyama, J., Yamauchi, H.; Synthesis and Electrical-Conductivity of Spinel Compounds in the $MgTi_2O_4.Mg_2TiO_4$ System; Physical Review B-Condensed Matter, 1994, Vol.49, No.2, pp.1462- 1465

{207} Pyun, S.I. and Kim, C.H.; Role of Hydrogen in the Electronic Transport Through Passivating TiO_2 Films; International Journal of Hydrogen Energy, 1992, Vol. 17, No.3, pp 205-9

{208} Eurocat oxide, Catalyst Today, 1994, Chapter 3.5, pp 20

{209} Sasaki, T.A., Baba, Y., Yamamoto, H., Sasase, M., and Isobe, S.; Photoelectron Spectroscopic and Surface-Resistance Measurements of TiO_2 and V_2O_5 after Rare-Gas Sputtering; Surface and Interface Analysis, 1993, Vol. 20, No. 8, pp 682-86

{210} Almond, D.P. and Vainas, B.; The Dielectric Properties of Random R-C Networks as an explanation of the Universal Power Law Dielectric Response of Solids; Journal of Physics: Condensed Matter, !999, Vol 11, pp 1-13

{211} Vainas, jB, Almond D.P., Luo, J. and Stevens, R.; An evaluation of Random R-C Networks for modelling the bulk ac electrical response of ionic conductors; Solid State Ionics., 1999, Vol.126, pp 65-80